

Towards the Understanding and Development of Single Atom Alloy Catalysts from First Principles

A doctoral thesis by

Matthew T. Darby

In partial fulfilment of the requirements for the degree of

Doctor of Philosophy

at

University College London

Supervised by

Dr. Michail Stamatakis & Prof. Angelos Michaelides

Department of Chemical Engineering

UCL

I, Matthew T. Darby confirm that the work presented in this thesis is my own. Where information has been derived from other sources, I confirm that this has been indicated in the thesis.

Signed:

I dedicate this thesis to my darling wife, Caroline and our beautiful son, Jacob.

Abstract

Many industrial heterogeneous catalysts often use precious metals such as Pt and Pd thanks to their ability to catalyse a vast array of chemical reactions with exceptional activity. Unfortunately, the excellent reactivity of these metals results in poor selectivity, high susceptibility to poisoning and catalyst deactivation. One strategy that has been fruitful in overcoming these shortcomings is to alloy the catalytically active metals with those that are more selective, for example the coinage metals. A special class of these bimetallic surfaces may be formed by doping the inert host metal with a sufficiently low concentration of the catalytically active metal such that these dopant atoms isolate as individual, atomic dispersed ensembles in the surface layer of the host metal; such a material is known as a *Single Atom Alloy (SAA)*.

In this thesis, we use a dual-scale theoretical approach to develop a fundamental understanding of SAAs and their behaviour in catalytic systems. On the atomistic level, we make use of density functional theory (DFT) to investigate the electronic structure of SAAs, evaluating their thermodynamic stability and quantifying their surface interactions with various chemical species. Combining data acquired from DFT with kinetic Monte Carlo (KMC) simulation, we perform dynamic studies on length scales that are more relevant to real catalysis, allowing for the prediction of catalytic metrics. In particular, we show that the surface chemical heterogeneity of a SAAs results in novel catalytic properties, arising from combined weak adsorption and low activation energies for several bond dissociation reactions; that Pt/Cu SAAs can perform low temperature C-H bond without carbon deposition; and that SAAs offer strong resistivity to catalytic poisoning.

Our findings will facilitate the discovery of new alloy catalysts that exhibit novel catalytic behaviour that can be fine-tuned in terms of activity, selectivity and stability.

Impact Statement

The global chemical industry is estimated to produce over £4.0 trillion in revenue during 2017. Forecasts suggest that an increasing population, evolving technologies and ultimately higher demand, will lead to significant market growth over the coming years. The majority of industrial chemical processes employ catalysts to improve efficiency, lower costs and reduce environmental impact. In fact, the industrial catalysis market is estimated to be worth over £15.0 billion where £10.8 billion is attributed to precious, platinum group metal (PGM) catalysts such as those made from Pd, Pt, Rh, Ir and Ru. PGMs find application in countless catalytic reactions and although they offer excellent performance, they are scarce and therefore very expensive. Seeking alternatives to traditional PGMs that exhibit as good, or better, levels of performance is very much a non-trivial task. It is on this topic that this thesis is based.

In this thesis, we study the catalytic properties of bimetallic alloys that are formed of single, dispersed PGM atoms in coinage metal host materials. These Single Atom Alloys (SAAs) are extremely economical, making use of the least amount of rare PGM as possible, yet still exhibiting excellent catalytic properties. However, research into SAAs is very much in its infancy, with only a few metal-metal combinations and a limited number of chemistries having been studied.

In order to search for viable SAAs that exhibit useful properties, experimentally one must resort to expensive and time-consuming trial-and-error methodologies. Such techniques, due to their very nature, inhibit the development of novel and exciting catalysts. Instead, in this thesis, we have used state-of-the-art theoretical modelling to aid in the design of SAA catalysts from first principles. We model SAAs on the molecular level before bridging length scales to that of real catalysts, allowing us to develop fundamental understanding of the physiochemical phenomena governing the excellent performance of SAAs, as well as to make predictions about which SAAs can catalyse which chemistries.

The work presented here will serve as a guide for experimental development of SAAs, facilitating their design and thereby promoting faster commercialisation of SAA catalysts. Once commercialised, SAAs will find application in petrochemicals, fine chemicals, pharmaceuticals, agrochemicals and many more. If indeed SAAs offer as good, or even better performance than traditional PGM catalysts, they will also significantly reduce costs as well as lowering environmental impact through lesser production of waste bi-products. The widespread use of PGM catalysts in the chemical industry means that there are many processes which stand to be optimised by the use of SAAs, to which this thesis will contribute.

Acknowledgements

I would like to extend my deepest gratitude to my advisor, Michail, for his constant support and guidance throughout my PhD. Without Michail, I certainly would not have enjoyed embarking on this journey quite as much as I have, and he has inspired me to continue on to a career in academia. In addition to supervision from Michail, Angelos has provided much insight as well as always being on hand to participate in useful discussions for which I am very grateful.

Also, I would like to thank Charlie Sykes and members of his research group at Tufts University, who helped to guide the research presented in this thesis from a practical, experimental point of view.

In my personal life, I am lucky enough to have a wonderful wife, Caroline, who's love, support and understanding have helped me through these last 4 years more than I can express in words. I'd like to thank her for putting up with me and always listening even when I ramble on about "catalysis this... and catalysis that", in fact I'm sure she knows just as much about the field as I do!!! Our son Jacob was born in August 2017 and though 5 weeks early (and 3 weeks before my original submission date), the thought of seeing him helped me to finish the writing of this thesis. I'd like make special mention to Luca, Lilly and Leo who I have had many interesting discussions with.

Finally, I would like to thank my family as well as that of Caroline, who have always wished for the best for me and have shown me endless love.

Thank you.

List of Publications

A list of publications that are a result of works carried out during this PhD is given below:

- i. **M. T. Darby**, S. Piccinin and M. Stamatakis (2016). “Chapter 4: First Principles-based Kinetic Monte Carlo Simulation in Catalysis”. Institute of Physics e-book on “Physics of Surface, Interface and Cluster Catalysis”, edited by Kasai, H. and M. C. S. Escaño.
- ii. F. R. Lucci, **M. T. Darby**, M. F. G. Mattera, C. J. Ivimey, A. J. Therrien, A. Michaelides, M. Stamatakis and E. C. H. Sykes (2016). “Controlling Hydrogen Activation, Spillover, and Desorption with Pd–Au Single-Atom Alloys”. *Journal of Physical Chemistry Letters*, **7**(3): 480-485.
- iii. Z. Wang, **M. T. Darby**, A. J. Therrien, M. El-Soda, A. Michaelides, M. Stamatakis and E. C. H. Sykes (2016). “Preparation, Structure, and Surface Chemistry of Ni-Au Single Atom Alloys”. *Journal of Physical Chemistry C*, **120**(25): 13574–13580.
- iv. Guoliang Liu, A. W. Robertson, M. M. Li, W. C. H. Kuo, **M. T. Darby**, M. H. Muhieddine, Y. Lin, K. Suenaga, M. Stamatakis, J. H. Warner and S. C. Edman Tsang (2017). “MoS₂ Monolayer Catalyst Doped with Isolated Co Atoms for the Hydrodeoxygenation Reaction”. *Nature Chemistry*, **9**: 810-816.
- v. M. D. Marcinkowski, **M. T. Darby**, J. Liu, J. M. Wimble, F. R. Lucci, S. Lee, A. Michaelides, M. Flytzani-Stephanopoulos, M. Stamatakis and E. C. H. Sykes (2018). “PtCu Single Atom Alloys as a Coke Resistant Strategy for Efficient C-H Activation”. *Nature Chemistry*, **10**: 325–332.
- vi. **M. T. Darby**, E. C. H. Sykes, A. Michaelides and M. Stamatakis. “Elucidating the Stability and Reactivity of Surface Intermediates on Single Atom Alloy Catalysts (2018)”. *ACS Catalysis*, ASAP online publication.
- vii. F. R. Lucci, **M T. Darby**, M. D. Marcinkowski¹, A. Michaelides, M. Stamatakis and E. C. H. Sykes, “Hydrogen Uptake on and Release from Pt-Cu Alloys with a “Leaky” Molecular Cork” (2018), *Journal of Physical Chemistry C*, manuscript under review.
- viii. **M T. Darby** and M. Stamatakis, “Enhanced CO Tolerance during the Selective Hydrogenation of Acetylene on Cu-based Single Atom Alloy Catalysts” (2018), manuscript in preparation.

Table of Contents

Chapter 1 Background and Overview.....	19
Introduction	19
An Overview of Heterogeneous Catalysis.....	19
Fundamental Concepts in Heterogeneous Transition Metal Catalysis.....	21
The Sabatier Principle	22
Rationalising Trends in Adsorption Behaviour Across the Transition Metals	24
Predicting Adsorption Energies using Thermo-chemical Scaling.....	25
Using Descriptors to Bridge Thermochemistry with Kinetics.....	26
Bimetallic Alloys in Catalysis.....	30
Modifying the Surface Reactivity by the Ligand Effect.....	31
The Influence of Spatial Distribution and the Ensemble Effect	32
Single Atom Alloys as Novel Catalytic Materials	33
Chapter 2 Theoretical Methods.....	39
Introduction	39
Schrödinger's Equation.....	39
The Born-Oppenheimer Approximation	40
Hartree-Fock Molecular Orbital Theory.....	44
Density Functional Theory	50
The Uniform Electron Gas “Jellium” and the Thomas-Fermi Model.....	52
The Hohenberg-Kohn Theorems	53
Kohn-Sham Theory.....	55
Approximating the Exchange-Correlation Term.....	57
The Generalised Gradient Approximation.....	59
Hybrid Functionals and Self-Interaction	62
Practical Considerations	64
Brief Summary	68
Kinetic Monte Carlo.....	69
Rare Event Dynamics and the Timescale Problem.....	69
The KMC Trajectory and Coarse-grained Time Evolution	70
The Master Equation	73
Determining the Rate Constants of an Elementary Process.....	76
Algorithms and Implementation	84
Brief Summary	97

Conclusion	98
Chapter 3 Towards the Development of Single Atom Alloy Catalysts as a Means of Escaping Linear Scaling Relations	99
Introduction	100
Computational Details	103
Results and Discussion.....	105
Thermo-chemical Scaling Relations on Single Atom Alloys.....	105
Escaping the Brønsted-Evans-Polanyi Relationship using Single Atom Alloys	111
Conclusion	123
Chapter 4 Pt/Cu Single Atom Alloys as a Coke Resistant Strategy for Efficient C-H Activation	125
Introduction	126
Reaction Network and Lattice Model	128
Rate Constants from DFT	130
Computational Details.....	130
Density Functional Theory Setup.....	130
Kinetic Monte Carlo Setup	131
Results and Discussion.....	132
C _x H _y Adsorption Geometries and Energetics.....	132
Activated Complexes and Potential Energy Surface.....	138
Energy Landscape for Methane Dehydrogenation.....	146
Thermal Desorption Simulations.....	149
Conclusion	172
Chapter 5 Carbon Monoxide Poisoning Resistance and Structural Stability of Single Atom Alloys.....	175
Introduction	176
Computational Details	178
Density Functional Theory Setup.....	178
Kinetic Monte Carlo Setup	179
Rate Constants from Density Functional Theory	179
Results and Discussion.....	180
CO Adsorption on Pure Metal and SAA Surfaces.....	180
Temperature Programmed Desorption Simulations	184
Simulated Desorption Peak Temperatures	184
Adsorbate-Induced Structural Changes in SAAs	187

Surface Segregation	188
CO Induced Surface Segregation	189
Surface Aggregation and Island Formation	192
CO Induced Aggregation and Island Formation.....	194
Conclusion	198
Chapter 6 Concluding Remarks and Future Work.....	201
Summary and Conclusion	201
Further Avenues of Research	203
Fast Prediction of SAA Catalytic Behaviour using Descriptors	204
Selective Hydrogenation of Unsaturated Hydrocarbons	206
Carbon-Carbon Coupling on Pt/Cu Single Atom Alloys	208
Structure-Activity Relations in Single Atom Alloy Nanoparticles	209
Conclusion.....	211
Final Remarks.....	211
Chapter 7 Bibliography.....	213

Chapter 1 Background and Overview

Introduction

The global chemical industry is estimated to produce over £4.0 trillion in revenue during 2017.¹ Forecasts suggest that an increasing population, evolving technologies and ultimately higher demand, will lead to significant market growth over the coming years. The majority of industrial chemical processes employ catalysts to improve efficiency, lower costs and reduce environmental impact. In fact, the industrial catalysis market is estimated to be worth over £15.0 billion where £10.8 billion is attributed to precious, platinum group metal (PGM) catalysts such as those made from Pd, Pt, Rh, Ir and Ru.²

Catalysts may be used in homogeneous, single-phase processes or heterogeneous, multi-phase processes.^{3, 4} Industrial scale application of homogeneous catalysis will typically result in difficulties with large scale separation of the catalyst and products, thereby making their industrial use somewhat limited.³ Much more commonly, heterogeneous catalysts (typically solids with liquid and gas phase reactants or products) are found in industrial settings as they are much more practical to use on a large scale.^{4, 5} There are many examples of industrial heterogeneous catalysts, with the most common types including zeolites and transition metals, as well as oxides and alloys thereof.^{4, 5}

It is on the latter, heterogeneous transition metal alloy catalysts that this thesis will be based. In this chapter, we continue from this point on to guide the discussion towards the fundamental aspects dictating the catalytic performance of these materials, before highlighting current progress in the research and development of a special class of highly dilute binary transition metals, known as *Single Atom Alloys*.⁶ It is these *Single Atom Alloys* that will form the focus of this thesis.

An Overview of Heterogeneous Catalysis

In general, a catalyst can reduce the energy required to perform a chemical conversion, allowing for a process to take place at low temperatures and pressures.³⁻⁵ Thus, choosing

the best possible catalyst can dramatically reduce industrial operating costs, maximise output and prevent unnecessary damage to the environment.³⁻⁵ An optimal catalyst should promote fast conversion of reactants (activity) over a long operating time (stability) and exhibit a strong preference for desired products (selectivity).^{4, 5} Therefore, in order to make an informed decision about which catalyst to use when, one must have an understanding of the fundamental chemical properties of the material and its interaction with substrates.

A heterogeneous catalytic process may be thought of in terms of elementary steps and events. Most processes begin with adsorption of reactants followed by surface diffusion, reactions and the eventual desorption of products. The role of the catalyst in this process is to offer a pathway from the substrate to the desired product with a high activity and high selectivity.⁵ The observed rate of reaction is linked to the activation barriers for each microscopic elementary process, which when combined together, contribute to the macroscopic reaction.^{4, 7-10} Thus, it follows that a fundamental understanding of each elementary process can be used to comprehend the catalytic cycle as a whole.

The key properties of catalysts that give rise to high performance are often difficult to decompose due to the intricacy of the networks of elementary steps that underpin the catalytic cycle.^{4, 7-10} From an experimental point of view, it is often only possible to observe the net effect of a microscopic reaction network, thereby limiting the scope for fine-tuning catalytic properties and indeed designing catalysts.¹¹ It follows that the complexities within even the most simple heterogeneous catalytic process have ensured that more commonly than not, new catalysts are developed based on trial-and-error methods rather than by design.

One strategy that can enable the full decomposition of a reaction network and subsequent comprehension of macroscopic observables, is to use theoretical modelling that bridges multiple length and time scales.¹¹ One can employ atomistic modelling using theoretical methods derived from first principles, such as Density Functional Theory (DFT), to study the interaction of substrates with catalytically active sites.¹¹ Kinetic Monte Carlo (KMC)

simulation can facilitate the transition from the molecular level to macroscopically relevant length scales, allowing one to evaluate the performance of a catalyst based on criteria such as activity, selectivity and stability.^{8, 10}

By using a multiscale hierarchical modelling approach, a fundamental understanding of the inner-workings of a catalyst can be achieved whilst retaining a strong link to the macroscopic performance.¹⁰ The application of such a methodology will ultimately facilitate the optimisation and rational design of catalytic materials.^{11, 12} It is this approach that the author has taken in this thesis. Here, we will be using cutting-edge modelling techniques to assess the catalytic performance of a special class highly dilute binary transition metal alloys, known as *Single Atom Alloys*.⁶

We will proceed by giving a brief overview of fundamental concepts underpinning heterogeneous catalysts. These concepts are currently used to rationalise and predict the behaviour of transition metal heterogeneous catalyst and are referred back to throughout this thesis. Finally, at the end of this chapter, we will introduce the topic of bimetallic catalysis and in particular focussing on *Single Atom Alloys*.⁶

Fundamental Concepts in Heterogeneous Transition Metal Catalysis

As we alluded to earlier, the most commonly used types of heterogeneous catalyst are transition metal element based; these come in many forms including carbides, chalcogenides, oxides and of course pure elemental metals and bimetallic alloys thereof.³⁻⁵ Historically, the latter two have found major application in a variety of industrial processes, from the generation of synthesis gas¹³ though to the production ammonia¹⁴, as well as in the hydrogenation of unsaturated hydrocarbons and for the manufacture of vast quantities of nitric acid.⁵ Transition metals and their alloys have found such broad catalytic application as a direct result of their widely ranging chemical properties; the late transition metals are much more commonly used as heterogeneous catalysts than those appearing earlier in the d-block.⁵

In general, for a given catalytic process there is a small subset of metals that offer superior catalytic performance over others. In many cases, this subset is the platinum group metals (PGMs) consisting of Pd, Pt, Rh, Ir, Ru and Os.⁵ The PGMs offer the best catalytic activity for the widest range of chemistries compared to any other subset. The Ferrous metals consisting of Fe, Co and Ni often exhibit strong catalytic properties in applications that require the scission of strong chemical bonds, such as for the use of Fe in the dissociative chemisorption of N₂ during the Haber process.^{5, 14} Though a Ferrous metal, Ni is often similar in catalytic behaviour to the PGMs and in some cases has comparable reactivity to Pt, albeit has a narrower range of applicability.¹⁵ Generally speaking, the coinage metals are somewhat inert when compared to the PGMs, typically exhibiting low activities albeit with very high reaction selectivities.

The Sabatier Principle

The catalytic performance of the transition metals can be summarised well by the observations of Paul Sabatier in the early 1900s.¹⁶ Sabatier suggested that optimal catalytic activity will be exhibited when the interaction between the catalyst and the substrate is “just right” (**Figure 1**).¹⁶ That is, if the surface-substrate interaction is too weak, the catalyst will not bind the reactants, whereas if it is too strong, the products will not desorb and the surface will poison. Of the transition metals, it is the PGMs that most commonly have the balance of catalyst-substrate interaction that is closest to being “just right”, giving rise to excellent catalytic activity for many chemical conversions. Thus, it comes as no surprise that the PGMs are the most commonly used materials in heterogeneous catalysis.²⁻⁵

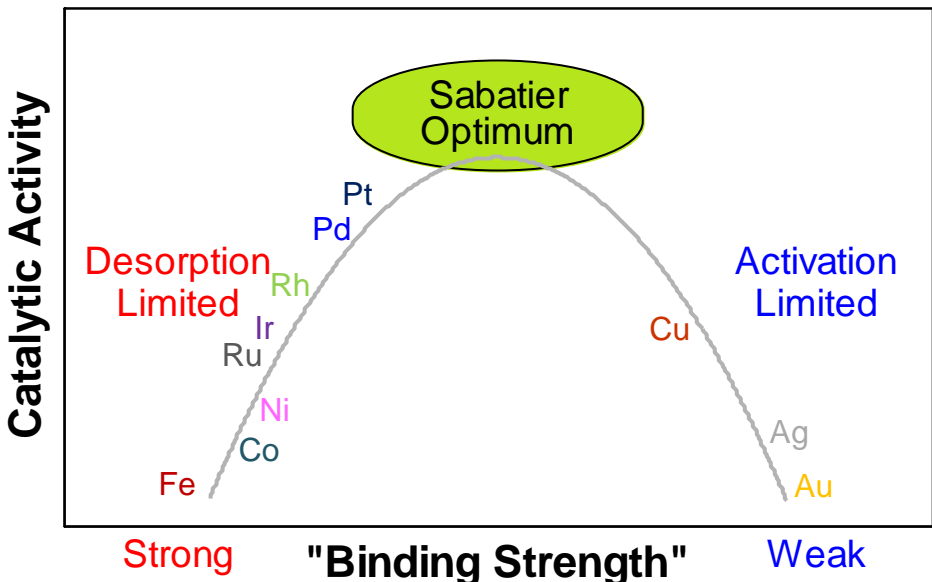


Figure 1: Illustration of the Sabatier principle as a volcano activity plot. The catalytic activity for a reaction is optimised when the catalyst binds substrates at an intermediate strength.

The relationship between catalytic activity and catalyst-substrate interaction strength gives rise to volcano-type plots (**Figure 1**) that have given a good, qualitative rationale to the reasons why we observe good activity for some catalysts but not for others.⁵ Moreover, the volcano-type structure of the relationship suggests that there exists a catalyst with optimal activity. This model is, as we suggest, qualitative and consequently it cannot be used to predict the activity of a catalyst.⁵ Though this relationship exists, it is unclear from the model how the “binding strength” is defined and what values it must take to optimise the catalyst.

Thus, the application of the Sabatier principle in the design of catalysts is somewhat limited.

Quantification of the binding strength is necessary in order to apply the Sabatier principle in design and indeed, quantitative analysis.^{7, 17} The advent of high performance supercomputing and efficient electronic structure methods such as DFT, have facilitated this. DFT has been employed to systematically investigate the catalytic behaviour of surfaces, considering their adsorptive and reactive properties with sufficient accuracy to strike comparison with experiment.

By performing a wide-ranging study across a range of catalytic surfaces (e.g. the transition metals), one can determine trends and correlations that lead to the identification of descriptors for catalytic activity.^{11, 12, 17, 18} A descriptor is a property of the catalyst that is

simple to quantify and is well correlated with an array of more complex catalytic properties.^{11, 12, 17, 18} Identification of descriptors will and thereby allow for fast identification of materials that may exhibit enhanced catalytic behaviour.^{11, 12, 17, 18} We briefly summarise some of the key descriptor based concepts that have revolutionised research and development on heterogeneous transition metal catalysis.

Rationalising Trends in Adsorption Behaviour Across the Transition Metals

Developing an understanding of how the adsorption energy of a species varies between transition metals is essential.⁵ Hammer and Nørskov derived the d-band model that uses the average energy of the d-band relative to the Fermi level as a descriptor for the adsorption energy;¹⁹⁻²¹ This energy is in turn a descriptor for the catalytic activity of the material (**Figure 1**). The “d-band model” assumes that transition metal s- and p-states interact with adsorbates to the same extent, irrespective of the metal,²² thereby contributing the same amount to the metal-adsorbate bond strength. Therefore, variation in the adsorption energies of a species across the transition metals is solely attributed to differences in the electronic structure of the d-band.¹⁹⁻²¹

The total value of the adsorption energy is determined by the sum of energy contributions from s/p/d-band coupling with the adsorbate molecular orbitals. According to Hammer and Nørskov, the contribution to the adsorption energy from the s/p-band coupling is constant across the metals. However, the energy contribution from the d-band depends on the extent of the hybridisation with the molecular orbitals of the adsorbate and the subsequent filling of hybrid bonding and anti-bonding orbitals by d-electrons. It follows that for a given adsorbate there exists a strong, linear correlation between the d-band centre (that is, the average energy of the d-states with respect to the Fermi level) and the adsorption energy.¹⁹⁻²¹

The d-band model has been applied extensively to transition metals. It is applicable to materials with uniform or periodic surface electronic structures and in the vast majority of cases, has proven extremely useful in the facile extraction of adsorption energies. In particular, as we will allude to later, estimation of the adsorption energy on transition metal

alloys is facile and at least qualitatively accurate such that one can easily determine if the activity of that alloy is better than its monometallic counterparts.

The d-band model has provided us with a fundamental understanding of the reasons behind the observed adsorption behaviour of transition metals. However, to employ the d-band model, one must have information about the adsorption energy of an adspecies such that it may be correlated to the d-band centre before predictions based on the trend can be made. Thus, we now discuss a second descriptor based model that has the capacity to predict the adsorption energies of chemically related species from one another.

Predicting Adsorption Energies using Thermo-chemical Scaling

An extension of the d-band model by Abild-Pedersen *et al.*, considering the effect of the electronic structure of the adsorbate, gave rise to the concept of thermo-chemical scaling (TCS).²³⁻²⁵ TCS states that there is linear proportionality between the adsorption energy of two chemically similar species. That is, if a pair of adsorbates a_1 and a_2 interact with the surface via atom A, then their adsorption energies will be correlated irrespective of the rest of the adsorbate structure. Though the adsorption energies are linearly correlated, the constant of proportionality is shown to be dependent on the valency of the adsorbing atom A.²³ Thus, TCS is given by

$$E_{ads}(a_1) = \gamma \cdot E_{ads}(a_2) + \zeta; \quad (1)$$

where $E_{ads}(a_1)$ and $E_{ads}(a_2)$ are the adsorption energies of species a_1 and a_2 (both adsorbed via atom A), γ is the proportionality factor given by the valency divided by the maximum number of hybridised orbitals in atom A and ζ is a constant determined by the energetic reference state (usually $E_{ads}(a_1)$).²³

Given the adsorption energy of just a single adatom, one can easily approximate the adsorption energy of a more complex, though chemically similar species through TCS.^{18, 23-26} This is very useful as it is then possible to quickly approximate the value of the reaction energy (ΔE_{Rxn}) for an elementary process.

From a design point of view, TCS can give you the adsorption energy of all reaction intermediates in a catalytic pathway.^{18, 23, 26} One could employ TCS, for example, to easily identify materials that bind intermediates very strongly, thereby prompting one to rule them out as potential catalysts due to risk of poisoning. A similar analysis could be performed for the entire reaction pathway, looking for notably weak or strong binding adsorbates with a view of identifying the catalytic material that gets this balance “just right”.^{18, 23, 26}

The d-band model and its extension to TCS have proven tremendously useful to both theorists and experimentalists alike.^{7, 17, 27} Though the d-band model can predict the adsorption energy of a substrate binding to a catalyst and TCS can be used to ascertain ΔE_{Rxn} , they still do not directly give information about the specific value of the binding strength that corresponds to the Sabatier Optimum (**Figure 1**). One either requires prior knowledge of the catalytic activity, for example from experiment, in order to determine the activity-binding relationship, or must be able to calculate it using theoretical methods. Thus, we introduce our final descriptor based model that allows for prediction of the activation energy from the adsorption energy.

Using Descriptors to Bridge Thermochemistry with Kinetics

The activity of a catalyst is primarily a kinetic phenomenon. Thus in order to gauge this activity, it is necessary to determine the activation barriers for the elementary processes comprising the catalytic cycle. This can be achieved by using DFT, though transition state searches are computationally expensive and so are impractical for the kind of broad scale screening study required when searching for new catalytic materials.

Interestingly, a theoretical model posed by Ronald Bell²⁸ and separately by Meredith Evans and Michael Polanyi,^{29, 30} expresses the activation energy in terms of the enthalpy change upon a chemical transformation. This theoretical construct is known as the Brønsted-Evans-Polanyi (BEP) relationship and provides the final link that gives firm justification to the model suggested by Sabatier. The context of the model proposed by Bell, Evans and Polanyi is a little distant from something applicable to heterogeneous catalysis though the rationale, when reapplied, is very much relevant. In light of this, we briefly summarise a fine

interpretation of the BEP relationship by Rutger van Santen, that is within the remit of heterogeneous transition metal catalysis.⁹

Let us assume that the potential energy basin for a stable configuration can be approximately judged to be harmonic (**Figure 2**). Then define a reaction coordinate along the axis of a bond that is breaking during a simple chemical dissociation. If we envisage two cases; first the elongation of the dissociating bond from the initial state reactant and second, the coming together of the dissociated products. As both of these processes occur, the energy increases from each respective minimum, up the walls of the basins. At some point, the harmonic potentials intersect and this curve crossing corresponds to the transition state (TS).⁹

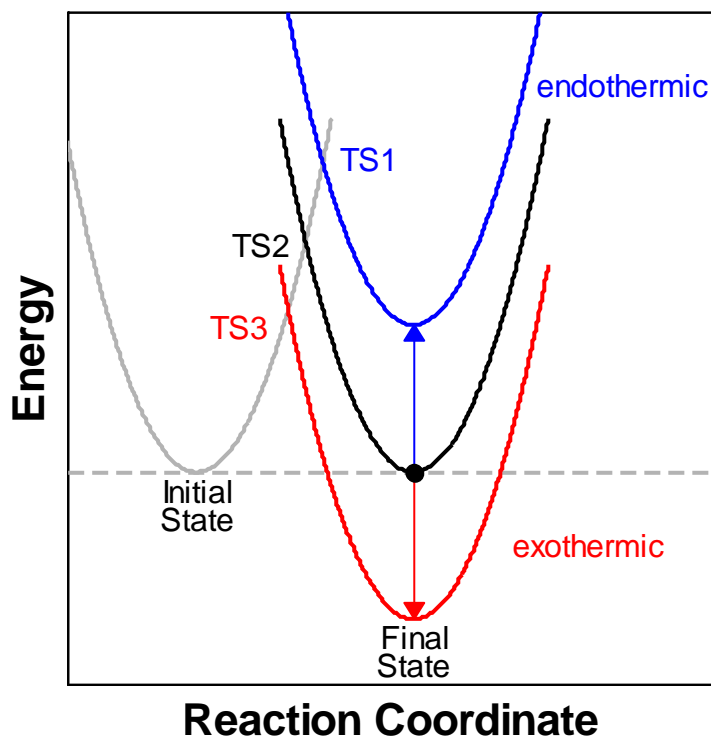


Figure 2: Schematic illustrating the principles underpinning the Brønsted-Evans-Polanyi relationship using harmonic potential energy plots as a theoretical example. Three reaction coordinates are shown for an endothermic reaction (blue) proceeding via transition state 1 (TS1), an isoenergetic transformation (black) proceeding via transition state 2 (TS2) and an exothermic reaction (red) proceeding via transition state 3 (TS3).

The point of intersection is proportional to the position of the harmonic potentials relative to each other.⁹ A change in the respective energies between the initial and final states is represented by a shift in the energy of the harmonics (**Figure 2**). We define the proportionality between the point of intersection and the relative position of the harmonic

minima using α . As the harmonic minima correspond to stable adsorbed species and the point of intersection is equivalent to the transition state, we can reinterpret this picture such that it becomes more physically relevant. Therefore, α is the proportionality constant between the reaction energy ΔE_{Rxn} and the activation barrier E_a which forms the premise of the BEP relationship.⁹ We define the BEP relationship such that

$$E_a = \alpha \cdot \Delta E_{Rxn} + \beta; \quad (2)$$

where β is an intrinsic energy barrier that defines the reference state (usually with respect to the energy of the reactant state) and is dependent on the material as well as the reaction.

For a reaction whereby the reaction energy is positive, the final state energy is destabilised with respect to the initial state, thereby increasing the energy of the curve crossing and indeed the activation barrier; this is depicted by TS1 and the blue line in **Figure 2**.⁹ On the other hand, for an elementary event with negative reaction energy the final state is more stable than the initial state, thereby lowering the energy of the curve crossing and correspondingly reducing the activation energy; this is depicted by the TS3 and red lines in **Figure 2**.⁹

The implications of the BEP relationship on heterogeneous catalysis are that materials which bind adsorbates weakly, will exhibit high activation barriers for surface bound processes, whereas those materials that bind adsorbates more strongly will exhibit analogously low activation barriers.⁹ The proportionality of the activation energy with the reaction energy in the BEP relationship links nicely back to the Sabatier principle. We discussed before how Sabatier suggested that to achieve optimal activity, the catalyst must find the right balance between strong and weak binding.

The BEP relationship tells us that those catalysts that bind adsorbates strongly also exhibit low activation barriers, thereby removing kinetic limitations for surface reactions to proceed.⁵

⁹ As a result, the surface catalysis will tend not to be kinetically limited and will proceed along the reaction coordinates with the most negative reaction energies. Consequently, the strong binding catalyst will not be able to desorb products without overcoming high activation

energy due to high adsorption energy. Thus, the activity of strong-binding surfaces is rate limited by the desorption of products, as was suggested by Sabatier (**Figure 1**). Even if it were possible to desorb products, the BEP relationship suggests that the strong binding will result in a large number of low-activation processes occurring on the surface, thereby giving poor reaction selectivity.

On the other hand, according to the BEP relationship surface elementary events from initial weakly bound states proceed with high activation barriers. This provides a kinetic limit that prevents surface elementary reactions from occurring without significant thermal activation. Consequently, weak-binding surfaces exhibit low activity as observed by Sabatier (**Figure 1**). However, surfaces that bind adsorbates weakly will be highly selective as alternate surface reaction pathways also have high activation barriers.^{5, 9}

Therefore, it comes as no surprise that for a set of materials that adhere to the BEP relationship, the optimal catalytic activity is achieved by the material that binds adsorbates at intermediate strength, thereby exhibiting intermediate activation energy.

Until recently, the BEP relationship was more of an empirical observation rather than a tool for catalyst design. However, extensive quantification using DFT has established the BEP relationship as a powerful method for quick and accurate prediction of the kinetics of elementary reaction events.^{9, 31-34} Moreover, when combined with TCS and the “d-band model”, the catalytic activity of a material or indeed a Sabatier volcano-plot, can be estimated from just a few simple calculations, thereby facilitating facile screening of a wide array of materials that adhere to such descriptor based models.^{11, 33, 35-38}

DFT calculations detailing the BEP and TCS relations show that there is near universality in their application across a wide range of materials, including transition metals and their alloys.^{23, 26, 27, 32-34, 39-45} This ubiquity has made the identification of the best catalytic surface for a particular chemistry much easier, from a given set of materials. Though extremely useful, the nature of the BEP relationship and TCS inevitably imposes limitations on the maximum performance of a catalyst.^{9, 18}

This raises the question, if a material did not adhere to the “d-band model”, TCS and the BEP relationship, could it offer enhanced catalytic behaviour that is beyond that predicted by these descriptor based linear models? In order to deviate from these models, the surface would need to have a non-uniform distribution of its density of states across the surface, which in turn will allow for variable adsorption properties across the surface thereby giving the opportunity to combine low activation energies with subsequent weak binding.

This combination is in direct violation of TCS and the BEP relationship, though as we show in this thesis can be achieved through the use of highly dilute binary metal alloys. Thus, these *Single Atom Alloys*⁶ are able to exhibit high reaction selectivities as well as excellent activity and strong resistance to catalytic poisoning. Therefore, in the following section, we will detail what a *Single Atom Alloy* is before giving examples of cutting-edge experimental and theoretical work on *Single Atom Alloy* catalysts. We will begin by make reference to bimetallic alloy materials in general, such that we can discern how *Single Atom Alloys* are unique.

Bimetallic Alloys in Catalysis

It is logical to think that alloying a catalytic metal, such as the PGMs, with a more inert metal, such as the noble coinage metals, would result in some hybrid material that can combine high activity with high selectivity. This rational is built upon knowledge that the PGMs exhibit low activation barriers, whereas the coinage metals bind adsorbates weakly. Therefore a combination of these properties would lead to enhanced catalytic performance.

The properties of bimetallic alloys are difficult to predict, they may adopt some of the characteristics of their constituent elements, however they also exhibit distinct properties^{15, 39, 46-48} that arise due to the interplay between modified electronic (ligand effects)⁴⁹⁻⁵¹ and geometric structures (ensemble effects).^{51, 52} Therefore, it is not as simple to describe binary alloys by taking a linear combination of their parent metal properties. We will briefly touch upon both ligand and ensemble effects here.⁵¹

Modifying the Surface Reactivity by the Ligand Effect

Bimetallic materials have modified electronic structures compared to their monometallic counterparts.⁵¹ The electronic structure of the material will determine its reactivity and therefore it is unsurprising that bimetallic alloys have different adsorption properties compared to pure transition metals. The electronic structure is composition dependent and contributions can be decomposed into effects caused by changes in the overlap of metal d-orbitals upon alloying; we refer to such changes in the overlap as the ligand effect.⁵¹

The ligand effect can be described by two qualitative arguments.⁴⁹⁻⁵¹ Incorporation of a secondary metal atom into a metal structure with a different lattice constant to that of the dopant, will result in a size mismatch and consequently, structural strain.⁴⁹⁻⁵¹ Strain can come in two forms; tensile, where a smaller atom is incorporated into a larger host matrix and compressive, where the solute atom is larger than the host matrix. Regardless of the type of strain caused by alloying, it will lead to a change in the average metal-metal bond compared to the monometallic metal lattices. A change in the metal-metal bond length results in a change in orbital overlap and thereby modifying the electronic structure of the material.⁴⁹⁻⁵¹ The second part of the ligand effect arises due to differing diffusivity as well as energy mismatches between the d-orbitals of different metal atoms.⁴⁹⁻⁵¹

This also affects the extent of the orbital overlap and therefore the electronic structure. Both of these ligand effects alter the alloy d-band width, energy and occupation compared to the pure constituents.⁴⁹⁻⁵¹ Using the d-band model, the effect of the modified electronic structure can be assessed. The ligand effect ultimately manifests as a change in the metal d-band centre, consequently altering the adsorption properties of the material.⁴⁹⁻⁵¹ The width of the d-band is modified as a cumulative effect from both components of the ligand effect as the width is proportional to the overlap of d-orbitals. To maintain constant d-band filling, the average energy of the d-band is increased or decreased depending on whether the d-band becomes narrow or wider.⁴⁹⁻⁵¹

The changes in the d-band for typical bimetallic alloys are reflected in changes in the adsorption energy of adsorbates on the material surface. In fact, the linear relationship found between the d-band centre and the adsorption energy on well-mixed alloy surfaces is preserved with the same fitting parameters as on the pure transition metals.⁴⁹⁻⁵¹ This indicates that despite variation of the atoms across the surface of well-mixed 1:1 composition binary alloys, the electronic structure is averaged across the material. Uniformity in the electronic surface structure is also preserved for monolayer or sandwich structure alloy types.^{39, 48}

Briefly re-visiting the Sabatier principle, as the binary alloy types mentioned in the previous paragraph adhere to the d-band model of the pure transition metals, it follows that they must offer adsorbate binding strength that places them on the Sabatier curve. The optimal blend of metals, for a particular reaction, can result in a climb up the volcano activity plot into the Sabatier Optimum region, thereby exhibiting the best possible activity for materials that adhere to the descriptor based models we have discussed so far.

The ligand effect is the major effect in play when considering well-mixed, comparable ratio alloys as well as monolayer and sandwich structures. However, when considering bimetallic alloys where metal atoms cluster, there is chemical heterogeneity in the surface we must consider the spatial distribution of each element in the ensemble effect.⁵¹

The Influence of Spatial Distribution and the Ensemble Effect

Aggregates of dopant atoms in an alloy surface tend to form when there is a notable disparity between the stoichiometry of each constituent. Depending on the mixing enthalpies, temperatures and methods of synthesis, ensembles such as monomers, dimers, trimers and general islands can form.⁵² These ensemble structures can have distinct catalytic properties that are linked to the spatial arrangement of the atoms within the structure. Such behaviour is known as the ensemble effect.^{51, 52}

Harnessing the power of the ensemble effect is a challenge experimentally.⁵² Without a well-defined ensemble size distribution, it is difficult to determine the cause of the catalytic activity

observed for a clustered metal alloy. The sophistication of modern surface science techniques has allowed for the characterisation of extended binary alloy surfaces. A combination of techniques, such as scanning tunnelling microscopy and temperature programmed desorption, can be used to relate the atomic structure of a surface to its reactivity.⁵ These techniques are essential to study the how the ensemble effect is linked to the chemistry of the bimetallic catalytic surfaces.

If one can determine the minimal ensemble size required to efficiently perform a particular catalytic reaction, one can reduce the cost of, for example, PGMs loaded into cheaper, less active materials. Moreover, if the ensemble size can be fine-tuned and well-characterised, it will be possible to select a catalytic architecture that gives the optimal balance of reaction selectivity and activity.⁵

It is with the ensemble effect in mind that we now proceed to our discussion on *Single Atom Alloys*⁶, which form the focus of this thesis. In the following section we will define exactly what a *Single Atom Alloy* is, we will convey why they are an exciting new class of material in the context of catalysis, as well as briefly highlighting the current status in their development.

Single Atom Alloys as Novel Catalytic Materials

The *Single Atom Alloys* (SAAs) of Sykes and co-workers are binary metal alloys of the catalytically active PGMs doped into inert noble metal hosts, whereby the concentration of PGM atoms is sufficiently low that the dopant will disperse as isolated, single atoms in the surface layer of the host material.^{6, 53-66} These SAAs are capable of exhibiting facile activation at the single atom sites, whilst retaining the high reaction selectivity of their noble metal host.^{6, 53-64, 67}

The first published article on SAA research was less than a decade ago.⁶³ It follows that the number of experimentally synthesised SAAs is few and includes alloy combinations of Pd-, Pt- and Ni-doped Cu in addition to Pd- and Ni-doped Au.^{6, 53-66} However with just these few surfaces, SAAs have been employed to catalyse the hydrogenation and dehydrogenation of

hydrocarbons,^{6, 53, 54, 58-63, 67} the hydrosilylation of α,β-unsaturated ketones and alkynes,⁶⁸ the decomposition of alcohol into organic acids^{57, 64} and the coupling of carbon-carbon bonds.

The catalytic activity in conversions performed by SAAs is enhanced dramatically compared to the pure noble metals and the reaction selectivity, as well as resistance to catalytic poisoning is unrivalled by other PGM catalysts.

Early research into SAAs and their catalytic properties has focussed mainly on hydrogenation.^{6, 53, 54, 58-63, 67} Surface science experiments were used to demonstrate that SAAs are capable of performing facile hydrogen activation at the PGM dopant atom, followed by subsequent spillover of hydrogen adatoms onto facets of the noble metal host.^{6, 54, 58, 62, 63} These principles have been tested under more practical operating conditions by using micro-reactors and nanoparticle SAA catalysts, with excellent catalytic performance exhibited in several cases.^{53, 59, 60}

The facile activation of molecular hydrogen by SAAs ensures that they do not suffer from the same rate limitations as the noble metals, which struggle uptake hydrogen onto their surfaces.⁵ Therefore by using SAAs, the hydrogenation of unsaturated hydrocarbons, can be carried out at low temperatures with high activity. Moreover, the product distribution during these hydrogenations is well-controlled compared to the PGMs.^{6, 53, 56, 57, 59, 60, 62} For example, Pd/Cu SAAs can be used to convert phenyl-acetylene to styrene with over 97 % selectivity and with activity comparable to pure Pt (**Figure 3**).⁶⁰

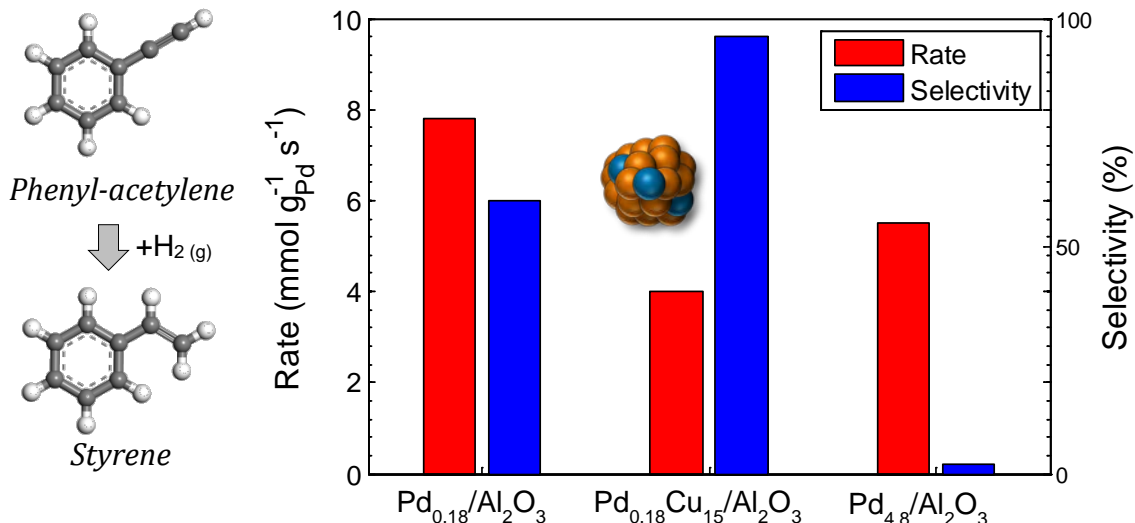


Figure 3: Catalytic rate (red) and selectivity (blue) plot for the hydrogenation of phenyl-acetylene to styrene using pure Pd and Pd/Cu nanoparticle catalysts supported on alumina. This figure is a representation of data published by Boucher *et al.*⁶⁰

The ensemble effect⁵¹ is at work in SAAs as the spatial distribution of monomer active, dopant sites is thought to be key to their novel catalytic properties. It follows that characterisation of SAAs is essential, for both extended model surfaces and catalytic nanoparticles. Regarding the former, scanning tunnelling microscopy (STM) is used to image SAA surfaces with atomic resolution and shows that, under optimised conditions of synthesis, isolated catalytically active atoms exist in the surface layer of these materials.^{58, 63, 65, 66} For example, in **Figure 4** we show high-resolution STM images produced by Sykes and co-workers for Pd/Cu(111),⁶³ Pt/Cu(111)⁶⁶ and Pd/Au(111)⁵⁸ all within the SAA limit.

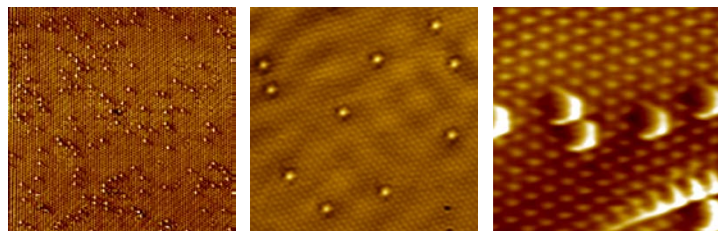


Figure 4: High resolution scanning tunnelling microscopy images of Pd/Cu(111) SAA, Pt/Cu(111) SAA and Pd/Au(111) SAA (in the order of left to right). The images are courtesy of the Sykes research group at Tufts University, though also appear in the referenced publications.^{58, 63, 66}

Assigning features on the STM image is generally simple, as single dopant atoms will appear as bright or dull spots depending on the imaging conditions or as protrusions or depressions depending on the size of the dopant atom relative to the host matrix (**Figure 4**).

^{58, 63, 66} In cases where it is not so clear, DFT can be used to simulate STM such that

comparison to experimental STM and subsequent assignment can be made; this is the case for Ni/Au(111) SAAs (**Figure 5**).⁶⁵ The more industrially practical nanoparticle SAAs can also be well characterised using techniques such as extended X-ray adsorption fine structure and Fourier transformed infra-red spectroscopy.

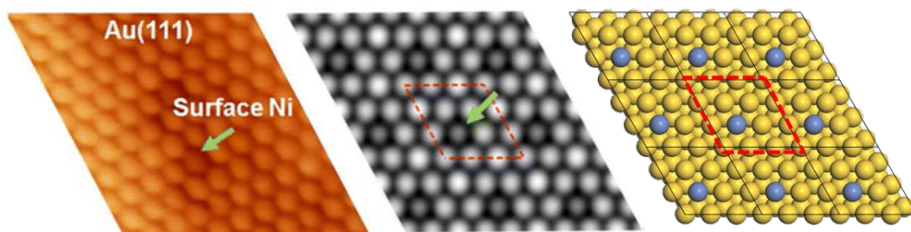


Figure 5: High resolution scanning tunnelling microscopy image of Ni doped into Au(111) as a SAA (left), and a simulated scanning tunnelling microscopy of the same surface from density functional theory (centre) as well as the model structure (Au and Ni atoms are yellow and purple, respectively) used in the calculation.⁶⁵

It is clear that the catalytic architecture of SAAs is unique compared to other binary metal catalysts. The excellent performance of SAAs as extended model surfaces and nanoparticle catalysts suggest that the ensemble effect is prevalent. The well-defined structure of SAAs, along with their excellent behaviour in catalytic applications, demonstrates that monomer ensembles of highly active metals are sufficient for facilitating surface catalysis.^{6, 53-64, 67}

As we alluded to earlier, the relative infancy of research into SAAs has meant that only a few examples of SAA materials have been tested for reactivity and catalytic performance. It follows that, even just considering the PGMs doped into coinage metal hosts, there are many combinations of alloys that have not yet been investigated. Moreover, the novelty of SAAs means it is still unclear why the performance of these alloys is so good and indeed, what other catalytic chemistries could they be employed in to improve the process.

Therefore, in order to further the understanding and aid in the development of SAAs we carried a theoretical study on many SAA systems to determine their behaviour and catalytic properties. We will show here that the catalytic performance of SAA materials is unique compared to traditional transition metal catalysts. We will assess the extent to which SAAs adhere to the descriptor based models discussed in the previous section and in fact, our investigation reveals that the behaviour of SAAs cannot be predicted by the same models

that are applied to transition metals because of the nature of the ligand and ensemble effects expressed by SAAs.

Our study will use state-of-the-art computational modelling in the form of DFT and KMC, to model SAA chemical behaviour in the context of catalysis. We will determine the applicability of TCS and the BEP relationship to SAA materials in Chapter 3, before demonstrating in Chapter 4 how a specific example of Pt/Cu SAAs can activate C-H bonds in light alkanes without coke formation and finally, that SAAs offer high tolerance to catalytic poisoning by CO as well as assessing their structural stability in Chapter 5. This information will prove invaluable to the development of SAA catalysts and will guide the experimental synthesis and catalytic application of these novel materials. As a prelude to this work, we will introduce the foundations of the theoretical methods that we have used throughout this thesis and in our investigation into SAAs as catalytically active materials.

Chapter 2 Theoretical Methods

Introduction

The concern of the work in this thesis is to investigate the fundamental surface properties of *Single Atom Alloys* (SAAs) using a multi-scale modelling approach. On the molecular level we will perform electronic structure calculations using density functional theory (DFT) to determine how SAAs surfaces interact with substrates. We will then employ kinetic Monte Carlo to assess the performance of SAAs on length scales relevant to catalysis.

We discuss here the foundations of these theoretical methods, giving an overview of several techniques but focussing on DFT and KMC. Starting at the molecular level, we explore the theoretical origins of DFT as a method for approximating solutions to Schrödinger's equation. We then consider how transition state theory (TST) provides a bridge to cross from static, atomistic calculations to dynamic, kinetic Monte Carlo (KMC) simulations on the catalyst level.

Schrödinger's Equation

Perhaps the most famous equation in the theoretical sciences, the Schrödinger equation is used to study matter on the molecular level. The Schrödinger wave equation gives us the time evolution of the wavefunction for physical and chemical systems. From this we can quantify important physical properties and observables.

$$i\hbar \frac{\partial \Psi}{\partial t} = \hat{H}_{tot} \Psi(x, t) \quad (3)$$

The total energy operator for a system of n electrons and N nuclei is known as the Hamiltonian, \hat{H}_{tot} . The Hamiltonian is constructed of terms accounting for the kinetic \hat{T} and potential \hat{V} energies of the nuclei and electrons.

$$\hat{H}_{tot} = \hat{T} + \hat{V} \quad (4)$$

$$\hat{H}_{tot} = \hat{T}_{Nu} + \hat{T}_e + \hat{V}_{eN} + \hat{V}_{NN} + \hat{V}_{ee} \quad (5)$$

The first two terms are the kinetic energy terms for the nuclei and electrons whereas the following three terms are the electrostatic terms for the interaction of nuclei with electrons, the inter-nuclear interaction and the inter-electron interaction. The Hamiltonian may be written in full (using atomic units) as

$$\hat{H}_{tot} = -\frac{1}{2} \sum_A^N \frac{1}{M_A} \nabla_A^2 - \frac{1}{2} \sum_i^n \nabla_i^2 - \frac{1}{2} \sum_{iA}^{nN} \frac{Z_A}{|r_i - R_A|} + \frac{1}{2} \sum_{iA}^{NN} \frac{Z_A Z_B}{|R_B - R_A|} + \frac{1}{2} \sum_{ij}^{nn} \frac{1}{|r_i - r_j|}. \quad (6)$$

Where M_A , Z_A and R_A are the mass, charge and position of nucleus A respectively and r_i is the position of electron i .

The wavefunction may be separated into temporal and spatial parts and the Schrödinger equation of the spatial wavefunction is the time-independent Schrödinger equation (TIDSE).

$$\hat{H}\psi(r, R) = E\psi(r, R) \quad (7)$$

The wavefunction $\psi(r, R)$ is an eigenstate of the Hamiltonian with the corresponding energies given by the eigenvalues. The variational principle tells us that minimisation of the energy gives us the ground state energy and corresponding ground state wavefunction, which may be related to the probability density ρ according to

$$\rho(r, R) = \psi^*(r, R)\psi(r, R). \quad (8)$$

The wavefunction is a highly dimensional entity that becomes increasingly more complicated to treat as we increase the number of particles. As a result, analytical solutions to the Schrödinger equation are impossible to find for the majority of systems, though have been expressed analytically for low dimensional problems such as H_2^+ and other theoretical systems. Consequently there are many approximations that aim to reduce the dimensionality of the problem.

The Born-Oppenheimer Approximation

Obtaining solutions to the Schrödinger equation is an $n + N$ dimensional problem for a wavefunction describing n electrons and N nuclei. Using the Born-Oppenheimer approximation we are able to reduce the wavefunction to be n -dimensional.⁶⁹ The Born-

Oppenheimer approximation decouples the nuclear and electronic degrees of freedom by assuming they are independent. Such a justification is made as nuclei are significantly heavier than electrons (three orders of magnitude or more) allowing for separation between the electronic and the vibrational and rotational components. As the nuclei are so much heavier, any change in the nuclear positions is sufficiently slow that the electrons are able to adapt instantaneously.

The nuclear components of the wavefunction are spatially more localised than the electronic component allowing us to view the nuclei as single points within the classical limit.⁷⁰ The motion of the electrons adapts adiabatically to nuclear motion. Mathematically this allows us to separate the total wavefunction and approximate it as a product of the decoupled nuclear and electronic wavefunctions. The resulting quasi-separable ansatz is given as

$$\psi(r, R) = \Phi(R)\psi(r; R), \quad (9)$$

such that the electronic wavefunction $\psi(r; R)$ is parametrically dependent on the nuclear coordinates.

The electrons now move in a potential given by the positions of the nuclei. We now have an electronic and a nuclear Schrödinger equation. Grouping the Hamiltonian into electron and nuclear dependent parts such that the electronic Hamiltonian is given as

$$\hat{H}_e = -\frac{1}{2} \sum_i^n \nabla_i^2 - \frac{1}{2} \sum_{iA}^{nN} \frac{Z_A}{|r_i - R_A|} + \frac{1}{2} \sum_{ij}^{nn} \frac{1}{|r_i - r_j|}. \quad (10)$$

Thus, we may evaluate the electronic energy E_e at a given nuclear configuration R according to the electronic Schrödinger equation

$$\left(-\frac{1}{2} \sum_i^n \nabla_i^2 - \frac{1}{2} \sum_{iA}^{nN} \frac{Z_A}{|r_i - R_A|} + \frac{1}{2} \sum_{ij}^{nn} \frac{1}{|r_i - r_j|} \right) \psi(r; R) = E_e(R) \psi(r; R). \quad (11)$$

Similarly, the nuclei move in a potential set up by the electrons. The nuclear Hamiltonian is grouped into nuclear dependent parts such that

$$\hat{H}_N = -\frac{1}{2} \sum_A^N \nabla_A^2 - \frac{1}{2} \sum_{iA}^{nN} \frac{Z_A}{|r_i - R_A|} + \frac{1}{2} \sum_{AB}^{NN} \frac{Z_A Z_B}{|R_B - R_A|}. \quad (12)$$

We make two assumptions. First we assume that the nuclear kinetic energy operator has no effect on the electronic wavefunction and also that the electronic kinetic energy operator has no effect on the nuclear wavefunction.

The nuclear and electronic kinetic operators contain second derivatives with respect to the nuclear and electronic coordinates respectively. The electronic kinetic energy operator contains derivatives that are with respect to only the electronic coordinates, therefore having no effect on the nuclear wavefunction.

$$\hat{T}_e(r, R)\psi(r; R)\Phi(R) = \psi(r; R)\hat{T}_e(r, R)\Phi(R) \quad (13)$$

Though the nuclear kinetic energy operator also has no effect on the electronic wavefunction, it is not as simple to justify as with the previous case. The nuclear kinetic energy operator contains only nuclear coordinate derivatives but must affect both parts of the wavefunction as the electronic wavefunction parametrically depends on R .

$$\hat{T}_N(R)\psi(r; R)\Phi(R) = \psi(r; R)\hat{T}_N(R)\Phi(R) \quad (14)$$

Using the chain rule on eq. (14) and substituting into the Schrödinger equation we find

$$\begin{aligned} & \psi(r; R)\hat{T}_N(R)\Phi(R) + \Phi(R)\psi(r; R)\left(E_e(R) + \hat{V}_{NN}(R)\right) \\ & - \left\{ \sum_A \frac{1}{2M} \left(2\nabla_R \psi(r; R) \nabla_R \Phi(R) + \Phi(R) \nabla_R^2 \psi(r; R) \right) \right\} \\ & = E_{tot}\psi(r; R)\Phi(R). \end{aligned} \quad (15)$$

We assume the bracketed term in eq. (15) has a negligible contribution to the energy in the adiabatic approximation as it scales with m/M and the mass of an electron is several orders of magnitude less than the nucleus, meaning the term is approximately zero. These terms are the non-adiabatic coupling elements and become important when we consider systems with multiple electronic surfaces, such as photochemical reactions. Moreover, the highly localised nature of the nuclear wavefunction ensures there is very high curvature close to the

nucleus whereas the electronic wavefunction is more delocalised and so the spatial variation of the electronic wavefunctions is much less extreme. As a result, the contribution of $\hat{T}_N(R)\psi(r; R)$ should be insignificant compared to $\hat{T}_N(R)\Phi(R)$. Thus within the Born-Oppenheimer approximation, we write the Schrödinger equation for the nuclear Hamiltonian as

$$\left(-\frac{1}{2} \sum_A^N \nabla_A^2 - \frac{1}{2} \sum_{iA}^{nN} \frac{Z_A}{|r_i - R_A|} + \frac{1}{2} \sum_{AB}^{NN} \frac{Z_A Z_B}{|R_B - R_A|} \right) \Phi(R) = E_{tot} \Phi(R). \quad (16)$$

Invoking the Born-Oppenheimer approximation allows us to evaluate the electronic energy at a given nuclear configuration. Computing the electronic energy across all R , we can construct a surface where the energy is a function of each nuclear degree of freedom. A construct like this is termed the potential energy surface (PES).⁷⁰⁻⁷² From the PES we can find stationary points through evaluation of Hellman-Feynman forces, giving vital information about stable configurations and transition states. Moreover, the PES may be used in dynamic simulations to predict the time evolution of nuclei according to Newtonian mechanics. Solutions to the nuclear Schrödinger equation give the vibrational and rotational energy levels, which are fundamental to spectroscopic techniques.

Despite the Born-Oppenheimer approximation reducing solving the Schrödinger equation to an n -dimensional from an $n + N$ dimensional problem, the task remains non-trivial with exact solutions being very difficult to compute. Quantum Monte Carlo (QMC) has been used to give solutions to the electronic Schrödinger equation for small systems, typically consisting of light atoms though it is limited by the enormity of the wavefunction.^{73, 74}

Consequently, significant research has gone into developing methods that reduce the complexity of the n -dimensional problem. Many approaches look to reduce the dimensionality of the electronic wavefunction. Such methods can be broadly classified as wave mechanics or density based methods. We will give a brief overview of both classes of method, focussing on Hartree-Fock theory and Density functional theory.

Hartree-Fock Molecular Orbital Theory

As we discussed above, solving the electronic Schrödinger equation after invoking the Born-Oppenheimer approximation remains non-trivial. The difficulty arises due to the high dimensionality of the wavefunction which is inseparable as a result of electrons being indistinguishable and interacting.

Hartree-Fock theory offers an approximation based on the idea that electrons occupy orbitals.^{70-72, 75-77} Orbitals are mathematical constructs defining a region of space which, to some extent, are a reasonable approximation, though in reality are an oversimplification. We are easily able to find solutions to the one electron problem (e.g. the H atom), though when we consider electron-electron interactions things become much more complicated. Assuming the electrons are non-interacting and that each electron occupies an orbital we can separate the electronic wavefunction to give the Hartree product of one electron wavefunctions ϕ where

$$\psi_H(r_1 r_2, \dots, r_n) = \phi_1(r_1) \phi_2(r_2) \dots \phi_n(r_n). \quad (17)$$

The Hartree product is a product of single particle spatial orbitals (effectively one-electron wavefunctions) with one electron occupying each. The Hartree product is an intuitive approach however it fails on several accounts. It is clear that entirely neglecting electron correlation can never reproduce reality. According to quantum mechanics, electrons are indistinguishable; though by stating that a particular electron occupies a given orbital we clearly violate this. Finally we fail to satisfy the fermionic properties of electrons as the Hartree product wavefunction is not antisymmetric. It is required that the electronic wavefunction must be antisymmetric with respect to the interchange of the electronic space-spin coordinates.

We may take a wavefunction of the form

$$\psi(x_1, x_2) = \frac{1}{\sqrt{2}} [\phi_1(x_1) \phi_2(x_2) - \phi_1(x_2) \phi_2(x_1)] \quad (18)$$

for a two-electron system whereby it is a sum of space-spin orbit exchanged Hartree products. A wavefunction of this form is antisymmetric. This form of the wavefunction is general and may be extended to an n -electron system. A convenient way to represent such a wavefunction is by using a Slater determinant. The normalised Slater determinant retains the antisymmetry in eq. (18) and indeed the generalised n -electron analogue. We write the n -particle Slater determinant as

$$\psi_{SD}(x_1, x_2, \dots, x_n) = \frac{1}{\sqrt{n!}} \begin{vmatrix} \phi_1(x_1) & \cdots & \phi_n(x_1) \\ \vdots & \ddots & \vdots \\ \phi_1(x_n) & \cdots & \phi_n(x_n) \end{vmatrix}, \quad (19)$$

where the $1/\sqrt{n!}$ coefficient is a result of normalisation of each single particle orbital. In addition to the antisymmetry achieved by the Slater determinant, we also ensure the electrons are indistinguishable as each electron is affiliated to every orbital.

Now we have reformulated the n -electron wavefunction into n one-electron wavefunctions using a Slater determinant, we now solve the electronic Schrödinger equation

$$\hat{H}_e \psi_{SD}(x) = E_e \psi_{SD}(x). \quad (20)$$

In order to find the optimal Slater determinant (the lowest energy) we use the variational theorem. Optimising the wavefunction using the variational theorem will allow us to find the best approximate solution to the electronic Schrödinger equation. For symmetric expressions, the variational principle states that the energy of any wavefunction is an upper bound of the true energy. Therefore, by minimising the energy with respect to a Slater determinant wavefunction we approach the exact energy, though will never converge to it unless $\psi_{SD} = \psi$. The expectation value for the electronic energy under the Born-Oppenheimer approximation is given as

$$E = \langle \psi_{SD}(x) | \hat{H}_e | \psi_{SD}(x) \rangle. \quad (21)$$

The electronic Hamiltonian established in the Born-Oppenheimer approximation may be grouped into no-electron, one-electron and two-electron terms. Under the Born-Oppenheimer approximation the nuclear potential V_{NN} energy has no dependence on

electronic coordinates, and so when inserted into the energy expression it is an integral over a constant; this is the Coulombic repulsion between nuclei. The electronic kinetic energy and the nuclear-electronic interaction operators are dependent on the coordinates of a single electron. We sum the one-electron operators to give \hat{h} where

$$\hat{h}_i = \frac{-\nabla_i^2}{2} + \sum_A^N \frac{-Z_A}{|r_i - R_A|}, \quad (22)$$

$$\hat{h} = \sum_i^n \hat{h}_i. \quad (23)$$

The expectation value of the one electron operators is simple to compute. Orbital orthogonality and the antisymmetry of the wavefunction mean that the total electronic kinetic energy and the potential due to the nuclear-electronic Coulombic attraction are sums of the expectation values for each single particle orbital,

$$\sum_i^n h_{ii} = \sum_i^n T_{e,i} + V_{Ne,i}, \quad (24)$$

where $h_{ii} = \langle \phi_i | \hat{h} | \phi_i \rangle$.

The electronic interaction operator is dependent on the coordinates of two electrons, meaning the expectation value is more complicated to obtain as a result of the antisymmetric element of the Slater determinant wavefunction. Multiplying out the two electron operator, we find two terms arise. Firstly we see the classical two-electron Coulomb interaction J_{ij} between two electrons which is expressed as

$$\iint \phi_1^*(r_1) \phi_2^*(r_2) \frac{1}{|r_i - r_j|} \phi_1(r_1) \phi_2(r_2) dr_1 dr_2. \quad (25)$$

We interpret this Coulomb integral as the overlap of electron densities $|\phi_1(r_1)|^2$ and $|\phi_2(r_2)|^2$. In addition we see a term that has no classical explanation, though arises due to the wavefunction antisymmetry.

$$-\iint \phi_1^*(r_1)\phi_2^*(r_2) \frac{1}{|r_i - r_j|} \phi_2(r_1)\phi_1(r_2) dr_1 dr_2. \quad (26)$$

Despite eq. (26) having no apparent classical description, it is the consequence of electron-electron exchange allowed for by the antisymmetry of the wavefunction – thus we term this the exchange integral K_{ij} . The expectation value for the electronic energy of a Slater determinant is given as the sum of the one-electron Coulomb term, the two-electron Coulomb term and the exchange term. We write the expectation value as

$$E_{HF} = \sum_i^n h_{ii} + \frac{1}{2} \sum_i^n \sum_j^n (J_{ij} - K_{ij}). \quad (27)$$

The total energy can be found by adding the contribution from the nuclear potential such that $E_{tot} = E_{SD} + V_{NN}$.

We look to minimise the Hartree-Fock energy using the Hartree-Fock method such that we may find the Slater determinant wavefunction that is closest to the true wavefunction. As we mentioned above, the Slater determinant is symmetric and so we may apply the variational theorem. The minimisation must retain the orbital orthonormality and so we employ Lagrange undetermined multipliers to achieve this. We use a Lagrange functional L for the minimisation to ensure the minimisation is with respect to the orbitals. We now write

$$L[\phi_i] = E_{HF}[\phi_i] - \sum_{ij} \epsilon_{ij} (\langle \phi_i | \phi_j \rangle \delta_{ij}), \quad (28)$$

where the additional term is a constraint on the orbital orientation with ϵ_{ij} being the Lagrange undetermined multiplier and $\langle \phi_i | \phi_j \rangle$ is the overlap of single particle orbitals i and j .

From minimisation using the Lagrange undetermined multipliers, we arrive at the Hartree-Fock equations

$$\hat{f}\phi_i(r) = \epsilon_i\phi_i(r), \quad (29)$$

where \hat{f} is the Fock operator such that $\hat{f} = V_{NN} + h_{ii} + \sum_i^n (J_i - K_i)$. We now have a set of coupled non-linear equations which need to be solved. However, the coupling of these

equations means that we cannot solve for the minimised wavefunction directly and instead we must use a procedure known as the self-consistent field method. Starting from a guessed wavefunction we can iterate to refine the energy (and the wavefunction) until it converges. Convergence will be reached when the interaction operators acting on the wavefunction are identical to the previous iteration.

Hartree-Fock theory can be applied to many systems, however its accuracy is limited. The Hartree-Fock method accounts for electrons moving in the total potential given by all other electrons. As a result, Hartree-Fock theory accounts for electron correlation in a mean-field fashion. Though we account for non-local average correlation, using a single-determinant form for the wavefunction means we neglect local electron correlation.

Only considering the non-local potential means we only approximately describe the electronic structure of a system and are only able to account for 99 % of the energy of the system. The helium atom serves as a good example; Hartree-Fock is unable to distinguish between situations a) and b) in **Figure 6**. Electrons feel repulsion between one another and in reality case b) is highly improbable compared to a).

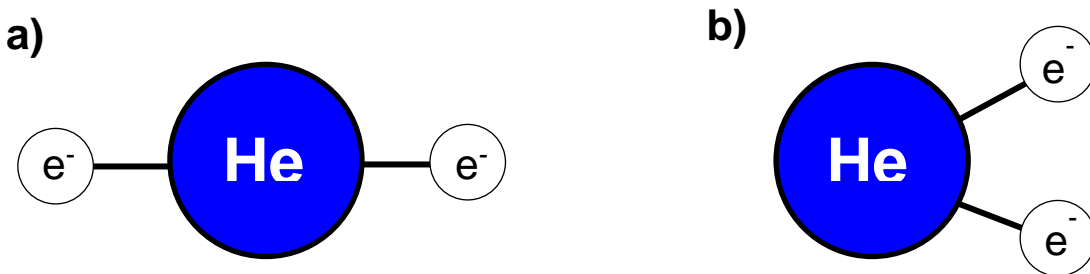


Figure 6: A simplified diagram of a He atom showing two electrons (white) and the nucleus (blue). a) shows the most likely 2D separation of two electrons as a result of minimising the electron-electron repulsion; b) shows a less likely configuration in 2D that has greater electron-electron repulsion. Hartree-Fock theory is unable to distinguish between the two cases.

The local electron correlation has a negative energetic contribution and so within the Hartree-Fock framework we always predict the energy of the system to be too high. The limit in accuracy of Hartree-Fock theory is known as the Hartree limit. Compared to the exact solution of the non-relativistic Schrödinger equation, the Hartree limit is greater than the exact energy by an amount known as the electron correlation energy. Physically speaking,

the electrons are further apart in reality than as predicted by Hartree-Fock theory due to the poor representation of the correlation energy.

The accuracy of the Hartree-Fock method is limited without local correlation, though we may use it to qualitatively predict many general features of the electronic structure just not accurate chemical features. The Hartree-Fock method is used as a starting point for many other computational methods that treat correlation much more rigorously known as post Hartree-Fock methods. We will not discuss these in detail here as their relevance in the work is limited. Though in general, post Hartree-Fock methods try to minimise the electron correlation energy bringing the Hartree limit closer to the exact energy by using non-single determinant wavefunctions. Using many determinants allows for a better description of the correlation and hence they are able to account for some of the electron correlation energy – this methodology is carried out with techniques such as the configuration interaction (CI) and coupled cluster (CC).⁷⁸

We may also use perturbation theory such that the Hartree-Fock non-local correlation is replaced by a Coulomb operator generated from Rayleigh-Schrödinger perturbations of the Hartree-Fock wavefunction to higher orders. Using perturbation theory is non-exact and indeed non-variational, though may be used to correct for some of the correlation energy. Methods using perturbation theory in this way are named after Møller and Plesset⁷⁹ (MP) in addition to the order of the perturbation expansion e.g. MP2, MP3 and MP4 are Møller-Plesset second, third and fourth order perturbations respectively.

Whichever approach is used, post Hartree-Fock methods are expensive and are therefore limited in application, often scaling poorly with the basis set size. The CC method with single, double and triple excitations CCSD(T)⁸⁰ is widely regarded as the gold-standard for all other first principles calculations, though due to the high cost, we rarely see a CCSD(T) approach applied to more than a few tens of atoms.

Density Functional Theory

We have seen so far that the wavefunction for a molecular system is enormously complicated. Hartree-Fock theory is able to reduce the complexity of the electronic wavefunction by expressing it in terms of orbitals. Hartree-Fock theory fails to compute the correlation energy and we briefly mention that post Hartree-Fock methods are able to largely correct for this, though are very expensive.

The Hamiltonian requires lots of information from the wavefunction, including the electronic and nuclear coordinates, as well as the atomic number of each nucleus and the total number of electrons. It follows that all of this information is actually contained in the electron density. If we can readily extract this data, the electron density is a three-dimensional function that we may exploit rather than handling the much more complicated n-dimensional wavefunction. Moreover, unlike the wavefunction, the electron density is a physical observable that we may obtain through experiments using techniques such as X-ray diffraction.

E. Bright Wilson showed us that we can ascertain the total number of electrons in a system from the electron density.^{70, 71} Integrating the electron density σ over all space we get n such that

$$\int d\vec{r} \rho(\vec{r}) = n. \quad (30)$$

Crucial to the assumptions made in the Born-Oppenheimer approximation is the fact that the nuclear wavefunction is highly localised, whereas the electronic wavefunction is not. We use this fact again in our interpretation of the density to say that the positions of nuclei correspond to local maxima in the electron density. Furthermore, the effective nuclear charge can be determined by the gradient of the cusps about the nuclear positions.⁸¹ The nuclear cusp condition shows the monotonic decay of the ground state electron density as a function of distance from the cusp discontinuity corresponding to a nuclear position. We write the nuclear cusp condition as

$$\lim_{r_A \rightarrow R_A} [\nabla_r + 2Z_A] \bar{\rho}(\vec{r}) = 0, \quad (31)$$

$$\left. \frac{\partial \bar{\rho}(\vec{r})}{\partial r_A} \right|_{r_A=R_A} = -2Z_A \rho(r_A), \quad (32)$$

where Z is the nuclear charge of A, r_A is the radial distance from A and $\bar{\rho}(\vec{r})$ is the spherical average of the electron density.

Therefore from the electron density, we are able to find the average position of the electrons, the total number of electrons, the positions of the nuclei and their corresponding nuclear charges. Thus the density provides sufficient information in order to form the Hamiltonian operator and solve the Schrödinger equation.

When using the density we convert the electronic Schrödinger wave equation into functional form. The energy functional is separated into three parts - kinetic energy, nuclear-electron potential and electron-electron potential such that

$$E[\rho] = T[\rho] + V_{Ne}[\rho] + V_{ee}[\rho] \quad (33)$$

As with Hartree-Fock theory, we further separate the electron-electron potential into a classical Coulomb interaction functional and an exchange functional,

$$V_{ee}[\rho] = J[\rho] + K[\rho]. \quad (34)$$

We are able to easily determine the forms of the Coulomb and nuclear-electron potential functional as they are given by simple classical equations for Coulombic interaction

$$V_{Ne}[\rho] = - \sum_A^{nuclei} \int \frac{Z_A}{|r - R_A|} \rho(r) dr, \quad (35)$$

$$J[\rho] = \frac{1}{2} \iint \frac{\rho(r)\rho(r')}{|r - r'|} dr dr'. \quad (36)$$

On the other hand, the functional forms of the kinetic energy and the exchange energy are much more complicated. The search for these functional forms is the basis of all density based methods.^{70, 82} We will begin by briefly examining one of the first density based

methods, the uniform electron gas (UEG) developed by Thomas and Fermi and also density functional theory as developed by Hohenberg, Kohn and Sham.

The Uniform Electron Gas “Jellium” and the Thomas-Fermi Model

Thomas and Fermi both realised that they were unable to quantify the kinetic and exchange energy functionals. Both created a theoretical “substance” known as the uniform electron gas (UEG) otherwise known as “Jellium”. Jellium is composed of an infinite number of electrons that are uniformly distributed creating a field over a uniformly distributed positively charged potential such that the electron density is constantly non-zero.^{70, 82}

The Thomas-Fermi kinetic energy functional is derived using fermionic statistical mechanics as

$$T_{TF}[\rho] = \frac{3}{10} (3\pi^2)^{\frac{2}{3}} \int \rho^{\frac{5}{3}}(r) dr \quad (37)$$

The Thomas-Fermi model (TF) was developed in the classical framework and so did not attempt to account for exchange. However, Bloch and Dirac introduced the exchange energy functional into the TF model where

$$K_D[\rho] = - \frac{3}{4} \left(\frac{3}{\pi}\right)^{\frac{1}{3}} \int \rho^{\frac{4}{3}}(r) dr \quad (38)$$

Bloch and Dirac's improved method was named the Thomas-Fermi-Dirac (TFD) method.⁸³ Despite the inclusion of the exchange functional, neither the TF method or TFD method are able to produce accurate molecular calculations – in fact both methods suggest that all molecules are unstable with respect to separation into their constituent atoms. Though no meaningful data can be produced from the TF and TFD models they serve an illustrative purpose, showing that the energy can be computed from the electron density without the use of the wavefunction.

Errors in the TF and TFD models may be reduced by using gradient corrections. Correction terms are used in powers of the higher order derivatives of the density which make the UEG essentially non-uniform. Correcting the kinetic energy functional in this way allows the TF and TFD models to be applied to systems with lower variation in the electron density such as

metals. The UEG model has been applied to large solid state systems, though the errors were so significant that the impact of the method was negligible.

The Hohenberg-Kohn Theorems

It wasn't until 1964 that a significant breakthrough in density based methods was made.

Hohenberg and Kohn put forward two ground breaking theorems using an inhomogeneous electron gas.⁸⁴ Firstly, they state that for any system of interacting particles that move within an external potential $v(r)$, the external potential may be uniquely determined by the ground state density. It can be shown that this is the case using a proof by contradiction. It must be shown that two different external potentials cannot produce the same ground state density.

Consider two different n-electron Hamiltonians that both have exact ground state solutions.

We assume that the two different potentials (in the two different Hamiltonians) lead to the same ground state density.

$$\hat{H}_a \psi_a = E_a \psi_a, \quad \hat{H}_b \psi_b = E_b \psi_b \quad (39)$$

where $\hat{H}_a \neq \hat{H}_b$, $\psi_a \rightarrow \rho$ and $\psi_b \rightarrow \rho$. From the variation theorem, the expectation value of Hamiltonian \hat{H}_a operating on wavefunction ψ_b must be greater than the ground state energy such that

$$\langle \psi_b | \hat{H}_a | \psi_b \rangle > E_a \quad (40)$$

Rewriting given that $\hat{H}_a = \hat{H}_b + [\hat{H}_a - \hat{H}_b]$ we find that

$$\langle \psi_b | \hat{H}_b + [\hat{H}_a - \hat{H}_b] | \psi_b \rangle > E_a, \quad (41)$$

$$\langle \psi_b | \hat{H}_b | \psi_b \rangle + \langle \psi_b | \hat{H}_a - \hat{H}_b | \psi_b \rangle > E_a, \quad (42)$$

$$E_b + \langle \psi_b | \hat{H}_a - \hat{H}_b | \psi_b \rangle > E_a. \quad (43)$$

The only difference in the Hamiltonians is given in the one-electron potential terms. Thus we may evaluate the second term on the LHS in terms of the ground state density

$$E_b + \int [v_a(r) - v_b(r)]\rho(r)dr > E_a \quad (44)$$

However, we made no inference about the nature of a and b therefore meaning we could easily have done everything the other way around. Swapping the indices, we find

$$E_a - \int [v_a(r) - v_b(r)]\rho(r)dr > E_b \quad (45)$$

When adding the two expressions together, we find the contradiction

$$E_a + E_b > E_b + E_a, \quad (46)$$

proving that the initial assumption that two different wavefunctions (and Hamiltonians) lead to the same ground state density is invalid. In other words, the external potential for a system of interacting particles is uniquely determined by the ground state density – this is known as the first Hohenberg-Kohn theorem (HK1).

The second Hohenberg-Kohn theorem (HK2) states that the energy functional of the density is variational. This follows nicely from HK1; the energy with respect to the ground state wavefunction is variational and as the ground state density is unique to the ground state wavefunction, we might suspect it is also the case for the ground state density.

For the exact ground state density, we know that $E_0 = E[\rho]$. Similarly, from the wave mechanics approach, we also know that $\hat{H}\psi = E_0\psi$ where $\psi \rightarrow \rho$. Given that the energy of the Schrödinger wave equation is variational, we know that

$$\langle \psi' | \hat{H} | \psi' \rangle \geq \langle \psi | \hat{H} | \psi \rangle = E_0. \quad (47)$$

Also wavefunction ψ' must correspond to a unique density ρ' according to HK1. Therefore as $E[\rho'] = \langle \psi' | \hat{H} | \psi' \rangle$, it follows that

$$E[\rho'] \geq E[\rho]. \quad (48)$$

Thus the ground state electron density obeys the variational principle. In light of HK1 and HK2 we re-write the energy functional for a system of interacting particles moving in an external potential in terms of the Hohenberg-Kohn functional $F_{HK}[\rho]$,

$$E[\rho] = \int v(r)\rho(r)dr + F_{HK}[\rho]. \quad (49)$$

The Hohenberg-Kohn functional is a large unknown quantity and is comprised of the kinetic and electron-electron functionals $F_{HK}[\rho] = \langle \psi | \hat{T} + \hat{V}_{ee} | \psi \rangle$. Determining the exact form of this functional is non-trivial, though Kohn-Sham theory may be used to find a large part of it.

Kohn-Sham Theory

A year after Hohenberg and Kohn published their theorems, Kohn and Sham went on to make a very significant breakthrough in density functional based methods.⁸⁵ The Hohenberg-Kohn functional is a big unknown, though it is partly comprised of bits we do know. Breaking the functional down into smaller parts, it is a sum of the kinetic energy functional and the electron-electron functional,

$$F_{HK}[\rho] = T[\rho] + V_{ee}[\rho]. \quad (50)$$

Similarly, we know from Hartree-Fock theory that the two electron potential is made up of classical Coulomb and non-classical exchange elements $V_{ee}[\rho] = J[\rho] + E'_{xc}[\rho]$. Therefore we can rewrite the Hohenberg-Kohn functional as

$$F_{HK}[\rho] = T[\rho] + J[\rho] + E'_{xc}[\rho]. \quad (51)$$

Immediately we realise that within the Hohenberg-Kohn functional, the Coulomb energy functional $J[\rho]$ is known. Kohn and Sham realised that introducing an orbital based framework will provide a better representation for the kinetic energy, though the problem of particle interaction remains. Assuming that the system is non-interacting, we can greatly simplify the problem. We showed that using Hartree-Fock theory that we can derive the exact kinetic energy for a system of non-interacting particles using the determinant form of the wavefunction. A system of non-interacting electrons will inevitably have a different kinetic energy than if the electrons were interacting, though using this approach we can obtain a

large portion of the true kinetic energy leaving a small correction (assuming Hartree-Fock theory provides a good estimation of the wavefunction) to be made

$$T[\rho] = T_{SD} + T_c[\rho]. \quad (52)$$

In the formulation so far, Kohn-Sham and Hartree-Fock theory essentially have the same formulation as they obtain the kinetic, electron-nuclear and electron-electron energies in the same manner. Re-introducing orbitals and wavefunctions into the problem means that we increase the dimensionality. Using this approach Kohn and Sham showed how using a valid anti-symmetric wavefunction to generate n-representable trial densities allows them to receive a large portion of the kinetic energy.

Again, we can re-express the Hohenberg-Kohn functional to include the contribution to the kinetic energy functional from using the determinant wavefunction

$$F_{HK}[\rho] = T_{SD} + J[\rho] + E_{xc}[\rho]. \quad (53)$$

We incorporate the small kinetic correction into the exchange term such that $E_{xc}[\rho] = T_c[\rho] + E'_{xc}[\rho]$. This step is taken as we assume that the correction in the kinetic energy will be largely due to correlation in the interacting system over the non-interacting system. Thus the remaining unknown in the Hohenberg-Kohn functional is the exchange-correlation term which we express as

$$E_{xc}[\rho] = (T[\rho] - T_{SD}) + (V_{ee}[\rho] - J[\rho]), \quad (54)$$

with the Kohn-Sham total energy given as

$$E_{KS} = T_{SD} + J[\rho] + E_{xc}[\rho] + \int v_N(r)\rho(r)dr \quad (55)$$

where $v_N(r)$ is the external nuclear potential for which the density $\rho(r)$ is determined by. We minimise the Kohn-Sham energy with respect to the orbitals subject to the orthogonality constraint $\langle \phi_i | \phi_j \rangle$ such that $\frac{\delta E_{KS}}{\delta \phi_i} = 0$ giving us the Kohn-Sham equations

$$\left[-\frac{1}{2} \nabla^2 + \nu_N + \nu_J + \nu_{xc} \right] \phi_i = \epsilon_i \phi_i. \quad (56)$$

The Kohn-Sham equations are very similar to the Hartree-Fock equations (eq. (29)) except the non-local exchange K in Hartree-Fock theory is replaced by a local exchange-correlation potential ν_{xc} in Kohn-Sham theory.

Approximating the Exchange-Correlation Term

DFT as portrayed by Kohn and Sham is an exact technique providing that we have an exact functional form of the exchange-correlation term.⁸⁵ Sadly this feat is easier stated than achieved. Since Kohn and Sham published their work in 1965, the development of more accurate exchange correlation functionals has dominated the density functional theory world. Perdew and Schmidt introduce the notion of “Jacob’s ladder” of density functional approximations showing the spectrum of accuracy between the Hartree-Fock model and chemical accuracy when using different kinds of exchange-correlation functional in DFT.⁸⁶

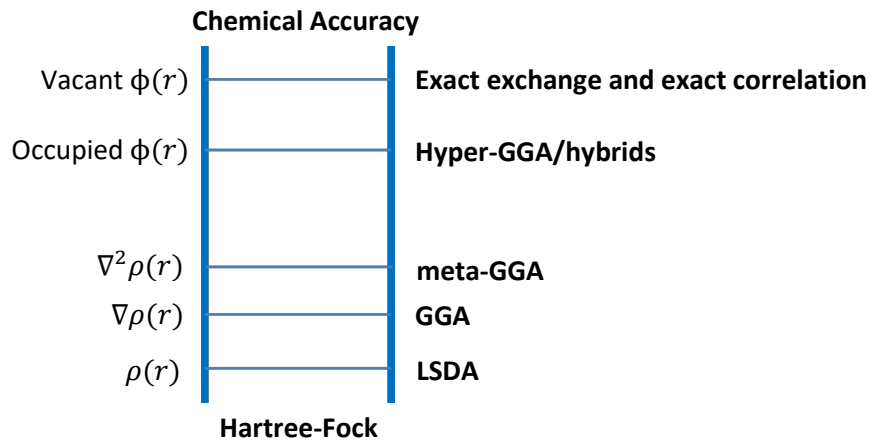


Figure 7: Jacob’s Ladder of chemical accuracy summarising a variety of approximations to the exchange-correlation energy. The bottom of the ladder corresponds to the most simple yet least accurate approach with the least simple and most accurate at the top of the ladder; we refer to the top of the ladder as “Chemical Accuracy”.

The applicability of functional types diminishes as we move up the ladder towards more accurate techniques. As a consequence we will only consider the 1st and 2nd rungs here as typically higher rungs are less applicable to large extended and many atom systems due to implementation costs.

The local spin density approximation (LSDA) was made by Kohn and Sham and for closed shell systems is equivalent to the local density approximation (LDA). The LDA makes some significant approximations, though facilitated the first applications of Kohn-Sham theory particularly to solid state problems. The LDA assumes that the density may be treated locally as a sum of UEGs, that is at each point in the system the exchange-correlation is evaluated for the density as if it were a UEG within an infinitesimal region of space dr . The exchange-correlation energy is thereby given as

$$E_{xc}^{LDA} = \int \epsilon_{xc}(\rho)\rho(r)dr. \quad (57)$$

Commonly the exchange-correlation is split into individual exchange and correlation potentials. We showed earlier that Dirac introduced eq.(38) to account for the exchange potential of the UEG. The dynamic correlation energy for the UEG has been determined in the limits of high and low density. QMC calculations have been used to determine values for intermediate densities, though interpolation schemes must be implemented to provide an applicable analytical form of the UEG correlation energy.

The LDA is exact for the UEG case in DFT. However variations in the density that are seen in real systems can cause significant errors. The applicability to molecular systems with small changes in the density (as often seen in solid state physics) is greater. We obtain acceptable accuracy from the LDA for geometric, vibrational frequency, elastic moduli and phase stability calculations though the LDA grossly overestimates the strength of bonding interactions.⁸⁷⁻⁸⁹ For extended solid state calculations, we find that there is typically an underestimation in the lattice parameter as a result.⁹⁰

Compared to accurate variational QMC calculations, the LDA tends to over-predict the contribution to the energy from correlation, though it under-predicts the contribution from exchange.⁹¹ We see some good agreement of the LDA with many experimental observations, though this has been attributed to the good description of the spherically averaged exchange-correlation hole (despite a poorly estimated pair-correlation function) in addition to the cancellation of errors in the exchange and correlation energies.⁹²

The Generalised Gradient Approximation

We can improve on the density representation in LDA by considering semi-local gradient expansions of the density. The gradient expansion approximation (GEA) incorporates first order derivatives of the density in the expansion of the density matrix.⁹³ Simply including higher order correction terms violates some of the physical principles that the LDA successfully reproduces. We find that integration of Fermi holes (describing exchange correlation) is no longer -1 as required nor is integration of Coulomb holes (describing primarily correlation between same spin electrons) zero.⁷⁰ These results are unphysical and we find that the GEA in general is actually a worse model than the LDA.

The generalised gradient approximation (GGA) is also based on the principle of using first order density derivatives though unlike the GEA, we include the first derivative of the density as a variable that is constrained to ensure integration of the Fermi hole is -1 and the Coulomb hole is zero.⁷⁰ From the gradient we gain information about the position of the density with respect to the nuclei. Generally it follows that sharper gradients correspond to nuclear positions whereas shallower gradients indicate the density is more delocalised (i.e. as with the nuclear cusp condition). Including first order derivatives gives us more non-local character of the density, though in reality the GGA is still far from the non-locality we see with the Hartree-Fock exchange energy.

Within the GGA we use functions of the density and gradient instead of adding power series expansions of the gradient. The exchange and correlation functionals may be treated separately so we write the GGA exchange energy functional as

$$E_x^{GGA}[\rho] = \int \rho(r) \epsilon_x^{UEG}(\rho(r)) F_x^{GGA}(s) dr, \quad (58)$$

where

$$s = \frac{|\nabla \rho(r)|}{2(3\pi^2)^{\frac{1}{3}} \rho(r)^{\frac{4}{3}}}. \quad (59)$$

The GGA exchange functional F_x^{GGA} is expressed in terms of s , the dimensionless reduced gradient. The form of F_x^{GGA} is variable with each variation giving rise to a different GGA exchange functional.

One of the first GGA exchange functionals was proposed by Becke in 1988 leading to its namesake, Becke '88 (B88).⁹⁴ B88 is a functional form gradient correction to the LDA exchange and is written as

$$\epsilon_x^{B88} = \epsilon_x^{LDA} + \Delta\epsilon_x^{B88}. \quad (60)$$

The final term is the gradient corrected function of the density. Writing the functional form in terms of a dimensionless density s such that

$$F_x^{B88} = 1 + \frac{\beta s(r)^2}{C(1 + 6\beta s(r) \sinh^{-1} s(r))} \quad (61)$$

where β is a constant that may be fit to the exact Hartree-Fock exchange and known quantities from the noble gases (optimised for $\beta = 0.0042$) and C is a constant of integration that may also be empirically fitted. Using the B88 functional, we can correctly reproduce the correct asymptotic behaviour of exchange potential exponential tails of the charge distribution.^{89, 94} The error in the B88 functional exchange energy is improved by several orders of magnitude compared to the LDA alone, particularly for bonding energies.

Perdew and co-workers have developed an array of functionals that don't require empirical fitting. Perdew wanted to retain all the good features of the LDA though correcting for some of its inadequacies without the introduction of non-fundamental constants using a pure *ab initio* approach. Several exchange-correlation functionals were proposed by Perdew, Wang, Burke and Ernzerhof all of which are related, these are PW86,⁹⁵ PW91⁹⁶ and PBE.⁹⁷ The hole contributions of each functional are different, though PW91 and PBE are frequently numerically equivalent. The PBE exchange is given as

$$F_x^{PBE} = 1 + \kappa - \frac{\kappa}{\left(1 + \frac{\mu s^2}{\kappa}\right)}, \quad (62)$$

where μ and κ are numerical constants not obtained through fitting to experimental data.

Similarly, PW86, PW91 and PBE also contain correlation parts. Notably for both functional types, in the limit of the gradient being zero, $F_x^{GGA}(s)$ must equal 1.

Lee, Yang and Parr (LYP) also developed a popular functional correction for the correlation energy, though has no relation to the UEG. The basis of the formulation is again on the first-order gradient of the density function though is fitted to exact data from the Helium atom.

The LYP correlation functional is often used in conjunction with Becke's formulation giving BLYP type functionals.

Compared to the LDA, GGA corrected calculations of atomisation energies are vastly improved. Since their introduction, many GGA functionals are now in general use with the GGA improvements being partly responsible for DFT launching into widespread use in the chemistry community. A multitude of xc-functionals have been developed all varying slightly in their parameterisation. As a result, a particular functional may be tuned to a specific problem, though the general applicability of many xc-functionals leads to lots of different data pertaining to the same problem which in some cases may be contradictory.⁸⁶

Meta-GGA Functionals

Though the atomisation energies are greatly improved using the GGA, it has been found that in some instances the approximation of bulk lattice parameters is worse. It follows that for lattice constants, values of μ that lead to slower variation in the density gradient may give a better approximation – obtaining high accuracy in both slow and fast varying density is a challenge for GGA functionals.

This conundrum leads to the idea of using an additional parameter based on the second derivative of the density and the kinetic energy of the orbitals; functionals of this kind are non-local functionals of the density though semi-local functionals of the orbitals.⁸⁶ Such functionals are known as meta-GGAs and are typically used to provide additional degrees of freedom accounting both for slow and fast varying density such that solid and molecular

regions are in general modelled more effectively. Meta-GGAs have shown some improved performance in atomisation energy calculations over LDA and GGA^{98, 99} and are typically not much more expensive than a GGA calculation thanks to avoiding the introduction of further integration terms. However, the application of meta-GGA functionals to solid state problems has been minimal.

Hybrid Functionals and Self-Interaction

When considering non-solid state problems, hybrid functionals such as B3LYP are among the most commonly used functionals. Typically their relative cost compared to LDA and GGA functionals makes them impractical for very large systems, due to long range screening of the exchange; though B3LYP is useful in solids with large self-interaction errors.^{70, 71}

Hybrid functionals were introduced in light of the self-interaction error. The self-interaction error is the incidental interaction of an electron with itself due to the way in which we define the exchange correlation in the LDA and as a result the GGA. Within the Hartree-Fock framework we construct the Coulomb and exchange operators in a way that we explicitly cancel the interaction of an electron with itself – this is not the case in the LDA.

Recalling eq.(25) and eq.(26) which are the Hartree-Fock Coulomb J_{ij} and exchange K_{ij} operators we can see exactly how the Hartree-Fock method explicitly and exactly cancels self-interaction. The self-interaction will occur when we are considering the same electron twice; that is when $i = j$. We see that the coulomb interaction is non-zero when $i = j$ however the exchange term is exactly equivalent and so the integrals cancel.

In the Kohn-Sham DFT formulation the self-interaction is not cancelled. This is clear to see when we consider a one electron system. We use the density in the Kohn-Sham formulation, therefore when integrating over the density the single electron will inevitably interact with the mean field created by itself. Cancellation of the self-interaction is possible if we know the form of the exchange-correlation term exactly. However, we approximate this term and so the cancellation is not exact. The mean field description of all of the electrons means that we incorporate the self-exchange interaction into the average of the total exchange.

Hybrid functionals look to correct for the self-interaction error by partially replacing some of the DFT exchange with exact Hartree-Fock exchange. Becke showed how an exact adiabatic connection can be made between the non-interacting Kohn-Sham picture and the exactly fully interacting system through a continuum of partially interacting systems.

$$E_{xc} = \int_0^1 U_{xc}^\lambda d\lambda \quad (63)$$

λ is the inter-electronic coupling strength parameter for $0 \leq \lambda \leq 1$ allowing for electron-electron interactions to be effectively switched off or on and U_{xc}^λ is the potential energy for the exchange-correlation at λ . The lower and upper limits of λ correspond to fully interacting Hartree-Fock exchange and non-interacting exchange respectively. The adiabatic connection allows us to use intermediate values of λ such that we may use some exact Hartree-Fock exchange to replace the Kohn-Sham exchange. Thus we may write

$$E_{xc} = E_x^{GGA} + a(E_x^{HF} - E_x^{GGA}) \quad (64)$$

as a correction to the GGA exchange-correlation where a is the fraction of exact exchange that replaces Kohn-Sham exchange. Hybrid functionals such as B3LYP, B3PW91 and PBE0 show improvements in many calculations. The optimum fraction of exchange to replace depends on the problem at hand meaning different variations of hybrid functionals are better suited to certain problems than others. Hybrid functionals partly correct for the self-interaction error, though a balance must be struck between using a DFT approach with correlation and Hartree-Fock with exact exchange.

The self-interaction error can cause some general issues in DFT calculations. Typically we see issues with DFT from self-interaction when considering localised electrons and so problems arise when treating radical dissociations and charge-transfer complexes. The self-interaction correction may also raise DFT activation barriers that may be under-predicted due to self-interaction. Moreover, the self-interaction affects the asymptotic behaviour of the exchange-correlation potential. We should see dependence of $-1/r$ for the potential, though this is not the case with self-interaction. The results of using an incorrect asymptotic form

may lead to a poor qualitative picture of Rydberg excited states.¹⁰⁰ Other than hybrid functionals, correction schemes which remove the self-interaction have been implemented for instance by Perdew and Zunger¹⁰¹ through modifications to the potential such that it is no longer treated as a global potential but a sum of orbital potentials.

In addition to the self-interaction error, DFT fails to account for dispersion forces. Dispersion is a result of dynamic correlation which cannot be captured by the Coulomb interaction between two densities as in DFT. Much research has gone into the development of DFT functionals that include London forces. Dispersion is well modelled by a long range Lennard-Jones-type interaction and so we may add semi-empirical pairwise corrections to the total energy in order to incorporate this.^{102, 103}

Alternatively, we may add an additional non-local functional to an existing exchange-correlation functional giving a dependence on the density. Non-local functionals such as this have shown improved behaviour in the interaction energies of dispersion bonded systems.

Notably for extended solid state systems optPBE-vdW, optB86b-vdW and optB88-vdW developed by Klimes *et al.* have shown a reduction in the absolute error in the bulk properties of an array of solids, including some transition metals.^{104, 105} Moreover, these functionals are becoming increasingly more popular in the calculation of adsorbate surface interactions.^{102, 106}

Practical Considerations

As we have discussed above, DFT is applicable to many chemical systems. Depending on the type of system we are considering, we take steps and practical considerations when performing DFT calculations in order to maximise the simulation efficiency. In this section we will discuss how in extended systems that we find in solid state and surface science, we make use of Blöch's theorem, allowing us to treat calculations periodically. Furthermore, Blöch's theorem allows us to truncate an infinitely large basis set for the potential to a finite basis set that we may represent using a set of plane waves with a finite energy cutoff. Finally we will also introduce the concepts of pseudopotentials and the projected augmented wave (PAW) approximation.

Periodicity and Blöch's Theorem

Extended solid state systems are crystalline and to certain extent we may assume their structure is periodic (obviously in reality this is not the case due to defects etc.). DFT calculations of a crystal should be a formidable task, though the introduction of periodic boundary conditions allows for an enormous reduction in the complexity. Blöch's theorem^{107, 108} states that for a periodic crystal structure, we can reformulate the electronic wavefunction as a product of a wavelike part for a wavevector k defined by the first Brillouin zone and a cell-periodic f_i part:

$$\psi_i(r) = \exp[i k \cdot r] f_i(r), \quad (65)$$

such that $f_i(r) = f_i(r + l)$ where l is the length of the periodic unit cell and i is the band index. We can expand f_i using a plane wave basis set constructed of wave vectors corresponding to the reciprocal lattice vectors G of the crystal unit cell. The cell-periodic element of the wavefunction is then given as

(66)

$$f_i(r) = \sum_G c_{i,G} \exp[i G \cdot r].$$

The reciprocal lattice vector G is subject to periodic boundary conditions such that $G \cdot R = 2\pi m$ where R is a real-space lattice vector and m is an integer. Thus we may write the electronic wavefunction as a linear combination of plane waves that are defined by the reciprocal lattice vectors of the unit cell

$$\psi_i(r) = \sum_G c_{i,k+G} \exp[i(k + G) \cdot r], \quad (67)$$

where $c_{i,k+G}$ are plane wave expansion coefficients.

Each electron occupies a definite state in k -space. It follows that for a solid with an infinite number of electrons, we would have an infinite number of definite k -points and so in order to evaluate the electronic potential of the system, we must in theory carry out an infinite number of calculations for all k -space. However, using Blöch's theorem, we reduce the number of electronic wavefunctions to a finite amount that are evaluated over this infinite

number of k -points. Though it follows that the electronic wavefunction is very similar when evaluated at specific k -points that are close in reciprocal space; we can approximate the contribution from a small region of k -space by a single k -point. Thus we reduce the need for an infinite number of electronic wavefunctions and infinite number of k -points to a problem using a finite basis set over a finite number of k -points.¹⁰⁸

k -space is periodic with the lattice spacing α such that $|k| \leq \pi/\alpha$; we term this interval the Brillouin zone. By carefully constructing a grid of k -points in the Brillouin zone, we are able to provide approximations to the electronic potential from the contribution from electronic states at each k -point.¹⁰⁹ The density of k -points is proportional to the volume of the unit cell. We must use denser k -point meshes for Fermi surfaces (i.e. metals) as oppose to insulating and semi-conducting materials. When computing the total energy using a finite k -point grid, we must ensure that enough k -points have been used to reach a desired accuracy. Using too few k -points, particularly for metal systems, can result in a poor evaluation of the electronic potential and indeed the total energy. Typically we converge the total energy (or quantities such as adsorption energies) with respect to the number of k -points used.

Plane Wave Basis Sets

Employing Bloch's theorem ensures that we can use a basis set formed from a discrete set of plane waves in place of the electronic wavefunction. The electronic wavefunctions at each k -point is expanded in terms of the plane wave basis set. In theory, expansion of the electronic wavefunction requires an infinite number of plane waves. However, we know that large values of the plane wave kinetic energy are less important than small kinetic energies as they refer to fast and slow varying functions respectively. Consequently, we are able to cutoff some of the large kinetic energy contributions and so we impose an energy cutoff for the plane wave basis set. Imposing a cutoff makes the basis set finite and significantly more manageable computationally.

Truncating the plane wave basis set in this manner may lead to errors in the total energy. As with k -point sampling, we can converge the total energy (or energy differences e.g.

adsorption energies) with respect to the size of the basis set by systematically increasing the energy cutoff. The most significant errors when using a plane wave energy cutoff are found in regions of rapidly varying wavefunctions. Typically, the most rapid variation in the wavefunction is seen closer to the nucleus particularly in hard potentials; a fast varying potential would require a higher energy cutoff to compensate for the large kinetic energy contributions. It is very common that the use of plane wave basis sets goes hand-in-hand with the use of pseudopotentials. A pseudopotential softens the nuclear part of the wavefunction and so removes the need for high kinetic energy terms in the basis set.

Pseudopotentials and Projector Augmented Wave Method

In general the chemical properties of atoms and molecules are heavily influenced by the valence electronic structure compared to their core electron structure. When we consider light elements, the number of core electrons is relatively low, although the nuclear potential is screened to a lesser extent. Heavier elements on the other hand have considerably more core electrons making the electronic wavefunction significantly more complicated though the core electron screening of the nuclear potential is also greater.¹¹⁰

As we touched on above, the number of plane waves required to model the core electrons, particularly for heavier atoms, is enormous and so we introduce the pseudopotential to reduce the kinetic energy contribution of the core electrons and thus reduce the basis set size. The combined effect of the core electron screening and the strong ionic nuclear potential may be averaged to give a much softer pseudopotential felt by the outer valence electrons. Similarly, we replace the valence wavefunction with a pseudo-wavefunction that has no radial nodes in the core region. Both the pseudopotential and pseudo-wavefunction are identical to the ionic potential and valence wavefunction beyond the core radius respectively.

A good pseudopotential retains properties of the original potential such that the scattering and phase shifts are identical in both wavefunctions. Moreover, we use different potentials for different angular momenta accounting for the differences in the phase shifts produced by

the ion core depending on the angular momentum – this is referred to as a non-local pseudopotential.

The pseudo-wavefunctions are subject to conservation of the norm. By conserving the norm we ensure that outside the core radius, the pseudo- and all-electron wavefunctions are identical and that the number of core electrons is also conserved. The concept of norm conservation was a key development in the use of pseudopotentials for accurate calculations as without it the transferability of the pseudopotential is very limited depending on its fitting. Norm conservation tends to limit how soft the pseudopotential can be made and so we limit the computational efficiency though retain a greater degree of reliability and transferability.

Similar to the pseudopotential approach is the projector augmented wave (PAW) method.¹¹¹ Auxiliary wavefunctions are generated through a transformation operator from the full wavefunction which may then be expanded using the plane wave basis set. The PAW method is as popular as the pseudopotential approach though often the transferability of the PAW method is better thanks to the use of the frozen-core approximation which formally retains the core electrons yet the core electron orbitals remain irrespective of the external molecular environment.

Brief Summary

In this section we have discussed the theoretical foundations of DFT, seeing how it has developed from a basic UEG model to a framework that is now applicable to molecular systems. We have briefly overviewed some of the practical considerations that must be taken into account when using DFT, in particular focussing on the application to solid state problems. In the next section we will show how using transition state theory we can bridge the gap from DFT and the molecular level to the mesoscale, where we can then use kinetic Monte Carlo methodology to model complex surface kinetics.

Kinetic Monte Carlo

In the following section we will focus on the catalyst scale and the kinetic modelling of processes thereon. One can employ a variety of approaches such as Langmuir-Hinshelwood models, Sabatier analysis, mean-field microkinetic modelling and kinetic Monte Carlo (KMC) modelling. The latter is perhaps the most advanced and sophisticated of these models, readily able to treat catalytic systems with structural complexity, extensive reaction networks and the intricate molecular interactions that one may find in a typical heterogeneous catalytic process. Thus, the remainder of this chapter will focus on KMC, delving into its theoretical origins, methods of implementation and its application as a powerful tool in the interpretation of interesting chemical, physical and catalytic phenomena.

Rare Event Dynamics and the Timescale Problem

Molecular dynamics (MD) has long been at the frontier of atomistic simulations. The numerical integration of Newtonian equations of motion evolves a system through time.¹¹² Such a simulation is performed on the PES whereby the potential gradient gives the forces in each degree of freedom. The time evolution of the position and momenta of atoms on the PES leads to interesting and often surprising dynamics. Accurate integration of Newton's equations requires time steps that are suitably short such that we may resolve atomic vibrations. An atomic vibration occurs on the picosecond scale meaning a characteristic time step for an MD simulation must be on the order of femtoseconds to ensure stability in the numerical integration scheme.¹¹² Short time increments such as this provide accuracy, yet limit the technique to shorter time scales. Even with the advent of modern computers, the total simulation time of an MD simulation rarely exceeds a few microseconds due to the enormity in cost.¹¹³

Typically as surface scientists, our interests lie in elementary events (e.g. adsorption, desorption, diffusion and chemical reactions) that when compared to atomic vibrations, occur on much longer timescales. The short timescales that an MD simulation can realise may not be enough to sample some elementary events, particularly those that are rare and infrequent

in occurrence. These “rare event dynamics” lead to the “timescale problem” which prevents simulating for long enough that we may reach experimentally relevant timescales.

A technique which can access longer timescales whilst maintaining the rigour of an MD simulation may be found in KMC.¹¹⁴⁻¹¹⁹ KMC simulations can easily surpass the microsecond limitation on an MD simulation and can often reach simulation times of seconds or even hours with comparatively low computational expense. Unlike in the MD framework, KMC employs the assumption that on longer timescales the dynamics of a system follow discrete state-to-state jumps rather than a continuous trajectory. KMC is able to overcome the time limitations of MD allowing us to simulate the dynamics of a system over time frames we may see in experiment.

The KMC Trajectory and Coarse-grained Time Evolution

Due to the necessity for short time increments when using MD, the simulation spends significant proportions of time vibrating within a potential basin, corresponding for instance to some reactants configuration. In order to leave this basin the system has to perform many vibrations therein, until it accomplishes a random “jump” of sufficient momentum and the correct directionality towards another basin representing for instance the products of the reaction. This traversing between reactant and product states, via a transition state is therefore a random process simulated explicitly by MD. KMC on the other hand, coarse-grains this barrier crossing information into a rate constant, such that the trajectory is no longer followed through every vibrational period. In KMC, the focus is on the statistics of barrier crossing; more specifically, the rate constant gives the average fraction of systems crossing the barrier per unit time, in a quasi-equilibrated ensemble of systems at the initial state.

This quasi-equilibrium assumption is of central importance in transition state theory. In the PES framework, the long dwelling time in a potential basin compared to the time of barrier crossing allows us to postulate that the system has sufficient time to forget where it may have been in the past. The rationale behind such a claim is simple. Clearly when a barrier has just been traversed and the system is entering a new basin there must be some

momenta carrying the system toward the potential minimum. The momenta along the reaction coordinate will then disperse over all degrees of freedom with time, as it vibrates around the basin in an attempt to thermally equilibrate. Such vibrations are, as discussed above, on the picosecond scale and are orders of magnitude faster than a typical rare event. Consequently, within the basin many vibrational periods are realised prior to traversing the next barrier. The initial momentum carrying the system into the basin is then dissipated such that its origin has no significance over the next transition. This kind of transition is said to be “memoryless”.

KMC exploits the memoryless nature of such transitions, creating a new kind of state-to-state trajectory. The KMC state refers to the current state the whole system at a point in time – a KMC state is analogous to a minimum found on the potential energy surface. Inter-state transitions are determined by a rate constant k_{ij} which is dependent on the topologies of the transition barrier, the initial state basin and the final state basin.

Consider a pure Cu(111) surface with no defects such as that shown in (a) **A** of **Figure 8**. Suppose the system is comprised of the Cu(111) surface and a gas phase hydrogen molecule. It follows that hydrogen may dissociatively adsorb (**B**) onto the surface through some transition state. It is now possible that hydrogen adatoms may diffuse over the surface between stable hollow sites (for succinctness we will only consider the transitions shown in **Figure 8 (a)**). The one-dimensional potential shown in **Figure 8 (b)** shows three minima corresponding to **A**, **B** and **C** separated by transition barriers – the one-dimensional potential is a slice of the PES along the reaction coordinate. The MD trajectory shown here exemplifies the ideas discussed above regarding the timescale separation. In each basin, the system undergoes many vibrations in the well before traversing the barrier via some mechanism and into the adjacent minimum.

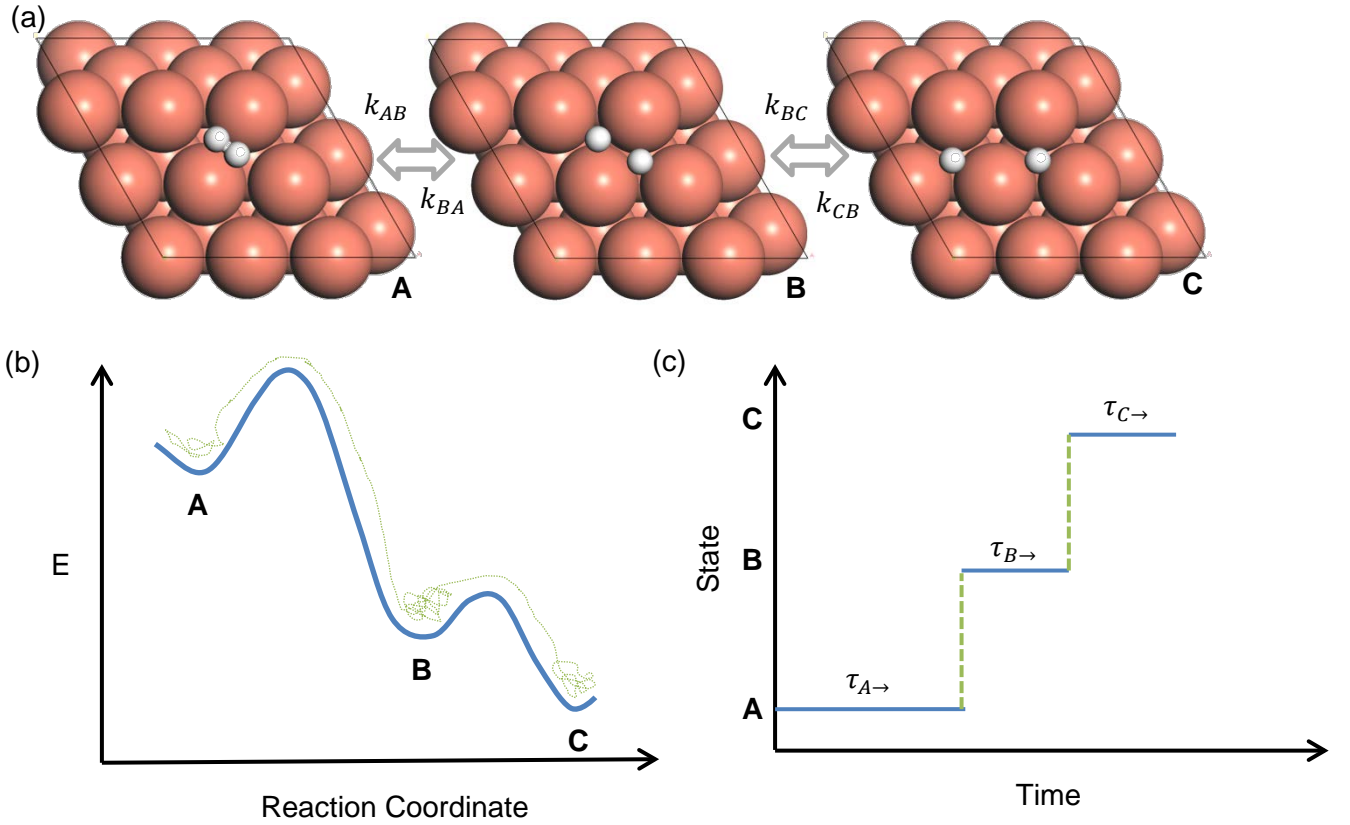


Figure 8: (a) Schematic for hydrogen adsorption on Cu(111) ($A \rightarrow B$) and a subsequent hydrogen adatom diffusive hop ($B \leftrightarrow C$). (b) 1D potential energy surface with a possible MD trajectory for the scheme shown above. (c) Coarse grained KMC trajectory using state-to-state dynamics, showing the temporal evolution of the system.

Figure 8 (c) shows how this potential and the MD trajectory are translated into the KMC framework. The now seemingly continuous MD trajectory has become a discrete trajectory that is a sequence of discrete hops between states. In KMC, the transition state is no longer explicitly accounted for, instead, we focus on the propensity of the transition, quantified by k_{ij} which can be calculated by an ensemble average of trajectories on the PES, or by invoking transition state theory approximations. The random times spent in each basin until the point of transition, for instance $\tau_{A \rightarrow B}$, are referred to as transition/waiting/inter-arrival times, or times of quiescence. If the conditions (e.g. temperature, pressure) remain constant, these times follow exponential distributions with rate parameter equal to the corresponding kinetic constant, for example $\tau_{A \rightarrow B}$ follows an exponential distribution with rate parameter $k_{A \rightarrow B}$, expressing the memoryless nature of the transition. We will elaborate on this point further in the following section, in the context of a detailed discussion of the mathematical formulation underpinning KMC simulation.

The Master Equation

KMC simulation is essentially a random walk on a discrete state space that occurs in continuous time. For our purposes, the state of the system is given by a variable that contains the complete information about the occupancy of all lattice sites, as well as the number of gas phase species produced or consumed. Each site can be vacant or occupied by a species, and the site's occupancy can change as a result of an elementary event/reaction. An event can also change the number of gas phase molecules, in the case of adsorption/desorption and Eley-Rideal reactions. The state space is thus a discrete set encompassing all possible lattice configurations and numbers of gas species. Since the times of elementary event occurrence are continuous and follow memoryless statistics, the random walk is described by a mathematical construct referred to as a Markov process.

A stochastic process whereby given the current state any future state is entirely independent from other states preceding the current state is the defining feature of a Markov chain.¹²⁰ The memoryless transitions described above are exactly this and so a KMC trajectory is merely a Markov walk. State-to-state transitions may be propagated through time using a stochastic procedure. The probability function $P_i(t)$ for finding the system in state i at time t may be evolved in time using a master equation (68) that captures all of the statistics governing a KMC simulation.

$$\frac{dP_i(t)}{dt} = - \sum_{j \neq i} k_{ij} P_i(t) + \sum_{j \neq i} k_{ji} P_j(t). \quad (68)$$

The master equation gives the evolution as a balance of probabilities accounting for the system leaving state i towards other states j or entering state i from any other state j . A KMC simulation is then a random walk governed by eq.(68) that simulates elementary events with rate constants k_{ij} that allow for transitions from state i to state j . Using exact rate constants for a given potential will in principle yield the same result as using MD on the corresponding surface, but with a fraction of the expense.

Satisfying Microscopic Reversibility

In order for any kinetic simulation to be able to reach the correct thermodynamic limits, first it must be ensured that detailed balance between any pair of connected states i and j is obeyed. Consider the master equation describing the evolution of an initially empty lattice in contact with a gas phase which is at thermodynamic equilibrium. When a steady state is reached (in terms of the coverages of the adsorbates), the system will be at thermodynamic equilibrium and the time derivative of the probability $P_i(t)$ will be zero, such that

$$\sum_{j \neq i} k_{ij} P_i^0 = \sum_{j \neq i} k_{ji} P_j^0 \quad (69)$$

$$k_{ij} P_i^0 = k_{ji} P_j^0 \quad (70)$$

where P_i^0 is the time-independent probability of finding the system in state i at equilibrium.

Eq.(70) expresses that (i) for every elementary process $i \rightarrow j$, there is a reverse process $j \rightarrow i$, in other words each microscopic event is reversible; and (ii) the average number of transitions from i to j per unit time is equal to the average number of reverse transitions from j to i when the system is at thermodynamic equilibrium. Detailed balance is satisfied for processes that satisfy eq.(70) and must also hold true even if the system is simulated at conditions far from equilibrium. Hence, this fundamental constraint has to be applied to the definition of rate constants, otherwise the evolution of the system may violate thermodynamics.

To apply this constraint, we note that in a chemical system at thermodynamic equilibrium, the population of states P_i^0 may be expressed in terms of the Boltzmann relationship, such that

$$P_i^0 \sim \exp\left(-\frac{F_i(T)}{k_B T}\right), \quad (71)$$

where $F_i(T)$ is the free energy of state i at temperature T . Thus, we may re-express the detailed balance principle in terms of eq.(71) as a Boltzmann population ratio: ¹¹⁷

$$\frac{k_{ij}}{k_{ji}} = \exp\left(-\frac{F_j(T) - F_i(T)}{k_B T}\right). \quad (72)$$

Stochastic Temporal Evolution

The microscopic reversibility and detailed balance based constraint just discussed makes the connection with thermodynamics, but provides no information about either the statistics of event occurrence or the detailed functional form of k_{ij} . In this section we discuss the former point, whereas the latter is analysed in the next section.

We have briefly mentioned already (in our discussion of **Figure 8**) that the transition times follow exponential decay statistics. This result is supported by the argument of memoryless transitions: whilst the system lingers near a potential energy minimum corresponding to the reactant state i , it is continually vibrating and after a series of vibrational periods will lose its memory, reaching quasi-equilibrium (note that we refer to equilibrium of positions and momenta of the atoms of the reactant(s)). If we consider an ensemble made of ‘quasi-equilibrated copies’ of a system in state i at time t , we pose the question: what is the fraction of systems in the ensemble that have not undergone a transition at time $t + \tau$?

Extending this argument, it follows that the probability of the system leaving the current state is also independent of the past and so over a short interval of time, is constant. If $k_{i\rightarrow} = \sum_{j\neq i} k_{ij}$ denotes the sum of all rate constants for elementary events resulting in the system leaving state i (via any possible transition), it follows that the fraction of the systems undergoing a transition is $k_i \rightarrow \delta\tau$. It can easily be shown that the fraction of systems that have not undergone a transition follows exponential decay statistics.^{121, 122} This fraction is essentially the probability density for the time of quiescence. Conversely, the probability of escape from i to any accessible state during the interval $[t, t + \tau]$ is given as:

$$P_{i\rightarrow}(\tau) = 1 - \exp(-k_{i\rightarrow} \tau), \quad (73)$$

From the properties of the exponential distribution, it follows that $\bar{\tau} = k_{i\rightarrow}^{-1}$, i.e. the average waiting time until the first escape from state i to any state is equal to the inverse of the sum of escape rate constants. We highlight that the equation above gives the distribution of time increments rather than absolute times, and we will use the notation:

$$\tau_{i \rightarrow} \sim Exp(k_{i \rightarrow}) \quad (74)$$

to express that random time increment $\tau_{i \rightarrow}$ follows an exponential distribution with rate parameter $k_{i \rightarrow}$.

The random selection of which elementary event to execute becomes the foundation of a KMC algorithm along with the selection of a corresponding time increment. Originally, the time average τ multiplied by the number of KMC steps simulated was used as an approximation to the clock update.¹²³⁻¹²⁵ However, more rigorous treatments have been introduced that determine the time increment per step.

The exponential probability distributions for escape from state i mean that the associated time increment follows exponential distributions also. Drawing an exponentially distributed, random transition time τ_{trans} is achieved by using a uniform deviate χ , where $\chi \in [0,1]$ and evaluating the following:

$$\tau_{trans}^{i \rightarrow j} = -k_{i \rightarrow j}^{-1} \ln(\chi). \quad (75)$$

Moreover, It can be shown that $\tau_{trans}^{i \rightarrow j} \sim Exp(k_{i \rightarrow j})$.^{126, 127}

We have so far discussed the statistics of transitions, which evidently are heavily based on the rate constants $k_{i \rightarrow j}$. In the next section, we will examine how these constants are obtained from information regarding the PES, which makes it possible to set up KMC simulations solely based on first principles.

Determining the Rate Constants of an Elementary Process

The outcome of a KMC simulation, evidently, is heavily based on the rate constant. A large amount of dynamical information is coarse-grained into the rate constant, so its formulation is critical to the success of the KMC method. The transition from simulating dynamics on a PES to simulating state-to-state jumps in KMC is analogous to moving from an analogue system to a digital one. The true PES picture is not explicitly composed of discrete configurations that are in a given state; rather the system will vibrate within basins centred about these configurations until sufficient energy and momentum is gathered such that a

transition barrier between configurations may be surmounted. In order to use KMC to represent this kind of picture, the rate constant must be able to capture, in detail, the statistics of elementary transitions.

Many KMC simulations in the past have used approximate rate constants in the definition of transition probabilities, some using logical guesses based on experimental constants while others have been fitted to other simulations and/or just arbitrarily set with no tie to the true reaction.¹²⁸ Evidently such an approach will have its limitations though a more rigorous approach can be employed using first principles data in conjunction with statistical mechanical frameworks such as transition state theory (TST).

The ideas underpinning TST lend themselves well to calculating the rate constant. The multi-dimensional barrier crossing problem on the PES is reduced into a one-dimensional problem defined along the minimum energy pathway between minima across a saddle point.⁷¹ TST assumes quasi-equilibrated reactant and transition states. Maxwell-Boltzmann averaging is performed for all degrees of freedom other than the position and momentum along the reaction coordinate. A key step in the derivation is to employ an *Ansatz* according to which the free energy of the transition state is decomposed into a free energy associated with the “other” degrees of freedom (except the reaction coordinate) and a kinetic energy along the reaction coordinate.¹²⁹ The kinetic constant is then calculated by considering the probability of the system visiting the transition state, and averaging over the “speeds” with which it is travelling towards the products state. Both the probability just noted and the distribution of speeds are given by the respective equilibrium distributions making the formal treatment possible. The final result for the TST rate constant k_{TST} is:^{71, 130, 131}

$$k_{TST} = \kappa \cdot \frac{k_B T}{h} \cdot \frac{Q^\ddagger}{Q_{reac}} \cdot \exp\left(\frac{-\Delta E_a}{k_B T}\right), \quad (76)$$

where κ is the transmission coefficient accounting for barrier re-crossings (typically taken to be 1), Q is the molecular partition function and ΔE_a is the activation barrier. We may determine Q for the stable and activated species by using *ab initio* calculations and a

harmonic approximation of the potential; this approach is known as harmonic-transition state theory (HTST). The molecular partition function is formed as a product of contributions from electronic, vibrational, rotational and translational degrees of freedom:

$$Q = q_{elec} \cdot q_{vib} \cdot q_{rot} \cdot q_{trans}. \quad (77)$$

Each component q of the molecular partition function represents the sum of electronic, vibrational, rotational and translational energies. For many systems of interest (as will be the case here) the energies of electronic states that are above the ground state are considered to be negligible as the spacing between energy levels is often far greater than $k_B T$; this is a fair assumption, though will clearly be invalid for non-adiabatic processes. The electronic partition function gives the average statistical occupancy in each energy level. Thus, we take $q_{elec} \approx 1$ implying that only a negligible portion of electronic states is occupied other than the ground state. Thus, Q is reduced to a product of vibrational, rotational and translational partition functions

$$Q \approx q_{vib} \cdot q_{rot} \cdot q_{trans}. \quad (78)$$

The vibrational partition function is expressed as a product of vibrational contributions from each degree of freedom. A harmonic oscillator model is used in the formulation of q_{vib} , assuming the potential is in the harmonic limit about the centre of a basin where the vibrational level spacing is equal. Within the harmonic approximation the vibrational energy levels ϵ_{vib} are $(n + \frac{1}{2})\hbar\nu$, $n = 0, 1, 2, \dots$ (it is noteworthy that expressing the energy levels in this manner ensures that zero-point energy contributions are accounted for). Thus, for a molecule with d vibrational modes with frequencies ν_i , $i = 1, 2, \dots, d$, it can be shown that:

$$q_{vib} = \prod_{i=1}^d \left(\exp\left(-\frac{\hbar\nu_i}{2k_B T}\right) / \left(1 - \exp\left(-\frac{\hbar\nu_i}{k_B T}\right)\right) \right). \quad (79)$$

Rotational energy levels may be found by solving the quantum mechanical rigid-rotor problem. In order to determine the rotational motion we fix the centre of mass of the molecule and calculate three principal moments of inertia I_A , I_B and I_C . We find the

expression for q_{rot} differs depending on the molecular symmetry, e.g. linear molecules have only two principal moments of inertia. The rotational partition function for an asymmetric top is given as:

$$q_{rot} = \frac{\pi^{1/2}}{\sigma} \left(\frac{8\pi^2 I_A k_B T}{h^2} \right)^{1/2} \left(\frac{8\pi^2 I_B k_B T}{h^2} \right)^{1/2} \left(\frac{8\pi^2 I_C k_B T}{h^2} \right)^{1/2}, \quad (80)$$

where σ is the symmetry number. Note that for a symmetric top, the final bracketed term is removed.

The translational partition function is expressed in terms of the volume of the space we are considering. That is for a typical Eley-Rideal reaction and assuming the ideal gas assumption, the volume V may be calculated for one gas molecule given the pressure of the gaseous phase. We write the translational partition function as

$$q_{trans} = V \cdot \left(\frac{2\pi m k_B T}{h^2} \right), \quad (81)$$

where m is the total mass of the molecule.

Each contribution to the molecular partition function can be calculated from DFT along with the saddle point energy in order to obtain the activation barrier for a process. Thus we can compute rate constants using HTST based solely on ab initio data, thereby bridging ab initio calculations (commonly from DFT) within the KMC method.^{128, 132-134}

Coverage-Dependent Activation Energies

The activation barrier ΔE_a for an elementary process (eq. (76)) is often strongly dependent on the locations of spectator species within the local neighbourhood of the adsorbed reactants and/or products. Such dependence arises due to lateral interactions exerted by the spectators to the reactants/products, which may stabilise or destabilise initial, transition and final states.¹³⁵⁻¹⁴¹ Since there may be several different spatial arrangements of the spectators in that neighbourhood, it is practically unfeasible to calculate distinct DFT barriers and rate constants for every possible arrangement.^{116, 128} In this section we outline some key methodologies that allow us to reduce the number of rate constants we must compute by

considering how the activation barrier for a small set of elementary events is affected by the surface coverage.

To better understand the influence of spectator species in the neighbourhood of a reaction event, consider an elementary event that involves gas and surface species. The energy change when such an event has taken place can be found by taking the sum of all product formation energies minus the sum of all reactant formation energies. The energies of gas phase species are additive, since no interactions are considered for these species (ideal gas assumption). For the adsorbed species a simple additive procedure would suffice if the particles are non-interacting. Yet, this is rarely the case: the neighbouring environment of the reacting adsorbates could affect the energy of the adsorbed species: for instance, adsorption on a site with all neighbours occupied would result in a higher (less negative) energy change compared to adsorption on a site with vacant neighbours, due to the destabilisation of the final (adsorbed) state.

In a similar way, lateral interactions may stabilise or destabilise initial and transition states as well, and consequently affect the activation barrier for a process. As an example, consider the elementary events and energy profiles shown in **Figure 9**.

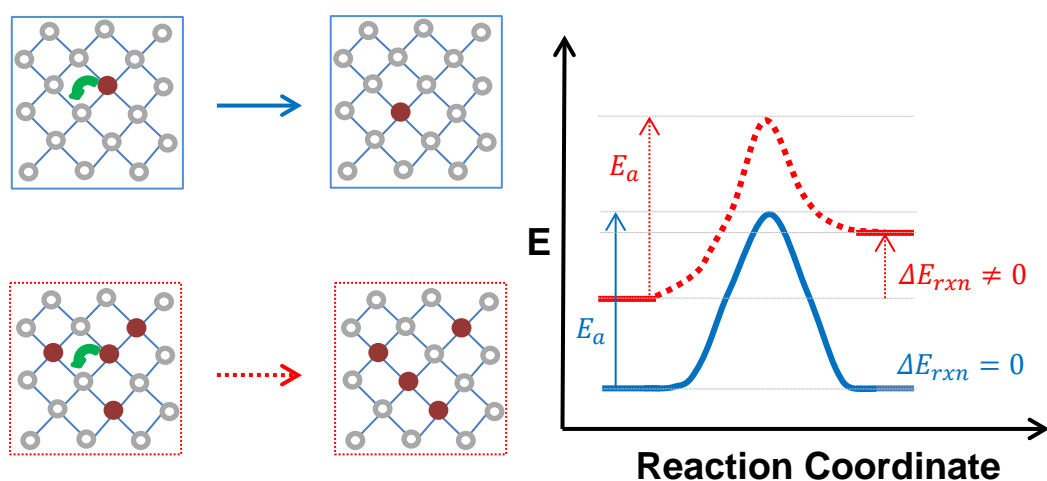


Figure 9: Energetic profiles for a diffusive hop of an adsorbate between sites. The elementary event is shown in the zero-coverage limit (blue) and with neighbouring adsorbates present (red).

This is a simplified model but shows us the effect of lateral interactions on a simple process. A diffusive elementary event is shown in both the zero-coverage limit and with neighbouring adsorbates present. The zero-coverage event (shown in blue) involves no adsorbates other

than the diffusing particle, so the total energy of the initial state is equal to the final state, with both being equal to the formation energy of the species on the surface. The same event but now in the presence of spectators, (shown in red) involves additional contributions to the total energy from lateral interactions. We assume that particles in neighbouring sites exert a repulsion that contributes positively to the energy of the lattice configuration. Thus, we see a rise in the energy of the initial state compared to the zero-coverage limit because of the presence of one neighbouring spectator. In the final configuration, the diffusing particle has two neighbours resulting in a change in the total lateral interaction energy and a non-zero value for ΔE_{rxn} .

In order to satisfy microscopic reversibility (eq.(70)) we must ensure that the difference in the forward and reverse activation energies of an elementary event is ΔE_{rxn} , for *any arrangement* of spectators in the neighbourhood of the reaction (denoted by σ), that is

$$\Delta E_{rxn}(\sigma) = E_a^{fwd}(\sigma) - E_a^{rev}(\sigma). \quad (82)$$

Using the Brønsted-Evans Polanyi (BEP) relation in addition to *ab initio* data, we can formulate a linear relationship for the activation barriers of elementary events affected by lateral interactions. Thus, we express the forward activation barrier in terms of the activation energy $E_{a,0}^{fwd}$ and reaction energy $\Delta E_{rxn,0}$ at the zero-coverage limit, as well as the net reaction energy ΔE_{rxn} at configuration σ which defines the states of neighbouring sites surrounding the reactants:

$$E_a^{fwd}(\sigma) = \max\left(0, \Delta E_{rxn}(\sigma), E_{a,0}^{fwd} + \omega \cdot (\Delta E_{rxn}(\sigma) - \Delta E_{rxn,0})\right), \quad (83)$$

where ω is the proximity factor and characterises the position of the transition state along the reaction coordinate ($0 \leq \omega \leq 1$). Using eq.(82) we may also express the reverse activation barrier E_a^{rev} at configuration σ as

$$E_a^{rev} = \max(-\Delta E_{rxn}(\sigma), 0, E_{a,0}^{rev} - (1 - \omega) \cdot (\Delta E_{rxn}(\sigma) - \Delta E_{rxn,0})). \quad (84)$$

Notably within the BEP relation, the pre-exponential factor written in eq.(76) is constant for each family of reactions – that is for BEP related elementary events with the same zero-coverage initial configurations and activated complexes.

Now we will discuss how one can parameterise an energetic model for the lateral interactions, via which one can compute $\Delta E_{rxn}(\sigma)$, then $E_a^{fwd}(\sigma)$ and $E_a^{rev}(\sigma)$ from the BEP and finally the thermodynamically consistent forward and reverse rate constants (k_{TST}) that satisfy micro-reversibility and detailed balance. Our discussion will focus on two models: pairwise additive interactions and the cluster expansion model.

Nearest Neighbour Pairwise Additive Interactions

The most basic treatment of lateral nearest neighbour energetics is to use an approach, similar to the one we used in our discussion of **Figure 8**. This approach is based on the assumption that interaction energies, are pairwise additive such that if an adsorbate i is interacting with adsorbate j and adsorbate k , then the total interaction felt by i is simply the sum of the two pairwise interactions.

Computing the total energy E_{Tot} for a given lattice configuration σ is straightforward. We sum the one-body energy contributions ε_1 from each adsorbate i (a.k.a. the formation energy of each adsorbate) and add an interaction energy contribution ε_2 for each distinct pair of neighbouring adsorbates i and j . We write

$$E_{Tot}(\sigma) = \sum_{i=1}^{N_{Sites}} \varepsilon_1 \cdot \sigma_i + \sum_{i=1}^{N_{Sites}} \sum_{j=i+1}^{N_{Sites}} \varepsilon_2 \cdot \sigma_i \cdot \sigma_j , \quad (85)$$

$$\sigma_i = \begin{cases} 0 & \text{vacant} \\ 1 & \text{occupied} \end{cases}$$

where σ_i defines the occupancy of state i and N_{Sites} is the total number of lattice sites.

Consider the example in **Figure 10**. We have a lattice with one site type and one type of adsorbate. Nine sites are occupied ($\sigma_i = 1$) with the remaining sites left vacant ($\sigma_i = 0$). The first term in Eq.(85) is then $(9 \cdot 1 + 21 \cdot 0)\varepsilon_1$. The total number of distinct pairwise interactions

is eight with two adsorbates experiencing no lateral interactions. Thus the second term in Eq.(85) is $8\varepsilon_2$ meaning $E_{Tot} = 9\varepsilon_1 + 8\varepsilon_2$.

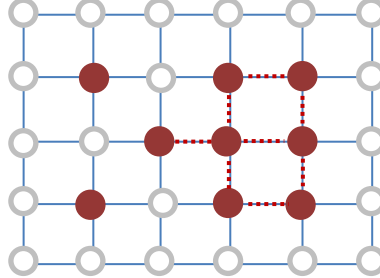


Figure 10: Lattice state σ constructed of a single site type with one species type adsorbed to the surface. The site occupancy is given by σ_i , where 0 corresponds to a vacant site (grey) and 1 corresponds to an adsorbed species i (red). The connectivity in the lattice is shown by blue horizontal and vertical lines with pair interactions shown by the dashed, red line.

Cluster Expansion Hamiltonian

The pairwise additive approach can be generalised to the so-called cluster expansion (CE) Hamiltonian model.¹⁴² This generalisation is built on the same principle as the pairwise model, namely summing up energy contributions between interacting adsorbates. However, a CE can encompass long range adsorbate interactions, and more importantly many-body contributions which are not pairwise additive. Hence, the CE is a powerful generalisation, and can capture *ab initio* data (energy versus configuration) at any desired level of accuracy, albeit at with corresponding computational expense.

In the CE model, contributions to the total energy are partitioned into small, characteristic sub-sets known as clusters.¹⁴² The most basic clusters are single adsorbates and neighbouring pairs which are analogous to those found in the pairwise additive approach. Additional higher order clusters such as triangles are also specified allowing for generalisation away from two-body and nearest neighbour interactions. This is important in reproducing long range order and increases the level of detail that KMC may adopt from first principles calculations.¹⁴³

The energy contribution of each cluster is often referred to as the effective cluster interaction (ECI). To determine the total energy of the lattice we scan the lattice configuration for instances of each cluster k , and add contributions equal to ECI_k times the number of symmetrically distinct such instances. The number of such instances is obtained as the total

number of instances n_k divided by a multiplicity factor m_k that takes care of over-counting.

For example, a pairwise-additive interaction between two adsorbates of the same type A₁, A₂, occupying equivalent sites will have $m_k = 2$, since both patterns A₁-A₂ and A₂-A₁ can be detected. Thus, we express the total energy E_{Tot} for a given configuration ω as:

$$E_{Tot}(\omega) = \sum_{k=1}^{N_P} \frac{n_k(\omega)}{m_k} ECI_k, \quad (86)$$

where N_P is the number of clusters in the CE.

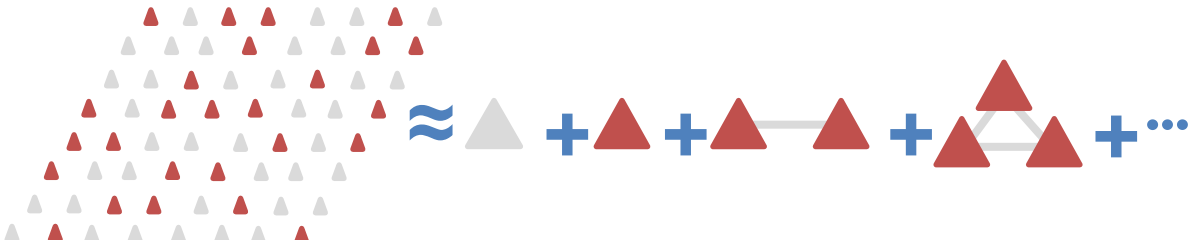


Figure 11: Illustration of the cluster expansion summation of energetic contributions. The total energy of the surface (left) is broken down into contributions from n-body clusters (right).

Ab initio techniques, for instance, periodic density functional theory (DFT), can be used to calculate the ECI values (e.g. adsorption and interaction energies) of clusters thereby parameterising a CE, which can then be used to calculate the energy of any configuration. The advantage of using CEs in KMC simulation therefore lies in the fact that even for small lattices the number of possible adsorbate configurations is large. Trying to use DFT to obtain the energies of all lattice configurations sampled during a KMC run would require an enormous computational effort. On the other hand, a well parameterised CE would be able to calculate these energies at a fraction of the computational cost. Fitting the ECI to *ab initio* data is a relatively simple yet time consuming task.¹¹⁵ The main challenge is to generate a dataset which is representative of the ensemble of configurations sampled during the KMC run. Particularly for systems with many species and site types, a large number of *ab initio* data needs to be obtained. On-the-fly cluster expansion training procedures may be adopted in place of an extensive *a priori* fitting.^{144, 145}

Algorithms and Implementation

We have introduced so far some of the basic concepts and theory underpinning the KMC method. It remains to be discussed how one can put together a KMC simulation of a catalytic

chemistry given the different pathways thereof. In its core, a KMC simulation involves the scheduling and random selection of elementary events such as adsorption, desorption, surface diffusion and reaction.

The computational implementation of KMC employs pseudo-random numbers to determine which elementary event is executed and how the simulation is evolved through time. How the psuedo-random numbers are utilised will determine the efficiency of a KMC simulation and many different methods of implementation have led to the development of several KMC algorithms. Despite differences in the pseudo-random number usage, all KMC algorithms follow a basic structure or backbone as depicted in **Figure 12**.

The KMC backbone is simple and allows the simulation of elementary events such that a trajectory is created that is in line with the statistics outlined by the master eq.(68). A general KMC algorithm begins by specifying the simulation parameters (see later) and initialising the system with a random or pre-specified configuration at time $t = 0$. Next, the simulation enters into a loop in which a process is chosen and executed with the clock being respectively updated. Once in the loop, a event is selected at random and is subsequently executed. Upon execution, the configuration is updated and the rate constants are recalculated accordingly. The time is then advanced and the simulation begins the next iteration in the loop until $t \geq t_{final}$, where t_{final} is the specified maximum simulation time.

Before diving into the details of specific KMC algorithms we will take a moment to distinguish between two types of KMC that may be more or less well suited to particular algorithms, namely well-mixed (off lattice) and spatial (on lattice) KMC.

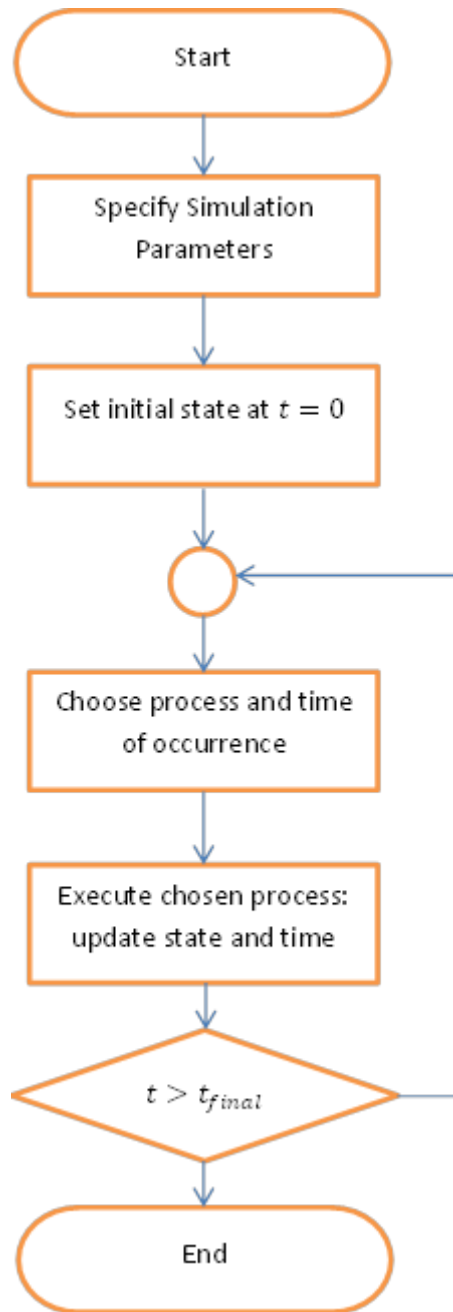


Figure 12: General schematic of the KMC algorithmic backbone. KMC algorithms all use this backbone, though vary in the way in which processes are selected, executed and in the clock advancement.

Well-mixed and Spatial KMC

Originally KMC was used to model the temporal evolution of Ising spin systems, whereby the state-to-state dynamics involved transitions between spin states.¹⁴⁶ Naturally it followed that KMC could also be employed to treat well-mixed chemical systems that only considered the number of species in a system rather than explicitly accounting for their spatial configurations. An example of a well-mixed system would be the two component reversible gas phase model where A undergoes some process (e.g. an isomerisation) to form a product B and in turn, B may undergo the reverse process to form A (**Figure 13**). The KMC

trajectory of this system would then propagate the mole fractions of A and B using rate constants assigned to both transitions.

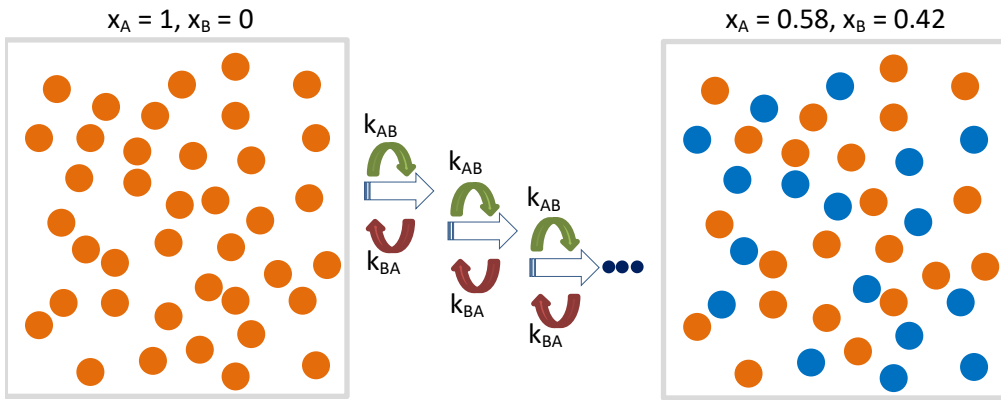


Figure 13: A well-mixed system of A (orange) and B (blue). A may isomerise into B and B into A with rate constants k_{AB} and k_{BA} . Many KMC steps are performed as the system begins to equilibrate over time.

Well-mixed KMC simulations are very useful for modelling certain systems however, in heterogeneous catalysis there are many complexities that such simulations cannot account for.^{116, 147} The intricacy of many catalytic mechanisms often means that accounting for specific spatial configurations of the species involved is necessary for a complete description of the reaction kinetics.

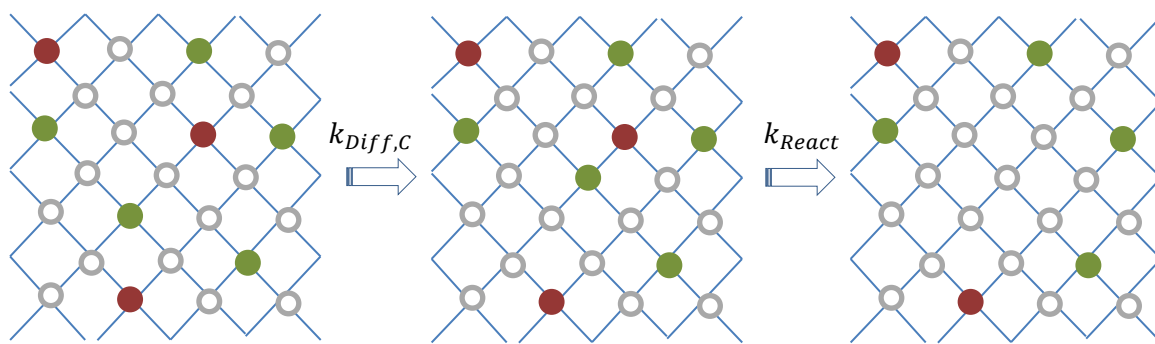


Figure 14: On-lattice spatial KMC showing discrete sites in a lattice network that are unoccupied (grey) or occupied by species C (green) and D (red). Step one shows the diffusion of C into close proximity with D with corresponding rate constant $k_{Diff, C}$. Subsequently, the second step is the reaction of C and D described by the rate constant k_{React} to form a gaseous product.

Consider for instance a surface reaction where reactants C and D react via some mechanism to produce a gaseous product (**Figure 14**). Suppose that in order to react, C and D must be within close enough proximity on the surface and that the reaction is diffusion limited. Using a well-mixed system we can only account for this diffusive limit by modifying the rate constant yet to do this rigorously is difficult.

Introducing the concept of a lattice into the simulation allows us to explicitly account for the spatial configuration of species within a system. The lattice is a portrayal of the catalytic surface and as we will see later, can vary in its complexity. A KMC lattice is built of discrete sites that are distributed in a network such that each unique site has a set of neighbours. On lattice KMC then allows for a more in depth description of elementary events. For example a site on the lattice can now become occupied through adsorption of a gas phase species, diffusion of an already adsorbed species from a neighbouring site or through some reaction. The state of the system is then defined as the occupation of the lattice and the pattern of adsorbed species. In the above reaction of C and D, we can now determine where each reactant is on the surface and by assessing the neighbouring sites, we can see if C and D are proximal. We now no longer need to modify the reaction rate constant but simply need to include a new rate constant of a well-mixed model for the diffusive processes that will enter the master equation and become part of the KMC trajectory.

Representing the Catalytic Surface

As we discussed in the Algorithms and Implementation section, KMC simulation algorithms have been developed for both spatially distributed and well-mixed systems. Spatially distributed lattice-based KMC can treat the inhomogeneity of the catalytic surface and the ordering of surface adlayers. Thus, we will briefly discuss how the catalytic surface is represented by a lattice in spatially distributed KMC approaches.

The first step in constructing such a representation is to discretise the catalytic surface into sites, based on information about the locations on which adsorbates can be found in stable binding configurations. Any site can be assigned a type, for instance the (111) surface of an FCC metal can be represented by a lattice with four site types: top, bridge and fcc hollow and hcp hollow. Different site types have different properties, for instance a species may exhibit different binding strengths towards each site type and different reactivity thereon.

After deciding how many site types will be considered, and given their spatial arrangement, one has to store the lattice structure in the memory of the computer, along with the state of the lattice containing complete information about the occupation state of each site.

A Simple Matrix-Grid Representation

The simplest treatment of the catalytic surface is to transform the network of discrete sites into a grid, conveniently represented by vectors or matrices.^{133, 148} As an initial simplification, we will consider the surface to be formed of one site type. A matrix is constructed wherein each element corresponds to a site as shown in (**Figure 15**). The value each element takes corresponds to the occupancy. In the lattice gas model, 0 corresponds to a vacant site and 1 an occupied site. Modifications to the lattice gas model can be made such that higher values correspond to other species, allowing for reactive systems with multiple adsorbate types.

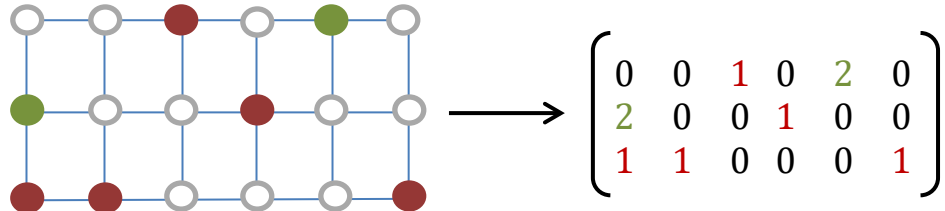


Figure 15: Matrix-grid lattice representation of a surface. The occupation matrix shows the occupation of different species on the surface (0 – vacancy; 1 – species red; 2 – species green).

Elementary events are generated and executed by changing the matrix elements. An adsorption event for example would involve changing a zero element to be non-zero and whose value is determined by the species type being adsorbed.^{133, 149}

The current state of the lattice determines the elementary events that can take place and also the energy of the system. Consider element [2, 1] of the matrix in **Figure 15**; the corresponding site is occupied by species 2. The elementary events which this species is directly involved in (assuming a non-reactive system) could be desorption and diffusion north, east or west (for a periodic lattice). No diffusion may occur to the south due to site [3, 1] already being occupied.

The connectivity of the sites (neighbouring structure) may be integrated into the framework in a variety of ways. One may simply define a set of rules when coding the event execution using matrix indices. The first nearest neighbouring sites of site $m_s n_s$ in an m -by- n matrix are $m_{s+1} n_s$, $m_{s-1} n_s$, $m_s n_{s+1}$ and $m_s n_{s-1}$. Sub-matrices containing this information for each site can be linked with the occupation matrix creating a network such that one can more

readily search through sites to find the local neighbouring patterns prior to event list population or the resolution of the adlayer energetics.

Provided the lattice has two-dimensional translational symmetry, such that the position of any site on the lattice is a linear combination of two vectors, we can represent the lattice as an array of unit-cells formed by the primitive vectors. Thus, we may reference any site on the lattice using the vector coefficients of the unit cell to which the site belongs, and the location of the corresponding site in the primitive cell. Moreover, the neighbouring sites may be specified in the same manner. Periodic boundary conditions are introduced in representations such as these, such that elementary events are not inhibited by the boundary.¹⁴⁹ However, small lattices may lead to artefacts, referred to as “finite size effects”, and it is always advisable to perform comparisons with results obtained from larger lattices, thereby measuring and ensuring the accuracy of the employed simulation scheme.

Graph-Theoretical Framework

The majority of KMC frameworks only consider single site elementary events with unidentate species. Representations such as the grid based method described above cannot account for multi-dentate adsorbates. Hansen and Neurock were the first to allow for bidentate adsorbates and for three-site reaction patterns, although this approach was not generalised to arbitrarily complex reaction patterns and multi-dentate adsorbates.¹⁵⁰

A graph-theoretical framework developed by Stamatakis and Vlachos is unique in that it is able to effectively account for multi-dentate binding in a general way.¹⁵¹ Furthermore, graph-theoretical KMC can capture the complex reactivity of real-life surface chemistries. The formulation is general and widely applicable; in particular when combined with the more advanced elements of KMC such as cluster expansion energetics and efficient algorithms, the graph-theoretical method becomes a powerful tool.¹⁴³

Similarly to other methods of surface representation, graph-theoretical KMC uses well-defined discrete sites with corresponding site types and can incorporate periodic boundary conditions as well as treating finite systems. In this approach the lattice is represented as a

graph. The position of each lattice site is given by Cartesian coordinates and with vertices representing sites and connecting edges showing their neighbouring relations. An adjacency list is generated stating the site coordination number along with the indices of any neighbouring sites as shown in **Figure 16**.

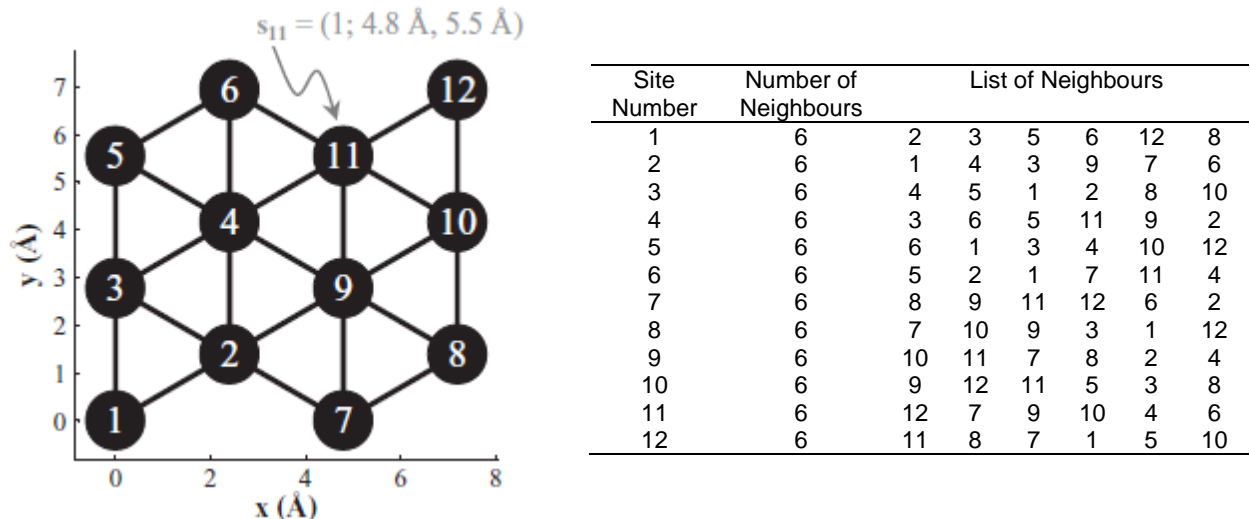


Figure 16: Graphical representation of the KMC lattice using the graph-theoretical method.¹⁵¹ Graph vertices correspond to sites with edges showing the lattice connectivity. A list of neighbours is given for each site number.

The state variable contains all of the information about the state of each site and a definition is given containing the entity number, the adsorbate type and its orientation. The orientation is determined first by the dentate number d corresponding to the number of sites the adsorbate binds to. The entity is decomposed into d sub-units whereby each sub-unit is labelled and assigned a site number to which it is occupying. We see in **Figure 17** that ambiguity in the orientation of identical molecules on the surface is dealt with effectively. (a) and (b) show two species that are indistinguishable in each picture, except for the orientation. The sub-unit or entity number allow for the orientation to be specified is shown in the table of **Figure 17**.

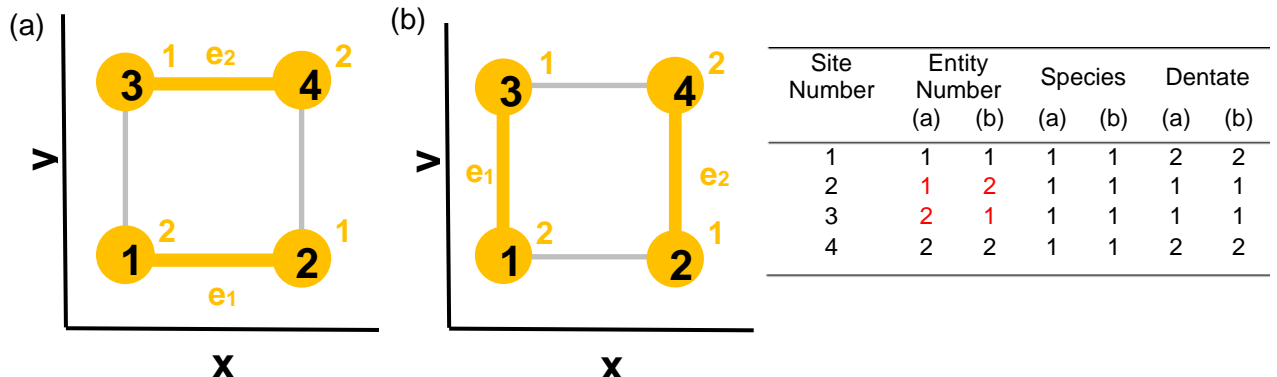


Figure 17: Illustration of how the graph-theoretical method accounts for the exact orientation of adsorbates using site numbers, entity number, species and denticity.

Concisely describing the adjacency allows us to readily detect adsorbate and site patterns on the surface that may be crucial to determining the adlayer energetics or prospective elementary events. The denticity and sub-unit structure combined with the lattice neighbouring pattern and structure enable efficient mapping of the graph pattern onto the lattice graph through solving a sub-isomorphism problem. One searches for mappings of the pattern corresponding to vertex and edge combinations on the graph. Such a formalism allows for complex adsorbate interactions to be modelled and the graph-theoretical framework lends itself well to be used synchronously with the cluster expansion method discussed next. Pre-defined energetic clusters may be found efficiently using the aforementioned mapping and are used in the cluster expansion.

Kinetic Monte Carlo Algorithms

Many KMC algorithms have been developed, with variations existing for both on- and off-lattice KMC procedures. Well-mixed off-lattice KMC has very limited application in surface science with its applications typically seen in growth/aggregation as well as diffusion problems. The most cutting-edge surface science simulations are performed using spatial treatments and so we will introduce three KMC algorithms here, one which is specific to on-lattice KMC and two of which may be used for both types of KMC (Gillespie type algorithms). These algorithms are the null-event method, the first reaction method and the direct method, respectively.

The Null-Event Method

One of the earliest-employed KMC algorithms is the null-event or random selection method.^{116, 119} According to this algorithm, a site S_{exe} is first randomly selected among all sites of the lattice. Note that each site has equal probability of being selected. Once S_{exe} is determined, an elementary event is selected out of the list of all events that have been defined. In this second selection process, events with higher kinetic constants have higher probability of being chosen; in fact, the probability of choosing event $i \rightarrow j$ is equal to its normalised rate constant, namely $k_{i \rightarrow j}$ divided by the rate constants of all elementary events.

Note that this selection process does not take into account any information about the state of site S_{exe} . Thus, the independent selection of the site and the event to be executed can lead to situations where a non-realisable event may be selected. For instance, let us consider a system with two possible elementary events, adsorption and desorption, and suppose that in the current state, the lattice is partially saturated. Clearly, the only realisable events are adsorption at a vacant site and desorption from occupied sites. However, in the null-event method it is possible to choose an occupied site and attempt to execute an adsorption event thereon. This kind of event is a “null-event” and will result in an unsuccessful (rejected) trial; the KMC clock will be advanced, but the state of the system will remain the same, and the two random numbers generated in the site- and event-selection processes will be wasted.

Hence, the efficiency of null-event algorithm critically depends on the probability of attempting to realise such null events. When this probability is low, the null-event algorithm may be very efficient. However, as the system becomes more complex, the probability of selecting null events increases and so the efficiency of the algorithm is reduced.¹¹⁶

The First Reaction Method

The first reaction method algorithm intuitively says that the next event that is executed is the event that will occur the earliest in time.^{121, 128} This directive means that the algorithm must be able to determine all of the relevant escape times from the current state and compare

them to find the shortest time and hence the “first reaction” that can occur – the first reaction method is a kind of rejection-free algorithm.

Random numbers are drawn for every process and the corresponding random inter-arrival time t_{trans}^j is generated in line with eq.(75). The process to be executed j_{exe} is the process with the smallest value of t_{trans} i.e. the state-to-state transition with the shortest inter-arrival time,

$$j_{exe} = \operatorname{argmin}_{j=1,2,\dots,jmax}(t_{trans}). \quad (87)$$

The computational burden of calculating a large number of random times at every KMC step is significant and may hamper the efficiency of the algorithm particularly in large systems that give rise to numerous potential state-to-state transitions.

One can reduce the computational cost by saying that if the outcome of an executed event has no influence on a second process j_α then we may assume that process j_α retains the same random time until any of the following occurs: (i) the secondary process j_α is executed; (ii) an event is executed that consumes the reactants of this process; or (iii) the local environment of the reactants is perturbed such that lateral interactions influence $k_{j\alpha\rightarrow}$ and it must be re-calculated.¹⁵² As we will see later, most lateral interaction models used in KMC account for a discrete number of nearest neighbour sites and so the size of the system along with the number of nearest neighbours considered will to some extent determine the relative efficiency of the first reaction method.

One may employ advanced book-keeping methodology to keep track of the synergy between different events. Retaining information about the sites which a given event is dependent on allows for efficient deletion and updating of event lists, corresponding rate constants and inter-arrival times.¹⁵³

Direct Method

The direct method is another rejection-free algorithm that does not attempt to execute non-realisable events. We achieve this simply through the way in which the rate constant is used.

We begin with the system in state i and generate a list of all processes leaving state i . The rate constants for each of these processes is also found before summing the rate constants to give $k_{i \rightarrow \cdot}$, the sum of all rate constants for processes leaving the current state i . The event to be executed is selected by drawing a uniform deviate χ where $\chi \in [0, 1]$ and scaling it by $k_{i \rightarrow \cdot}$ such that a random event j_{exe} is chosen and the inequality in eq.(88) holds,

$$\sum_{j=1}^{j_{exe}} k_{i \rightarrow j} \geq \chi \cdot k_{i \rightarrow \cdot} > \sum_{j=1}^{j_{exe}-1} k_{i \rightarrow j}. \quad (88)$$

The probability of selecting an event is proportional to its rate constant. Events that are non-realisable (as we encountered in the null-event method) must have a rate constant of zero and consequently do not contribute to $k_{i \rightarrow \cdot}$. Hence such events cannot be selected and so no rejections occur.

The N-fold way is a variation of the direct method that uses the same probability weighting but groups events according to class, aiming at improving search efficiency.¹⁴⁶ A class can be defined by symmetry on the lattice; for instance we can group instances of an elementary event on the lattice for which the arrangements of neighbouring spectators are identical up to a symmetry operation (e.g. rotation or reflection). Searching for the event j_{exe} is thus performed more efficiently, by searching for a class rather than individual events. As an example, consider the desorption of a single species from a rectangular lattice and assume that only first nearest neighbour repulsive interactions are important. Instead of performing repetitive summations of the desorption rate constants for each and every desorbing particle, we can identify five groups. The first one consists of the particles which have no spectators in their four neighbouring sites; the activation energy of desorption will be equal to the binding energy (BE) of the particle. The propensity of the entire class will be equal to the number of particles with no neighbouring spectators, multiplied by the kinetic constant for desorption at the zero coverage limit. The second group consists of the particles which have one neighbouring spectator (irrespective of which of the four sites this spectator is bound on). The activation energy for the second group will be equal to the BE reduced by the

repulsive interaction energy between the two particles. Similarly, the third group has three neighbours and an activation energy equal to the BE minus twice the interaction energy, and so on. Following a procedure like the one outline above, one can now select one of the five classes (note that the summation is now much easier since only five terms are summed).

Once a class has been selected for execution, the actual event to be executed is chosen by drawing a uniform integer in the range of 1 to the number of events in the class (multiplicity).

The N-Fold way can thus markedly accelerate the first-event method. However, when we consider systems with greater complexities such as long range lateral interactions, multiple adsorbate types and non-uniform catalytic surfaces the N-fold way becomes impractical due to the sharp increase in the number of classes and the corresponding decrease in class multiplicity.

Equivalence of Well-mixed and Spatial Stochastic Kinetic Simulations

Despite the differences we have discussed between well-mixed and spatial KMC simulations, realisations of the Master equation using Gillespie type or on lattice KMC algorithms have been shown to be equivalent within the limit of fast surface diffusion.¹⁵⁴ That is, the Master equation for the dynamics of a surface species is shown to reduce to that of a well-mixed chemical system, assuming very fast diffusion.¹⁵⁴ This mapping between on-lattice microscopic lattice propensities and a well-mixed procedure retains equivalency as the rate of surface diffusion is reduced, though incurs error that is linearly proportional to the inverse of the macroscopic diffusion rate constant.¹⁵⁴

It is common in spatial KMC simulations that there is a timescale separation between interesting reactive elementary events and somewhat less interesting (under the remit of surface science and catalysis) dynamical events such as surface diffusion. Surface diffusion is very fast and as a result KMC simulations sample many diffusive events before any reactive events. Simulations like this are grossly inefficient, spending the majority of the computational time executing diffusion events without sampling reactive events. Reducing the magnitude of the surface diffusion rate constant(s) will improve the efficiency and as we

discussed in the previous paragraph, will impact upon the accuracy of the simulation with an error that is linearly proportional to the inverse of the diffusion rate constant.

From a practical standpoint in a large scale simulations scaling of the diffusion may lead to unwanted changes in the kinetics, though some implicit averaging due to the size of the lattice will reduce the impact of the scaling. It follows that convergence of the kinetics can be achieved by ensuring that quasi-equilibration of forward and reverse elementary events is maintained and no changes in the kinetics are seen.¹⁵⁴ For example, **Figure 18** shows an Arrhenius rate plot of the log of the kinetic constant against inverse temperature for some fictitious elementary process (red) with a corresponding, couple diffusion (blue).

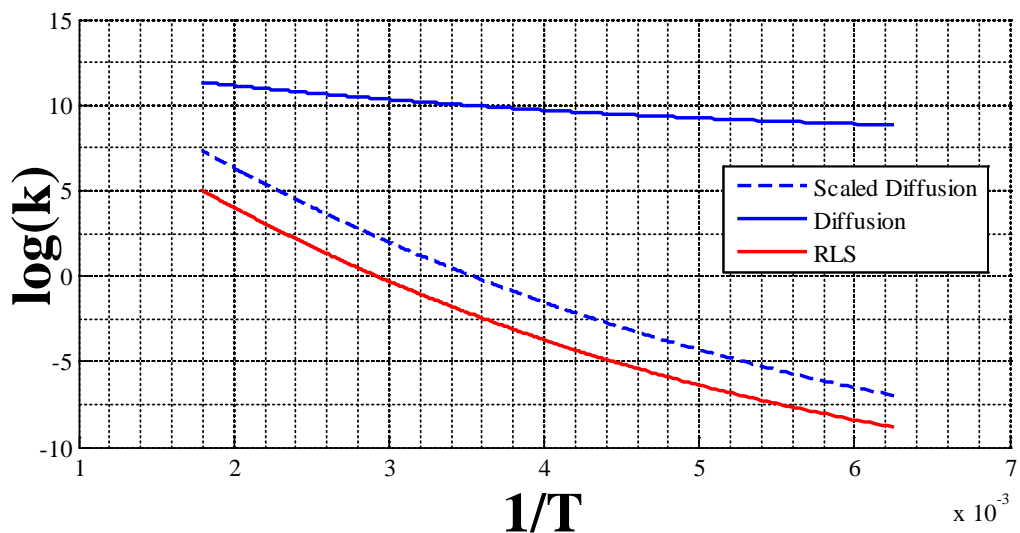


Figure 18: Example of an Arrhenius plot showing the scaling of the rate of diffusion with temperature. The activation barriers for diffusive events are adjusted such that the gradient of the diffusion in the Arrhenius plot is the same a dynamical event that we are interested in studying. The diffusion pre-exponential factors are scaled, ensuring the adsorbate over-layer remains quasi-equilibrated with the rate of diffusion approximately two orders of magnitude greater than that of the “interesting” event.

In order to maximise the simulation efficiency the rate of diffusion is reduced. Optimal efficiency can be obtained by arbitrarily setting the diffusion rate constant to be a few order of magnitude greater than that of the fictitious elementary event. When doing do, one must ensure that the adsorbate over-layer is quasi-equilibrated such that the rate of diffusion does not become artificially rate limiting.

Brief Summary

In this section of the Chapter, we have focussed on the theoretical origins and the practical implementation of the KMC method. We considered the issue of timescale separation within

the context of the potential energy surface and chemical transformations, showing how coarse-graining of dynamic information into KMC can be used to simulate the temporal evolution of a system. We highlighted some of the methods and practical considerations in the implementation of KMC within the setting of heterogeneous catalysis.

Conclusion

We have briefly introduced some of the key ideas behind *ab initio* KMC simulations focussing on DFT, TST and KMC. We move on, in the remainder of this thesis, to discuss the application of these theoretical methods in our study of bimetallic alloy surfaces in heterogeneous catalysis.

Chapter 3 Towards the Development of Single Atom Alloy

Catalysts as a Means of Escaping Linear Scaling Relations

The advent of linear scaling relations has had significant impact on studies that investigate the catalytic properties of materials leading to the rational design of heterogeneous catalysts. Albeit tremendously useful in the prediction of catalytic performance, linear scaling relations by their very nature, impose limitations on the ultimate performance of a catalyst. We propose a simple yet effective strategy for escaping traditional linear scaling relations through the use of highly dilute, atomically dispersed bimetallic alloys known as Single Atom Alloys (SAAs). Using Density Functional Theory we examine the chemisorption properties of simple adsorbates on a range of SAAs, demonstrating that high surface chemical heterogeneity can result in significant deviations from adsorption energy linear scaling. We show that the SAA surface structure forces deviations from the Brønsted-Evans-Polanyi relationship for several key catalytic bond dissociation reactions (H-H, C-H, N-H, C=O and O-H). These insights into SAAs and their ability to break linear scaling relations will facilitate the discovery of new alloy catalysts that exhibit novel catalytic behaviour that can be fine-tuned in terms of activity, selectivity and stability.

Introduction

Electronic structure methods have provided tremendous insight into the workings of many heterogeneous catalytic systems through the prediction of adsorption geometries and their associated energies, as well as the identification of transition states and their respective activation barriers for elementary reaction events. Unfortunately, such studies are time- and resource-intensive due to the complexity of electronic structure calculations; for example using Density Functional Theory (DFT). Consequently, it is difficult to accurately screen the catalytic behaviour of a large ensemble of materials without the use of simpler, more efficient methods.

Within the last two decades, linear scaling relationships, such as thermo-chemical scaling (TCS) that describes the linear correlation between the adsorption energies of chemically related species,²³ and the Brønsted-Evans-Polanyi (BEP) equation that relates the activation energy of an elementary process to its reaction energy,³¹⁻³⁴ have been warmly welcomed by the catalysis community and offer an extremely useful methodological framework for identifying materials with desired catalytic properties.¹⁵⁵ Extensive quantification of TCS and the BEP relation has been carried out using DFT, through studies on a vast array of chemistries on variety of materials.^{23, 26, 27, 32-34, 39-45} When combined, TCS and the BEP relation, the kinetics of a complex catalytic reaction can in principle be determined from just a few descriptors making these linear relationships extremely powerful.^{11, 33, 35-38}

Linear scaling relations rationalise the Sabatier principle which states that optimal catalytic performance will be achieved by the material that binds substrates neither too strongly, such that the desorption of products is prevented leading to poisoning, nor so weakly that adsorption and activation are inhibited, but instead at some intermediate strength.¹⁵⁶ From TCS, intermediate adsorption strength must coincide with intermediate reaction energy, and by the BEP relation, an intermediate activation barrier. Despite the evident predictive power of TCS and the BEP relation, the linear nature of these scaling relationships actually imposes limitations on how effective a newly designed catalyst can be, if indeed such scaling

is ubiquitous.⁹ Consequently, a new challenge arises in the discovery of novel materials that can deviate from these trends, unlocking the potential for the enhancement of catalytic behaviour beyond the limits defined by linear scaling.

Several strategies have been suggested to escape traditional linear scaling relations.^{44, 157-159} For example, changes in the surface structure of the catalyst, as well as changes in the surface atom coordination number lead to different dependencies between correlated quantities such that these materials follow their own unique TCS or BEP relation.⁴⁴ Other strategies encourage an escape from linearity through the decoupling of correlated adsorption energies by tuning the affinity of different species towards different sites on the material.¹⁵⁷⁻¹⁵⁹ Methods that are capable of achieving decoupling and a deviation from TCS include binding promoters to the surface, tethering adsorbate specific ligands and alloying with a secondary element.¹⁵⁷ The focus of this article will be on the latter.

Linear scaling relationships have been identified on several classes of bimetallic alloy surfaces. Uniform secondary metal overayers or subsurface layers on or in a host transition metal adhere to TCS due to uniformity in the electronic structure across the surface, with the scaling relationship able to be described simply in terms of the valency of the alloying metals and the adsorbate.^{48, 49, 160} On the other hand in the case of H₂ activation, it has been shown that the interaction of Pt and Pd terminated alloy overayers with bonding orbitals is decoupled from that with anti-bonding orbitals, allowing for BEP relationships that combine weak adsorption of intermediates with low transition state energies.³⁹ These surfaces are ideal and in many cases are unfeasible under real catalyst operating conditions,¹⁶¹ though serve as a very useful proof-of-concept that not all transition metal surfaces adhere to linear scaling relations.

Atomically smooth intermixed binary alloys have a higher degree of spatial heterogeneity and an increased number of surface site types compared to uniform overlayer or subsurface layer alloys. Many studies on these types of alloys implicitly assume that TCS and BEP scaling hold on these surfaces and experimental evidence gives reasonable justification to

this.¹⁶²⁻¹⁶⁴ In several cases where a complete DFT study has been carried out, TCS holds well on intermixed alloy surfaces though only when the same site type is considered for adsorption;¹⁶⁵ TCS may be broken when a pair of adsorbates favour different site types.^{157, 158} The BEP relationship for pure transition metals is also valid for intermixed alloys for O₂, H₂O and CH₃OH dissociation.¹⁶⁶⁻¹⁷⁰ For intermixed alloys, it has been shown that the activation energy as well as the adsorption energy are related to the Bader charge and electronic structure of the surface atoms; these properties can be linearly interpolated from the analogous monometallic properties when the alloy consists of two surface metals with comparable molar fractions.¹⁷⁰⁻¹⁷² Increasing the dilution of binary alloys causes this model to become less effective¹⁷³ and as we show here, highly dilute Single Atom Alloys (SAAs) are also capable of escaping TCS and the BEP relationship because of their surface composition.

SAAs are bimetallic alloys of catalytically active transition metals doped at low concentrations into a more inert metal, such that the dopant disperses in the form of individual, isolated atoms in the surface layer of the host material.^{6, 56-63, 65, 66} Dispersion at the single atom limit introduces significant chemical heterogeneity into the surface layer of the material whilst considerably reducing the symmetry of adsorption sites, thereby making SAAs, as we will demonstrate herein, excellent candidates for escaping the monometallic TCS and BEP relations. Interestingly, SAAs have already shown promising catalytic behaviour, such as for facile activation of hydrogen and subsequent spillover,^{6, 58, 61-63} as well as for performing selective hydrogenation reactions,^{6, 59, 60, 174-176} readily activating C-H bonds without suffering from coke formation, efficiently and selectively converting methanol to formaldehyde,⁵⁷ fast and selective hydrosilylation of α,β -unsaturated ketones and alkynes⁶⁸ and exhibiting tolerance to poisoning by CO.⁵⁶ In this work, we perform a screening of the adsorption properties of a range of SAAs, as well as their catalytic properties towards simple bond dissociation events, and evaluate the applicability of linear scaling relationships to these novel materials.

We use DFT to examine the chemistry of nine SAAs, derived from the group 10 metals (Ni, Pd and Pt) doped in the coinage metals (Cu, Ag, and Au). These bimetallic combinations are likely to result in high activities (from the group 10 metals) along with potentially high selectivities (from the coinage metals). We determine the adsorption energies of atoms and small molecules, as well as the pathways for simple bond dissociation reactions with catalytic importance, namely H-H, C-H, C-O, N-H and O-H cleavage. Then we go on to examine the validity of TCS and BEP relationships for these adsorbates and chemistries on SAAs, comparing and contrasting our results with those on pure metals. We thus identify materials that break linear scaling, and therefore could be used in improving activity and/or selectivity for the catalytic chemistries of practical interest.

Computational Details

Periodic plane wave DFT calculations were performed using the Vienna *Ab Initio* Simulation Package version 5.4.1.¹⁷⁷⁻¹⁷⁹ A plane-wave kinetic energy cut-off of 400 eV is used for the valence electron expansion and the core electrons are accounted for using projector augmented wave (PAW) potentials.^{111, 180} Methfessel-Paxton smearing is used with a smearing width of 0.1 eV. The non-local optB86b-vdW exchange-correlation functional is used, which is a revised version of the van der Waals density functional of Dion et al.^{104-106,}¹⁸¹ Lattice constants for the bulk pure metals are optimised and agree well with those reported in the literature.¹⁰⁵ A p(3 × 3) surface unit cell was used with five layers of metal atoms for all calculations, where the topmost four layers and all adsorbates are allowed to fully relax. For SAA calculations, one surface atom of the host metal is replaced by a single dopant atom (**Figure 19**), prior to relaxation; the surface dopant atom density is similar to that in experiment in high density regions that are still in the SAA regime (~10 %).⁶⁶ The p(3 × 3) unit cell is large enough to have dopant atoms as fifth nearest neighbours, thus suppressing short range ordering. A vacuum region of approximately 10 Å is included in the supercell in the z-direction to prevent interaction between periodic images along this direction. The Brillouin zone is sampled with a gamma-centred 13 × 13 × 1 Monkhorst-Pack k-point grid which is sufficiently dense to ensure convergence in the adsorption energy of all

species considered. The Hellmann-Feynmann forces acting on all free atoms are optimised to below $0.01 \text{ eV}\cdot\text{\AA}^{-1}$. We ensure electronic self-consistency at each ionic step to a tolerance of 10^{-7} eV . The transition state energies were found using the climbing image nudged elastic band (CI-NEB) and dimer formalisms of Jónsson and Henkleman.^{182, 183} Vibrational frequency calculations were performed using the finite displacement method with a step size of 0.05 \AA to ensure all transition states are first order saddle points.

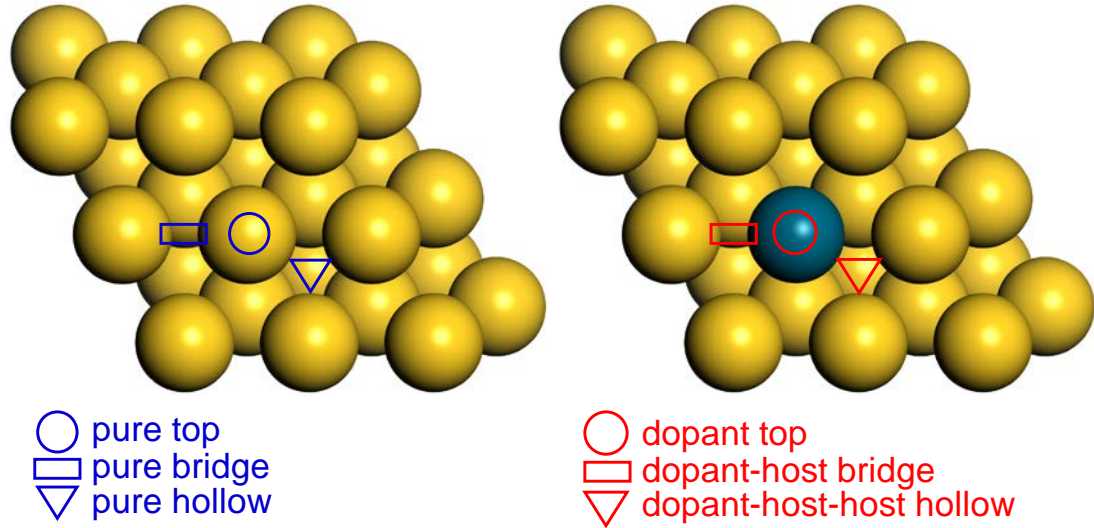


Figure 19: A typical SAA (111) surface (left) and pure metal (111) surface (right). Top sites are marked by circles, bridge sites are marked by rectangles with the shorter edges marking the two contributing atoms and hollow sites are marked by triangles with the vertices marking the three contributing atoms.

Given the large number of chemical species involved in this study, we define the formation energy of each adsorption system relative to a number of stable gas phase molecules ($\text{H}_{2(g)}$, $\text{CH}_{4(g)}$, $\text{NH}_{3(g)}$, and $\text{CO}_{2(g)}$), thereby allowing the stability of different fragments to be compared to one another within the same reference. In the case of a generic adsorbate A, we give the formation energy E_f as

$$E_f(A) = E_{Tot}(M + A) - E_{Tot}(M) - E_{Tot}(G), \quad (89)$$

where $E_{Tot}(M + A)$ is the DFT total energy of A adsorbed on the metal slab (M), $E_{Tot}(M)$ is the DFT total energy of clean M and $E_{Tot}(G)$ is a linear combination of gas phase DFT total energies whose atoms constitute A; e.g. for A = CO, $E_{Tot}(G) = \frac{1}{2}E_{Tot}(\text{CO}_{2(g)}) + \frac{1}{2}E_{Tot}(\text{CH}_4) - E_{Tot}(\text{H}_{2(g)})$ or for A = NH₂, $E_{Tot}(G) = E_{Tot}(\text{NH}_{3(g)}) - \frac{1}{2}E_{Tot}(\text{H}_{2(g)})$. We note

that more negative values of E_f imply higher stability of the adsorbed configurations they correspond to.

The activation energy E_a for a given chemical reaction is the difference in the DFT-calculated formation energy of the transition state E_f^{TS} and the DFT energy of the initial state of the reaction E_f^{IS} where

$$E_a = E_f^{TS} - E_f^{IS}. \quad (90)$$

Note that the “initial state” for H₂, CH₄, NH₃ and CH₃OH dissociation is an adsorbed state on all surfaces (unless stated) whereas for CO₂ dissociation we use the gas phase. The “final states” are for infinitely separated products on the sites where they are located post-dissociation. The study we have performed here is very data intensive; therefore, for clarity we give only graphical data for formation and activation energies however, the raw data can be found in the appendices.

Results and Discussion

Thermo-chemical Scaling Relations on Single Atom Alloys

Our calculations show that the most stable adsorption energies for CH_x and NH_x fragments on SAAs follow simple valency rules (**Figure 20**) that govern adsorption site preference (**Figure 19**). For CH₃ and NH₃ adspecies, the most stable adsorption is on the dopant top site. However, for CH₂ and NH₂, we determine the preferred adsorption geometry to be on the bridge site shared between one dopant atom and one surface host atom. Finally, for CH and NH as well as C, N and H atoms, the most stable adsorption site is the hollow site where bonding is split between one dopant atom and two surface host atoms. This site-valency relationship is also valid on the subset of monometallic surfaces used here (notably with the exception of CH₃ adsorption on Cu(111) which is preferential in threefold hollow sites) and agrees well with many studies in the past.^{23, 24, 184-189}

Fragment		Linear Regression Parameters						
		Pure Metal			SAA			
1 (x-axis)	2 (y-axis)	a	b / eV	R ²	a	b / eV	R ²	
C	CH	0.84	-0.74	1.00	0.93	-0.95	0.99	
C	CH ₂	0.51	-0.08	0.97	0.62	-0.48	0.85	
C	CH ₃	0.26	-0.20	0.89	0.23	-0.23	0.26	
C	CH ₃ OH	0.08	-0.88	0.96	0.13	-1.07	0.28	
C	CO	0.43	-2.53	0.96	-0.11	-1.26	0.02	
C	H	0.21	-0.92	0.88	0.20	-0.94	0.42	
N	NH	0.71	-0.62	0.99	0.90	-0.98	0.98	
N	NH ₂	0.37	-0.65	0.96	0.51	-1.03	0.92	
N	NH ₃	0.19	-1.30	0.80	0.11	-1.20	0.11	
N	H	0.26	-0.75	0.97	0.21	-0.69	0.83	
O	H ₂ O	0.09	-0.51	0.54	0.04	-0.48	0.04	
O	OH	0.54	-0.32	0.77	0.70	-0.59	0.93	
O	CH ₃ OH	0.09	-0.74	0.43	0.05	-0.68	0.12	
O	CH ₃ O	0.67	-0.72	0.93	0.67	-0.85	0.95	
O	CO	0.60	-1.81	0.56	0.29	-2.01	0.40	
O	H	0.35	-0.63	0.73	0.21	-0.46	0.91	
CO	H	0.49	0.31	0.91	0.16	0.01	0.12	
CO	H ₂ O	0.15	-0.25	0.99	-0.12	-0.63	0.07	
CO	CH ₃ OH	0.18	-0.43	0.98	-0.04	-0.70	0.02	
CO	NH ₃	0.42	-0.42	0.92	-0.28	-1.39	0.18	
NH ₃	CH ₃ OH	0.41	-0.27	0.98	0.54	-0.14	0.72	
NH ₃	H ₂ O	0.33	-0.12	0.92	0.66	0.19	0.87	
H ₂ O	CH ₃ OH	1.20	-0.14	0.98	0.88	-0.27	0.82	

Table 1: Thermo-chemical scaling relations for fragments adsorbed in their most favoured adsorption sites on pure metals and SAAs. Linear Regression parameters (gradient a and intercept b in eV) are given in addition to coefficients of determination (R²).

It is well established that on transition metal surfaces, CH_x and NH_x adsorption energies are linearly correlated with the adsorption energies of atomic C and N, respectively. Our results on pure transition metal (111) surfaces agree well with this, and we calculate linear regression parameters that are in good agreement with the work of others (**Table 1**).^{23, 24, 26,}

¹⁹⁰ The strength of the correlation is attributed to the binding atom in the fragment requiring the same total electron density, irrespective of the fragment.²³ The number of H atoms in the fragment, or more generally, the adsorbing atom valency will determine how much additional density is required from the surface.²³ On a pure metal surface, the density from the surface can be approximately split into equal contributions from each surface atom involved. That is, for an adsorbate bound to a top site the bonding is primarily to one surface atom whereas for a bridge site the bonding is shared between two atoms and for a hollow site, three atoms are involved directly in the bonding.

On a SAA there are two different metals directly bonding to an adsorbate when it is bound to bridge or hollow sites, though only one metal when bonding to the top site. As a result, linear

scaling between shared hollow site bound atoms (C or N) and shared bridge (CH_2 or NH_2) or hollow site (CH or NH) fragments hold. On the other hand, CH_3 preferentially binds to SAA top sites meaning these adsorption energies are poorly correlated with a C atom found in shared hollow sites (NH_3 also scales poorly due to it being a closed shell molecule, though we discuss this later). Notably, we can significantly improve the correlation for CH_3 or CH_2 vs. C and NH_2 vs. N linear scaling by constraining the relaxation of both fragments to the top site only. No improvement is seen for CH vs. C or NH vs. N scaling due to these fragments being much more stable when adsorbed in hollow sites instead of top sites (**Figure 20**,

Table 2).

Fragment		Linear Regression Parameters			
1 (x-axis)	2 (y-axis)	Pure Metal		SAA	
		a	b / eV	R ²	a
C	CH	0.78	0.05	0.90	1.07
C	CH_2	0.59	-0.73	0.99	0.70
C	CH_3	0.33	-1.12	0.89	0.30
C	CH_3OH	0.10	-1.16	0.99	0.03
C	CO	0.56	-4.09	0.99	0.13
C	H	0.32	-1.56	0.89	0.36
N	NH	0.67	0.25	0.78	1.05
N	NH_2	0.41	-1.00	0.96	0.55
N	NH_3	0.26	-1.99	0.78	0.09
N	H	0.34	-1.29	0.66	0.16
O	OH	0.50	-0.65	0.98	0.57
O	H_2O	0.12	-0.75	0.65	0.09
O	CH_3OH	0.14	-1.01	0.56	0.06
O	CO	0.85	-3.44	0.68	0.27
O	H	0.35	-0.83	0.31	0.10
H	CH_3	1.04	0.51	0.99	1.21
H	CH_3OH	0.28	-0.67	0.90	-0.49
H	CO	1.50	-1.34	0.83	0.05
H	NH_3	0.70	-0.98	0.96	-0.20
H	H_2O	0.22	-0.44	0.81	-0.77

Table 2: Thermo-chemical scaling relations for fragments constrained to adsorption at top sites on pure metals and SAAs. Linear Regression parameters (gradient a and intercept b in eV) are given in addition to coefficients of determination (R^2).

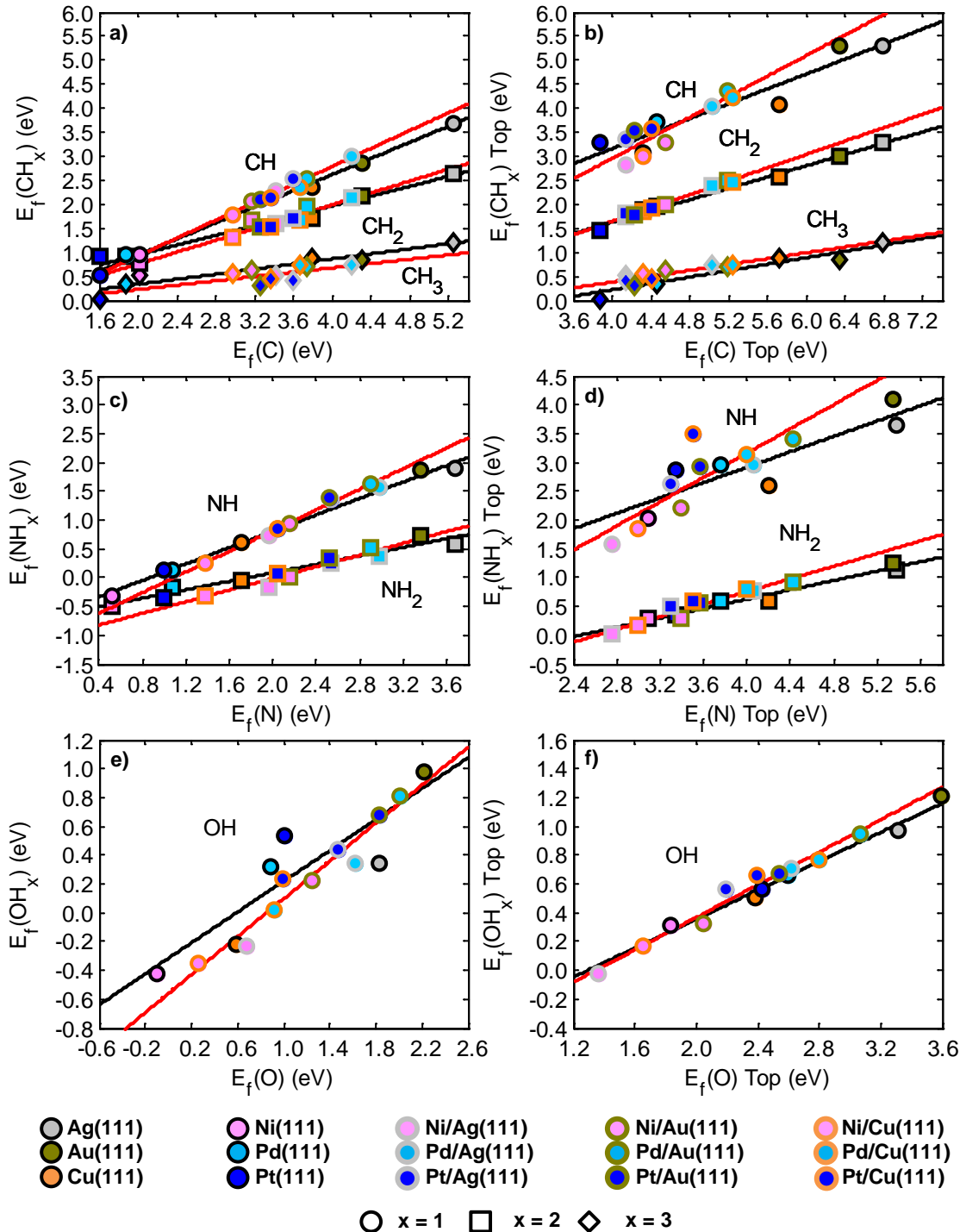


Figure 20: Thermo-chemical linear scaling relations on pure metals (black) and SAAs (red) for a) CH_x vs. C with each fragment in the most stable adsorption site; b) CH_x vs. C with each fragment fixed at the top site; c) NH_x vs. N with each fragment in the most stable adsorption site; d) NH_x vs. N with each fragment fixed at the top site. e) OH_x vs. O with each fragment in the most stable adsorption site; f) OH_x vs. O with each fragment fixed at the top site. The number of H atoms in the fragment are denoted by circles ($x = 1$), squares ($x = 2$) and diamonds ($x = 3$). Metals are colour coded with pure metal data points outlined in black. SAA data points are outlined in the host metal colour with the dopant metal colour in the centre.

We clarify the site specificity of SAA scaling relations by correlating the adsorption energy of C, N and O adatoms constrained to a particular site type with the adsorption energy of the same adatoms respectively, at a different site type. As expected, there is a strong linear

correlation between these quantities on pure metals but not on SAAs. In the latter materials, there is a larger variation in electronic properties between dopant only top sites and shared hollow sites meaning adsorption energies between these sites are uncorrelated (**Figure 21**).

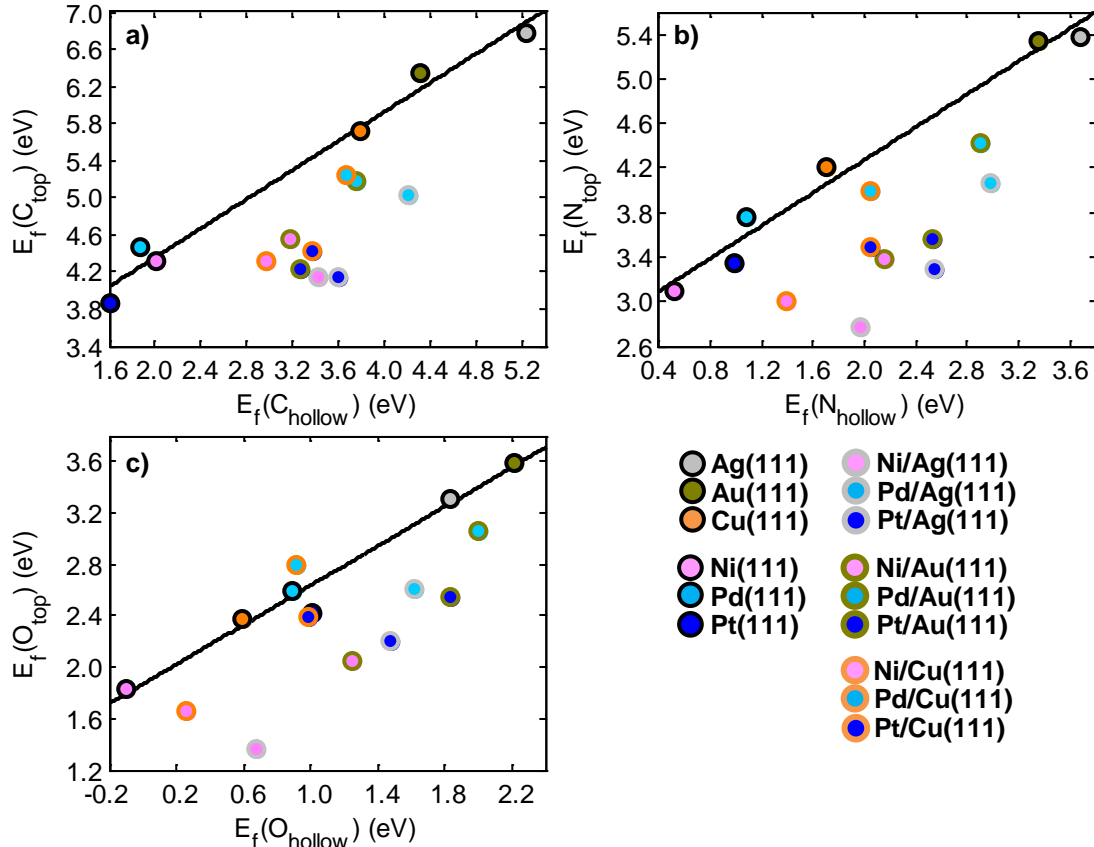


Figure 21: Thermo-chemical linear scaling plot of Top vs. A_{hollow} ($A = \text{C}, \text{N}$ or O) on the pure metals (black line). SAA data points are included but significantly deviate from linearity so no trendline is plotted. Metals are colour coded with pure metal data points outlined in black. SAA data points are outlined in the host metal colour with the dopant metal colour in the centre.

NH_3 , H_2O and CH_3OH adsorption energies are well correlated with one another on both surface types (**Table 1**). NH_3 , H_2O and CH_3OH adsorption energies also scale very well with N, H and C, respectively (**Table 2**) on pure metal surfaces however, there is no correlation on SAAs. All of these molecules are closed shell species and contain at least one lone pair of electrons on the adsorbing atom that is directly involved in the bonding (σ -donating). This makes these molecules distinct from the fragments already explored in this study, as they do not require electron density from the surface but instead donate to it. As a result, the TCS for σ -donating adsorbates depends on the ability of each surface to accept electron density rather than the ability of the adsorbate to accept it; the surface accepting properties remain

constant, irrespective of the adsorbate and so σ -donating species adsorption energies are correlated with one another.

We investigate and discuss why the pure metals have scaling between atoms and σ -donating species, whereas the SAAs do not by using CO as a probe molecule as it both accepts electron density from, and donates electron density to, the surface. We find no correlation between CO and any other fragment in this study when adsorbing to SAAs (**Table 1**), though correlations with C, H, NH₃, H₂O and CH₃OH are very strong on the pure metals; this is also true when adsorption is constrained to top-sites only (**Table 2**). By measuring the M-C distance (metric for surface accepting density) and C-O bond length (metric for surface donating density) for chemisorbed CO on pure metals^{191, 192} we determine the adsorption energy is moderately correlated with each bond length and that there is a strong correlation between the bond lengths themselves. However, on SAAs we note no correlation of the adsorption energy with the M-C bond length but some correlation with the C-O bond length, providing evidence that there is a large variation in the electron accepting properties of SAAs, but significantly less variation in their electron donating properties when comparing the two surface types.

CO is often used as a probe molecule for general reactivity in surface science experiments, though it may not be applicable for SAAs as its adsorption properties do not scale well with other fragments. More pertinently however, a lack of CO linear scaling with other fragments can allow for enhanced CO poisoning resistance as CO may adsorb less strongly on SAAs compared to other surfaces, while still allowing for adsorption of other species. We have observed this resistance to CO poisoning and reduced CO adsorption strength in the past, in conjunction with enhanced activity of SAAs towards hydrogen and in hydrogenation reactions.^{56, 58, 62}

Our findings demonstrate that linear scaling still applies to SAAs in several cases, although is broken when adsorbates vary between shared and non-shared adsorption sites. The adsorption geometry of the species in question is a significant factor that has previously not

been considered nor has been an issue on chemically uniform surfaces. Additionally, we have shown that SAAs are more sensitive to the manner by which the adsorbate interacts with the surface, though fragments with similar bonding modes can exhibit scaling relations. Thus, SAA catalysts can be tailored to have favourable thermochemical reaction energies that will lead to improved selectivities over traditional transition metal catalysts. However, an understanding of the effect on catalytic activity will require a study of SAA reaction kinetics and thus we go on in the next section to discuss the decoupling of transition state geometries compared to the reaction initial and final states as a result of the SAA surface structure, and determine whether the BEP relation can be “broken” in the same manner as in TCS.

Escaping the Brønsted-Evans-Polanyi Relationship using Single Atom Alloys

We have seen already that for stable binding of intermediates, the high surface heterogeneity of SAAs can result in the decoupling of adsorption energies and a breakdown of TCS. In this section, we demonstrate that based on the same principles, SAAs are capable of also decoupling activation and adsorption energies leading to deviations from BEP relationships and some novel catalytic properties.

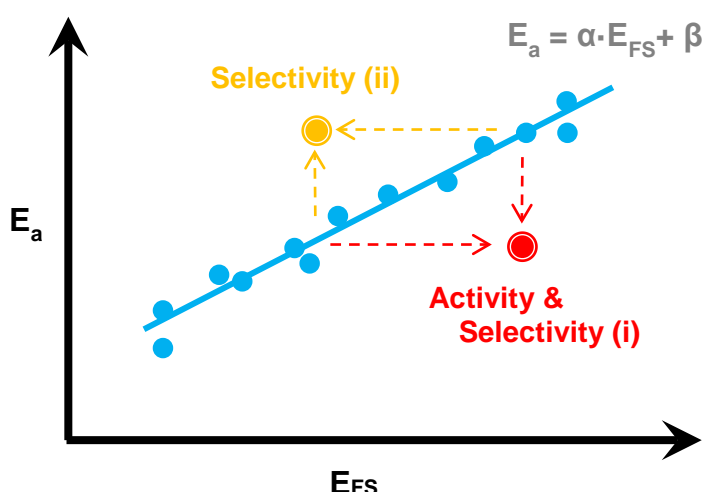


Figure 22: Diagram showing a Brønsted-Evans-Polanyi relationship of activation energy as a linear function of the adsorption energy of the final state of reaction. Two deviations from linearity are shown; (i) for low activation energy in conjunction with weak binding of intermediate and (ii) high activation energy for correspondingly strong binding.

A deviation from the pure metal BEP relationship can manifest in two ways; firstly, having a SAA that is capable of facile bond activation at the more reactive dopant atom site, yet

weakly binds adsorbates at shared dopant-host or host only sites (**Figure 22 (i)**); or secondly, having a SAA that exhibits little or no improvement on the activation barrier compared to the host metal in conjunction with an increased binding strength of intermediates at the dopant (**Figure 22 (ii)**). The former will result in increased reaction rate over the pure host but also increased selectivity against poisoning by intermediates compared to the pure dopant. The latter will have a similar or reduced reaction rate compared to the host material, which will reduce selectivity towards this product allowing for enhanced selectivity in favour of other products.

In our BEP relationship study, we consider five simple bond dissociation reactions with catalytic relevance involving the scission of H-H, C-H, N-H, O-H and C=O bonds in H₂, CH₄, NH₃, CH₃OH and CO₂ respectively (**Table 3**). We explore the validity of BEP relationships for each reaction and discuss the implication for catalysis using SAAs. We correlate the activation energy of each bond scission with the energy of the dissociated final state of the reaction, and show each BEP relationship in **Figure 23**. As with the TCS calculations, we use linear regression to assess the correlations for the BEP relations for each reaction on the pure metals and SAAs, giving details in **Table 3**.

Reaction	Surfaces	α	β (eV)	R²
$H_2^* \rightarrow 2H^*$	Pure Metal	0.83	0.94	0.94
	SAA	0.55	0.49	0.64
$CH_4^* \rightarrow CH_3^* + H^*$	Pure Metal	0.87	0.91	0.99
	SAA	0.74	0.71	0.71
$NH_3^* \rightarrow NH_2^* + H^*$	Pure Metal	0.40	1.84	0.98
	SAA	0.47	2.02	0.83
$CO_{(g)} \rightarrow CO^* + O^*$	Pure Metal	0.67	0.85	0.98
	SAA	0.75	0.83	0.98
$CH_3OH^* \rightarrow CH_3O^* + H^*$	Pure Metal	0.47	1.29	0.76
	SAA	0.52	1.31	0.89

Table 3: Linear regression gradients (a), intercepts (b, in eV) and coefficients of determination (R²) for the BEP relationship for five reactions; hydrogen dissociation, methane activation, ammonia dehydrogenation, carbon dioxide reduction and methanol O-H dehydrogenation. For hydrogen dissociation on Cu, Ag, Au, and Pt there is no physisorbed state and the data correspond to dissociation from the gas state. Data is given for these reactions on pure metal (111) surfaces (black) and SAA (111) surfaces (red).

We find that H₂, CH₄ and NH₃ activation follow different BEP relations on SAAs compared to pure metals. On the other hand, the fitted trendlines for CO₂ and CH₃OH dissociations show little difference between the SAAs and pure metals, with the lines actually crossing around medium range activation energy and mid-strength adsorption energy. Moreover, the SAA BEP lines that deviate from the pure metal BEP trends also have a greater degree of data scatter about the regression fits. It is interesting to note that the degree to which SAAs follow BEP trends can change depending on the reaction. We attribute this variation to the surface structure of SAAs in combination with the mechanism of the reaction in question. That is, the high surface heterogeneity of a SAA means that for a bond dissociation reaction, the transition state and final products may bind to different sites with different bonding contributions from each metal in the alloy. In the remainder of this section we will analyse each reaction in turn and rationalise the agreement with or deviations from traditional BEP scaling.

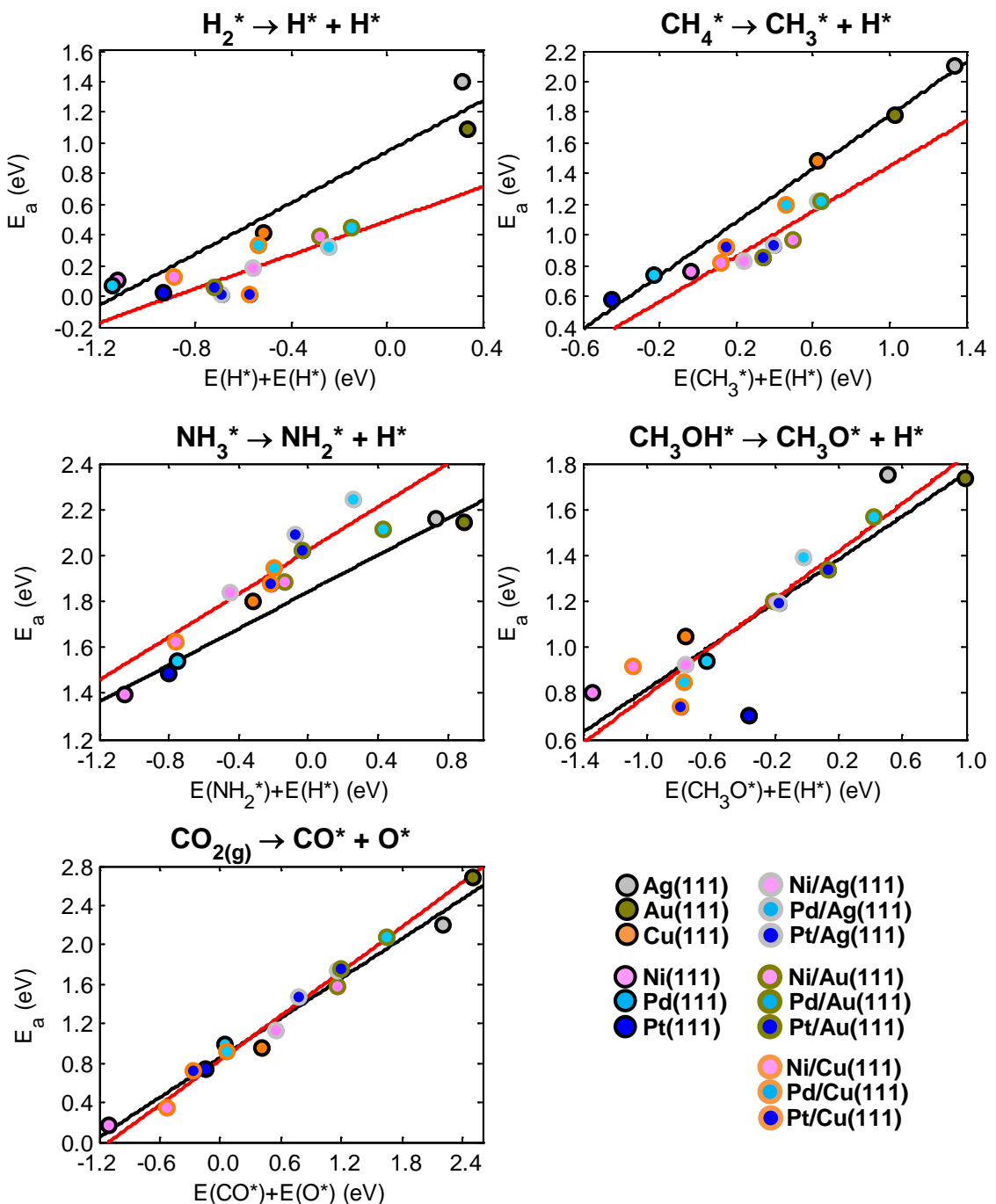


Figure 23: Brønsted-Evans-Polanyi relationships for five simple catalytic bond scissions on pure metal (111) surfaces (black) and SAA (111) surfaces (red). Plots are of the activation energy (E_a) as a function of the sum of post-dissociation fragment adsorption energies. Linear regression fits are drawn for each reaction on each surface and corresponding equations are shown. Metals are colour coded with pure metal data points outlined in black. SAA data points are outlined in the host metal colour with the dopant metal colour in the centre.

Hydrogen Dissociation

The most notable deviation from the pure metal BEP relationship is for the H_2 dissociation reaction. In the case of all the SAAs, H_2 physisorbs onto the top site of the dopant atom prior to dissociation; this is also the case for pure Ni(111), Pd(111) and Pt(111). The mechanism for H_2 activation over these metal surfaces involves a top bound transition state (Figure 24),

whereas for Ag(111), Au(111) and Cu(111) the transition states are located in fcc hollow, fcc hollow and bridge sites respectively. For all of the pure metals and the majority of SAAs the final dissociated hydrogen adatoms are bound in hollow sites (PtAg(111) and PtAu(111) are exceptions as H* preferentially adsorbs to top dopant sites and so the final state consists of one top H* and one hollow H*).

The top dopant atom bound transition state is stabilised to a greater degree than the bound H* in shared dopant-host-host hollow sites due to sole interaction with the more reactive dopant atom. It then follows that for a given adsorption strength of H*, there will be a lower activation energy on SAAs and so the corresponding BEP trendline falls below that of the pure metals (**Figure 23**). Notably there is significantly more scatter in the SAA regression compared to the pure metals underscoring the lack of correlation between shared and unshared site adsorption energies seen earlier in TCS (**Figure 21**).

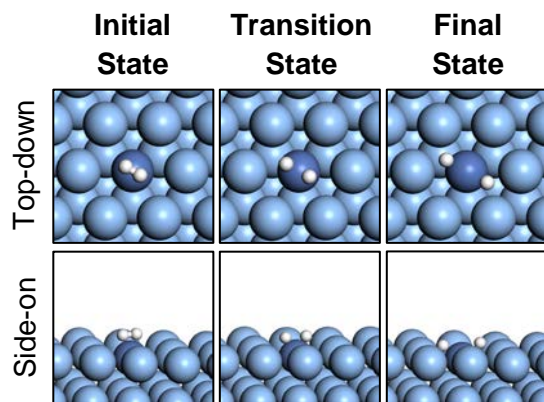


Figure 24: Top-down and side-on views of the initial (left), transition state (middle) and final dissociated state (right) for H₂ dissociation on Ni/Ag(111) SAA. A five layer slab was used in these calculations along with a p(3 × 3) unit cell. Only a portion of the cell is shown for clarity.

The dissociation of H₂ is often the rate limiting step in hydrogenation reactions on pure Cu, Ag and Au. On the other hand, pure Ni, Pt and Pd can easily activate hydrogen though suffer from poor selectivity towards hydrogenated products. Entropic effects arising from the high number or less active sites (host metal atoms) in a SAA promote H adatom spillover thereon, allowing them to participate in hydrogenation reactions. This gives SAAs reaction selectivity comparable to the pure group 11 metals, in addition to the ability to readily activate hydrogen, thanks to the isolated dopant atom. We have previously observed several

instances of this using a combination of STM, TPD and reactor studies on PdCu, PtCu and PdAu SAAs.^{58-63, 67}

Methane C-H Activation

Another reaction that shows clear deviations from pure metal BEP scaling is C-H bond scission in CH₄ activation. Prior to dissociation, CH₄ physisorbs via H on the top site of all of the pure metals and the SAAs. The transition state for C-H activation is over the top site (**Figure 25**). The dissociated CH₃* fragment in the final state is located on the top site for all surfaces except Cu(111) where it is most stable in hollow sites. As for H₂ activation, the dissociated H* moves away from the top site where the transition state is located to an adjacent hollow site which, in the case of SAAs is a dopant-host-host shared site.

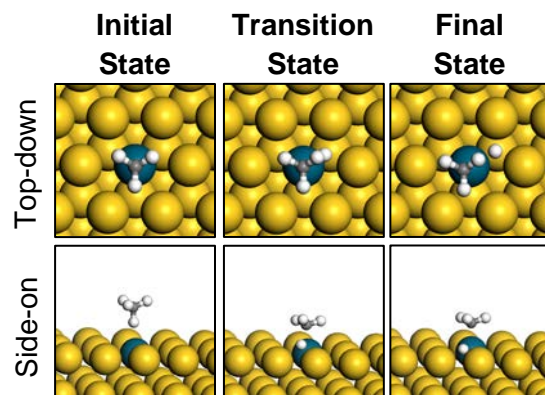


Figure 25: Top-down (top) and side-on (bottom) views of the initial (left), transition state (middle) and final dissociated state (right) for CH₄ activation on Pd/Au(111) SAA. A five layer slab was used in these calculations along with a p(3 × 3) unit cell. Only a portion of the cell is shown for clarity.

The top dopant bound transition state is stabilised to a greater degree than the bound H* in shared dopant-host-host hollow sites. It then follows that for a given adsorption strength of H*, there will be a lower activation energy on SAAs and so the corresponding BEP trendline falls below that of the pure metals (**Figure 23**). Notably there is significantly more scatter in the SAA regression compared to the pure metals reiterating the lack of correlation between shared and unshared site adsorption energies seen earlier in TCS.

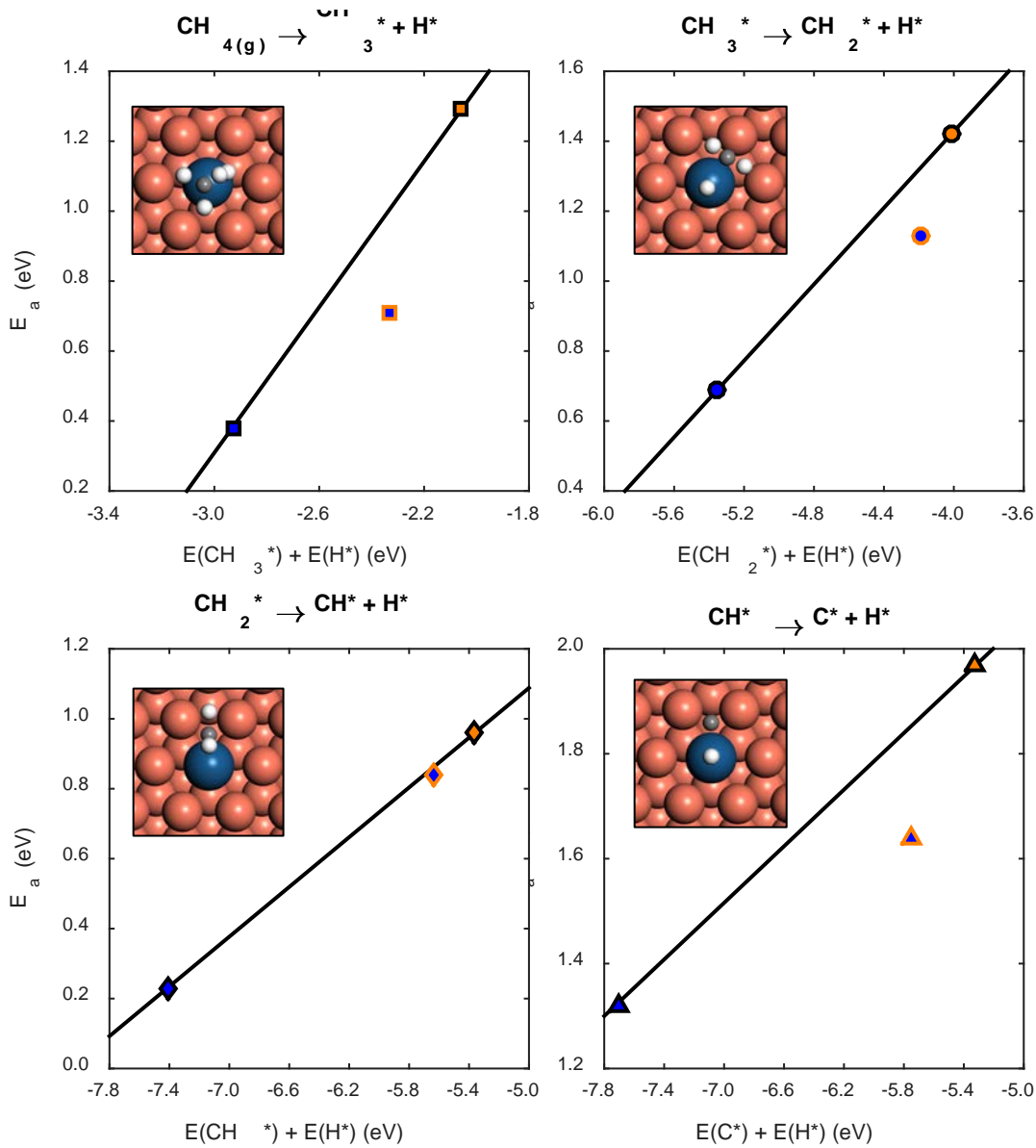


Figure 26: Brønsted-Evans-Polanyi relationship for four successive C-H scissions on Cu(111) (orange/black), Pt(111) (blue/black) and Pt/Cu(111) SAA (blue/orange); a) $\text{CH}_4\text{(g)} \rightarrow \text{CH}_3^* + \text{H}^*$ (squares); b) $\text{CH}_3^* \rightarrow \text{CH}_2^* + \text{H}^*$ (circles); c) $\text{CH}_2^* \rightarrow \text{CH}^* + \text{H}^*$ (diamonds); and d) $\text{CH}^* \rightarrow \text{C}^* + \text{H}^*$ (triangles). Top-down views of the transition states are shown as insets on each plot.

As we will discuss in Chapter 4, we have investigated the pathways for CH_4 dehydrogenation on a Pt/Cu(111) SAA where we observed that the SAA exhibits excellent coking resistance, unlike Pt(111), but also has the ability to activate C-H bonds at much lower temperatures than Cu(111). Looking more closely at the scaling relations for Pt/Cu(111), Cu(111) and Pt(111) (Figure 26) we can see that C-H scission in CH_2^* does not deviate from the pure metal BEP relation whereas all other C-H scissions notably fall below the trendline. We can rationalise this as the transition state in CH_2^* scission is located in a shared dopant-host-host hollow site as are the final dissociated products. On the other hand,

the remaining transition states are located on the top dopant site whereas the final states have at least one fragment in a shared site and thus fall below the pure metal BEP line. In Chapter 4, we will analyse these DFT calculations in more depth in addition to performing kinetic simulations that highlight the macroscopic effects of breaking linear scaling in this fashion.

We expect that other SAAs will also exhibit some deviation from linear scaling for this CH₄ dehydrogenation system, with superior C-H scission activity thanks to low activation energies and moderate adsorption strengths, especially when considering entropically favoured dopant to host spillover post dissociation (**Figure 23**). We also expect that these materials will exhibit coking resistance, as a result of kinetic limitations in the dehydrogenation pathways, as in the case of H abstraction from CH₂ on Pt/Cu(111) SAA.

Ammonia N-H Activation

NH₃ dissociation on SAAs shows clear deviation from BEP pure metal scaling (**Figure 23**). In this case, NH₃ chemisorbs via N onto top sites on both pure metal and SAA surfaces. The transition state is located over a hollow site adjacent to the top site involved in NH₃* chemisorption. In the case of SAAs, this hollow site is a shared dopant-host-host site (**Figure 27**). The dissociated NH₂* and H* products are most stable in bridge and hollow sites (shared dopant and host on SAAs), respectively.

Unlike with CH₄ and H₂ activation, the BEP line for SAA NH₃ activation lies above the BEP line for the pure metals with the SAAs having higher activation energies compared to the pure host metals in several instances. In this case, the binding strength increase on the SAAs compared to pure hosts is less significant in the transition state than in the initial and final states due to their positions relative to the dopant atom. The transition state appears in a shared dopant-host-host hollow site and the initial chemisorbed NH₃* fragment is bound to the dopant atom only which results in a large activation energy due to greater stabilisation of the initial state compared to the transition state. Moreover, the final state has the NH₂* fragment in a shared dopant-host hollow site that has a greater dopant bonding contribution

than the transition state in the shared hollow site. Both of these factors result in the SAA BEP line lying above the pure metal line. The correlation of this BEP relationship is also quite strong compared with CH₄ and H₂ activation as a result of moving from shared hollow to shared bridge and hollow sites, rather than directly from the unshared top to shared hollow site.

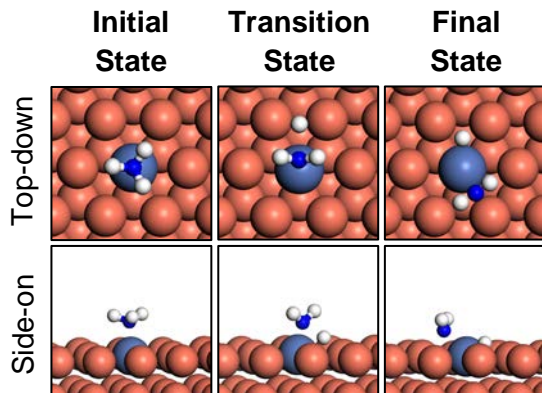


Figure 27: Top-down (top) and side-on (bottom) views of the initial state (left), transition state (middle) and final dissociated state (right) for NH₃ activation on Ni/Cu(111) SAA. A five layer slab was used in these calculations along with a p(3 × 3) unit cell. Only a portion of the cell is shown for clarity.

Our data suggests that there is little to gain by using a SAA for NH₃ activation rather than a pure metal catalyst. However, the lack of reactivity of a SAA dopant atom towards N-H bonds could allow for selective C-H activation or hydrogenation reactions on amines.

Methanol O-H Activation

We have determined a BEP relationship for O-H scission in CH₃OH on SAAs that agrees well with that of the pure metals (**Figure 23**). CH₃OH* datively bonds via O to the top site of all surfaces with the O-H bond nearly parallel to the surface plane in each case, and is in good agreement with earlier work.¹⁹³ The O-H scission transition state is generally located in a shared dopant-host-host hollow site on SAAs with the O--H bond directed away from the dopant atom (**Figure 28**). The most stable adsorption site for CH₃O* and H* on SAAs is the shared dopant-host-host hollow site with CH₃O* binding via O and tilting towards the single atom in several cases.

One exception to the above description of initial, transition and final state geometries in this reaction is Pt/Cu(111). Though the mechanism in **Figure 28** is also valid on Pt/Cu(111), unusually strong chemisorption of CH₃O* on Cu(111) results in a second mechanism with a

lower energy transition state. In this mechanism, the O-H bond vector is reversed on Pt/Cu(111) so that dissociated CH₃O* adsorbs to pure Cu and H* adsorbs in a Pt-Cu-Cu hollow site in the final state (**Figure 29**). The activation energy of this mechanism is much lower when compared to that of **Figure 28** (despite CH₃OH adsorbing on a Cu top site in the initial state with an energy stabilisation of 0.3 eV compared to the Pt top site) and is also around 0.3 eV lower than that for pure Cu(111). Interestingly, this is not the case on Ni/Cu(111) and Pd/Cu(111) SAAs which follow the mechanism in **Figure 29** because CH₃O* is more stable in shared dopant-host-host hollow sites than on Cu facets in these alloys. CH₃O* binds relatively weakly to Pt(111) but strongly to Ni(111) and Pd(111). This is noted in the BEP plots where Pt(111) lies well below the line as a direct result of weak CH₃O* binding.

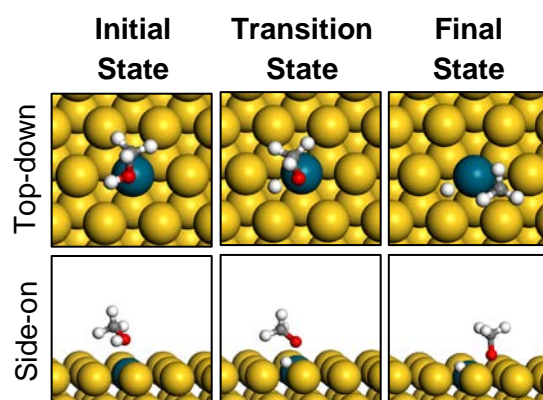


Figure 28: Top-down (top) and side-on (bottom) views of the initial state (left), transition state (middle) and final dissociated state (right) for CH₃OH O-H scission on Pd/Au(111) SAA. A five layer slab was used in these calculations along with a p(3 × 3) unit cell. Only a portion of the cell is shown for clarity.

When a linear regression is carried out for this reaction on all surfaces together, there is a very strong correlation showing there is little deviation from the pure metal BEP for the SAAs. Individually, SAAs adhere to the linear BEP more strongly than the pure metals since for the latter, Pt(111) is an outlier due to weak CH₃O* binding. The strong correlation for the SAA BEP is the result of the transition and final states both being located in shared dopant-host-host sites.

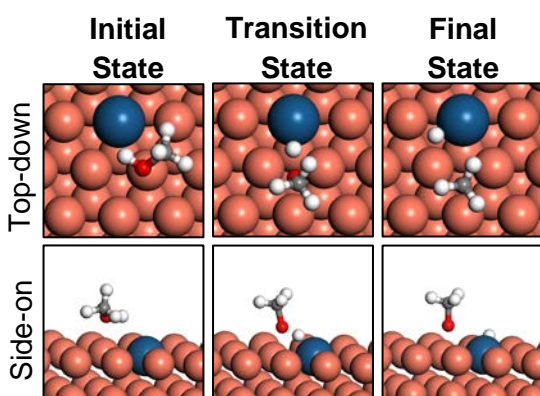


Figure 29: Top-down (top) and side-on (bottom) views of the initial state (left), transition state (middle) and final dissociated state (right) for CH_3OH O-H scission on $\text{Pt}/\text{Cu}(111)$ SAA. A five layer slab was used in these calculations along with a $p(3 \times 3)$ unit cell. Only a portion of the cell is shown for clarity. Notably these geometries are for the lowest energy transition state and stable adsorption of CH_3O^* and H^* . The mechanism in Figure 28 is also valid for $\text{Pt}/\text{Cu}(111)$, though the reaction here proceeds with much lower activation energy.

Despite negligible deviation from the pure metal BEP relationship, several SAAs in this study show promise as CH_3OH dehydrogenation catalysts by offering very low O-H scission barriers compared to the host metals. $\text{Pt}/\text{Cu}(111)$ SAAs and PtCu SAA nanoparticles have already been used to perform highly selective formaldehyde production from CH_3OH with significantly higher activity than for pure Cu.⁵⁷ Due to good agreement between the BEP relationship of pure metals and SAAs in this case, the optimal SAAs for CH_3OH O-H scission are easier to identify. Comparing BEP plots for the O-H scission in CH_3OH and C-H scission in CH_4 , it is apparent that some SAAs, including $\text{Pd}/\text{Ag}(111)$, $\text{Pd}/\text{Au}(111)$ and $\text{Pt}/\text{Au}(111)$, offer low activation energies for C-H scission though relatively high barriers for O-H scission. As a result, alkyl dehydrogenation and alcohol dehydrogenation are decoupled and selectivity may be tailored towards alkyl group activation and reaction whilst preserving the alcohol functionality, when a SAA is used.

Carbon Dioxide Reduction

Finally for CO_2 reduction, we compute very similar regression parameters for the SAAs compared to the pure metals meaning no deviation from the BEP relation; there is almost perfect linearity in the scaling for both surface types (**Figure 23**). The transition state geometries for this reaction are found to be located over shared dopant-host-host hollow sites. The CO portion of the transition state is between the dopant top site and shared dopant-host-host hollow site whereas the dissociating O portion lies on an adjacent pure

host bridge site (**Figure 30**). The OC–O bond length in the transition state is found to be very long (~1.80 – 2.10 Å) compared to the non-dissociating O–C bond length (~1.14 – 1.18 Å). The final state geometries are geometrically similar to the transition states, with CO* being on the top dopant site whereas O* is in a pure host hollow site. For this reaction, the long C–O bond in the transition state means the C atom is predominantly interacting with the dopant atom and the O atom is exclusively interacting with the host.

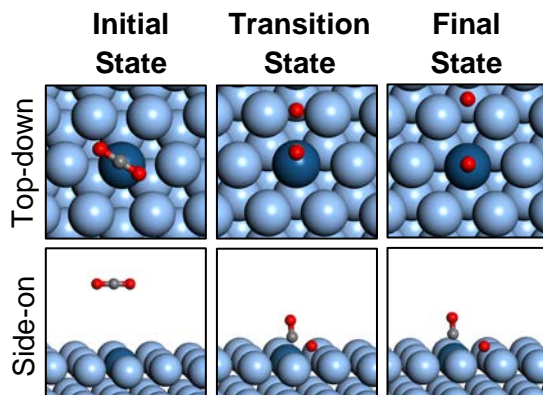


Figure 30: Top-down (top) and side-on (bottom) views of the initial state (left), transition state (middle) and final dissociated state (right) for CO₂ reduction on Pt/Ag(111) SAA. A five layer slab was used in these calculations along with a p(3 × 3) unit cell. Only a portion of the cell is shown for clarity.

The lack of any deviation from traditional pure metal BEP scaling makes the behaviour of SAAs more like what is expected from a pure metal for CO₂ reduction or CO oxidation. Interestingly, CO oxidation on SAAs with Ag and Au hosts have generally lower barriers as a result of weaker binding of CO to the dopant single atom compared to the pure dopant metal. A study on the competitive pathways for electrochemical CO₂ reduction on SAAs indicates that doping Ag and Au with transition metal atoms such as Pd, Pt, Co, Rh and Ir allows for tandem catalysis, where the Au or Ag host material reduces CO₂ to CO* which is subsequently reduced by hydrogen at the dopant metal to C₁ hydrocarbons.¹⁹⁴ In that study using SAAs a decoupling of the hydrogen evolution reaction, the CO oxidation and the CO hydrogen reduction pathways is observed. We pose this is due to the deviations (shown in this work) of these materials from the TCS relations and the hydrogen evolution reaction BEP relationship, while the CO BEP relationship is still adhered to. This is an excellent example of how a complex reaction pathway with multiple competing routes can be optimised if some reactions follow a BEP relationship and others do not.

Conclusion

We have demonstrated that single atom alloys, thanks to their high surface heterogeneity, are capable of decoupling the adsorption properties of stable intermediates and transition states, thereby escaping from pure metal TCS and BEP relations. Indeed, SAAs do follow their own TCS and BEP relations, though significant scatter and changes in regression parameters compared to pure metals reduce the effectiveness of simple linear models to predict the reactivity of SAA catalysts. These deviations are attributed to the atomic dispersion of active sites that allows for dramatic changes in adsorption behaviour between dopant only, host only and shared sites that is less pronounced or non-existent on other alloy surfaces because of higher molar fractions of their metal constituents. Furthermore, we show that deviations from linear scaling provide an opportunity to optimise catalytic pathways to yield high selectivities by only lowering the barriers of desirable reactions whilst minimising the benefit to competing chemistries, something that is not possible for homogeneous surfaces following universal linear scaling. SAAs will ultimately provide more freedom in catalyst design allowing for potential fine-tuning of activity, selectivity and stability.

In the next chapter, we will discuss a specific example of a SAA capable of escaping linear scaling relationships in the dehydrogenation of methane. We focus on a Pt/Cu(111) SAA and use a combination of DFT with KMC to examine the energetics and kinetics of C-H and H-H activation on this surface, making reference to monometallic surface and comparing to experimental work.

Chapter 4 Pt/Cu Single Atom Alloys as a Coke Resistant Strategy for Efficient C-H Activation

The recent discovery of rich reserves of shale gas has led to rekindled interest in the activation of C-H bonds in methane as an initial step in the synthesis of fuels and fine chemicals. Pt catalysts readily activate C-H bonds in hydrocarbons, though suffer from coke formation and deactivation. On the other hand, Cu catalysts require elevated temperatures to break C-H bonds though are capable of performing C-C bond coupling reactions and do not form carbon deposits on the surface. We show here using ab initio kinetic Monte Carlo simulations that highly dilute Pt/Cu(111) Single Atom Alloys (SAAs) exhibit significantly enhanced C-H activation activity over pure Cu(111) catalysts, lowering the temperature of activation in methyl by over 100 K. Moreover, we show that this Pt/Cu SAA is resistant to coke formation and therefore is an amalgamation of the desirable characteristics of each of its monometallic counterparts. Our theoretical study is complemented by experimental data produced from the Sykes and Flytzani-Stephanopoulos labs at Tufts University (USA), which we summarise briefly at the end of the chapter.

Introduction

Upgrading methane to higher order hydrocarbon fuels as well as fine chemicals has been a longstanding challenge faced by the catalysis community. Recent discoveries of shale gas reserves, for example in the UK and USA, in conjunction with modern methods of extraction and recovery, have dramatically increased the availability and supply of low molecular weight alkanes thereby reigniting the search for effective C-H activation catalysts.^{195, 196}

The high stability of light alkanes makes it difficult to find low-carbon footprint methods for the conversion of these gases to more useful commodity chemicals and fuels,¹⁹⁷ for example steam reforming is the most common process though is energy-intensive and has low efficiency.¹⁹⁶ Catalytic processes are sought after to potentially improve the energy balance sheet. Facile activation of C-H bonds in alkanes would open new routes to synthesise commodity and fine chemicals.¹⁹⁷⁻²⁰⁰

Ni catalysts are often used for C-H activation, as Ni is inexpensive, but these suffer from coking since Ni breaks C-C bonds in alkanes and can completely dehydrogenate alkanes to carbon.^{201, 202} Preventing coking is indeed an active, yet challenging area of current research.²⁰³ Pt catalysts also suffer from coking and Pt's high price prohibits widespread use.²⁰⁴⁻²⁰⁸ Cu catalysts are typically not considered viable due to a high C-H activation barrier on Cu surfaces, but are resistant to coking.²⁰⁹⁻²¹³

Alloys often exhibit unique properties compared to their constituent metals.^{46, 47} For example, using a combination of surface science, theory, and high surface area catalysis Besenbacher et al. showed that small amounts of Au dispersed in Ni can suppress carbon deposition in methane steam reforming by both raising the barrier to C-H activation and decreasing the binding strength of carbon to the surface.⁴⁷ We take the opposite approach, using the smallest amount of a catalytic metal (Pt) in the form of single atoms in the surface layer of a more inert host metal (Cu) to facilitate C-H activation while avoiding coking that typically occurs on larger ensembles.⁴⁶ We showed in Chapter 3 how these Pt/Cu *Single*

Atom Alloys (SAAs)^{54, 59, 66} are capable of escaping linear scaling relations thereby unlocking the potential to exhibit superior catalytic performance over their monometallic counterparts.

In this chapter, we will evaluate the kinetics of methane dehydrogenation on Cu(111), Pt/Cu(111) and Pt(111) using first principles kinetic Monte Carlo (KMC) simulations. We will simulate temperature programmed reaction/desorption (TPR/TPD) of species from CH₃* as well as CH₃* and H* pre-covered lattices and analyse the rate of CH_{4(g)} desorption as a function of temperature. This kind of simulation is analogous to experimental protocol for studying the fundamentals of C-H activation from a surface science perspective. We will compare macroscopic data such as desorption profiles, surface coverage and product selectivity to experimental work.

As we discussed in Chapter 2, a KMC simulations consists of a set of elementary events that we execute to simulate the dynamic evolution of a system. The elementary events in this case include the dissociative adsorption of H_{2(g)} and CH_{4(g)}, C-H bond scissions in chemisorbed CH_x* fragments and surface diffusion of CH_x* and H* surface species, all of which are reversible processes.

To execute an elementary in a KMC simulation, one must know the value of the kinetic rate constant for the chemical transformation described by the elementary event. In order to evaluate the kinetic constants for all of our events, we use density functional theory (DFT) and transition state theory (TST). Finally, we define a hexagonal lattice model that is a mapping of the DFT unit cell onto a length scale more practical for catalysis. This lattice is comprised of high symmetry surface site types that our DFT calculations show correspond to minima on the potential energy surface for adsorption of CH_x* and H* adspecies. Our simulations account for lateral adsorbate-adsorbate interactions between H* adatoms as this is necessary to reproduce the correct desorption kinetics of H_{2(g)}. However, we neglect any additional lateral interactions between carbonaceous species as comparison with experiment suggests their inclusion is non-essential.

Unlike with experiment, our DFT parameterised KMC simulations will allow us to analyse and identify the elementary processes contributing to the desorption of $\text{CH}_4\text{(g)}$ and the rate thereof. We will also be able to determine the typical reaction temperatures for successive scissions of C-H bonds in methane derived species on each surface and ascertain the reasons for differences in their performance from activity, selectivity and coke resistance perspectives.

Reaction Network and Lattice Model

We model exclusively a single terrace of the (111) surfaces of Cu, Pt/Cu SAA and Pt. Each metal surface is fcc stacked and we approximate the lattice constant of Pt/Cu as that of pure Cu, due to the very low concentration of Pt in the alloy. We construct the lattice as in the Graph Theoretical approach of Stamatakis *et al.*^{143, 151} Our lattice is built of vertices corresponding to high symmetry surface adsorption sites (top, hollow) that are connected by edges describing neighbouring relations. On pure metal lattices ($M = \text{Pt}, \text{Cu}$), we have only two sites types namely top and hollow.

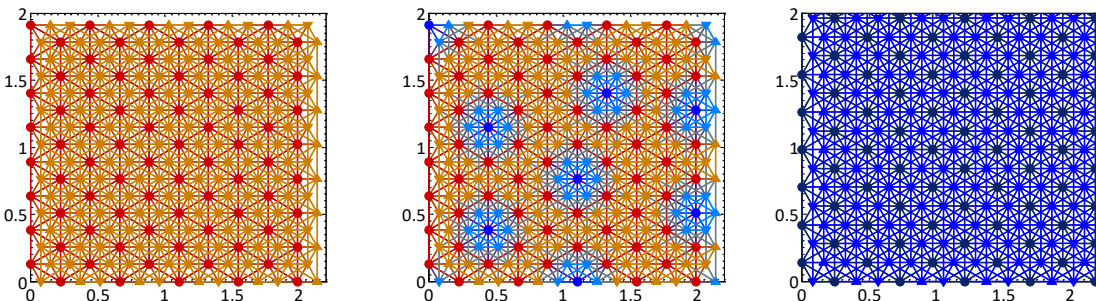


Figure 31: Schematics representing a small portion of the lattice models for the (111) surfaces of Cu (left), Pt/Cu SAA (middle) and Pt (right). Top sites are represented by circles for Cu atoms (red), Pt atoms as isolated single atoms (light blue) and Pt atoms in the pure metal (dark blue). Threefold hollow sites are depicted as upper and lower triangles for fcc and hcp site types respectively. Neighbouring relations are represented by connecting lines between sites.

On the SAA lattice, the surface symmetry is reduced by random substitutions of Cu atoms with Pt atoms that are isolated to represent single, non-clustered surface Pt atoms; the density of these Pt dopant atoms is approximately 3 %, in agreement with the coverage on experimental model Pt/Cu(111) SAA terraces that are within 10 nm of a step edge.⁶⁶ This reduction in symmetry necessitates the definition of four site types, two for facets of pure Cu

as before and a further two sites for top of Pt single atoms and for adjacent hollow sites.

Representations of a small portion of each lattice are given in **Figure 31**.

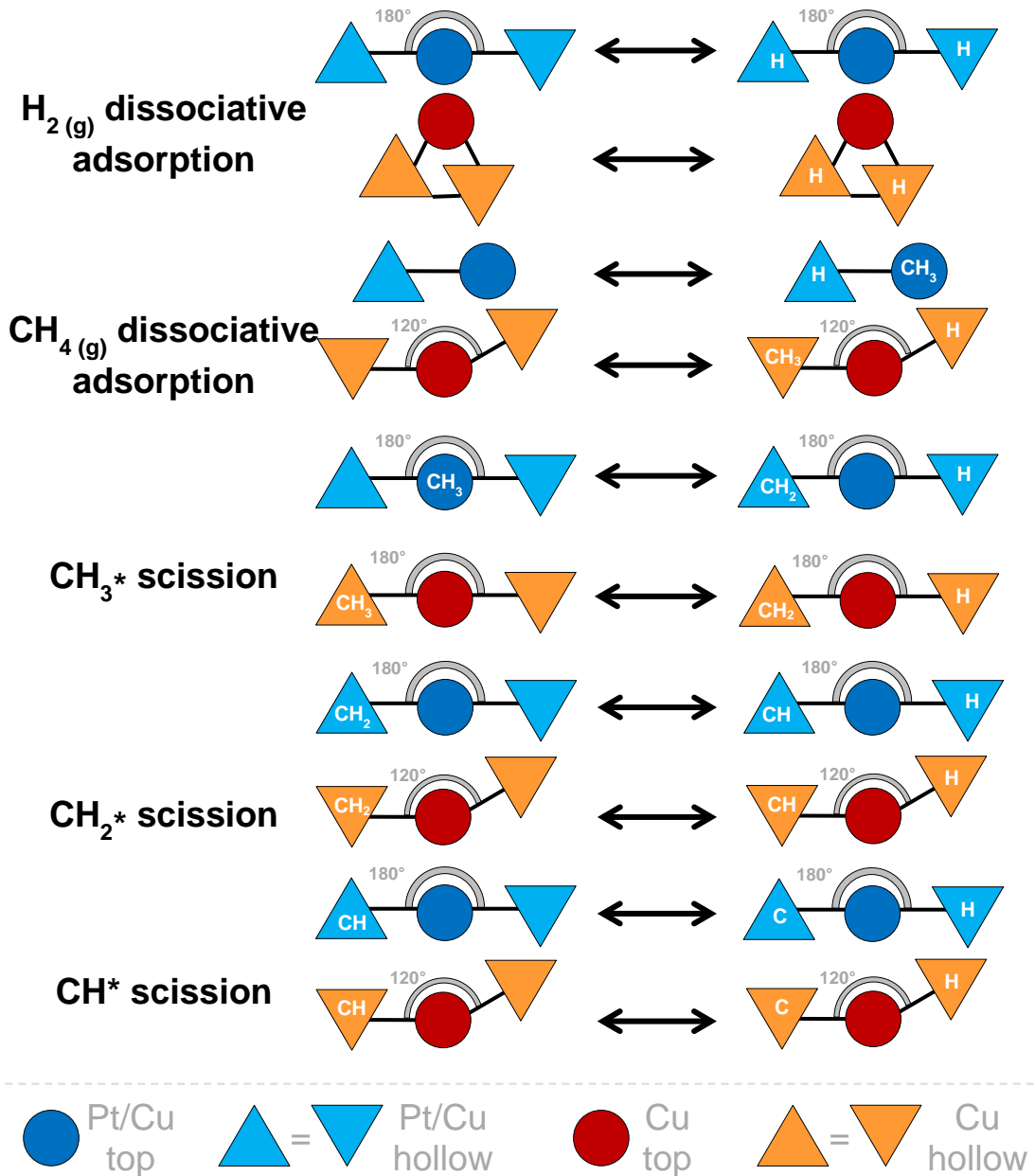


Figure 32: Graph-theoretical KMC representations of all non-diffusive elementary events involved in the full dehydrogenation pathway of methane on Pt/Cu(111) SAA; colour schemes are in line with the schematics of the lattice in **Figure 31**.

We generate a list of elementary events that we have calculated using DFT and corresponds to minimum energy pathways connecting initial and final states; we discuss this DFT in detail later in the chapter. The elementary events are all reversibly by microscopic reversibility and include the dissociative adsorption of H₂(g) and CH₄(g) and C-H bond scissions in

chemisorbed CH_x^* fragments (**Figure 32**). We also account for surface diffusion of CH_x^* and H^* surface species, though for brevity these are not shown in **Figure 32**.

We should note that the elementary events on Pt/Cu(111) SAA are the only ones explicitly shown in **Figure 32**, however the events using Cu sites only are also valid on Cu(111). Additionally, the events for Pt/Cu sites are interchangeable with pure Pt sites as we calculate analogous elementary events on pure Pt(111) though the energetics and kinetic constants are different as we allude to later.

Rate Constants from DFT

We compute first principles rate constants for each elementary event in **Figure 32** using DFT and TST. To compute k_{TST} for an elementary event we require the activation energy, E_a , relative to the initial state. From a DFT perspective, this means we must perform total energy minimisation calculations for initial and final (for the backward process) states, in addition to transition state searches linking those states via a minimum energy pathway. Moreover, in the computation of k_{TST} we must calculate a prefactor for the exponent in the Eyring equation (76). We achieve this by using harmonic TST which breaks the prefactor into contributions, including terms from the molecular partition functions of the reactants Q_{reac} and transition state Q^\ddagger . Further, DFT vibrational frequency calculations were performed to compute the vibrational contribution in each molecular partition function. The rotational contributions were computed using bond length measurements from fully relaxed geometries to determine the moments of inertia of gaseous species. For further details regarding k_{TST} and the corresponding prefactor, please see the “*Determining the Rate Constants of an Elementary Process*” section in *Chapter 2 Theoretical Methods*.

Computational Details

Density Functional Theory Setup

Periodic density functional theory calculations were performed using the Vienna *ab initio* Simulation Package (VASP) version 5.4.1.^{42,43} The exchange-correlation functional used is the non-local OptB86b-vdW functional,^{47,48} which is a revised version of the van der Waals

density functional of Dion et al.⁴⁹ We use a $3 \times 3 \times 5$ slab unit cell whereby the top-most four layers are allowed to fully relax while the bottom-most layer is fixed at the OptB86b-vdW bulk FCC lattice constant ($\text{Cu} = 3.608 \text{ \AA}$, $\text{Pt} = 3.958 \text{ \AA}$) and a vacuum length of 10 \AA separates periodic images in the z-direction. For surface calculations on Pt/Cu(111) SAA we use the lattice constant of FCC Cu and replace a single atom of Cu in the surface layer of the Cu(111) slab with a Pt atom. The Brillouin zone is sampled by a $13 \times 13 \times 1$ Monkhorst-Pack k-point mesh and the planewave kinetic energy cutoff is set to 400 eV. We ensure electronic self-consistency up to a tolerance of $<10^{-7}$ eV and the Hellmann-Feynman forces on free atoms during ionic relaxation are optimized to be $<10^{-2} \text{ eV}\cdot\text{\AA}^{-1}$. We present formation energies (E_F) of surface species with respect to gas phase CH_4 and H_2 , which we take as references (having formation energies equal to zero).

The transition state energies were found using the climbing image nudged elastic band (CI-NEB) and dimer formalisms of Jónsson and Henkleman.^{182, 183} Vibrational frequency calculations were performed using the finite displacement method with a step size of 0.02 \AA to ensure all transition states are first order saddle points.

For a given surface species C_xH_y $x = \{0,1\}$, $y = \{1,2,3,4\}$, we write the formation energy ($E_F(C_xH_y)$) as

$$E_F(C_xH_y) = E_{tot}(C_xH_y + \text{slab}) - \left\{ E_{tot}(\text{slab}) + x \cdot E_{tot}(\text{CH}_4) - \left(\frac{4x - y}{2} \right) \cdot E_{tot}(\text{H}_2) \right\} \quad (91)$$

We write the activation energy (E_a) as the formation energy of the transition state (E_F^{TS}) minus the formation energy of the initial state (E_F^{IS}):

$$E_a = E_F^{TS} - E_F^{IS}. \quad (92)$$

Kinetic Monte Carlo Setup

We perform simulations within the graph-theoretical KMC framework as implemented in Zacros version 1.02.^{47,48} The simulation temperature is ramped at a rate of $1 \text{ K}\cdot\text{s}^{-1}$ to model

TPR, over various temperature ranges depending on the chemistry in question. The partial pressures of gas phase species (CH_4 and H_2) are set to zero in order to reproduce ultra-high vacuum conditions. The simulation cell is formed of (50×51) fcc unit cells (5100 atoms, 15300 total sites) with periodic boundary conditions. Simulations for the Pt/Cu(111) SAA make use of a lattice whereby Cu sites have been randomly substituted with Pt sites giving a Pt density of 3 %; this is slightly higher than the overall Pt concentration in experiment (1 %) in order to reflect a marginally higher density of Pt atoms closer to step edges.⁶⁶ We scale down the surface diffusion rate constants to optimise efficiency though ensure quasi-equilibration of the adsorbate overlayer and convergence of the overall kinetics.

Results and Discussion

We present here DFT calculations for the geometries and corresponding adsorption energies of methane dissociation intermediates on Cu(111), Pt(111) and Pt/Cu(111) SAA. We then show how we use transition state search methods within the DFT framework to determine the geometry and energy of the transition states for C-H scissions between each methane-derived intermediate. Subsequently, we calculate activation barriers that are then used to generate kinetic constants for use in KMC simulations of methane TPR. Finally, we compare our proposed DFT structures, energetics, reaction pathways and kinetic simulations, with experimental work from our collaborators at the Sykes and Flytzani-Stephanopoulos research groups.

C_xH_y Adsorption Geometries and Energetics

Using DFT, we study the successive scissions of C-H bonds from methane through to atomic carbon. First, we find the most stable configurations for all C_xH_y species ($x = \{0,1\}$, $y = \{1,2,3,4\}$) on the (111) surface of Cu, Pt and Pt/Cu SAA. Three adsorption sites are considered for each adsorbate on each surface, namely top, bridge and hollow. We provide the formation energies (E_F) of the most stable surface species in addition to metal-adsorbate bond distances in **Table 4**; the most stable adsorption structures are shown in **Figure 33** and the corresponding vibrational frequencies are given in **Table 5**. The formation energies

of all adsorption configurations, including those exhibiting lower binding energies are given in

Table 6.

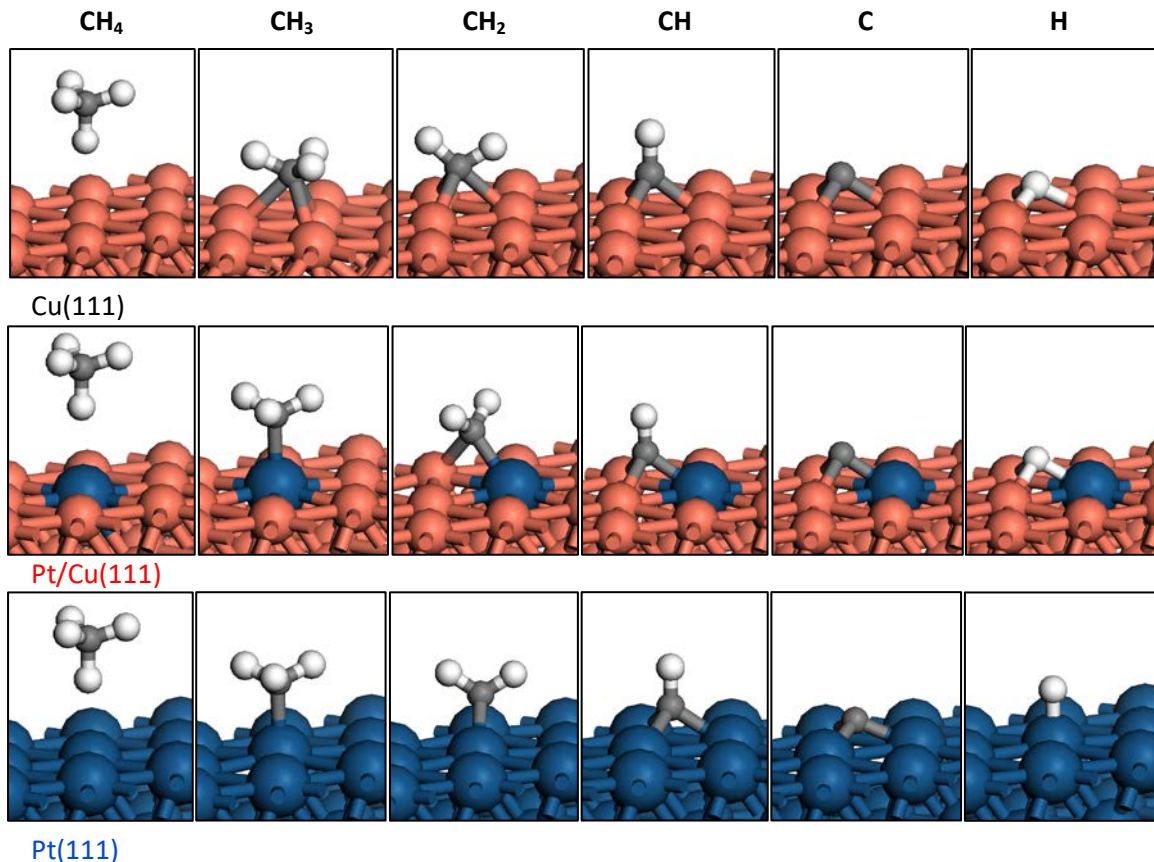


Figure 33: The most stable configurations calculated using DFT, for each C_xH_y species ($x = \{0,1\}, y = \{1,2,3,4\}$) on Cu(111) (top), Pt/Cu(111) SAA (middle) and Pt(111) (bottom).

For CH_4^* it was found that the preferred orientation is for adsorption via H (where C-H is perpendicular to the surface) with CH_4^* in its typical tetrahedral geometry. The adsorption on all three surfaces is to the top site with long M-H distances and correspondingly weak adsorption energies. Our calculations of the geometry on monometallic surfaces agree nicely with previous studies that take dispersion forces into account.²¹⁴ Other works using traditional xc-functionals that do not account for London forces, predict negligible CH_4^* adsorption energies, with physisorbed CH_4^* having geometric and vibrational properties akin to that of gaseous $\text{CH}_4(g)$ thereby suggesting very weak or no binding at all.^{213, 214} Our use of a dispersion optimised functional is able to capture the weak M-H interaction more effectively than traditional DFT functionals.²¹⁴ Additionally, when comparing our data to using non-dispersion corrected functionals, we compute slightly shortened M-H bond lengths and

slightly stronger adsorption²¹⁴ with formation energies of -0.19 eV, -0.21 eV and -0.24 eV for Cu(111), Pt/Cu(111) SAA and Pt(111), respectively.

Surface	Species	Most stable Site	E _F (eV)	M-A distance (Å)
Cu(111)	CH ₄ *	top	-0.19	2.46
	CH ₃ *	hollow	0.68	2.23
	CH ₂ *	hollow	1.72	2.00
	CH*	hollow	2.37	1.91
	C*	hollow	3.79	1.85
	H*	hollow	-0.26	1.75
Pt/Cu(111)	CH ₄ *	top	-0.21	2.56
	CH ₃ *	top	0.44	2.11
	CH ₂ *	bridge	1.57	2.03(2.01)
	CH*	hollow	2.13	1.97(1.94)
	C*	hollow	3.36	1.88(1.91)
	H*	hollow	-0.29	1.57
Pt(111)	CH ₄ *	top	-0.24	2.34
	CH ₃ *	top	0.01	2.07
	CH ₂ *	bridge	0.58	2.05
	CH*	hollow	0.53	2.00
	C*	hollow	1.62	1.91
	H*	top	-0.52	1.57

Table 4: The formation energies and bonding metal (M) to adsorbing atom (A) bond lengths of the most stable C_xH_y species ($x = \{0,1\}$, $y = \{1,2,3,4\}$) on Cu(111), Pt/Cu(111) SAA and Pt(111). Formation energies are with respect to gaseous CH₄(_g) and H₂(_g). Bond lengths in two- and three-fold sites on Pt/Cu(111) are reported to Pt and Cu in brackets. Bond lengths in high symmetry sites are equal and symmetric unless stated.

For CH₃* adsorption we find that there is stable chemisorption on top sites of Pt/Cu(111) and Pt(111), but not on Cu(111) (this appears to be a diffusion transition state as evidenced by an imaginary frequency and a diffusion-like vibrational mode). On Cu(111) and Pt(111) we calculate stable adsorption on two and threefold sites; however minimisation in the same manner from shared Pt-Cu bridge and hollow sites on Pt/Cu(111) SAA results in relaxation to the top Pt site. Adsorption of CH₃* on top sites is via C with a C₃ axis of CH₃* perpendicular to the metal surface and C sitting closer to the surface than any H (**Figure 33**). These top site modes of adsorption are the most stable geometries of chemisorbed CH₃ on Pt/Cu(111) SAA and Pt(111), with formation energies of 0.44 eV and 0.01 eV respectively; the latter is in good agreement with past studies.^{188, 214-216} On the other hand, on Cu(111) CH₃* is most stable in the threefold hollow site with a formation energy of 0.68 eV compared with 0.88 eV when top and 0.78 eV on the bridge site (though both are unstable modes as identified by vibrational analysis) which is consistent with the findings of others.^{208, 213}

Vibrational Frequencies (cm ⁻¹)													
	ν_1	ν_2	ν_3	ν_4	ν_5	ν_6	ν_7	ν_8	ν_9	ν_{10}	ν_{11}	ν_{12}	
Cu(111)													
CH ₃ *	2915	2914	2853	1355	1355	1164	533	532	320	279	142	140	
CH ₂ *	2956	2825	1313	646	461	397	311	234	101				
CH*	3005	596	595	540	387	383							
C*	494	483	481										
H*	1041	830	822										
PtCu(111) SAA													
CH ₃ *	3033	3032	2944	1396	1393	1153	725	725	474	83	81	43	
CH ₂ *	3012	2942	1335	716	666	546	441	310	36				
CH*	3001	685	602	571	397	357							
C*	651	415	392										
H*	1424	581	480										
Pt(111)													
CH ₃ *	3039	3035	2934	1385	1384	1170	765	764	509	111	109	22	
CH ₂ *	3014	2926	1327	874	701	653	571	391	167				
CH*	2996	767	766	598	467	466							
C*	621	621	460										
H*	1039	597	583										

Table 5: Vibrational frequencies (computed from DFT using the finite differences method) for chemisorbed species in the most stable site type on each surface.

For CH₂* there is stable adsorption in two and threefold symmetry sites. On Cu(111) we find the most favoured adsorption site to be the threefold hollow site with formation energy of 1.72 eV, whereas on Pt(111) we find the most stable adsorption on the bridge site with formation energy of 0.59 eV (**Figure 33**); these findings are also in good agreement with the work of others.^{188, 208, 213-216} In the case of Pt/Cu(111) SAA, we find the most stable adsorption site to be the shared Pt-Cu bridge site, where adsorbed CH₂ has a formation energy of 1.57 eV. The geometry of CH₂* on Cu(111) is orientated with C in the geometric centre of the hollow site with one C-H bond pointing above a Cu atom with the other C-H bond pointing above an adjacent bridge site (**Figure 33**). The H-C-H plane is perpendicular to the surface though the molecule tilts slightly in favour of the C-H hovering over the Cu atom. On Pt(111), there is a C₂ symmetry axis perpendicular to the surface from the bridge to the C (**Figure 33**). Finally on Pt/Cu(111) SAA, the CH₂* orientation is similar though without C₂ symmetry as the bridge is between Pt and Cu atoms. The C atom in CH₂ on Pt/Cu(111) SAA is slightly further from the Pt atom than Cu, though the Pt-C distance is shorter than on pure Pt as indeed the Cu-C distance is longer than on pure Cu, indicating a preference for binding more strongly with Pt than Cu in the alloy.

The most stable adsorption sites for CH* on all surfaces are the hollow sites, with formation energies of 2.37 eV, 2.13 eV and 0.53 eV for Cu(111), Pt/Cu(111) SAA and Pt(111), respectively. In all cases chemisorption is via the C atom, with the C-H bond being perpendicular to the surface (**Figure 33**). For the pure metals, the CH* adsorbate is in the geometric centre of the threefold hollow site, in good agreement with other theoretical studies.^{188, 208, 213-216} For Pt/Cu(111) SAA, the M-C distance is 0.04 Å larger when M = Pt than M = Cu, due to the larger size of the Pt atom compared with Cu. The Pt-C distance in Pt/Cu(111) SAA is shorter than in pure Pt and the Cu-C distance is longer than in pure Cu, indicating Pt interaction with CH* is slightly stronger compared to Cu within the alloy.

Atomic C* adsorbs strongly on all surfaces, preferentially in threefold sites, with formation energies of 3.79 eV, 3.36 eV and 1.62 eV for Cu(111), Pt/Cu(111) SAA and Pt(111) respectively. As with CH* hollow site adsorption on Pt/Cu(111) SAA, C* is also drawn closer to Pt atom than in pure Pt(111) and further from Cu atoms than in pure Cu(111) with Pt-C distance of 1.88 Å and Cu-C distance of 1.91 Å.

Finally, H* adatoms are most stable in threefold hollow sites on Cu(111) and Pt/Cu(111) with formation energies of -0.26 eV and -0.29 eV, respectively. In the alloy, the top site adsorption configuration is also stable, though has positive formation energy (endothermic adsorption of H₂), whereas on all surfaces bridge site H* adatoms are an unstable diffusion transition states. On pure Pt(111), H* is actually more stable on the top site with a formation energy of -0.52 eV compare to -0.47 eV in hollow sites. This is in good agreement with previous reports that highlight the relatively flat nature of the Pt-H potential energy surface.^{217, 218}

	Species	Site Type	E_F (eV)
Cu(111)	CH ₄	top	-0.19
	CH ₄	bridge	-0.18
	CH ₄	fcc	-0.19
	CH ₃	top	0.88
	CH ₃	bridge	-
	CH ₃	fcc	0.68
	CH ₂	top	2.56
	CH ₂	bridge	1.88
	CH ₂	fcc	1.72
	CH	top	4.08
	CH	bridge	2.52
	CH	fcc	2.37
	C	top	5.72
	C	bridge	-
	C	fcc	3.79
	H	top	0.33
	H	bridge	-0.10
	H	fcc	-0.26
PtCu(111) SAA	CH ₄	top	-0.21
	CH ₄	bridge	-
	CH ₄	fcc	-
	CH ₃	top	0.44
	CH ₃	bridge	-
	CH ₃	fcc	-
	CH ₂	top	1.94
	CH ₂	bridge	1.57
	CH ₂	fcc	1.90
	CH	top	3.57
	CH	bridge	-
	CH	fcc	2.13
	C	top	4.41
	C	bridge	-
	C	fcc	3.36
	H	top	-0.27
	H	bridge	-0.10
	H	fcc	-0.29
Pt(111)	CH ₄	top	-0.24
	CH ₄	bridge	-0.22
	CH ₄	fcc	-0.22
	CH ₃	top	0.01
	CH ₃	bridge	0.64
	CH ₃	fcc	0.73
	CH ₂	top	1.47
	CH ₂	bridge	0.58
	CH ₂	fcc	-
	CH	top	3.29
	CH	bridge	1.22
	CH	fcc	0.53
	C	top	3.87
	C	bridge	2.43
	C	fcc	1.62
	H	top	-0.52
	H	bridge	-0.44
	H	fcc	-0.46

Table 6: Formation energies in eV with respect to CH_{4(g)} and H_{2(g)} for all C_xH_y species ($x = \{0,1\}$, $y = \{1,2,3,4\}$) on Cu(111), Pt/Cu(111) SAA and Pt(111). Calculations whereby a relaxation from an initial geometry with the adsorbate in “Site Type” results in a different, final “Site Type” configuration have formation energies reported as a dash.

Activated Complexes and Potential Energy Surface

Having considered the stable adsorption of C_xH_y species ($x = \{0,1\}, y = \{1,2,3,4\}$) on Cu(111), Pt/Cu(111) SAA and Pt(111), we will now consider the elementary processes that relate these fragments within the context of successive C-H bond scissions during methane dehydrogenation. We identify minimum energy pathways between stable initial state and co-adsorbed final state geometries, extracting optimised transition state energies (E_{Tot}^{TS}) and geometries for each of the elementary events involved in our system. We report corresponding activation (E_a) and reaction energies (ΔE_{Rxn}) for each transition state in **Table 7**, transition state configurations in **Figure 34**. Harmonic vibrational frequencies for each transition state are given in **Table 8** where a single imaginary frequency corresponds to a first order saddle point on the potential energy surface (as is the case for all transition states presented here).

Surface	Reaction	$E_F(TS)$ (eV)	E_a (eV)	ΔE_{Rxn} (eV)
Cu(111)	$CH_4^* \rightarrow CH_3^* + H^*$ (TS1)	1.29	1.48	0.61
	$CH_3^* \rightarrow CH_2^* + H^*$ (TS2)	-0.38	1.42	0.78
	$CH_2^* \rightarrow CH^* + H^*$ (TS3)	-2.80	0.96	0.40
	$CH^* \rightarrow C^* + H^*$ (TS4)	-3.14	1.97	1.17
Pt/Cu(111) SAA	$CH_4^* \rightarrow CH_3^* + H^*$ (TS1)	0.71	0.92	0.36
	$CH_3^* \rightarrow CH_2^* + H^*$ (TS2)	-0.92	1.13	0.85
	$CH_2^* \rightarrow CH^* + H^*$ (TS3)	-3.07	0.84	0.27
	$CH^* \rightarrow C^* + H^*$ (TS4)	-3.70	1.64	0.94
Pt(111)	$CH_4^* \rightarrow CH_3^* + H^*$ (TS1)	0.34	0.58	-0.51
	$CH_3^* \rightarrow CH_2^* + H^*$ (TS2)	-1.78	0.69	0.05
	$CH_2^* \rightarrow CH^* + H^*$ (TS3)	-4.66	0.23	-0.57
	$CH^* \rightarrow C^* + H^*$ (TS4)	-5.62	1.32	0.56

Table 7: Formation energies of the transition state ($E_F(TS)$) with respect to gaseous $CH_4(g)$ and $H_2(g)$, activation energies (E_a) and reaction energies (ΔE_{Rxn}) for C-H bond scissions in methane derivatives on Cu(111), Pt/Cu(111) SAA and Pt(111).

Methane Activation

For the initial activation of CH_4^* , we use the most stable CH_4^* configuration as our initial state, which corresponds to the top physisorbed state on all three surfaces. The CH_4^* adsorbate is then dissociated into $CH_3^* + H_{diss}^*$, with the C-H bond that is initially perpendicular to the surface being broken. This event proceeds via TS1 as shown in **Figure 34**. The final product geometry is the same on Pt/Cu(111) and Pt(111) with CH_3^* occupying a top site and H_{diss}^* occupying an adjacent hollow site, separated by the Pt atom which CH_4^*

initially physisorbed onto. On Cu(111), CH_3^* is most stable in a hollow site and will relax to this site in the presence of the adjacent H adatom.

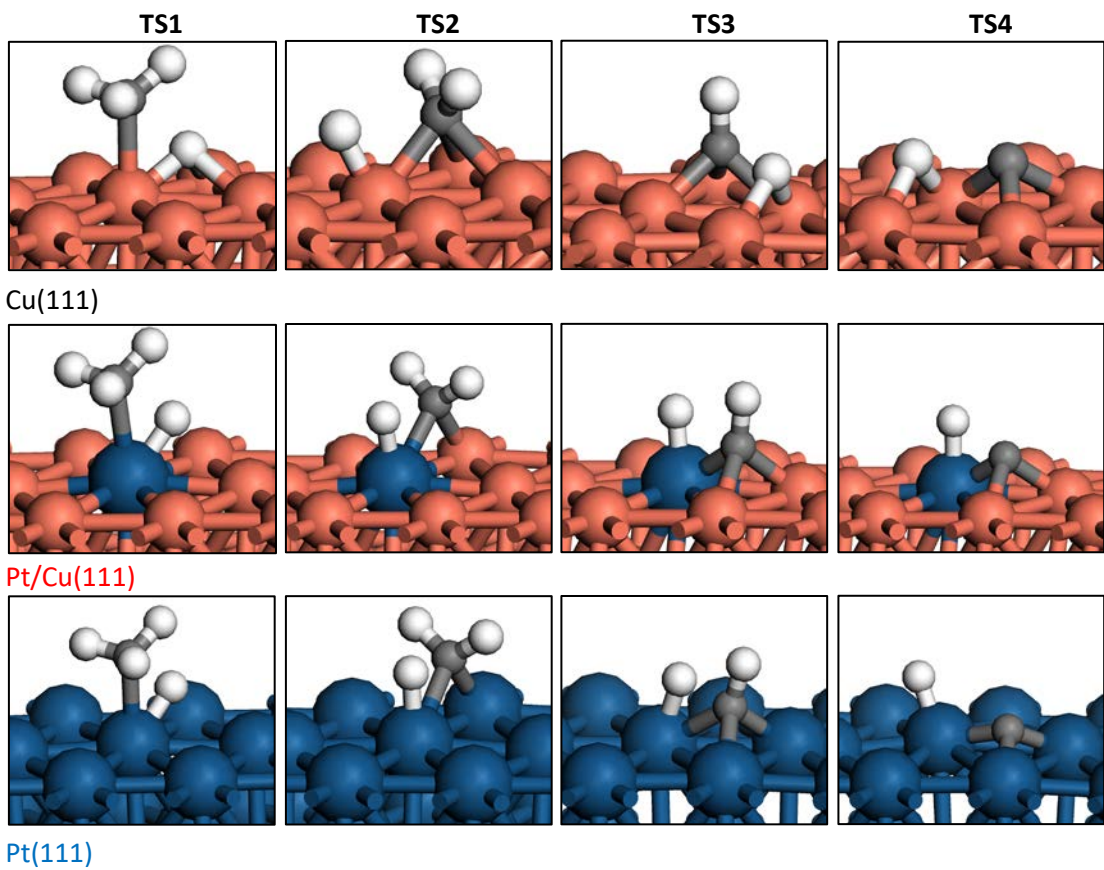


Figure 34: Schematic of the transition state geometries for the successive C-H scissions from methane to atomic C on Cu(111) (top), Pt/Cu(111) (middle) and Pt(111) (bottom).

Interestingly, the geometries of TS1 on each surface are similar, though vary slightly in how early or late they appear along the reaction coordinate. In the case of dissociation on Cu(111) the C-H_{diss} distance in TS1 is 1.78 Å, whereas with Pt/Cu(111) SAA and Pt(111) the C-H_{diss} distances in TS1 are 1.62 Å and 1.53 Å, respectively. The shorter dissociating bond distance over Pt is the result of Pt atoms in Pt/Cu(111) SAA and Pt(111) being better able to facilitate multiple adsorbate binding compared to Cu atoms in Cu(111); hence the C-H scission can occur earlier along the reaction coordinate.

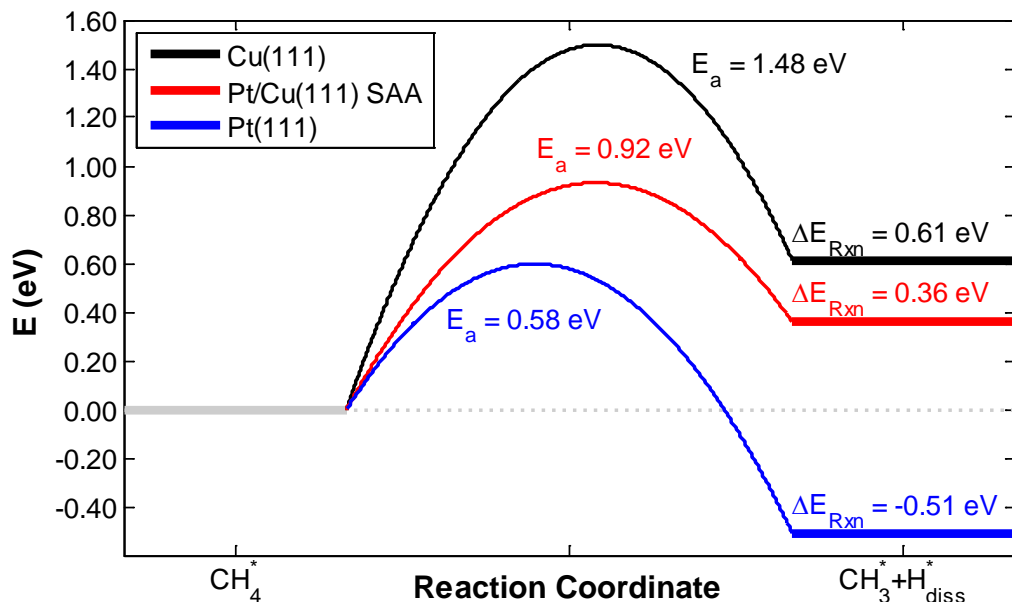


Figure 35: Energy profile for C-H bond scission of physisorbed CH_4^* to CH_3^* and H^* on Cu(111) (black), Pt/Cu(111) SAA (red) and Pt(111) (blue). Energies are relative to CH_4^* (initial state).

The decreasing C-H_{diss} distances in TS1 on Cu(111), Pt/Cu(111) SAA and Pt(111) are accompanied by decreasing activation barriers on these surfaces, which are found to be 1.48 eV, 0.92 eV and 0.58 eV, respectively. This result is in line with experimental observations that Pt catalysts exhibit relatively high activity towards C-H bond scission, whereas Cu(111) remains relatively inert.^{204, 207, 209} Moreover, the transition state geometries on Cu(111) and Pt(111) are in good agreement with that determined by others^{213, 215}; notably our values of the activation energy are consistently lower as we account for dispersion interactions that are not considered by others.

	Vibrational Frequencies (cm ⁻¹)														
	ν_1	ν_2	ν_3	ν_4	ν_5	ν_6	ν_7	ν_8	ν_9	ν_{10}	ν_{11}	ν_{12}	ν_{13}	ν_{14}	ν_{15}
Cu(111)															
TS4	1687	475	458	449	150	817i									
TS3	3020	1388	816	599	586	527	415	292	827i						
TS2	2952	2908	1678	1313	781	575	457	384	265	166	138	843i			
TS1	3072	3067	2957	1437	1397	1322	1083	764	619	447	329	144	81	41	891i
PtCu(111) SAA															
TS4	1848	547	440	407	320	822i									
TS3	3039	1878	923	555	536	383	359	336	760i						
TS2	3032	2965	1943	1356	878	789	575	508	310	277	59	705i			
TS1	3094	3043	2964	1965	1410	1394	1176	842	759	399	109	93	61	21	890i
Pt(111)															
TS4	1879	639	550	472	418	942i									
TS3	2967	1881	1089	738	593	502	427	416	472i						
TS2	3036	2950	1993	1334	1020	928	713	559	350	333	175	757i			
TS1	3115	3080	2976	1640	1378	1350	1155	825	811	420	315	132	130	122	896i

Table 8: Vibrational frequencies in wavenumbers (computed from DFT using the finite differences method) for each transition state (TS1, TS2, TS3 and TS4) for C-H scissions on Cu(111), Pt/Cu(111) SAA and Pt(111). Imaginary frequencies correspond to unstable modes.

Methyl Activation

The second C-H scission we study on Cu(111), Pt/Cu(111) and Pt(111) SAA is from chemisorbed CH_3^* to $\text{CH}_2^* + \text{H}_{\text{diss}}^*$. The initial state in each reaction corresponds to the most stable configuration of CH_3^* on each surface; for Cu(111) this is the fcc 3-fold hollow site, whereas for Pt/Cu(111) SAA and Pt(111) this is the top Pt site. CH_3^* has C_3 symmetry when chemisorbed in each of these configurations, meaning that the C-H bonds within CH_3^* are symmetrically equivalent. Dissociation of a C-H bond proceeds via TS2 (**Figure 34**).

The final dissociated products on Cu(111) are separated by a Cu atom neighbouring the hollow site in which CH_3^* is initially chemisorbed. Post-dissociation, H_{diss} relaxes across this atom to an fcc hollow site adjacent to the fcc hollow site of the initial state. CH_2^* relaxes to the adjacent bridge site, such that the final dissociated products are separated by the Cu atom across which H_{diss} relaxes. In the cases of Pt/Cu(111) SAA and Pt(111), CH_3^* dissociates into CH_2^* and H_{diss}^* on bridge and hollow sites separated by the Pt atom to which CH_3^* is initially chemisorbed.

All three TS2 structures are located over a top site that is adjacent to the binding site of the initial state; a Cu top site for Cu(111) and a Pt top site for Pt/Cu(111) and Pt(111). On Cu(111) the fcc bound CH_3^* in the initial state has C-H bonds pointing above the three surrounding Cu atoms. The dissociation proceeds with a C-H bond elongation of C-H_{diss} from 1.11 Å in the initial state to 2.00 Å in TS2, with the C atom displacing by 0.11 Å from the geometric centre of the initial fcc site in the same direction. The activation barrier for this dissociation on Cu(111) is 1.42 eV (**Figure 36**) in excellent agreement with 1.36 eV calculated by Gajewski *et al.*²¹³

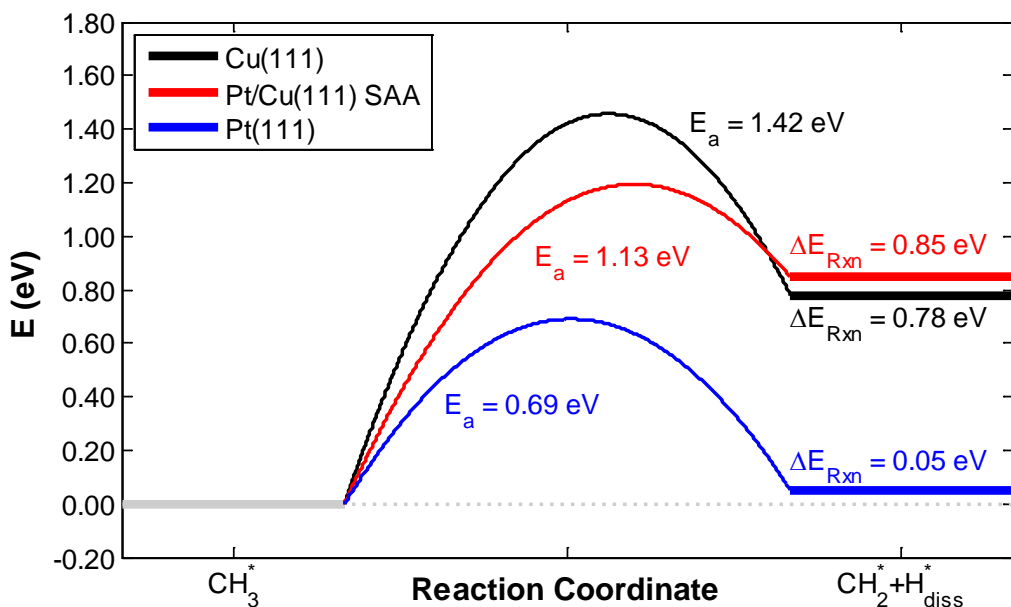


Figure 36: Energy profile for C-H bond scission of chemisorbed CH_3^* to CH_2^* and H^* on Cu(111) (black), Pt/Cu(111) SAA (red) and Pt(111) (blue). Energies are relative to CH_3^* adsorbed to each surface (initial state).

For Pt/Cu(111) SAA and Pt(111) the initial state has methyl adsorbed on the top site with C-H bonds orientated across Pt-Cu bridges. In both cases, the dissociation is across the top Pt site that the initial state CH_3^* was bound to. The C- H_{diss} bond elongation is in the plane of the C-H bond and the surface normal. The elongation is coincident with antiparallel movement of the C atom in the same plane onto an opposite bridge site with H_{diss} located on the top Pt site. The C- H_{diss} distance is significantly shorter for dissociation on Pt(111) (1.54 \AA) compared to Pt/Cu(111) SAA (1.77 \AA) though the C atom position is on the bridge site with the change C-Pt distance (for the central Pt atom) between final and transition states being shorter for Pt/Cu(111) SAA (0.09 \AA) compared to Pt(111) (0.13 \AA). Both CH_2^* fragments in Pt/Cu(111) SAA and Pt(111) dissociation are final state like, both in adsorbate geometry and in surface position. The calculated activation barriers for CH_3^* dissociation on Pt/Cu(111) SAA and Pt(111) are 1.13 eV and 0.69 eV, respectively (Figure 36).

Methylene Activation

The initial state for CH_2^* dissociation on Cu(111) has CH_2^* adsorbed on an fcc hollow site with one C-H bond pointing across a Cu-Cu bridge and the C- H_{diss} bond directed across the third Cu atom constituting the fcc site; this is the most stable adsorption geometry for CH_2^* on Cu(111). On Pt/Cu(111) SAA and Pt(111), the most stable surface site for the adsorption

of CH_2^* is also the initial state for C-H scission in CH_2^* , however on these two surfaces, this is the Pt-Cu bridge on Pt/Cu(111) SAA and the Pt-Pt bridge on Pt(111). In both cases, the C-H bonds are orientated perpendicular to the bridge; the C- H_{diss} bond is pointed towards an fcc hollow site and a single Pt atom.

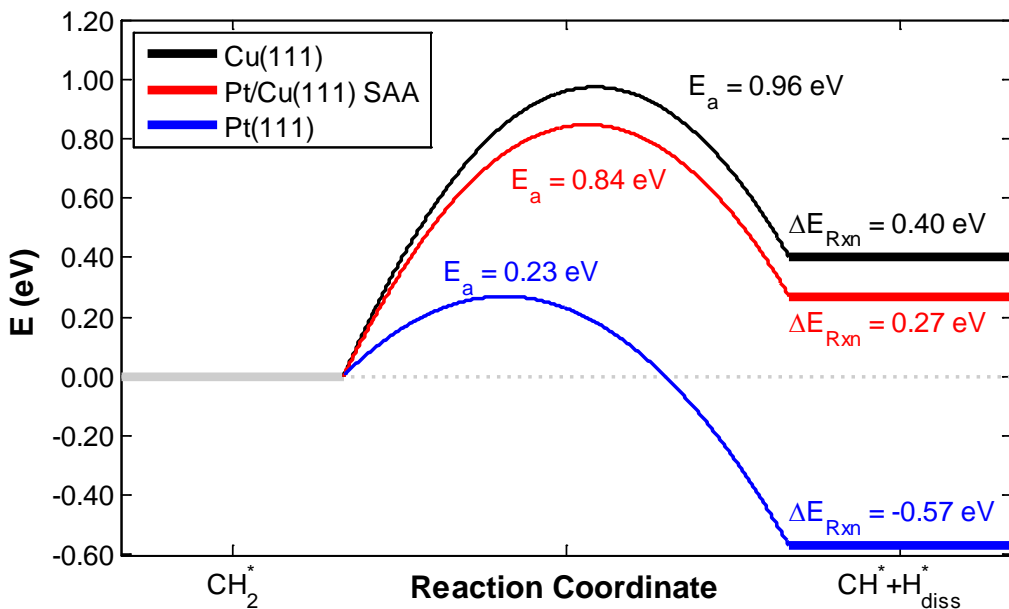


Figure 37: Energy profile for C-H bond scission of chemisorbed CH_2^* to CH^* and H^* on Cu(111) (black), Pt/Cu(111) SAA (red) and Pt(111) (blue). Energies are relative to CH_2^* adsorbed to each surface (initial state).

C-H_{diss} bond scission in CH_2^* on Cu(111) is across a hcp site neighbouring the fcc site to which CH_2^* is initially adsorbed. This results in the final dissociated CH^* and H_{diss}^* products relaxing to the initial state fcc site and a nearest neighbour fcc site, respectively; these two fcc sites are separated by the hcp site whereby TS3 is located (**Figure 34**). For Pt/Cu(111) SAA and Pt(111), the CH_2^* dissociates via TS3 across a Pt top site (**Figure 34**) that is one of the atoms forming the bridge site onto which CH_2^* is initially adsorbed. The final dissociated CH and H_{diss} products appear in the fcc and hcp sites with a site-Pt-site angle of 180°.

In all of the TS3 geometries there is significant tilting of the CH_2^* fragment. In fact, TS3 on Cu(111) has a geometry whereby the C-H_{diss} bond is parallel to the surface and the non-dissociating C-H bond is perpendicular to the surface. The analogous tilting on Pt(111) is still significant, though the C-H_{diss} bond makes a 17° angle with the surface plane whereas the non-dissociating C-H bond makes an angle of 34° with the surface normal. In the case of Pt/Cu(111) SAA, the adsorbed CH_2^* must rotate such that it is adsorbed to the fcc hollow

site prior to the dissociation; this is an endothermic transition with no additional activation barrier over the reaction energy for this process. Subsequent to the rotation, TS3 on Pt/Cu(111) SAA is akin to that on Pt(111), though the C-H_{diss} bond makes a 20° angle with the surface plane and the non-dissociating C-H bond makes a 17° angle with the surface normal.

There is notable elongation of the C-H_{diss} bond length in all TS3 structures, from 1.12 Å in the initial state to 1.83 Å in TS3. For Pt/Cu(111) SAA and Pt(111), the C-H_{diss} bond distance increases from 1.12 Å, 1.10 Å and 1.10 Å to 1.83 Å, 1.64 Å and 1.38 Å for Cu(111), Pt/Cu(111) SAA and Pt(111), respectively. The activation energies for CH₂* scission are 0.96 eV, 0.84 eV and 0.23 eV for Cu(111), Pt/Cu(111) SAA and Pt(111), respectively (**Figure 37**).

Methylidyne Activation

Finally, for scission of CH* to atomic C and H_{diss}, we find that on Cu(111), Pt/Cu(111) SAA and Pt(111) the CH* initial state is most stable in fcc hollow sites, where the C-H_{diss} bond axis is aligned with the surface normal. As in the scission of CH₂* we find that for Pt/Cu(111) SAA and Pt(111) the dissociation is across the Pt metal atom such that the final state has C and H in hollow sites with a site-Pt-site angle of 180°; unlike for CH₂*, no migration of CH* is necessary prior to bond scission. The final products of CH* dissociation on Cu(111) relax into fcc-fcc or hcp-hcp hollow site pairs with a site-Cu-site angle of 120°; the scission occurs over a low symmetry bridge-hollow site, similar to that in CH₂* C-H_{diss} scission.

In TS4 the C-H_{diss} bond distances on Cu(111), Pt/Cu(111) SAA and Pt(111) are 1.82 Å, 1.75 Å and 2.61 Å, respectively (**Figure 34**). For Pt(111) this is notably higher than the initial state C-H_{diss} bond length in CH* (1.10 Å on all surfaces) indicating a very late, product like transition state for this surface. The activation energies for C-H_{diss} bond scission in CH* are 1.98 eV, 1.64 eV and 1.32 eV for Cu(111), Pt/Cu(111) SAA and Cu(111), respectively (**Figure 38**).

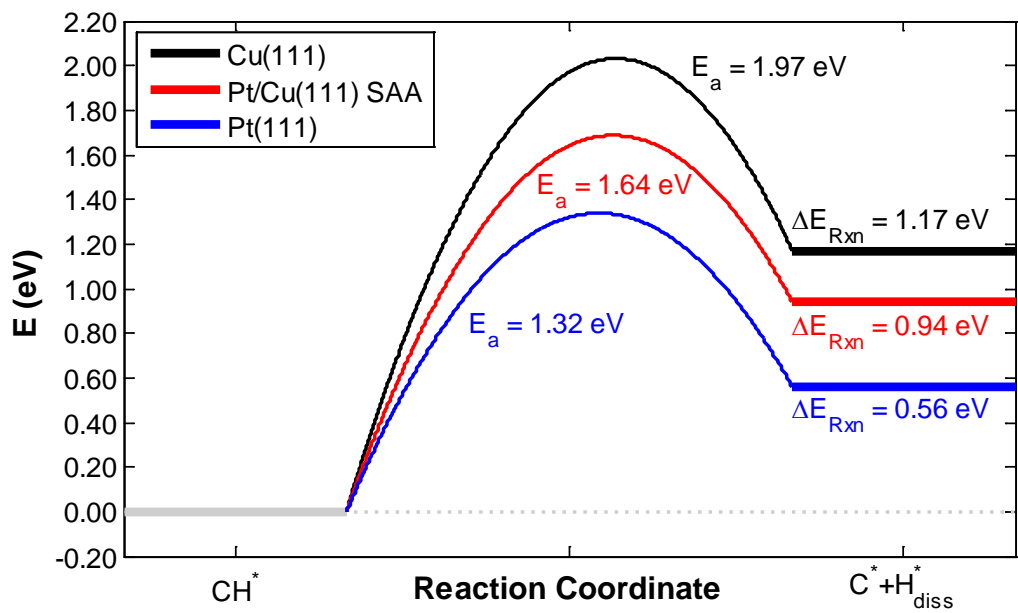


Figure 38: Energy profile for C-H bond scission of chemisorbed CH^* to C^* and H^* on Cu(111) (black), Pt/Cu(111) SAA (red) and Pt(111) (blue). Energies are relative to CH^* adsorbed to each surface (initial state).

Energy Landscape for Methane Dehydrogenation

From our stable configuration and activated complex calculations we are able to construct energy landscape of the successive dehydrogenations of methane on Cu(111), Pt/Cu(111) SAA and Pt(111). The use of formation energies allows us to plot all scissions on all surfaces on a single reaction coordinate. Combining stable adsorption energies and activation energies, a one dimensional potential energy diagram for the four dehydrogenations from methane to atomic C is plotted in **Figure 39**, thereby allowing us to compare and contrast the energetics of each pathway.

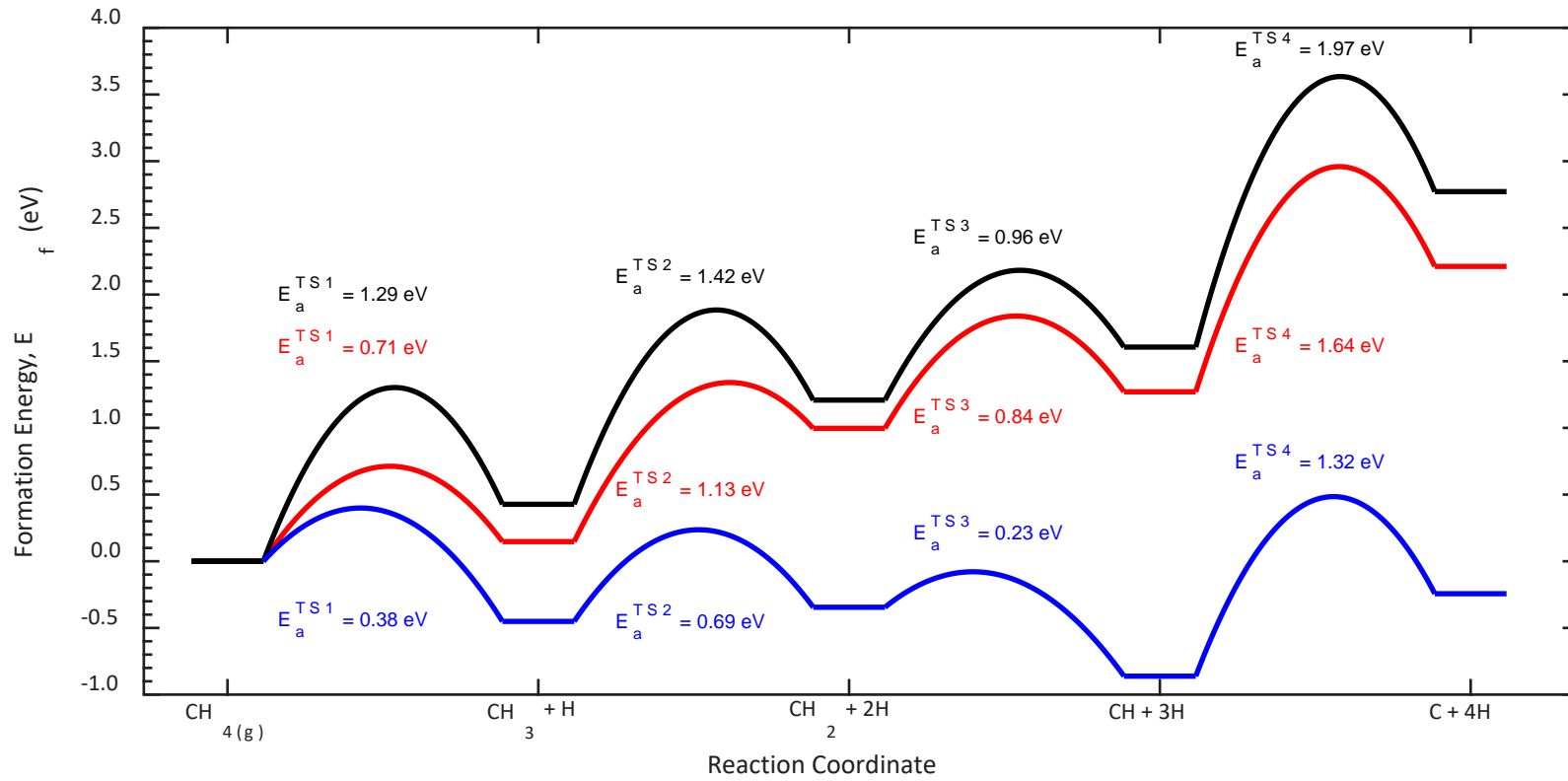


Figure 39: DFT calculated energetics of C-H activation and binding of intermediates for methane decomposition, giving a reaction coordinate corresponding to the lowest energy, full dehydrogenation pathway for methane over Cu(111) (black), Pt/Cu(111) SAA (red), and Pt(111) (blue). Formation energies (eV) are with reference to clean slabs of each metal, as well as methane and molecular hydrogen in the gas phase.

We note clear differences in the energetics of each pathway despite the comparable intermediate and transition state molecular geometries we have computed. **Figure 39** elucidates why Pt(111) is an active C-H activation catalyst, exhibiting much lower barriers for all C-H scissions considered when compared to Cu(111). However, the strong binding of CH_x intermediates to the Pt(111) surface compared to Cu(111) explains the tendency for coke to form on Pt C-H activation catalysts and the lack thereof on Cu. Interestingly the Pt/Cu(111) SAA exhibits intermediate barrier heights as well as intermediate binding strength of adsorbates compared to the two pure metals. This finding suggests that the Pt/Cu(111) SAA may readily activate adsorbed CH₃ while resisting coking by preventing subsequent C-H scissions.

Along the reaction coordinate in **Figure 39**, the potential energy diagram for methane dehydrogenation on Pt/Cu(111) SAA is similar to Pt(111) for the first dehydrogenation steps, whereas more Cu(111)-like as the reaction progresses. To evaluate the “intermediacy” of the SAA reaction barrier with respect to pure Cu and Pt, we introduce parameters α and β where

$$\alpha = \frac{E_a^{Cu} - E_a^{SAA}}{E_a^{Cu} - E_a^{Pt}}, \beta = 1 - \alpha. \quad (93)$$

A value of $\alpha = 0$ versus $\alpha = 1$ indicates that the SAA activation barrier is equal to the barrier on Cu(111) versus Pt(111), respectively. The first C-H scission (CH₄* to CH₃*) on the SAA has an activation barrier closest to that on Pt(111) ($\alpha = 0.64, \beta = 0.36$). The barrier of the next scission (CH₃ to CH₂) is closer to that on Cu(111) ($\alpha = 0.40, \beta = 0.60$) and the penultimate scission (CH₂ to CH) has an activation energy most similar to that on Cu(111) ($\alpha = 0.16, \beta = 0.84$). The final barrier (CH to C) is almost exactly intermediate ($\alpha = 0.51, \beta = 0.49$).

To evaluate the effect of the change in relative barrier intermediacy exhibited by Pt/Cu(111) SAA with respect to pure Pt(111) and Cu(111), we perform KMC simulations parameterised

by the DFT calculations we have computed for the methane system on each surface. More specifically, we will simulate temperature programmed reaction (TPR) of methane from methyl-pre-covered Cu(111), Pt/Cu(111) SAA and Pt(111). These KMC simulations will give us a platform to analyse the kinetics of C-H activation on each surface, and ascertain the temperature and extent of each activation during TPR. Such analysis will allow us to evaluate the level of coke resistance and activity exhibited by each material. Furthermore, we will compare TPR desorption profiles of methane from each surface to experimental data produced by the Sykes and Flytzani-Stephanopoulos groups.

Thermal Desorption Simulations

Using the KMC method, we simulate TPR of methane derivatives on Cu(111), Pt/Cu(111) SAA and Pt(111). Throughout the simulation, we record the coverage (θ) of all C_xH_y species ($x = \{0,1\}$, $y = \{1,2,3,4\}$) studied with DFT in this Chapter, in addition to the number of H_2 and CH_4 gas species that are evolved from the surface, at time intervals of 0.25 s (equivalent to temperature intervals of 0.25 K at 1 K·s⁻¹ ramp rate). We convert this information into a TPR signal by taking a moving average (at 10 K intervals) of the instantaneous desorption rate, thereby allowing us to determine the time and temperature that the desorption rate of each gas is greatest. We perform three types of simulations on each surface, with different surface initialisation, such that we may more easily decompose competing kinetic pathways; we consider the desorption of H_2 gas from H^* pre-covered surfaces, CH_4 gas from CH_3^* and H^* pre-covered surfaces and then CH_4 gas from CH_3^* only pre-covered surfaces. In as many cases as possible, we use experimental data to define the initial surface coverage in our simulations. Using this coverage in monolayers (ML) we perform an isothermal simulation at the experimental temperature of exposure in order to generate an equilibrated lattice whereby the lattice energy is minimised at that coverage. This equilibrium lattice state will serve as the initial configuration for TPR simulations.

Hydrogen Temperature Programmed Desorption

To isolate the kinetics of hydrogen surface diffusion and desorption, we pre-dose each surface with H^* only; it follows that the only elementary events from **Figure 32** that are

realisable in this simulation are H* surface diffusion and H*-H* re-combinative desorption (note the partial pressure of H_{2(g)} is set to zero, preventing dissociative adsorption). We run a constant temperature simulation at temperatures of exposure as given in experiment, such that the adsorbate over layer structure is minimised to its lowest energy configuration at the start of the TPD simulation.

Cu(111) Temperature Programmed Desorption

Our simulated TPD spectrum for H_{2(g)} evolution from Cu(111) is shown in **Figure 40**. Constant temperature simulations were performed using initially Θ_{H*} = 0.4 ML at 190 K as estimated by experiment,²¹⁹ though rapid recombination of 2H* results in a final maximum coverage of 0.33 ML. We use the final lattice state of this isothermal simulation as the initial state of the TPD simulation. We obtain a smooth, bell-shaped TPD trace whereby the peak maximum (corresponding to the fastest rate of desorption) is determined to be 312 K (**Figure 40**). This simulated desorption temperature agrees very well with experimental TPD performed by Anger *et al.*,²¹⁹ who observe a desorption temperature of 310 K when the surface is saturated by high H_{2(g)} exposure at 190 K; this “saturation” corresponds to an estimated coverage of approximately 0.4 ML, compared to 0.33 ML in our simulations.²¹⁹ Excellent agreement of our TPD trace with the experiments of Anger *et al.* at saturation suggests strong reliability for the Cu(111) hydrogen activation mechanism we predict using DFT, whereby two H* adatoms in neighbouring fcc and hcp sites recombine through a bridge site transition state as described in the “Hydrogen Dissociation” section of Chapter 3.

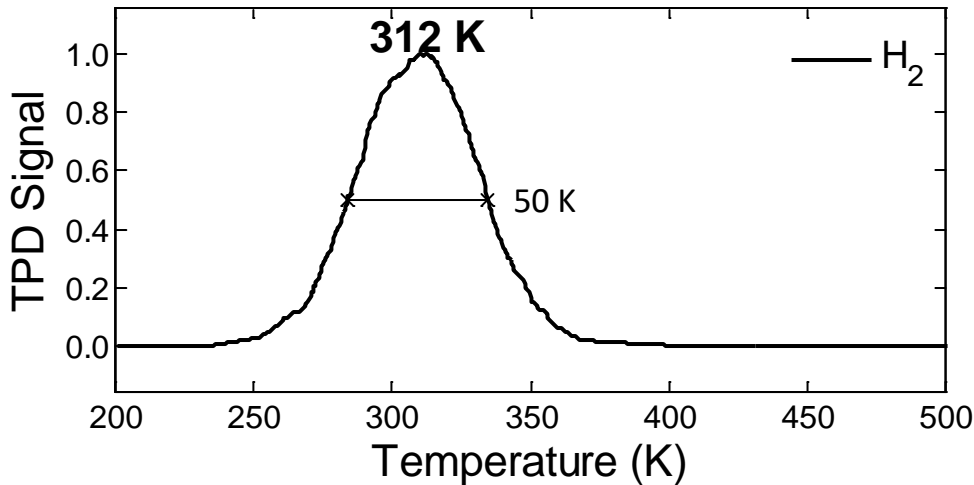


Figure 40: KMC simulated temperature programmed desorption profile for hydrogen on Cu(111). The peak desorption temperature is found to be 310 K with a half-peak maximum width of 51 K.

Pt(111) Temperature Programmed Desorption

On Pt(111), we perform an isothermal simulation at 150 K, which is deemed to be a sufficiently low temperature to saturate the surface with H* at high H_{2(g)} exposure.^{220, 221} Under low temperature conditions, the surface coverage of H* is estimated to be as high as Θ_{H*} = 0.8 ML to 1 ML.^{54, 206, 220-222} Our isothermal simulations suggest that Θ_{H*}(max) is actually 0.90 ML as there is some desorption at 150 K due to lateral interactions between H* adatoms on Pt(111). The smaller repulsive interaction energies on Pt(111) compared to Cu(111) arise due to larger inter-site distances on the former over the latter; consequently Pt(111) can facilitate much higher coverage of H* despite comparable desorption barriers.

We perform the TPD simulation from the Pt(111) lattice covered by Θ_{H*} = 0.9 ML whereby the lattice state energy is minimised by the isothermal simulation at 150 K. The TPD spectrum has a peak desorption temperature of 311 K with a half-peak maximum width of 45 K (**Figure 41**). This peak temperature agrees well with experimental TPD peak temperature from Pt(111) surfaces that are dosed with high H_{2(g)} exposure of 310 K.^{54, 221} The experimental peak is a doublet, whereby a slightly higher temperature peak with lower intensity is observed around 400 K. This peak corresponds to thermal desorption of H* bound to low-coordinate step edges which separate terraces of Pt(111); the step edges constitute 20 % of the total Pt sites.²²¹ We do not account for the step edges here, though a

useful decomposition of the double peak into two separate peaks by Collins *et al.* shows that the low temperature peak is in excellent agreement with our simulated peak.²²¹

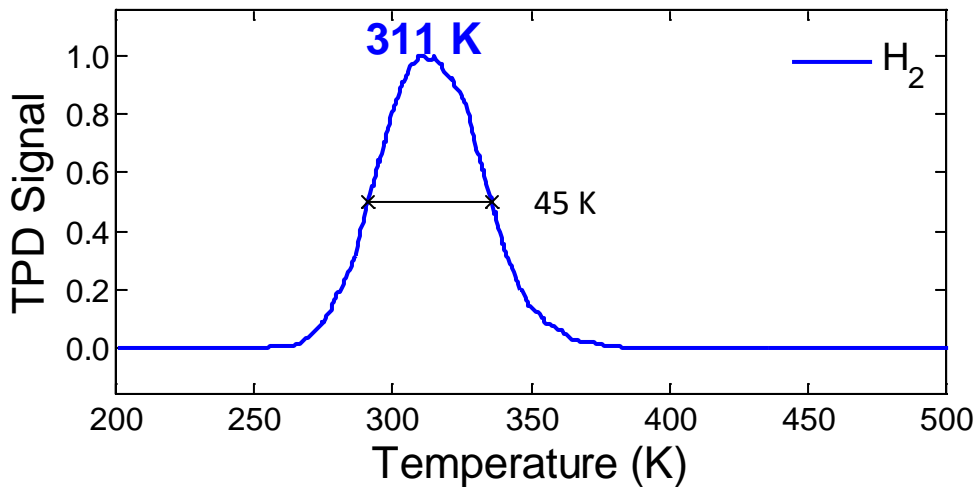


Figure 41: KMC simulated temperature programmed desorption profile for hydrogen on Pt(111). The peak desorption temperature is found to be 311 K with a half-peak maximum width of 45 K.

Pt/Cu(111) SAA Temperature Programmed Desorption

The high multiplicity of Cu sites compared to Pt sites and the facile spillover of H* observed experimentally on Pt/Cu(111) SAA leads us to believe that the surface coverage of H* on Pt/Cu(111) SAA should be approximately the same as for Cu(111), if not slightly higher.^{54, 59, 219} Thus, we initialise a surface with θ_{H^*} of 0.5 ML and perform an isothermal simulation at 150 K. We simulate low temperature desorption, giving a final coverage of $\theta_{H^*}(max) = 0.48$ ML. The isothermal simulation gives the lowest energy lattice configuration at this coverage, which we use to initialise our surface in the simulated TPD.

The equilibrium lattice state at 150 K has 55 % of Pt-Cu hollow sites occupied by H* and 48 % of Cu hollow sites occupied by this species. The majority of Pt atoms are saturated by three surface H* that are ordered symmetrically in three 2nd nearest neighbour Pt-Cu hollow sites surrounding the Pt atom; this is the result of repulsive pairwise lateral interactions. A small number of Pt atoms are surrounded by four surface H* as it more energetically favourable for the lattice to organise into this configuration rather than having all Cu atoms saturated by three H*. Our simulated equilibrium lattice state is in good agreement with low

temperature STM studies of H spillover on SAAs, where $H_{2(g)}$ readily dissociates over the single atom with subsequent facile spillover onto facets of the host metal.^{6, 54, 59, 62, 63}

The simulated TPD trace of $H_{2(g)}$ desorption from Pt/Cu(111) SAA (**Figure 42**) has a comparable bell-shaped curve to that of Cu(111) (**Figure 40**) and Pt(111) (**Figure 41**). However, the peak desorption temperature in the case of Pt/Cu(111) SAA is 218 K, a reduction of 94 K and 93 K from Cu(111) and Pt(111), respectively. Lucci *et al.* performed experimental TPD of $H_{2(g)}$ evolution from Pt/Cu(111) SAA and observe a peak desorption temperature of 230 K from saturation,⁵⁹ validating our calculated hydrogen activation pathway (“Hydrogen Dissociation” section of Chapter 3), associated energies and kinetic constants.

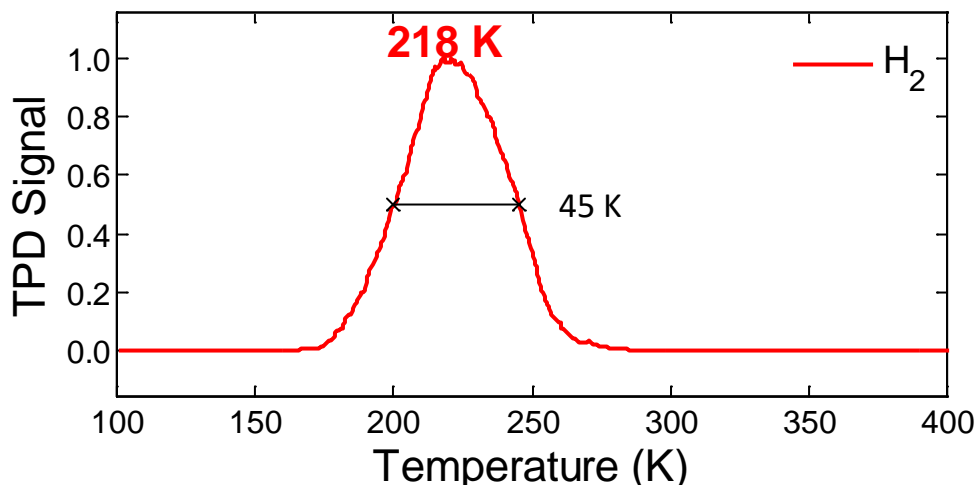


Figure 42: KMC simulated temperature programmed desorption profile for hydrogen on Pt/Cu(111) SAA. The peak desorption temperature is found to be 218 K with a half-peak maximum width of 45 K. It is interesting that the $H_{2(g)}$ desorption trace appears at much lower temperature on Pt/Cu(111) SAA compared to Cu(111) and Pt(111). Analysis of the reaction statistics reveals that all of the desorption events contributing to this peak are H^*-H^* recombinations via single Pt atoms, not from facets of pure Cu(111). The activation energy of H^*-H^* recombination $E_a(des)$ on each surface can be approximated as the difference in energy between the transition state formation energy E_F^{TS} and twice the formation energy of H^* $E_F(H^*)$, such that $E_a(des) = E_F^{TS} - 2 \times E_F(H^*)$. For recombination and desorption from Pt/Cu(111) SAA $E_a(des) = 0.01 \text{ eV} - (-0.58 \text{ eV}) = 0.59 \text{ eV}$. Qualitatively speaking (as we

neglect the effect of the pre-exponential on the kinetic constants), $E_a(\text{des})$ is lower for Pt/Cu(111) SAA compared to Cu(111) (0.93 eV) and Pt(111) (1.04 eV) thereby resulting in a low $\text{H}_{2\text{(g)}}$ desorption peak temperature of 218 K.

Cu(111) and Pt(111) have the similar activation barriers for $\text{H}^*\text{-H}^*$ recombination (0.93 eV and 1.04 eV, respectively) and consequently, similar TPD peak temperatures. Cu(111) binds H^* weakly (-0.25 eV) though has a high $\text{H}_{2\text{(g)}}$ activation barrier (0.42 eV) whereas on Pt(111) $\text{H}_{2\text{(g)}}$ dissociative adsorption is non-activated and H^* is strongly bound (-0.46 eV). Thus, the desorption properties of Pt/Cu(111) SAA are an amalgamation of those of the two surfaces, whereby the $\text{H}_{2\text{(g)}}$ activation barrier is very low yet the adsorption of H^* is also weak. As a result, the $\text{H}^*\text{-H}^*$ recombination barrier is much lower on Pt/Cu(111) SAA compared to both monometallic analogues and consequently we simulate low temperature $\text{H}_{2\text{(g)}}$ desorption from this surface.

Interestingly this is an excellent example of a violation of the Brønsted-Evans-Polanyi relationship, which we discussed in detail in Chapter 3. In several experimental cases, including on Pt/Cu(111) SAA, the hydrogenation activity and selectivity of SAAs has been shown to be dramatically improved over monometallic counterparts, which we attribute to facile hydrogen activation (i.e. non-rate limiting) and weak hydrogen adsorption (i.e. reducing the activation barrier to hydrogenation).^{6, 55-63, 67, 176, 223}

Having validated our calculations on the energetics and kinetics of hydrogen activation on Cu(111), Pt/Cu(111) SAA and Pt(111), we now consider methane dehydrogenation on each surface. We begin with systems whereby both H^* and CH_3^* are co-adsorbed to the lattice; by doing so, we isolate the kinetics of $\text{CH}_{4\text{(g)}}$ desorption without the need for prior activation of C-H bonds. Following this, we consider systems with only CH_3^* adsorbed; that is in order for $\text{CH}_{4\text{(g)}}$ to be evolved from the surface, a C-H bond must be broken in CH_3^* to liberate H^* that can diffuse and react with another CH_3^* species. In each case, we make comparisons to experimental work from the literature. For the Pt/Cu(111) system this experimental work was carried out by Dr. Matthew Marcinkowski under the supervision of Prof. Charles Sykes (Tufts

University) as well as Prof. Maria Flytzani-Stephanopoulos (Tufts University). The results of this collaborative effort (with the author of this thesis having performed the theoretical part of the work) have recently been accepted for publication in *Nature Chemistry*. *Note that the author declares that he has not contributed to this experimental work himself, though is including a summary of the data alongside his own theoretical study to ensure completeness in the arguments he is conveying. For clarity, contributions from others will be shown in italic font.*

Methane Temperature Programmed Reaction from Methyl and Hydrogen

In this section we discuss simulations where we initialise Cu(111), Pt(111) and Pt/Cu(111) SAA with H* and CH₃*; we simulate the desorption of CH_{4(g)} that results from the reaction of these adspecies and attribute variations in the CH_{4(g)} desorption profile to differences in the kinetics and energetics on each surface.

Cu(111) Temperature Programmed Reaction

We initialise the Cu(111) surface with a CH₃* coverage deduced experimentally by Lin *et al.* to be $\Theta_{CH_3^*} = 0.04$ ML; we match the coverage of H* such that $\Theta_{H^*} = 0.04$ ML, giving a 1:1 ratio of CH₃* to H*.²¹² We run a low temperature isothermal simulation (160 K) to find the equilibrium configuration of the lattice and use this as the initial lattice state for a TPR simulation. We observe no recombination of CH₃* and H* on Cu(111) at this temperature.

Simulating TPR from the initial lattice state, we obtain the CH_{4(g)} desorption spectrum shown in **Figure 43**. We simulate a bell-shaped TPR trace with a maximum rate of CH_{4(g)} evolution at 242 K and a half-peak maximum width of 36 K. This desorption peak temperature is in reasonable agreement with TPD experiments²¹² using a ramp rate of 2.5 K·s⁻¹ giving a peak temperature of 280 K (using this faster ramp rate in our simulations broadens the peak and gives the peak maximum at 265 K, though we discuss the 1 K·s⁻¹ trace to retain consistency throughout our simulations on different surface and for different systems).

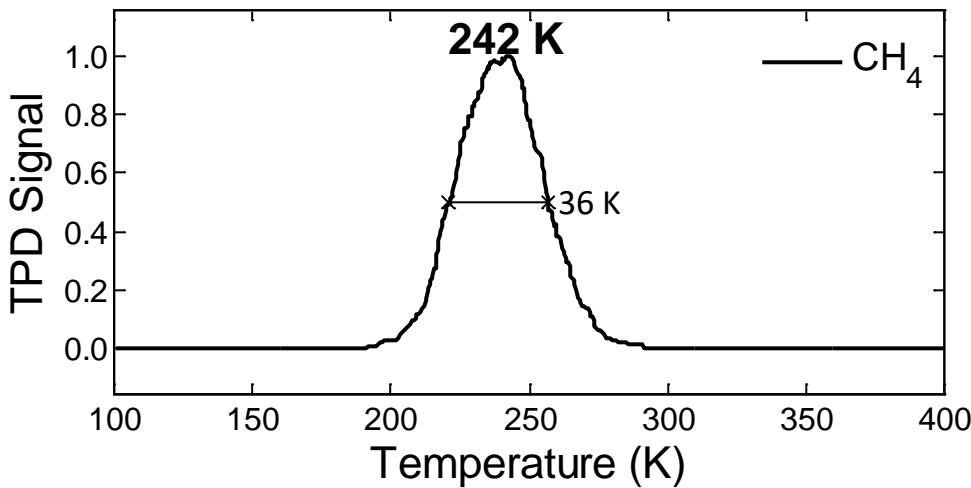


Figure 43: KMC simulated temperature programmed reaction profile for methyl and hydrogen recombination to evolve methane on Cu(111). The peak desorption temperature is found to be 242 K with a half-peak maximum width of 36 K.

Analysis of the KMC reaction statistics shows that $\text{CH}_{4(g)}$ is produced through CH_3^* recombination with H^* without any C-H scission to lower order carbonaceous fragments. As a result, all of the CH_3^* dosed on the surface is converted to $\text{CH}_{4(g)}$. Additionally, we simulate no $\text{H}_{2(g)}$ desorption, despite overlap of the desorption temperature range in H^* only on Cu(111) simulations as shown in **Figure 40**. In addition to the barrier for CH_3^* and H^* recombination being 0.87 eV compared to a slightly larger barrier of 0.93 eV for H^* and H^* recombination, the temperature dependent pre-exponential factor for the former is consistently greater than that of the latter over this temperature range; hence we observe only CH_3^* and H^* recombination for a 1:1 $\Theta_{\text{CH}_3^*}$ to Θ_{H^*} ratio. Additional H^* dosing on the Cu(111) surface (e.g. for $\Theta_{\text{H}^*} = 0.4$ ML) results in no change in the $\text{CH}_{4(g)}$ desorption peak, though a slight increase of 5 K in the $\text{H}_{2(g)}$ peak temperature compared to for H^* only dosing.

Pt(111) Temperature Programmed Reaction

Isothermal simulations on Pt(111) at 100 K show that, as in the case of H^* simulations, this surface can facilitate the adsorption of much greater CH_3^* coverage, without any C-H activation or $\text{CH}_{4(g)}$ evolution. Experimentally, low temperature adsorption of CH_3^* on Pt(111) may be achieved by using bromo- or iodo-methane species which will readily dissociate at 100 K. The dissociated adspecies have a 1:1 ratio and so an experimental coverage of $\Theta_{\text{CH}_3^*} = 0.33$ ML corresponds to a total coverage of 0.66 ML.²²² Alternatively, methyl radicals

produced through azomethane (CH_3NCH_3) pyrolysis may be adsorbed onto the surface at 150 K with a coverage of $\Theta_{\text{CH}_3^*} = 0.45 \text{ ML}$.²⁰⁶ In this case the total surface coverage (accounting for N deposits blocking some of the surface sites) is $\frac{3}{2}\Theta_{\text{CH}_3^*}$ which is approximately the same as when using halomethane.²²²

Performing isothermal simulations with Θ_{H^*} and $\Theta_{\text{CH}_3^*} = 0.33 \text{ ML}$ or 0.45 ML or 0.66 ML , we simulate no desorption or C-H scission events at 150 K, though raising the coverage of each adsorbate to 0.70 ML is sufficient to induce low temperature desorption. Thus, we take the experimental, surface saturation point (in the absence of foreign adspecies) to be more realistically represented using $\Theta_{\text{CH}_3^*} = 0.66 \text{ ML}$ coverage. The importance of correctly estimating the coverage in this case will become more relevant in the discussion of CH_3^* only simulations on Pt(111) in the next sub-section.

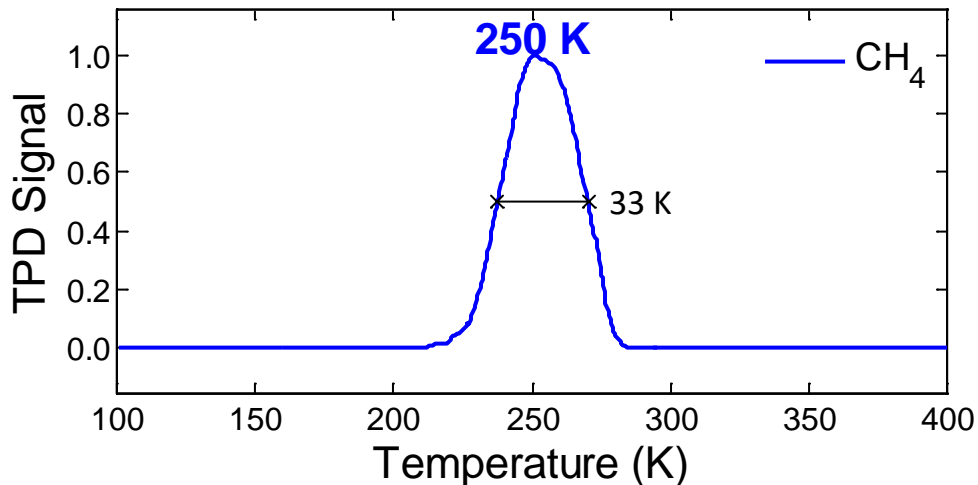


Figure 44: KMC simulated temperature programmed desorption profile for methane from a methyl and hydrogen pre-covered Pt (111) surface. The peak desorption temperature is found to be 250 K with a half-peak maximum width of 33 K.

Using the initial lattice state whereby the coverages of Θ_{H^*} and $\Theta_{\text{CH}_3^*}$ are set to 0.66 ML and a 100 K isothermal simulation is performed to minimise the lattice energy, we simulate the TPR on Pt(111). The desorption trace of $\text{CH}_4(g)$ is shown in **Figure 44** and has a peak temperature of 250 K with a half-peak maximum of 33 K. Notably, our simulation shows that only 31 % of carbon bound to the surface is evolved as methane, despite an initial 1:1 ratio of CH_3^* to H^* .

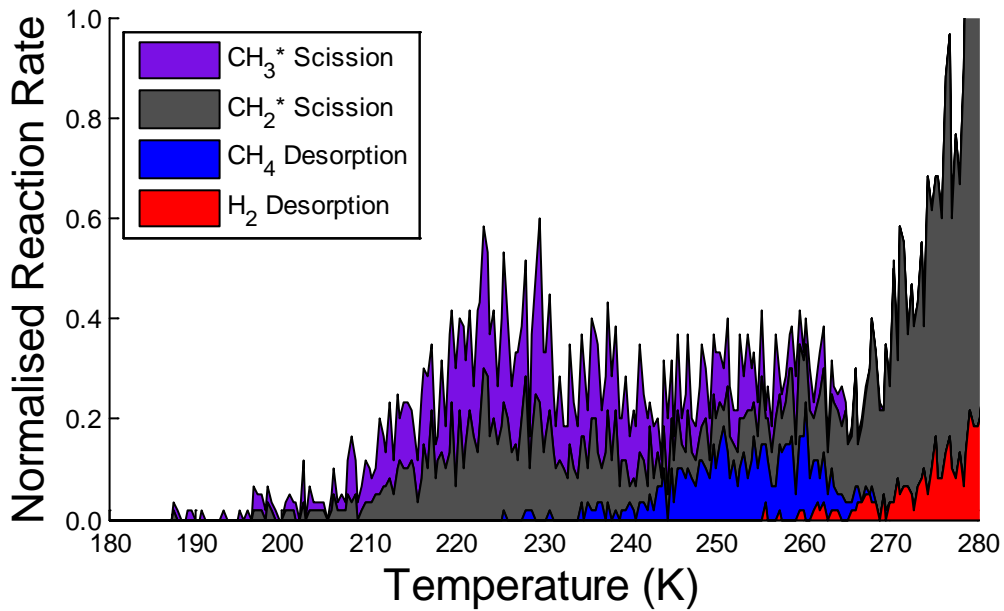


Figure 45: Normalised reaction rates for elementary events occurring between 180 K and 280 K during TPR on Pt(111) after CH_3^* and H^* dosing. Only non-diffusive events that are executed over this temperature range are shown. Also, only the forward reaction of CH_3^* and CH_2^* C-H bond scissions are shown for clarity.

Analysis of the reaction statistics (**Figure 45**) for simulated CH_3^* and H^* TPR on Pt(111) shows that the desorption of $\text{CH}_{4(g)}$ through the recombination of CH_3^* and H^* does not occur until 225 K, much later than C-H bond scissions of CH_3^* and CH_2^* around 186 K. It follows that the desorption of $\text{CH}_{4(g)}$ must either be thermally rate limited or limited by $\theta_{\text{H}*}$. Performing simulations whereby we prevent C-H scission reactions by setting arbitrarily high activation barriers for these processes, we simulate a peak desorption temperature of 253 K; only 3 K higher than in the original simulation. This indicates that desorption of $\text{CH}_{4(g)}$ is limited by the temperature, requiring greater thermal activation than in the case of C-H scission reactions from CH_3^* and CH_2^* .

Additionally the reaction statistics show that CH_2^* scission is rate limited by CH_3^* scission. The former event occurs instantaneously after the formation of the CH_2^* adspecies from CH_3^* ; consequently the lifetime of CH_2^* on the surface is very short and we report zero coverage for this species at all temperatures within the tolerance of our reporting scheme. We do however report high coverage of CH^* , which, at 400 K corresponds to 69 % of carbonaceous species originally dosed on the surface. No C-H scission from CH^* to C^* and

H^* is observed within our simulated temperature range, highlighting the very high energetic barrier of 1.32 eV for this process.

We simulate $H_{2(g)}$ evolution from the surface starting at approximately 255 K, after the rate maximum for $CH_{4(g)}$ desorption. Withdrawal of H^* from the surface drives the scission of C-H bonds and, in addition to unfavourable energetics, further prohibits the hydrogenation of lower order carbonaceous fragments to those with higher orders and indeed, $CH_{4(g)}$. The peak desorption temperature of $H_{2(g)}$ evolved from Pt(111) after CH_3^* and H^* dosing is 312 K, almost identical to the H^* pre-dosed-only analogue shown in **Figure 41**. This is in good agreement with experiments showing that $H_{2(g)}$ desorption from CH_3^* and H^* pre-covered Pt(111) is H^* recombination-limited.²⁰⁶

Pt/Cu(111) SAA Temperature Programmed Desorption

On Pt/Cu(111) SAA, we pre-cover the surface with H^* and CH_3^* where $\Theta_{CH_3^*} = 0.08$ ML (*in line with experimental data, from Dr. Matthew Marcinkowski*) and $\Theta_{H^*} = 0.08$ ML such that the total surface coverage Θ_{Tot} is 0.16 ML; as with the Cu(111) and Pt(111) simulations we match the number of H^* adspecies to that of CH_3^* to ensure no leftover carbonaceous species remain on the surface after $CH_{4(g)}$ desorption. We perform an isothermal simulation at 100 K and observe no desorption or C-H scissions. The adsorbate overlayer is optimised by minimising the lattice energy and is subsequently used as the initial lattice state during TPR simulations on Pt/Cu(111) SAA.

The equilibrated lattice state has 86 % of H^* on facets of Cu(111), with the remaining 14 % in Pt-Cu shared sites; this corresponds to 4 % of Cu hollow sites and 5 % of Pt-Cu shared hollow sites being covered by H^* . 61 % of CH_3^* is found in Cu hollow sites, corresponding to a 3 % of saturation; the remaining 39 % of CH_3^* is adsorbed to Pt top sites, which is equivalent to 84 % of Pt sites being occupied. The high multiplicity of Cu sites compared to Pt or Pt-Cu shared sites is sufficient to ensure a greater absolute number of H^* and CH_3^* reside on facets of pure Cu(111), though the more favourable energetics of adsorption to Pt

sites for both adspecies ensures higher occupation on Pt relative to the number of available sites.

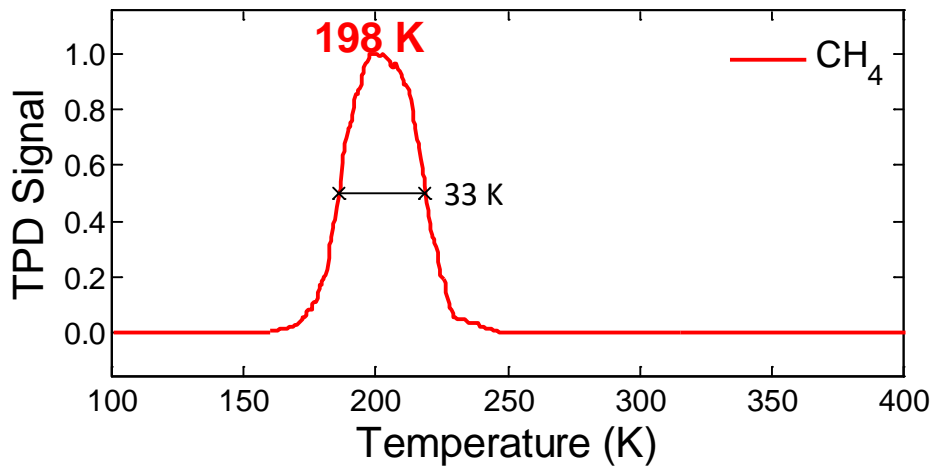


Figure 46: KMC simulated temperature programmed desorption profile for methane from a methyl and hydrogen pre-covered Pt/Cu(111) SAA surface. The peak desorption temperature is found to be 198 K with a half-peak maximum width of 33 K.

Simulating TPR of CH_3^* and H^* on Pt/Cu(111) SAA (using the optimised lattice state at 100 K as the simulation initial state), we observe rapid hydrogenation of CH_3^* to $\text{CH}_4\text{(g)}$. Desorption of $\text{CH}_4\text{(g)}$ occurs with a rate maximum at 198 K and a half-peak width temperature of 33 K (**Figure 46**). Analysis of reaction statistics (**Figure 47**) reveals that the desorption of $\text{CH}_4\text{(g)}$ from Pt/Cu(111) SAA is solely through recombination of CH_3^* and H^* at the single Pt atom as we simulate no desorption of $\text{CH}_4\text{(g)}$ via Cu. Moreover we simulate the conversion yield of pre-dosed CH_3^* to evolved $\text{CH}_4\text{(g)}$ to be 100 % as on Cu, since no C-H scission events are executed, nor any $\text{H}^* \text{H}^*$ recombination events.

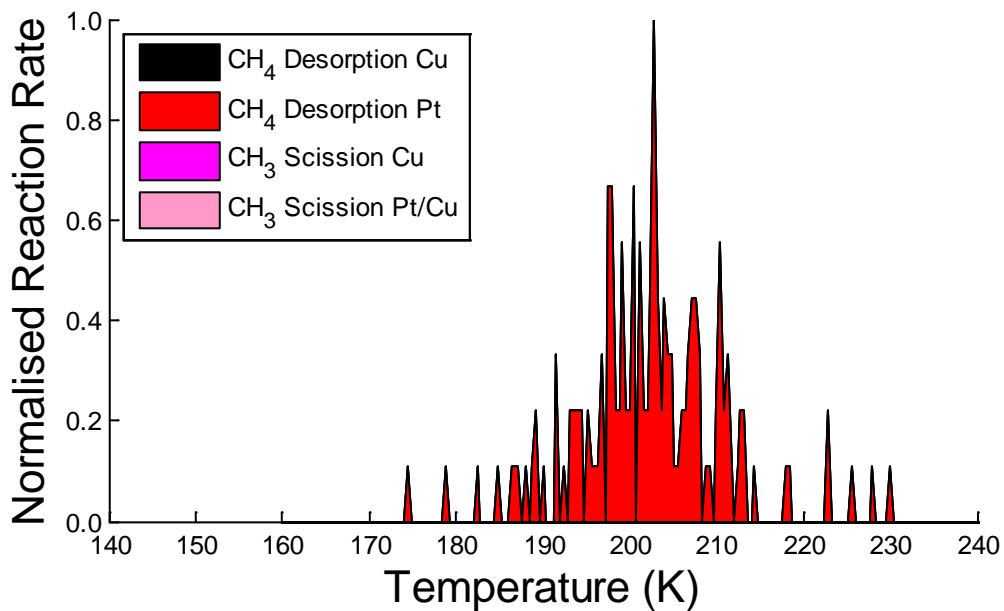


Figure 47: Normalised reaction rates for elementary events occurring between 180 K and 280 K during TPR on Pt/Cu(111) SAA after CH_3^* and H^* dosing. Only non-diffusive events that are executed over this temperature range are shown. In this case, this corresponds to $\text{CH}_4(g)$ desorption via single Pt atoms only; desorption via Cu and CH_3^* scission data is included for clarity, though these all have zero occurrence.

The low temperature recombination of CH_3^* and H^* is another example of an escape from linear scaling relationships as discussed in Chapter 3. We calculated weak adsorption of H^* and CH_3^* on the Pt/Cu(111) SAA surface compared to Pt(111); this weak adsorption is comparable to that on Cu(111). Yet, the Pt single atom in Pt/Cu(111) SAA is capable of stabilising the transition state, thereby lowering the barrier of CH_3^* and H^* recombination in light of their weak binding. The effect of escaping the BEP relationship in this manner is that the Pt/Cu(111) SAA exhibits low $\text{CH}_4(g)$ desorption temperature with high yield, such that no coke is deposited on the surface.

Comparing our simulated TPR with experimental work by Dr. Matthew Marcinkowski, we see that our simulations are in good agreement. *Dr. Marcinkowski examined the direct hydrogenation of methyl groups to methane, by performing experiments in which CH_3I was introduced to a 0.01 ML Pt/Cu SAA that had been pre-covered with H^* at 80 K; dissociative methyl halide adsorption on transition metal surfaces typically proceeds with low activation energy and so is a facile method for adsorbing CH_3^* on the surface. On this hydrogen pre-covered surface, the product $\text{CH}_4(g)$ desorbs at 210 K, well below the temperatures $\text{CH}_4(g)$*

desorbs from either clean Cu(111) (265 K at $2.5 \text{ K}\cdot\text{s}^{-1}$)²¹² or Pt(111) (250 K at $1.5 \text{ K}\cdot\text{s}^{-1}$)²⁰⁶ surface.

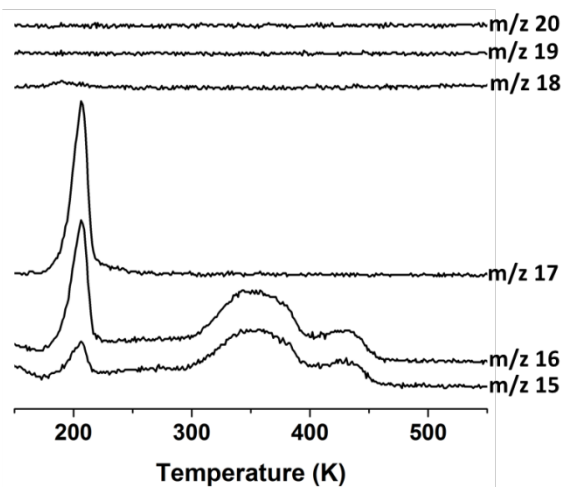


Figure 48: Experimental TPR spectra of possible methane products resulting from the reaction of methyl iodide on a D-pre-covered 0.01 ML Pt/Cu(111) surface. *Image courtesy of Dr. Matthew Marcinkowski, Sykes laboratory, Tufts University.*

Further to this, Dr. Marcinkowski performed an experiment using a deuterium pre-covered Pt/Cu(111) surface to exact whether any C-H scission occurs at such low temperatures. M/z 15 through 20 were tracked to detect $\text{CH}_4(g)$, $\text{CH}_3\text{D}_{(g)}$, $\text{CH}_2\text{D}_2(g)$, $\text{CHD}_3(g)$, and $\text{CD}_4(g)$ (**Figure 48**). Dr. Marcinkowski observed predominately m/z 17 with a large contribution from m/z 16 and a small amount of m/z 15. In other words, if we assign the parent ion as M, we observe M, M-1, and M-2. M/z 16 (M-1) is ~70 % of the signal from m/z 17 while m/z 15 (M-2) is ~20 % of the signal from m/z 17. Normally the primary contributor to CH_4 's cracking pattern is the parent ion m/z 16. According to the US National Institute of Standards and Technology's webbook the cracking pattern for methane, m/z 15 (M-1) and m/z 14 (M-2) both contribute with relative intensities 89 % and 20 % of m/z 16 respectively. Therefore, the cracking pattern observed by Dr. Marcinkowski is in good agreement with the sole desorption product at 210 K being CH_3D . This indicates that the $\text{CH}_4(g)$ results from hydrogenation of the CH_3^* groups, and no C-H activation occurs at this temperature, as predicted by our simulations. The production of methane at low temperature is limited by the saturation of hydrogen on the 0.01 ML Pt/Cu(111) surface, which is 0.1 ML. As the experimental coverage of CH_3^* groups present on the surface is greater than the dosed H^* , some $\text{CH}_4(g)$ desorbing at 350 K is observed and is the result of C-H activation in methyl groups at temperatures above 210 K.

We have ascertained the desorption temperature of $\text{CH}_4\text{(g)}$ as a result of CH_3^* and H^* recombination and noted that no C-H activation occurs on Cu(111) and Pt/Cu(111) SAA prior to $\text{CH}_4\text{(g)}$ evolution. This is not the case on Pt(111) and we simulate notable C-H activation on this surface, such that only 31 % of $\text{CH}_4\text{(g)}$ desorbs from all available CH_3^* used in the pre-dosing. The temperature of desorption from Pt/Cu(111) SAA is lower than both Cu(111) and Pt(111), another example of an escape from monometallic linear scaling relationships whereby weak binding of adsorbates is combined with low activation energy.

In the next section, we impose a rate limit on the evolution of $\text{CH}_4\text{(g)}$ by initialising each surface with CH_3^* only. In the absence of pre-dosed H^* , CH_3^* must first dehydrogenate in order for H^* to recombine CH_3^* and $\text{CH}_4\text{(g)}$ to be desorbed. We will analyse the effects of this rate limit on each surface by studying the TPR spectra and reaction statistics before comparing to experimental work.

Methane Temperature Programmed Reaction from Methyl Only

In this section we initialise simulations with CH_3^* as the only adsorbate on Cu(111), Pt/Cu(111) SAA and Pt(111). We determine the $\text{CH}_4\text{(g)}$ desorption temperature and evaluate the extent to which dehydrogenation occurs on the different surfaces. In the absence of H^* , C-H activation must take place in CH_3^* in order for $\text{CH}_4\text{(g)}$ to be evolved. For each surface, we run a low temperature, isothermal simulation to determine the lowest energy lattice configuration to be used as the start of thermal desorption simulations. We proceed to ramp up the temperature and determine the rate of gas evolution from the surface as a function of time. We analyse the reaction statistics highlighting any rate-limiting steps and the preferred modes of C-H scission and gas desorption on each surface. Finally, we make comparisons with experimental data.

Cu(111) Temperature Programmed Reaction

On Cu(111) we set the coverage of CH_3^* to be $\theta_{\text{CH}_3^*} = 0.04 \text{ ML}$. We perform an isothermal simulation at 200 K with diffusions as the only events permitted (no desorption or C-H scission), and thus find the optimal distribution of CH_3^* on the lattice.

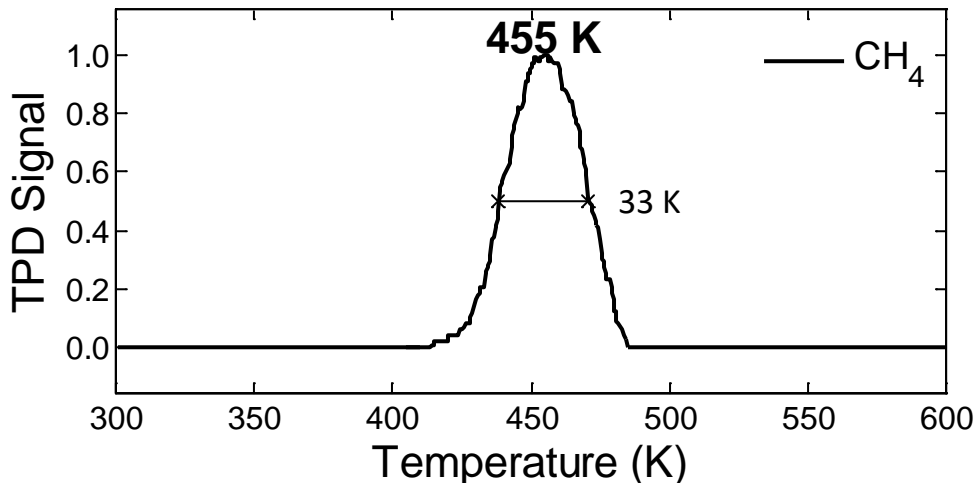


Figure 49: KMC simulated temperature programmed desorption profile for methane from a methyl pre-covered Cu (111) surface. The peak desorption temperature is found to be 455 K with a half-peak maximum width of 33 K.

Performing TPR simulations on Cu(111) from the initial configuration determined by the 200 K isothermal simulation, we show that $\text{CH}_4^{(\text{g})}$ evolution has a rate maximum at 455 K with a half-peak maximum width of 33 K(**Figure 49**). Experimentally, the desorption peak is 450 K, to which our simulations are in excellent agreement.²¹² This desorption temperature is much greater than that for the simulations where the lattice is initialised with H^* as well as CH_3^* (**Figure 43**), because the evolution of $\text{CH}_4^{(\text{g})}$ is actually rate limited by the scission of C-H bonds in CH_3^* . Further analysis of the reaction statistics (**Figure 50**) reveals that this rate limitation is more accurately expressed in terms of the coverage of H^* θ_{H^*} ; that is, there is no immediate recombination of CH_3^* and H^* at the onset of C-H scission from CH_3^* . In fact, the desorption of $\text{CH}_4^{(\text{g})}$ does not begin until over 30 K after the C-H bonds begin breaking in CH_3^* and actually coincides with the onset of CH_2^* C-H scission.

Briefly re-visiting the activation barriers for C-H scission and recombination; we recall that on Cu(111) C-H scission from CH_3^* and CH_2^* have activation barriers of 1.42 eV and 0.96 eV, respectively whereas the recombination barriers for the reverse reactions are 0.64 eV and

0.56 eV (**Figure 39**). It follows that the recombination, post-dissociation of these fragments is much faster than the scissions themselves. Moreover, the recombination barrier for H^* and CH_3^* to produce CH_4 (g) is 0.87 eV.

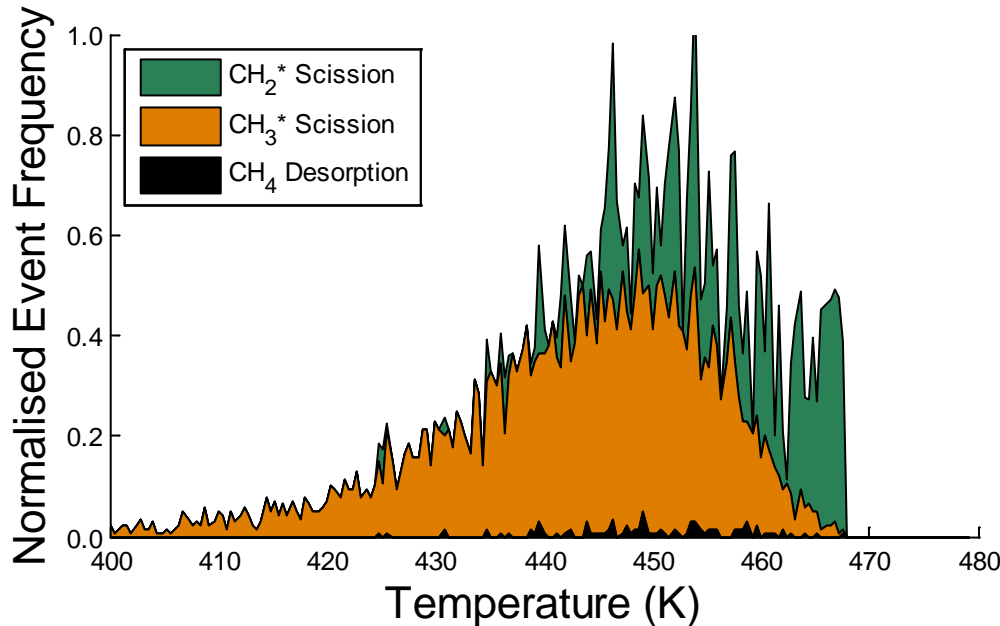


Figure 50: Normalised event frequencies for elementary events occurring between 400 K and 480 K during TPR on Cu(111) after dosing with CH_3^* only. The desorption of CH_4 (g) (black) and any non-diffusive events that are executed over this temperature range are shown. Also, only the forward reaction of CH_3^* (orange) and CH_2^* (green) C-H bond scissions are shown for clarity.

The very fast rate of H^* recombination with CH_2^* and CH^* on Cu(111) compared to C-H scission from CH_3^* and CH_2^* prevents a build-up of $\Theta_{\text{H}*}$ which directly affects the rate of CH_4 (g) desorption. The greater barrier for CH_4 (g) desorption ensures that at low $\Theta_{\text{H}*}$, recombination to CH_3^* and CH_2^* is the preferred process. We simulate an abrupt end to the TPR trace just below 470 K where all of the liberated H^* has recombined with CH_3^* groups and there is no other source of H^* on the surface except for CH^* adspecies; this temperature is not sufficient to overcome the 1.97 eV activation barrier for C-H scission in CH^* . The CH^* remaining on the surface here is exactly 1/3 of the total carbon initialised onto the surface and only remains due to no further C-H scission events happening and subsequently no more H^* being produced.

Experimentally, no carbonaceous species are detected on the surface of Cu(111) after TPR,²¹² however ethane, ethylene and propylene are evolved as gas phase products around

450 K. We do not account for such C-C coupling reactions that are required to form C_2 and C_3 species, therefore we simulate small deposits of CH^* left on the surface.

Pt(111) Temperature Programmed Reaction

Continuing our investigations for Pt, we initialise a Pt(111) lattice with $\Theta_{CH_3^*} = 0.66$ ML and perform an isothermal simulation at 100 K. At this low temperature, we simulate diffusions only, no desorption of $CH_4(g)$ nor any C-H scission events. Using the optimised lattice configuration as the initial state, we perform a TPR simulation and monitor the evolution of $CH_4(g)$ (**Figure 51**). The simulated TPR trace for $CH_4(g)$ on Pt(111) has a peak desorption temperature at 246 K which is in good agreement with the experimental desorption temperature of 250 K,²⁰⁶ and a half-peak maximum width of 34 K. The trace is very similar to that in **Figure 44** for the TPR or $CH_4(g)$ from Pt(111) after pre-dosing with CH_3^* and H^* .

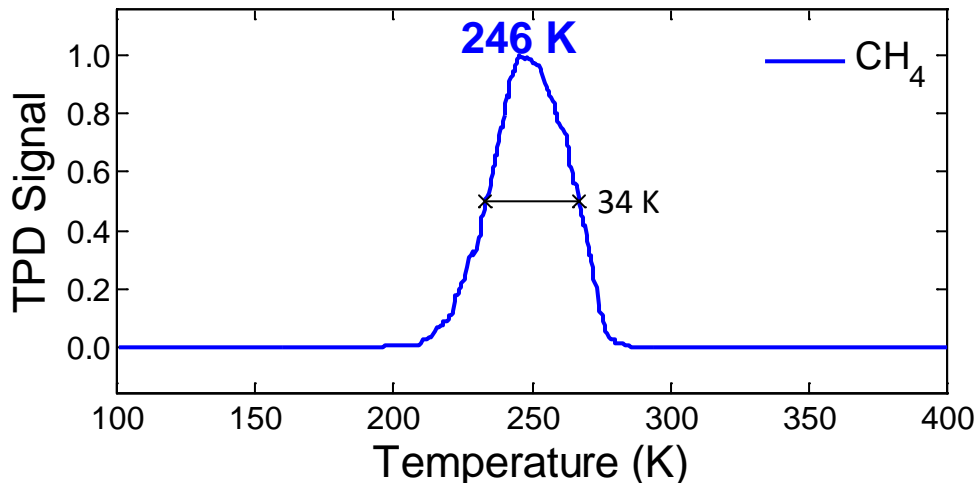


Figure 51: KMC simulated temperature programmed desorption profile for methane from a methyl pre-covered Pt (111) surface. The peak desorption temperature is found to be 246 K with a half-peak maximum width of 34 K.

Looking more closely at the reaction statistics (**Figure 52**) we can see that there are some quantitative differences in the elementary event execution between the CH_3^* only dosed Pt(111) TPR and that with CH_3^* and H^* . Notably, the C-H scissions of CH_3^* and CH_2^* occur at the same temperatures with comparable event frequencies to the previous system (**Figure 45**). However, the frequency of $CH_4(g)$ desorption is much lower though is spread across a similar temperature range. The lower frequency of $CH_4(g)$ desorption compared to that in the CH_3^* and H^* pre-dosed TPR, can be solely attributed to the low Θ_{H^*} and results in

91 % of the carbonaceous species dosed on the surface remaining as carbon deposits until high temperatures are reached, instead of desorbing. In particular, with an initial 1:1 ratio of CH_3^* to H^* on Pt(111), 69 % is deposited. This reiterates the fact that Pt catalysts, though excellent at activating C-H bonds, are very prone to coke formation that may require intense heating or exposure to $\text{H}_{2(g)}$ to fix this.^{206, 222, 224}

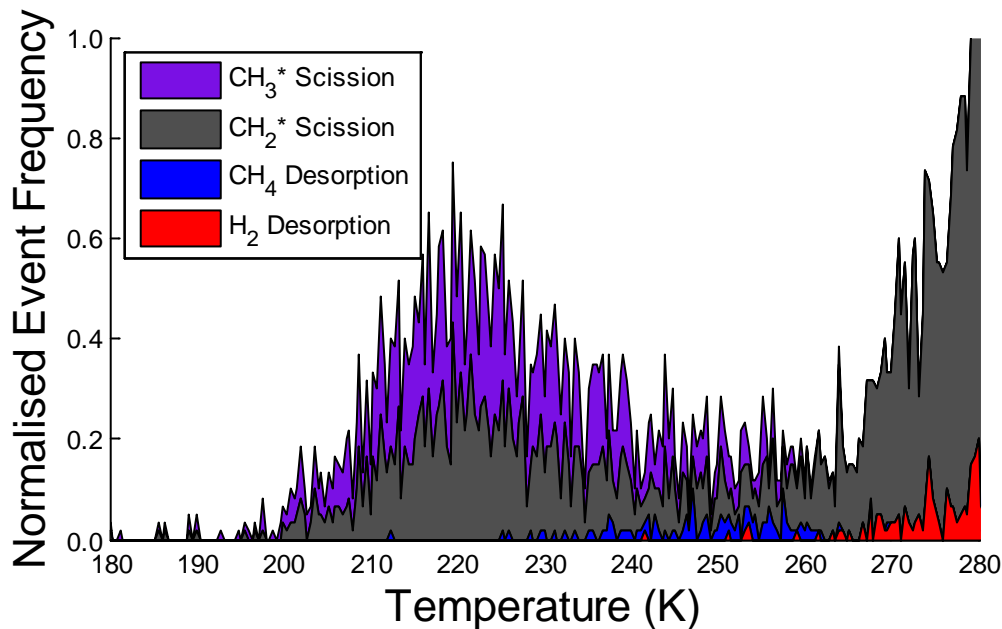


Figure 52: Normalised event frequency for elementary events occurring between 180 K and 280 K during TPR on Pt(111) after dosing with CH_3^* only. Only non-diffusive events that are executed over this temperature range are shown. Also, only the forward reaction of CH_3^* and CH_2^* C-H bond scissions are shown for clarity, though the forward and reverse rates are quasi-equilibrated after adjustment for desorbing CH_4 fragments is accounted for.

The surface coverage of H^* Θ_{H^*} increases dramatically around 270 K and is coincident with a sharp increase in the rate of CH_2^* C-H scission as well as the tail of the $\text{CH}_{4(g)}$ desorption (**Figure 52**). Once sufficient Θ_{H^*} has accumulated, desorption of $\text{H}_{2(g)}$ becomes prominent and has a peak temperature of 315 K, slightly higher than for H^* only simulations (**Figure 41**). The desorption of $\text{H}_{2(g)}$ further promotes coke formation by removing H^* from the system, leaving a high coverage of CH^* .

In the previous sub-section, we mentioned the importance of including the coverage of other adspecies (e.g. iodine from CH_3I) in the total surface coverage on Pt(111). Experimentally, iodine atoms are spectators with the main effect of iodine being a site blocker; the

temperature of C-H activation is relatively unaffected across a range of iodine coverages.²²⁵

226

In order to observe any desorption of $\text{CH}_4\text{(g)}$ on Pt(111) we must use the surface saturation coverage of CH_3^* ; otherwise, the rate and extent to which the exothermic dehydrogenation proceeds are both too great so that no CH_3^* recombination occurs in our simulations. Even by using this high initial coverage, very little $\text{CH}_4\text{(g)}$ is desorbed and instead there remains a coverage of CH^* on the surface that is 91 % of the initial CH_3^* dosing. The dissociated H^* that does not recombine with CH_3^* is desorbed as $\text{H}_2\text{(g)}$. The good agreement of our simulations with experiment when matching the coverage of CH_3^* to the total experimental coverage (i.e. including “site blocking by iodine) promotes the validity of this argument.

Pt/Cu(111) SAA Temperature Programmed Reaction

Focusing on the Pt/Cu SAA, we perform an isothermal simulation at 200 K of CH_3^* dosed on the Pt/Cu(111) SAA lattice; the initial coverage of CH_3^* $\Theta_{\text{CH}_3^*}$ is set as 0.08 ML in line with experimental work by *Dr. Matthew Marcinkowski* (see later in this sub-section for details). At 200 K we observe no C-H scissions and as a result, no desorption of any gaseous species. The optimised lattice state has 47 % of all CH_3^* on Pt top sites with the remaining 53 % on pure Cu hollow sites. Such a distribution corresponds to 100 % saturation of CH_3^* on available Pt sites, compared to just 2 % of all Cu hollow sites. This is a direct result of the formation energy difference of 0.24 eV between the CH_3^* adsorbed state on the Pt top site versus the Cu hollow site.

Using the lattice configuration optimised at 200 K as the initial lattice state, we simulate TPR of CH_3^* pre-covered Pt/Cu(111) SAA (**Figure 53**). Our simulated desorption trace for $\text{CH}_4\text{(g)}$ has a peak temperature of 331 K and a half-peak maximum width of 38 K. We simulate no evolution of $\text{H}_2\text{(g)}$ over this temperature range.

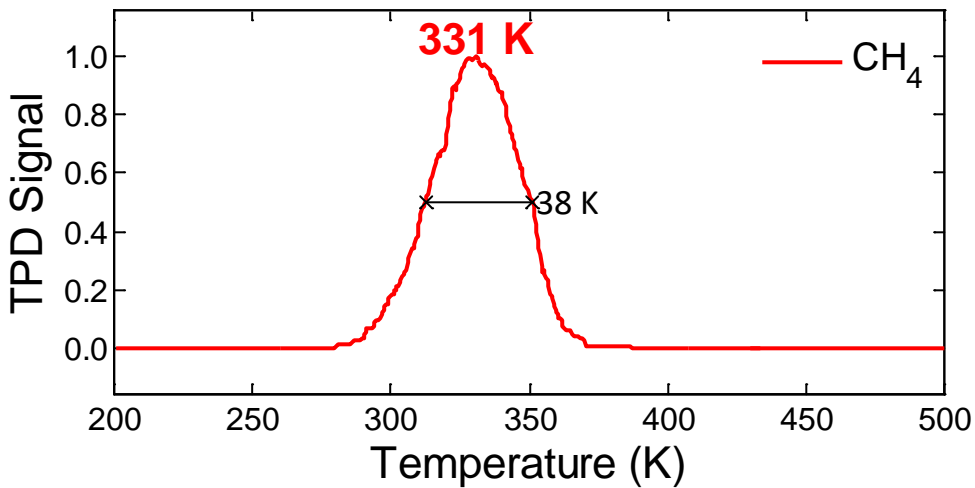


Figure 53: KMC simulated temperature programmed desorption profile for methane from a methyl pre-covered Pt/Cu (111) SAA surface. The peak desorption temperature is found to be 331 K with a half-peak maximum width of 38 K.

Further analysis of the simulation results shows that $\text{CH}_4\text{(g)}$ desorption is rate limited by the availability of surface H^* , as in the case of Cu(111). Pre-dosing with CH_3^* only ensures that the only way to increase $\Theta_{\text{H}*}$ is to perform C-H scission reactions. The onset of C-H scission from CH_3^* is as low as 270 K, though $\text{CH}_4\text{(g)}$ does not begin until 295 K. At 295 K we simulate the onset of C-H scission in CH_2^* ; this helps to increase $\Theta_{\text{H}*}$ such that H^* may recombine with CH_3^* .

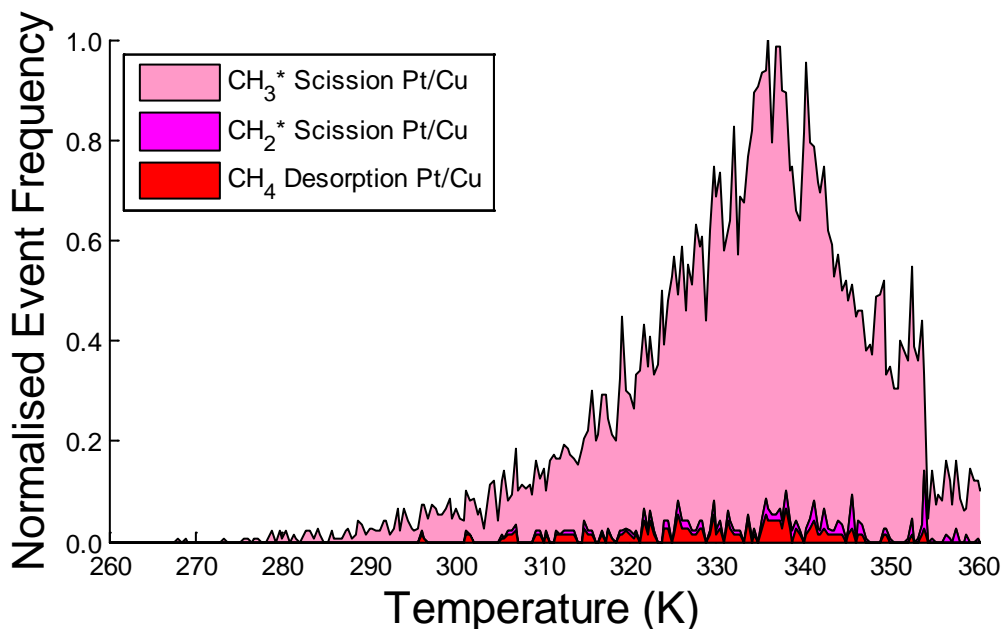


Figure 54: Normalised event frequency for elementary events occurring between 180 K and 280 K during TPR on Pt(111) after dosing with CH_3^* only. Only non-diffusive events that are executed over this temperature range are shown. Also, only the forward reaction of CH_3^* and CH_2^* C-H bond scissions are shown for clarity.

The yield of pre-dosed CH_3^* that are converted to molecules of CH_4 (g) is 66 %, identical to the yield for the analogous simulation on Cu(111). This conversion yield is 2/3 of the initial CH_3^* surface dose and is so because there are no more H^* sources without dehydrogenating CH^* which has a high activation energy (1.64 eV). On the other hand, our simulations on pure Pt(111) gave a desorption yield of just 9 %. The exothermicity of the dehydrogenation pathway in conjunction with the high hydrogenation kinetic barriers on Pt(111) promote coke formation whereas on Cu(111) and Pt/Cu(111), the endothermicity of the dehydrogenation pathway and the low hydrogenation kinetic barriers prevent carbon deposition.

It is evident from the low temperature of CH_4 (g) desorption on Pt/Cu(111) SAA compared to Cu(111), that isolated dopant Pt atoms have a marked effect on the C-H activation temperature. The C-H bond activation temperature for CH_3^* scission (i.e. the thermal onset of this process) is reduced by approximately 130 K on Pt/Cu(111) SAA compared to Cu(111); the corresponding temperature for Pt(111) is 100 K lower than that on the Pt/Cu(111) SAA.

By employing the Pt/Cu(111) SAA surface we have shown that during TPR we can combine low temperature C-H activation with excellent coke resistance. As we have discussed in the CH_3^* and H^* , as well as the H^* only TPR simulations, this is another example of an escape from the BEP relationship. The activation barrier for C-H bond scissions on Pt/Cu(111) SAA is lowered from that on Cu(111) to values more comparable to Pt(111). However, the weak binding of adsorbates ensures the overall dehydrogenation pathway is endothermic on Pt/Cu(111) SAA such that the hydrogenation barriers are low. This combination of weak binding and low activation energy conflicts with the “universality” of the BEP relationship (Chapter 3) and provides scope for the design of materials such as Pt/Cu(111) SAA that exhibit enhanced activity and selectivity.

Finally comparing our TPR simulations of CH_3^* only dosed Pt/Cu(111) SAA with experiment, we again refer to as yet unpublished work by Dr. Matthew Marcinkowski (Tufts University,

USA). That work is an experimental counterpart of the simulations we have performed here. The findings are briefly summarised below.

TPR spectra resulting from the reaction of 4.5 Langmuirs ($1 \text{ L} = 1 \times 10^{-6} \text{ Torr}\cdot\text{s}$) of CH_3I on 0.01 monolayers (ML) Pt/Cu(111) SAA are presented in Figure 55. The major desorption product from 0.1 ML Pt/Cu(111) SAA is $\text{CH}_{4(g)}$ with m/z of 15 and 16. Other higher order hydrocarbons including ethylene, ethane, and propylene are also observed with m/z of 27, 30 and 41, respectively. Desorption of intact CH_3I is not detected at these exposures. Desorption of these C_2 and C_3 products is reaction rate limited as small hydrocarbons normally desorb from Cu(111) at very low temperatures.²¹⁰⁻²¹²

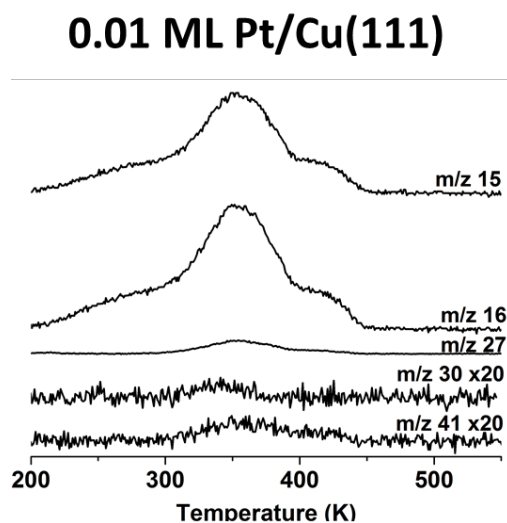


Figure 55: TPR traces for all desorption products observed following 4.5 L exposure of methyl iodide on both 0.01 ML Pt./Cu(111). m/z indicates the mass-to-charge ratio of fragments detected by mass spectrometry.

On the SAA surface, methane and carbon coupling products desorb at ~350 K, 100 K cooler than on the pure Cu(111) surface; this is in excellent agreement with the simulated TPR data we presented here. Because the rate limiting step in methane evolution is C-H activation, this 100 K temperature shift reveals that single Pt atoms in the Cu surface significantly lower the barrier to C-H activation in CH_3^ ; our theoretical analysis shows this is indeed correct. Experiments adding deuterium to the surfaces verified that C-H activation was still the rate limiting step on the SAA. The formation of ethene, ethane and propene implies the 0.1 ML Pt/Cu(111) SAA maintains the ability of Cu to avoid coking via C-C coupling. The coupling of*

C-C products is not accounted for in our model, though we simulate the maximum possible yield of $\text{CH}_4\text{(g)}$ desorption that leave small amounts of CH^ behind on the surface that can participate in C-C coupling.*

No hydrogen desorbs from Cu(111) or the 0.1 ML Pt/Cu(111) SAA surfaces during CH_3l dosed TPR confirming their resistance to coking and agreeing with our simulations.

Changing the alloy surface composition by increasing the Pt loading from to 0.01 ML and 1 ML Pt, reveals that generally as the amount of Pt increases the temperature of C-H activation drops, but so does the production of coupling products. The TPR profiles begin to converge to that of pure Pt(111) with Pt loading, soon after the SAA phase; in fact with ML or greater Pt loading on Cu(111) the TPR spectra from these alloys are identical to that of Pt(111). This demonstrates the importance of the SAA structure in maintaining coke resistance.

Conclusion

We simulated TPR profiles and desorption peak temperatures with high accuracy as compared to experimental work and have provided insight into the energetics and kinetics of C-H bond scissions in methane derivatives. Our calculations showed that the activation energy for C-H bond scissions on Cu(111) may be significantly lowered by the incorporation of just a single Pt atom into the surface later of the material, such that the resulting Pt/Cu(111) SAA has C-H activation properties akin to pure Pt(111). However, we also show that dilution of the single Pt atom in Cu(111) reduces the chemisorption strength of C_xH_y species compared to pure Pt(111), such that successive C-H scissions from $\text{CH}_4\text{(g)}$ are endothermic on Pt/Cu(111) SAA. This endothermicity helps to prevent the formation of carbon deposits on the surface and in fact, shows coke resistance that is of the same degree as with pure Cu(111). We have briefly discussed that the combination of coke resistance and good C-H scission activity is a violation of the BEP relationship discussed extensively in Chapter 3.

In the next chapter, we consider the structural properties of SAAs in an attempt to ascertain their stability under realistic catalytic conditions. We use DFT and KMC to evaluate the tolerance of a variety of SAAs to CO poisoning, their thermodynamic structural stability and how the chemisorption of CO may impact upon this.

Chapter 5 Carbon Monoxide Poisoning Resistance and Structural Stability of Single Atom Alloys

Platinum group metals (PGMs) serve as highly active catalysts in a variety of heterogeneous chemical processes. Unfortunately, their high activity is accompanied by a high affinity for CO and thus, PGMs are susceptible to poisoning. Alloying PGMs with metals exhibiting lower affinity to CO could be an effective strategy toward preventing such poisoning. In this work, we use density functional theory to demonstrate this strategy, focusing on highly dilute alloys of PGMs (Pd, Pt, Rh, Ir and Ni) with poison resistant coinage metal hosts (Cu, Ag, Au), such that individual PGM atoms are dispersed at the atomic limit forming Single Atom Alloys (SAAs). We show that compared to the pure metals, CO exhibits lower binding strength on the majority of SAAs studied, and we use kinetic Monte Carlo simulation to simulate relevant temperature programmed desorption spectra, which are found to be in good agreement with experiments. Additionally, we consider the effects of CO adsorption on the structure of SAAs. We calculate segregation energies which are indicative of the stability of dopant atoms in the bulk compared to the surface layer, as well as aggregation energies to determine the stability of isolated surface dopant atoms compared to dimer and trimer configurations. Our calculations reveal that CO adsorption induces dopant atom segregation into the surface layer for all SAAs considered here, whereas aggregation and island formation may be promoted or inhibited depending on alloy constitution and CO coverage. This observation suggests the possibility of controlling ensemble effects in novel catalyst architectures through CO-induced aggregation and kinetic trapping.

Introduction

The platinum group metals (PGMs), including Pd, Pt, Rh and Ir as well Ni, are well-known for their excellent activity in a wide variety of heterogeneous catalytic systems; however these metals suffer from CO poisoning as a consequence of their high reactivity.²²⁷⁻²²⁹ In order to prevent CO poisoning, one has to promote the desorption of CO, for instance by operating at elevated temperatures.²³⁰ Not only are high reaction temperatures expensive to employ, but then due to the exothermic nature of adsorption, this would result in low coverages for other important reactants, resulting in hampered activity. In addition, the risk of deactivation due to sintering is increased, particularly with supported catalysts. Another strategy that has proven useful for circumventing poisoning (whilst retaining reasonable activity) has been to alloy less reactive metals such as Cu, Ag and Au, with the PGMs; these coinage metals exhibit high tolerance to poisoning, albeit typically having reduced catalytic activity.²³¹⁻²³⁶ Generally, alloying in this manner quenches the affinity of the PGMs to CO, though it may also inhibit their activity.²³¹⁻²³⁶

In several cases it has been shown that by doping the coinage metals with PGMs at very low molar fractions, such that these more reactive metals disperse as isolated single atoms in the surface layer of the host material, the activity of the coinage metal surface can be dramatically enhanced whilst retaining excellent reaction selectivity.^{6, 55-63, 65, 66, 174, 237} These *Single Atom Alloys* (SAAs) of Sykes and co-workers exhibit tolerance to CO⁵⁶ and have been employed to catalyse hydrogenation,^{6, 56, 59, 62, 174} dehydrogenation,^{55, 57} C-H activation and hydrosilylation⁶⁸ reactions with high activity and selectivity, as extended model surfaces and/or as real catalyst nanoparticles.

Temperature programmed desorption (TPD) of CO from Pt/Cu(111) SAA model surfaces revealed that CO desorbs at 350 K from this SAA compared to 450 K from pure Pt(111), indicating weak binding of CO.⁵⁶ Under micro-reactor conditions, it was shown that in the presence of 200 ppm CO (a typical industrial concentration in H₂ streams) the activity of Pt/Cu SAA nanoparticle catalysts for acetylene hydrogenation is reduced 2-fold, however

when compared to monometallic Pt nanoparticles there was a 15-fold activity decrease.⁵⁶ It follows that the weak binding of CO to single, isolated Pt atoms in Pt/Cu SAAs compared to that on pure Pt is sufficient to give this material notable resistance to CO poisoning, despite a relatively low number of active sites compared to monometallic Pt.⁵⁶

It is with this in mind that we carry out a detailed theoretical study of the effects of CO on an assortment of SAAs comprising single atoms of Ni, Pd, Pt, Rh and Ir doped into Ag(111), Au(111) and Cu(111) surfaces. We perform atomistic calculations using density functional theory (DFT) that are then used to parameterize temperature programmed desorption (TPD) simulations using kinetic Monte Carlo (KMC). Thus, we are able to determine the strength of the interaction of CO and its relation to temperature of desorption from this set of candidate SAAs, with the aim of identifying materials that may exhibit good resistance to CO poisoning.

Additionally, we recognize that the presence of adsorbates may induce structural changes in binary alloy materials, such as segregation of atoms from the bulk into the surface layer, as well as promoting aggregation and island formation.^{176, 238-245} Such changes are caused by differences in adsorption behaviour between an adsorbate on each metallic component of the alloy; these differences can offset or increase the energy change upon restructuring of the material. Thus, we perform calculations to determine the segregation and aggregation energies of PGM dopant atoms in highly dilute binary alloys in the absence and presence of CO, allowing us to gauge the stability of SAA materials.

The rest of the paper is organised as follows: we first present the setup of the DFT and KMC calculations in section “Computational Details”, continuing with our “Results and Discussion” where we explore the interactions of CO with SAAs, in the context of poisoning resistance and adsorbate-induced structural changes. We finally summarise our findings and lessons learned in the “Conclusions” section. Our study should provide a valuable guide for the choice of catalytically active and selective binary alloy combinations that exhibit improved CO tolerance and structural stability.

Computational Details

Density Functional Theory Setup

We perform periodic density functional theory calculations using the Vienna *ab initio* Simulation Package (VASP) version 5.4.1.¹⁷⁷⁻¹⁷⁹ with the projector augmented wave (PAW) method to model core ionic potentials^{111, 180} and the revised Perdew-Burke-Ernzerhof (RPBE) exchange-correlation functional.^{97, 246} RPBE is chosen in this instance as it was specifically designed to overcome issues of over-binding using other xc-functionals and is proven to give CO adsorption energies that are close to those from experiment.^{97, 246} We use a $3 \times 3 \times 5$ slab unit cell whereby we fully relax the top-most four layers while we fix the bottom-most layer at the RPBE bulk FCC lattice constant of the corresponding metal (for SAAs, we use the host material lattice parameters). A vacuum region with thickness of 10 Å separates periodic images in the z-direction. We model exclusively the (111) surface of all materials as this is the surface with the lowest surface free energy for the each host metal in this study.²⁴⁷ For binary surface alloy calculations, we replace one, two or three surface host atoms with dopant atoms. For calculations where the dopant is in the bulk, we replace a single atom in the 3rd layer of the unit cell with a dopant atom. We use a $13 \times 13 \times 1$ Monkhorst-Pack k-point mesh to sample the Brillouin zone and the planewave kinetic energy cutoff is set to 400 eV. The Methfessel-Paxton smearing width is set to 0.1 eV. We ensure electronic self-consistency up to a tolerance of 10^{-7} eV and during ionic relaxation, we perform minimization of the Hellmann-Feynman forces on free atoms to within a tolerance of 10^{-2} eV·Å⁻¹. We present adsorption energies $E_{ads}(mCO)$, relative to m gas phase CO molecules such that

$$E_{ads}(mCO) = E_{Tot}^{mCO+slab} - E_{Tot}^{slab} - m \cdot E_{Tot}^{CO(g)}, \quad (94)$$

where $E_{Tot}^{mCO+slab}$, E_{Tot}^{slab} and $E_{Tot}^{CO(g)}$ are the DFT total energies of m CO molecules adsorbed on a slab, the clean slab and gas phase CO, respectively. Thus, negative $E_{ads}(mCO)$ means exothermic adsorption. All adsorption configurations of m CO with distinct geometries are given in the supporting information; those with comparable geometries are also noted here.

Kinetic Monte Carlo Setup

We perform simulations within the graph-theoretical KMC framework as implemented in *Zacros*, version 1.02.^{140, 143, 151} We ramp the simulation temperature at a rate of 1 K·s⁻¹ to simulate TPD. The partial pressure of gas phase CO is set to zero in order to reproduce ultra-high vacuum conditions. The simulation cells consist of (30 × 31) rectangular unit cells with 6-fold symmetry. Simulations on SAAs use lattices where host metal sites have been randomly substituted with dopant metal sites giving a final dopant atom percentage density of approximately 1 %. We initialize the surface with only dopant sites covered entirely by CO adsorbates (1:1 dopant:CO coverage), since in these materials CO binds significantly more strongly on the dopant, compared to the host sites. We do not account for any CO-CO lateral interactions in TPD simulations on SAA lattices; the high dispersion of single atom sites results in CO adsorbates that reside far from each other and therefore do not interact.

Rate Constants from Density Functional Theory

In order to perform a KMC simulation, we must first calculate rate constants for CO desorption on each surface. According to transition state theory (TST), the rate constant k_{TST} of an elementary process can be calculated as

$$k_{TST} = \frac{k_B T}{h} \cdot \frac{Q^{TS}}{Q^{IS}} \exp\left(-\frac{\Delta E_a}{k_B T}\right) \quad (95)$$

where k_B is the Boltzmann constant, h is Planck's constant, T is the temperature, Q^{TS} and Q^{IS} are the molecular partition functions for the transition state and initial state, respectively, and ΔE_a is the activation barrier. The adsorption of CO is non-activated, so ΔE_a for CO desorption is taken to be $E_{ads}(CO)$. Moreover, this implies there is no "explicit" transition state, therefore a 2D gas phase CO transition state is assumed (the third translational degree of freedom is the reaction coordinate: the distance from the surface).¹⁰ Thus, equation (76) for CO desorption becomes

$$k_{TST} = \frac{k_B T}{h} \cdot \frac{Q^{CO(g)}}{Q^{CO^*}} \cdot \exp\left(\frac{E_{ads}}{k_B T}\right). \quad (96)$$

We compute the partition functions Q using the vibrational frequency data in **Table 9**, under the harmonic approximation.¹⁰ The pre-exponential factor in (3) is temperature dependent,

both due to the thermal factor of $k_B T/h$, but also because $Q^{CO(g)}$ and Q^{CO^*} are functions of T ;¹⁰ this is accounted for in the KMC simulation using fitted functions of T .

Results and Discussion

CO Adsorption on Pure Metal and SAA Surfaces

Using DFT with the RPBE xc-functional, we calculate the geometry of a CO molecule chemisorbed on pure metal and SAA (111) surfaces. For the pure metal (111) surfaces, our calculations are in excellent agreement with the works of others.^{191, 248} We determine that the CO interactions with Ag(111), Au(111) and Cu(111) are much weaker than for Ni(111), Pd(111), Pt(111), Rh(111) and Ir(111) (**Figure 57, Table 9**).

For CO adsorption on a top site on Ag(111), we calculate the value of $E_{ads}(CO)$ to be 0.02 eV indicating a slightly endothermic binding with the functional used, whereas on the top site of Au(111) there is a marginally exothermic CO adsorption energy $E_{ads}(CO)$ of -0.05 eV. These values are in agreement with experimental observations that CO binds weakly to these surfaces only at low temperatures.²⁴⁹⁻²⁵¹ CO adsorption on Cu(111) is exothermic and is most favourable in fcc hollow sites though much stronger than on Au(111), with an adsorption energy of -0.51 eV with the functional used. For Ni(111), Pd(111) and Pt(111), the most stable site for adsorption is also the fcc hollow site with adsorption energies of -1.50 eV, -1.67 eV and -1.48 eV. CO adsorption on Rh(111) is most favourable on the hcp hollow site with an adsorption energy of -1.65 eV. Finally, for Ir(111) the most stable adsorption site is the top site with the largest pure metal adsorption energy of -1.83 eV.

Though our predictions of both the adsorption energy and preferred adsorption site for CO agree well with the theoretical work of others, it should be noted that the prediction of adsorption site preference by DFT under the generalized gradient approximation is qualitatively incorrect; several explanations and remedies for this phenomenon have been reported, with an excellent discussion by Kresse *et al.* suggesting this is due to an overestimation of the HOMO-LUMO gap in CO.^{252, 253} Low temperature experiments reveal

that CO prefers to bind on one-fold rather than three-fold adsorption sites on Cu(111) and Pt(111), in disagreement with DFT.

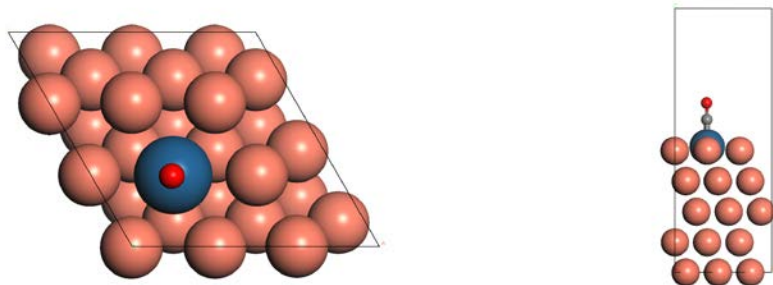


Figure 56: DFT optimized adsorption configuration for CO on a Pt/Cu(111) SAA from a top-down (left) and side-on (right) perspective. This configuration is the most stable for CO adsorption Pt/Cu(111) SAA and is analogous to on other SAA surfaces. For all SAAs, attempting to relax CO in a shared hollow or bridge site results in CO displacement back to this configuration.

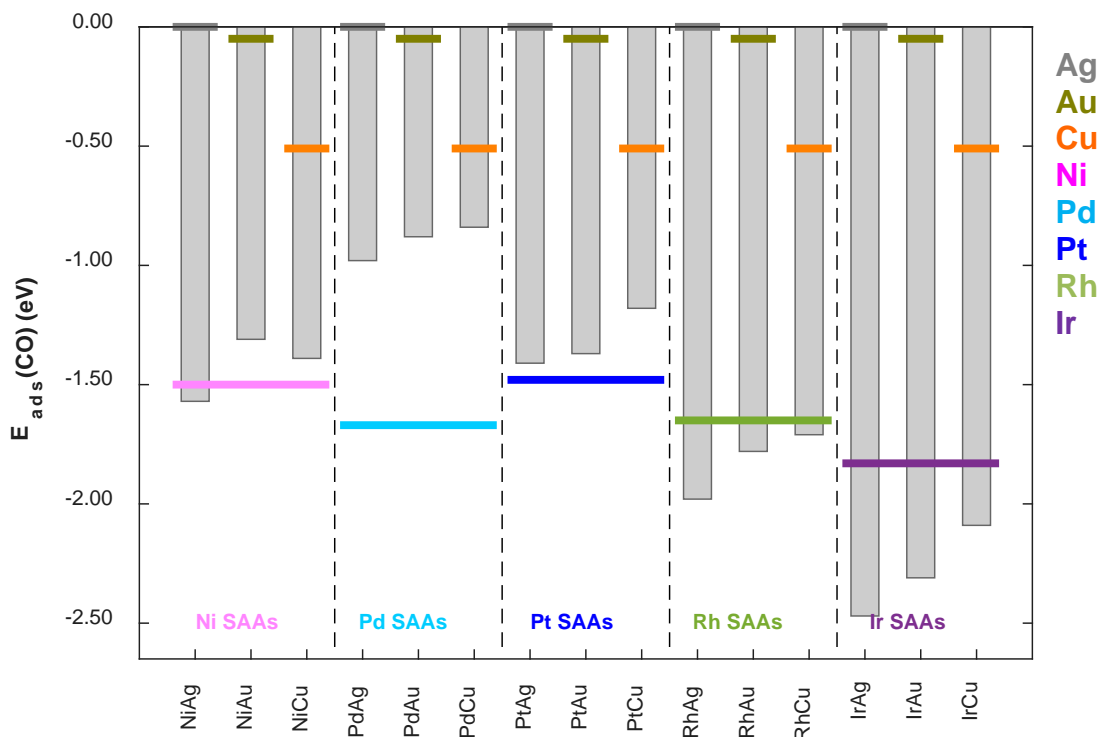


Figure 57: Adsorption energies (E_{ads}) of CO on the most stable sites of SAA (111) surfaces. Corresponding values of E_{ads} for pure metal(111) surfaces are shown by coloured horizontal lines (Ag (grey), Au (gold), Cu (orange), Ni (pink), Pd (cyan), Pt (blue), Rh (green) and Ir (purple)).

We determine that on each of the SAAs considered here, the most favoured adsorption site for CO is the top site of the single dopant atom (**Figure 56**); geometry optimizations starting with CO on shared bridge or hollow sites of SAAs typically result in CO being displaced back to the dopant top site. We report adsorption energies of CO in the most favourable adsorption sites on SAA (111) surfaces in **Figure 57** and **Table 9**. The calculations on Pt/Cu(111) and Ni/Cu(111) are in good agreement with previous works on the adsorption of CO on Ni and Pt impurity atoms at $\frac{1}{4}$ ML coverage in Cu(111).²⁵⁴

To quantify the relative change in CO adsorption strength on SAAs $E_{ads}^{SAA}(CO)$ relative to its monometallic host $E_{ads}^{host}(CO)$ and dopant $E_{ads}^{dopant}(CO)$, we use the following equation

$$\varphi(CO) = \frac{E_{ads}^{dopant}(CO) - E_{ads}^{SAA}(CO)}{E_{ads}^{dopant}(CO) - E_{ads}^{host}(CO)}. \quad (97)$$

Values of $0 < \varphi(CO) < 1$ indicate that CO adsorption on these SAAs is weaker than on pure dopant surfaces but stronger than on pure host materials, whereas values where $\varphi(CO) < 0$ indicate CO adsorption strength that is greater than on the monometallic dopant. We see for all Pd- and Pt-doped materials, as well as Ni/Au(111) and Ni/Cu(111) that $0 < \varphi(CO) < 1$, therefore CO adsorption on these SAAs is weaker than on pure dopant surfaces (Ni, Pd, Pt) though stronger than on pure host surfaces (Ag, Au, Cu). The most notable reductions in CO adsorption strength compared to the pure dopant materials are on Pd SAAs with $\varphi(CO)$ calculated to be 0.40, 0.49 and 0.72 for Pd/Ag(111), Pd/Au(111) and Pd/Cu(111) respectively. For Pt SAAs, there is still a significant $\varphi(CO)$ for Pt/Cu(111) of 0.31, though only smaller values of 0.05 and 0.08 for Pt/Ag(111) and Pt/Au(111), respectively. Ni/Au(111) and Ni/Cu(111) have $\varphi(CO)$ values of 0.13 and 0.12, respectively. However, Ni/Ag(111) as well as all Rh- and Ir-doped SAAs have values of $\varphi(CO) < 0$. CO binds more strongly to these SAAs and thus these materials will not offer any resistance to CO poisoning. However, if we use the adsorption energy of CO as a gauge of reactivity, these Rh- and Ir-doped SAAs may be useful for other applications, such as CO dissociation catalysts.

Surface	Site	$E_{\text{ads}}(\text{CO})$ (eV)	Vibrational Frequencies (cm ⁻¹)					
			ν_1	ν_2	ν_3	ν_4	ν_5	ν_6
Ag(111)	top	0.02	2015	144	121	120	11	20i
Au(111)	top	-0.05	2035	257	169	168	33	3i
Cu(111)	fcc	-0.51	1800	263	224	223	113	110
Ni(111)	fcc	-1.50	1749	331	267	266	138	134
Pd(111)	fcc	-1.67	2011	394	296	295	32	28
Pt(111)	fcc	-1.48	1728	329	301	300	155	153
Rh(111)	hcp	-1.62	1726	329	274	274	147	147
Ir(111)	top	-1.83	1998	497	446	446	67	63
Ni/Ag(111)	top	-1.57	1946	412	334	333	53	45
Ni/Au(111)	top	-1.31	1991	395	336	336	51	48
Ni/Cu(111)	top	-1.39	1972	407	342	342	49	44
Pd/Ag(111)	top	-0.98	1982	367	261	260	45	36
Pd/Au(111)	top	-0.88	2018	353	268	268	41	37
Pd/Cu(111)	top	-0.84	2007	357	277	276	33	23
Pt/Ag(111)	top	-1.41	1977	449	334	333	52	46
Pt/Au(111)	top	-1.37	2014	450	352	352	53	51
Pt/Cu(111)	top	-1.18	2001	439	345	345	48	47
Rh/Ag(111)	top	-1.98	1939	446	358	357	51	46
RhAu(111)	top	-1.78	1977	440	375	375	57	48
Rh/Cu(111)	top	-1.71	1972	432	371	370	49	42
Ir/Ag(111)	top	-2.47	1938	507	413	412	57	51
Ir/Au(111)	top	-2.31	1977	503	429	429	63	59
Ir/Cu(111)	top	-2.09	1970	488	418	417	54	50

Table 9: Adsorption energies ($E_{\text{ads}}(\text{CO})$) and vibrational frequencies (ν) for CO chemisorption at the most favourable adsorption site on pure metal and SAA (111) surfaces. The vibrational modes can be described as follows; ν_1 C-O stretch, ν_2 M-C stretch, $\nu_{3/4}$ hindered rotations and $\nu_{5/6}$ hindered translations. The imaginary frequencies on Ag and Au can be attributed to numerical artefacts in the calculations of the soft translational modes.

Temperature Programmed Desorption Simulations

Reductions in the adsorption strength of CO on SAAs compared to pure dopant surfaces will result in an increased tolerance to catalytic poisoning by CO. We quantify this resistance to poisoning by simulating CO TPDs from (111) surfaces of metals and alloys of interest using KMC and comparing desorption peak temperatures. To evaluate the quality of our dataset, we compare these peak temperatures to experimental ones for the pure metals (excluding Ag and Au, due to weak or no binding) and several SAAs that have been synthesized experimentally (Ni/Cu(111), Pd/Au(111), Pd/Cu(111) and Pt/Cu(111)).

Simulated Desorption Peak Temperatures

We now examine the thermal desorption of CO on each pure metal and SAA (111) surface. During a TPD simulation, we record the coverage of CO^* (Θ_{CO}) on the lattice, as well as the number of gas molecules evolved from the surface, at intervals of 0.25 s. The TPD signal is obtained as a moving average of the instantaneous desorption rate, thereby allowing us to determine the time and temperature (1 K·s⁻¹ ramp rate) that the rate of CO desorption is greatest. The corresponding peak desorption temperature, T_{sim} , is plotted for all surfaces in **Figure 58**, alongside any known experimental data.^{56, 58, 62, 221, 255-257} Comparing our simulated TPD peak temperatures to this data, we can see that there is excellent agreement with a mean absolute error of 13 K, providing good support for the reliability of our model and dataset.

The majority of SAAs show reductions in CO desorption temperature over their monometallic dopant analogues, including all Ni-, Pd- and Pt-doped SAAs. In particular, we see that there is over a 220 K decrease in the desorption temperature of Pd/Au(111) and Pd/Cu(111) SAAs compared to monometallic Pd, as well as a 185 K decrease with Pd/Ag(111). For Pt doped SAAs, the largest peak temperature reduction of 102 K is simulated for Pt/Cu(111), whereas Pt/Ag(111) and Pt/Au(111) exhibit desorption temperature reductions of over 40 K compared to pure Pt(111). Despite a higher adsorption energy on Ni/Ag(111) compared to pure Ni(111), CO desorbs with a peak temperature that is 22 K lower from this SAA. This

qualitative deviation from the expected relationship between adsorption energy and TPD peak temperature is attributed to the soft vibrational modes of CO bound to Ni/Ag(111) (**Table 9**, ν_5 and ν_6) giving a lower desorption pre-exponential for this material. This difference offsets the stronger adsorption of CO on Ni/Ag(111) (0.07 eV difference versus Ni(111)). We also simulate TPD peak temperatures for Ni/Au(111) and Ni/Cu(111) that are 85 K and 34 K below that of Ni(111), respectively.

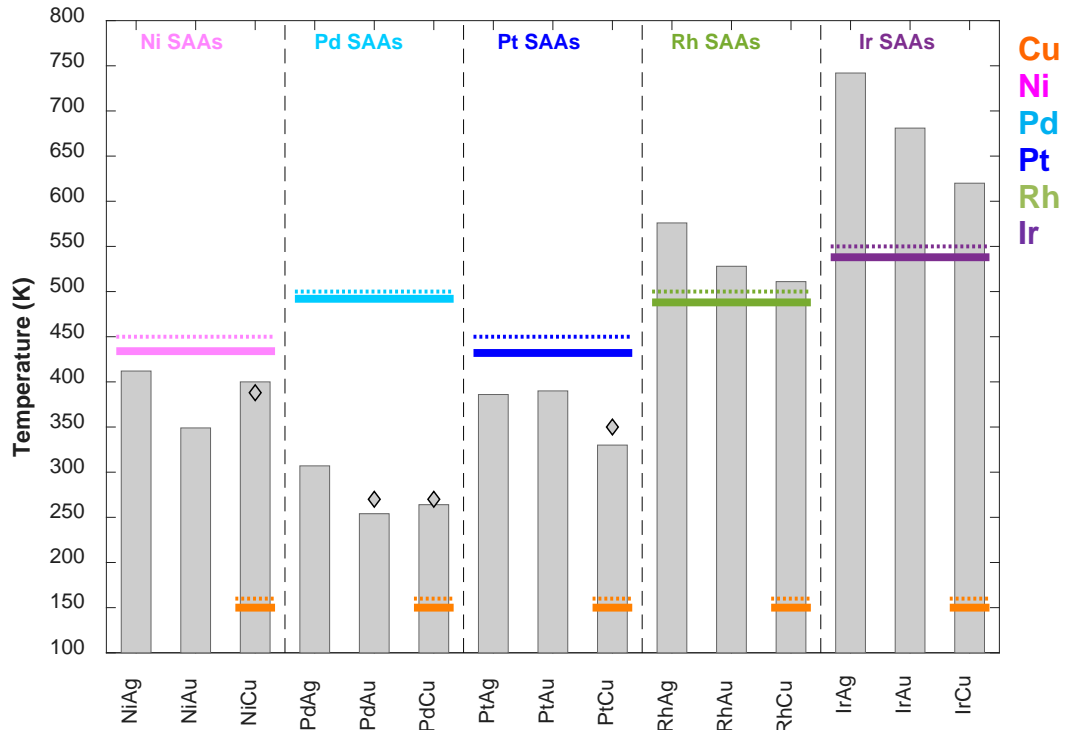


Figure 58: Peak desorption temperatures from KMC simulated TPD of CO on SAA(111) surfaces. Temperatures from pure metal simulations are shown as full-horizontal lines whereas corresponding temperatures from experiment^{221, 255-257} are shown as dotted-horizontal lines (Cu (orange), Ni (pink), Pd (cyan), Pt (blue), Rh (green) and Ir (purple); Au and Ag not shown due to weak or no CO binding). Experimental SAA temperatures are shown with diamonds.^{56, 58, 62, 255}

For Ir- and Rh-doped SAAs, we simulated CO TPD peak temperatures that are above the corresponding temperatures for desorption from pure Rh(111) and Ir(111), in line with stronger adsorption of CO on these SAAs. We calculate 88 K, 40 K and 23 K increases in the TPD peak temperatures for CO desorbing from Rh/Ag(111), Rh/Au(111) and Rh/Cu(111), respectively. For Ir-doped SAAs, the analogous temperature differences are greater, being 204 K, 143 K and 82 K for Ir/Ag(111), Ir/Au(111) and Ir/Cu(111), respectively.

Our data suggests that there exists a strong linear correlation between $E_{\text{ads}}(\text{CO})$ and the TPD peak temperature (both for T_{exp} and T_{sim}) (**Figure 59**). This finding is typical for a first

order desorption process as predicted by an equation first derived by Redhead.²⁵⁸ Though useful, the Redhead equation can often produce errors as a result of poor estimation of the pre-exponential; for example, arbitrarily choosing a pre-exponential value of $k_B T_{exp}/h$ (as is typical) gives a mean absolute error in the Redhead value of $E_{ads}(CO)$ of 0.20 eV compared to the DFT adsorption energy. In our case, we have calculated temperature dependent pre-exponentials using TST, assuming harmonic vibrational modes. This may not always be an accurate approximation, especially when considering very soft, frustrated translations or rotations in the partition function,²⁵⁹ though good agreement with experiment supports the use of harmonic TST in this case. We pose that our calibrated linear fitting of

$$E_{ads}(CO) = -3.30 \times 10^{-3} \cdot T_{sim} - 5.95 \times 10^{-2} \quad (98)$$

may be used for quick extraction of the CO adsorption energy from future experimental work. This fitting is specific for DFT using the RPBE xc-functional, though good agreement of our data with experiment supports the choice of this xc-functional in this case. We calculate the mean absolute error in the fitting to be 0.04 eV.

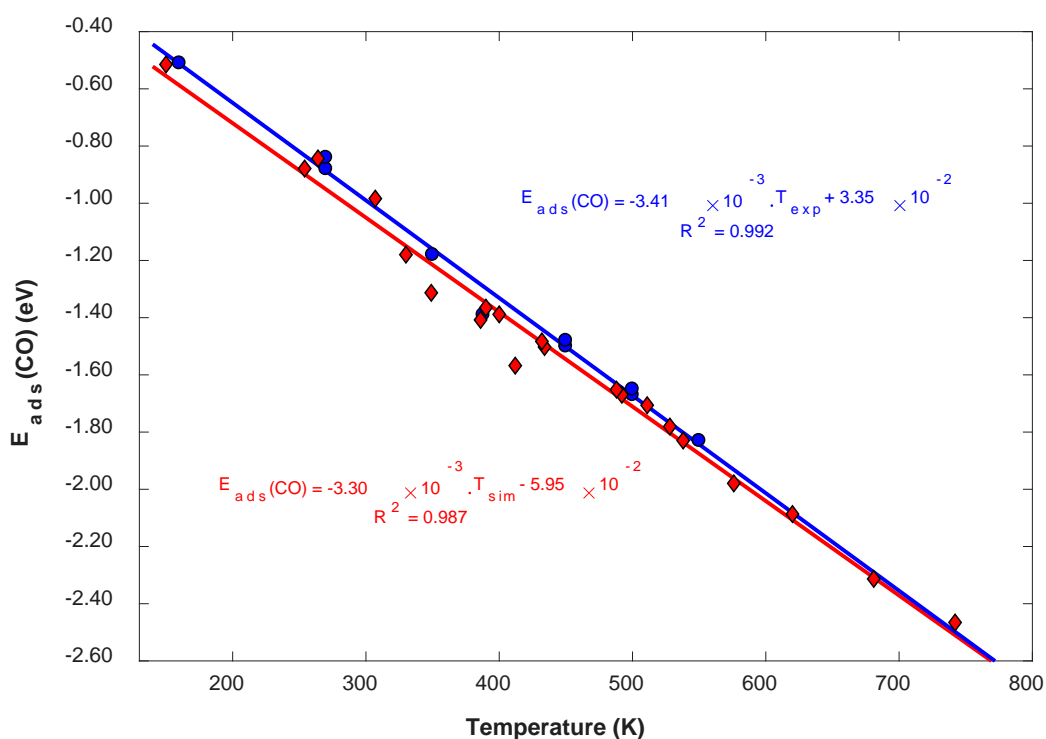


Figure 59: Linear correlation of TPD peak temperatures from experiment (blue) and KMC simulation (red) with the adsorption energy of CO calculated from DFT. Regression equations are shown with corresponding coefficients of determination (R^2). Standard errors in the slope and intercept for the

experimental case are $\pm 1.11 \times 10^{-4}$ and $\pm 4.51 \times 10^{-2}$, respectively. The analogous standard errors in the slope and intercept for the KMC simulated case are $\pm 8.79 \times 10^{-5}$ and $\pm 4.08 \times 10^{-2}$, respectively.

Our DFT results show that highly diluted alloys of single atoms, out of the catalytically active group 10 metals, dispersed into more inert hosts, out of group 11 metals, can reduce the adsorption strength of CO, compared to the pure dopants. In line with these results, KMC simulations reveal that the CO desorption temperature may be reduced by more than 220 K in some cases, thereby dramatically reducing the susceptibility of the surface to poisoning by CO. Decreased TPD peak temperatures imply that it is not necessary to heat these SAA catalytic systems to temperatures as high as on pure dopant surfaces in order to circumvent CO poisoning. Thus, one can carry out the reaction on SAAs at lower temperatures, thereby reducing the risk of catalyst sintering and hampered reaction selectivities. However, increases in the CO desorption temperature for Rh- and Ir-doped SAAs indicate reduced tolerance to CO over their monometallic constituents and an increased susceptibility to CO poisoning.

Our study so far has assumed that under conditions where CO is present, the SAA structure is indeed favourable. However it is well known that adsorbates, in particular those that are as potent as CO, may induce changes in the surface structure of a material through effects such as segregation or formation of islands (clusters) on the surface. It is with this in mind that we move on to study the stability of the SAA structure with respect to the aforementioned phenomena, both in the absence and presence of CO. This stability analysis will serve as a guide for the experimental synthesis of SAAs, highlighting those metal combinations with an enthalpic preference for the SAA structure over other phases, still consistent with high dopant dilution.

Adsorbate-Induced Structural Changes in SAAs

Under realistic conditions, restructuring of the surface of a catalyst can result in modifications to its function. The low concentration of dopant atoms in a SAA means that effects such as dopant atom segregation into the bulk or clustering on the surface, would result in a fundamental change in the surface structure of the material and transformation of a SAA into

some other class of binary alloy. In particular, segregation of a single dopant atom into the bulk may result in decreased catalytic activity that more closely resembles the host material. Moreover, clustering of dopant atoms in the surface layer may result in dimer, trimer and even island formation which will hamper the selectivity and poisoning resistance of the surface.

Thus, in this section we investigate the thermodynamic stability of SAAs under vacuum conditions and also in the inevitable presence of CO under operating conditions. We use DFT to calculate energy changes between the SAA structure and other highly dilute analogues where the SAA is buried into the bulk structure of the host or aggregated into clusters on the surface. By comparing the values of these energy changes in the absence versus presence of CO, we quantify the effect of this species in SAA stability.

Surface Segregation

We perform calculations for each binary alloy in structures where a single dopant atom is in the surface layer (i.e. a SAA) or immersed in the bulk material. For the latter, we approximate the “bulk” as a single dopant atom in the 3rd layer of the host material slab such that the dopant atom is fully coordinated to host atoms and the slab is symmetric. The segregation energy ΔE_{seg} is then computed relative to the SAA phase such that

$$\Delta E_{seg} = E_{Tot}(bulk) - E_{Tot}(SAA); \quad (99)$$

where $E_{Tot}(bulk)$ and $E_{Tot}(SAA)$ are the DFT total energies of the single dopant atom immersed in the 3rd layer of the host material slab and the single dopant atom in the surface layer of the host slab respectively. Note that positive values of ΔE_{seg} correspond to a preference for segregation of the dopant to the surface, not accounting for entropy.

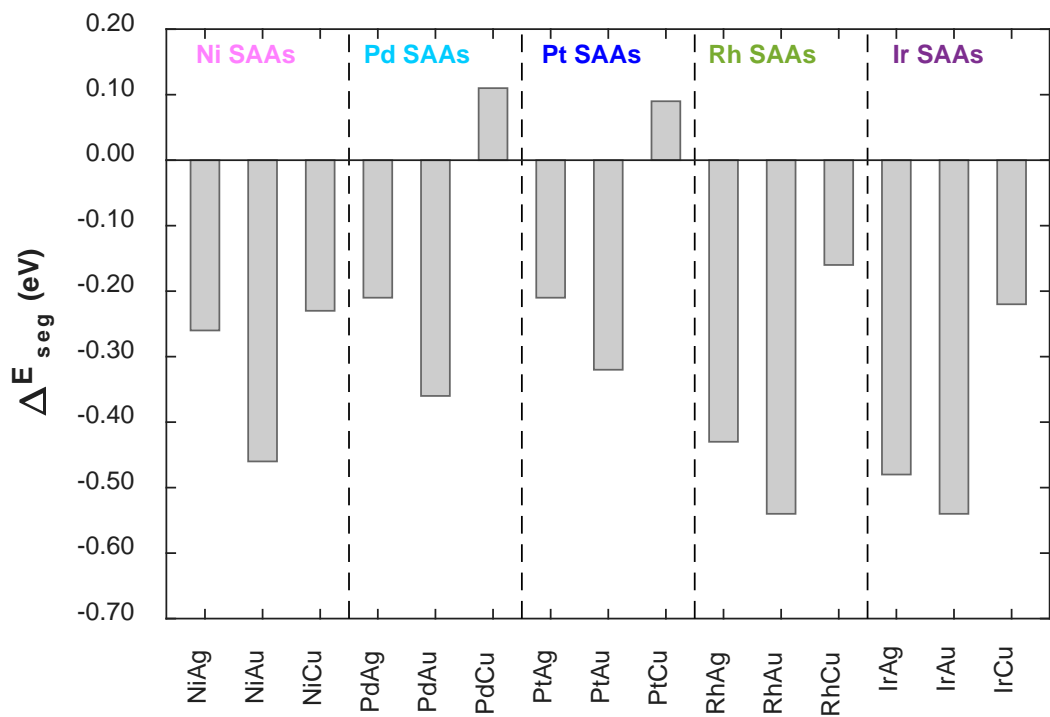


Figure 60: The segregation energy ΔE_{seg} for a single dopant atom to migrate from the (111) surface of a group 11 host material into the “bulk”. Positive values indicate a preference for segregation of the dopant to the surface, whereas negative values into the bulk.

Our calculations show that for most metal combinations considered here, it is more favourable for a single dopant atom to reside in the bulk rather than at the surface (**Figure 60**). The only exceptions are Pd/Cu(111) and Pt/Cu(111) whose ΔE_{seg} values are 0.11 eV and 0.09 eV, respectively. These results show good qualitative agreement with the work of Ruban *et al.* in a previous study on the surface segregation of transition metal impurity atoms in close-packed transition metal hosts.²⁶⁰

CO Induced Surface Segregation

In the presence of CO, our calculations suggest that it is strongly favoured for a single dopant atom to segregate to the surface. To deduce an expression for the segregation energy, we consider a cyclic process entailing: (i) desorption of CO from an alloy structure with the dopant in the bulk, (ii) segregation of the dopant in the surface, (iii) adsorption of CO in the dopant site of the SAA, and (iv) migration of the dopant back to the bulk in the presence of CO, such that the final state is identical to the initial configuration (**Figure 61**).

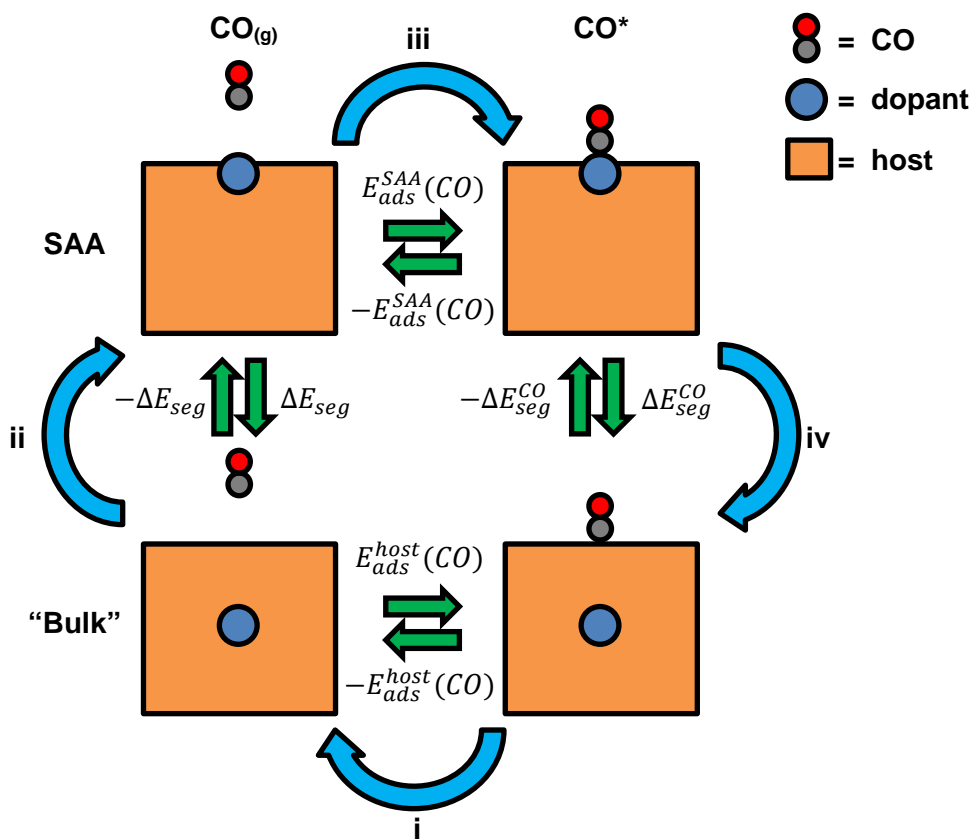


Figure 61: Energetic cycle for the segregation of a single dopant atom from the bulk to the surface layer of a host material in the presence and absence of CO. This cycle shows the link between the energies we define in the manuscript for the CO adsorption ($E_{ads}(CO)$), the segregation energy (ΔE_{seg}) and the CO induced segregation energy (ΔE_{seg}^{CO}). Conversions denoted by Roman numerals correspond to those discussed in the main manuscript, section “CO Induced Surface Segregation”.

The CO induced segregation energy ΔE_{seg}^{CO} is therefore given as:

$$\Delta E_{seg}^{CO} = \Delta E_{seg} + \{E_{ads}^{host}(CO) - E_{ads}^{SAA}(CO)\} \quad (100)$$

The adsorption strength of CO to SAAs $E_{ads}^{SAA}(CO)$ is sufficiently greater than that on the pure host materials $E_{ads}^{host}(CO)$, particularly when considering Ag and Au, such that ΔE_{seg}^{CO} is positive in all cases (Figure 62). Hence, the presence of CO is expected to induce the segregation of the dopant atom to the surface. This has previously been noted experimentally for dilute Pd/Cu SAA nanoparticles whereby exposure to CO pulls Pd to the surface and consequently enhances the activity of these nanoparticles towards acetylene hydrogenation.¹⁷⁶ Moreover, several theoretical studies have demonstrated the phenomenon of adsorbate induced segregation.²³⁸⁻²⁴⁴ For example a study by Sansa *et al.* on the CO induced segregation of single transition metal dopant atoms in Au reveals that the adsorption

energy of CO is sufficient to promote dopant atom segregation to both the Au(111) and Au(100) surfaces from the bulk.²⁴³ This study by Sansa *et al.* predict over-bound CO adsorption energies due to the use of the traditional PBE exchange-correlation functional rather than RPBE used in this case; though their values of ΔE_{seg}^{CO} are still in excellent agreement with ours due to a cancellation of the over-binding when the difference is taken between CO bound on a host and SAA material.²⁴³

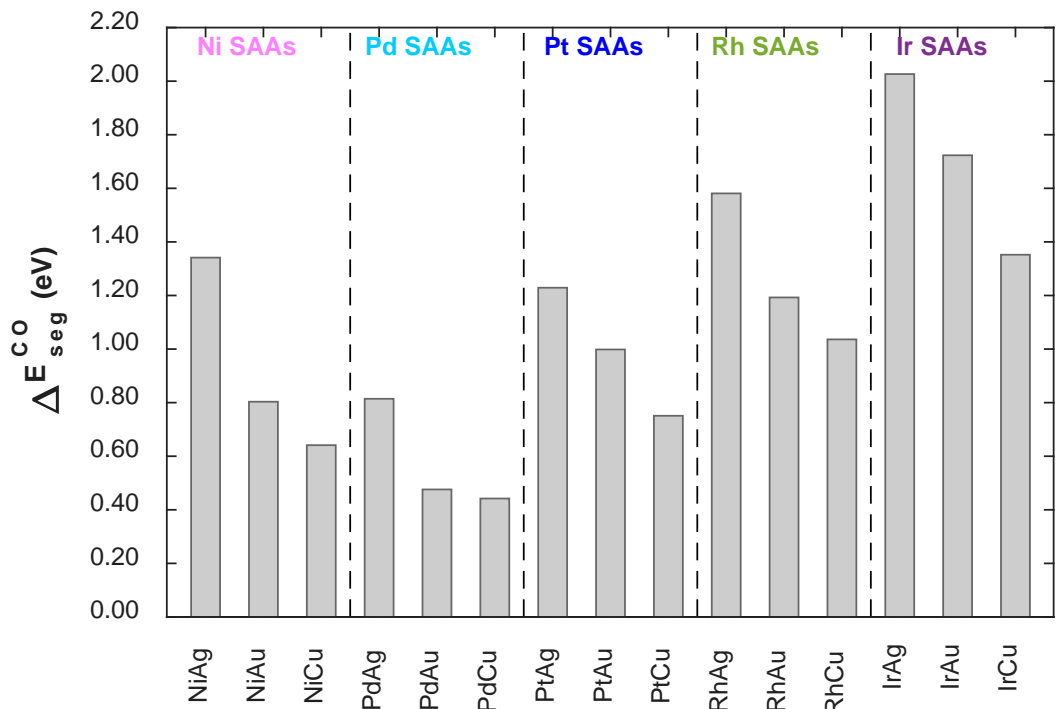


Figure 62: The CO induced segregation energy ΔE_{seg}^{CO} for a single dopant atom to migrate from the (111) surface into the “bulk” of group 11 metal host materials. Positive values indicate a preference for segregation of the dopant in the presence of CO to the surface, whereas negative values would indicate a preference for segregation into the bulk.

The CO induced segregation energy is sufficient to ensure dopant atoms will not segregate into the bulk material in the presence of CO. The configurational entropy of a single atom in the bulk is greater than that of the surface due to the high number of bulk sites relative to surface sites. This provides a driving force for dopant atom segregation into the bulk from the surface, though we believe this is likely to be relevant only in cases when CO is not present. However, we hypothesize that diffusion barriers of the dopant moving into the bulk will be sufficiently high to kinetically trap the dopant in the surface layer; this point is particularly pertinent due to the methods of synthesis (vapour deposition) for extended SAA surfaces and SAA nanoparticles (galvanic replacement) involving addition of the dopant

atoms directly into the surface layer. This hypothesis is evidenced to some extent thanks to the experimental synthesis of Ni/Au, Ni/Cu, Pd/Au and Pt/Au SAAs, all of which have negative values of ΔE_{seg} .

Surface Aggregation and Island Formation

To evaluate the stability of single isolated dopant atoms towards aggregation, we vary the molar fraction of CO in the surface layer and compute the DFT energies for dimer and trimer configurations on the surface (**Figure 63**). The aggregation energy for a cluster of n atoms $\Delta E_{agg}(n)$ is given relative to a SAA such that

$$\Delta E_{agg}(n) = E_{Tot}(n) + (n - 1) \cdot E_{Tot}(\text{host}) - n \cdot E_{Tot}(\text{SAA}); \quad (101)$$

where $E_{Tot}(n)$ and $E_{Tot}(\text{host})$ are the DFT total energies of an alloy surface with a cluster of n dopant atoms and the pure host material, respectively. In this case, values of $\Delta E_{agg}(n)$ that are negative correspond to a preference for surface clustering, whereas positive values correspond to a preference for dopant atom dispersion to the SAA structure.

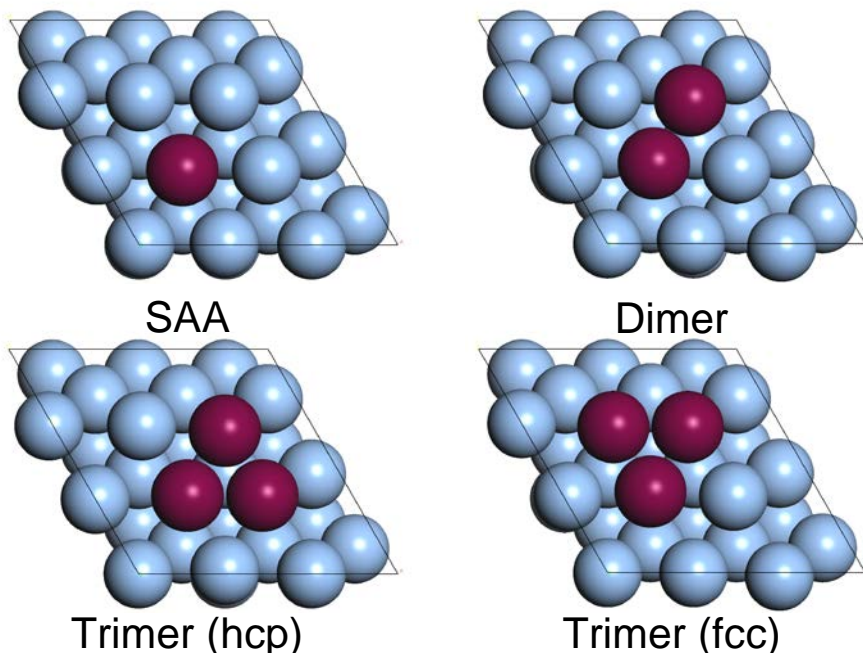


Figure 63: DFT optimized monomer (SAA), dimer and trimer (surrounding hcp and fcc sites) configurations for binary alloys of Ir-doped Ag(111) surfaces.

For the majority of metal combinations we consider here, our calculations show that single dopant atom isolation is favoured for unit cell concentrations up to 1/3 ML, with the exception of Ni-, Ir- and Rh-doped Ag(111), Ir/Au(111) and Ni/Cu(111) which have negative $\Delta E_{agg}(n)$ values (**Figure 64**). In the case of Ni/Cu(111), the values of $\Delta E_{agg}(2)$ and $\Delta E_{agg}(3)$ are so small that at temperatures likely to be used in experimental practice, there will be a sufficient entropic tendency to drive surface dopant atoms apart. In fact, configurational contributions to the entropy term, which we do not explicitly consider here, will always favour the SAA structure over aggregation due to the greater disorder of having several, isolated atoms over having a cluster. We can therefore conclude that any system with an enthalpic preference at 0 K for the SAA phase over the aggregated phase will also be more thermodynamically stable as a SAA (i.e. Ni- and Rh-doped Au(111), as well as Ir- and Rh-doped Cu(111) and all the Pd- or Pt-doped materials).

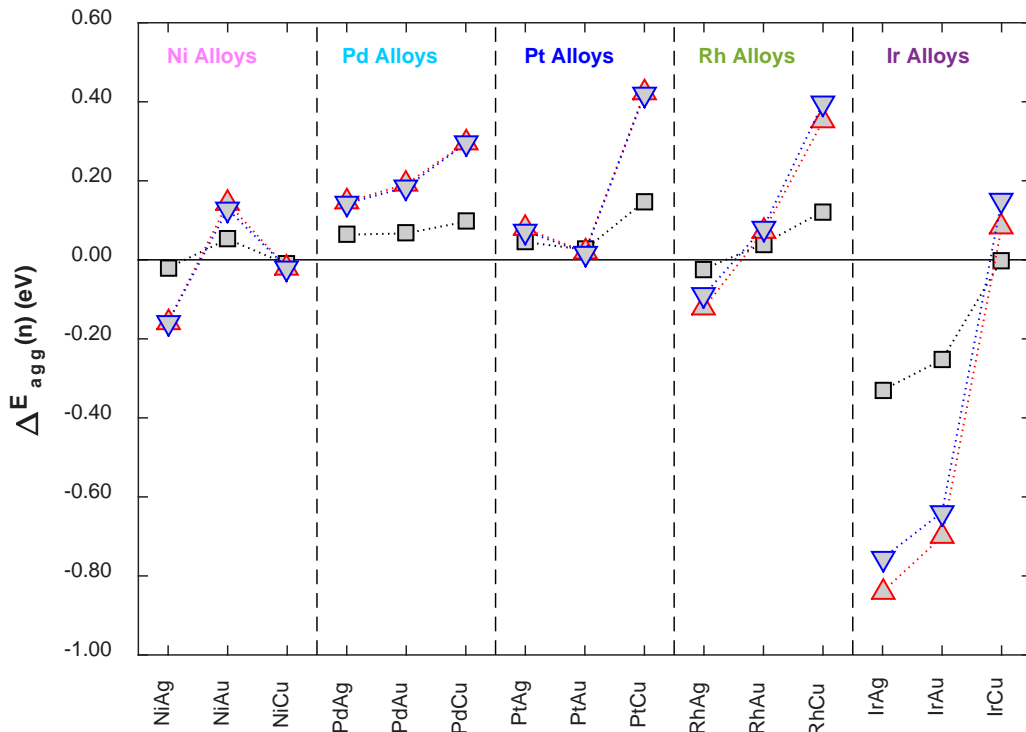


Figure 64: The energy of aggregation $\Delta E_{agg}(n)$ relative to the SAA phase for the clustering of group 10 dopant atoms in the (111) surface of group 11 metals into dimers (black squares) and trimers where dopant atoms surround fcc (red up-triangles) and hcp (blue, down-triangles) sites.

CO Induced Aggregation and Island Formation

To determine whether exposure of the surfaces to CO may induce aggregation, we compute the adsorption energies of 1, 2 and 3 CO molecules adsorbed to dimer and trimer dopant aggregates.

By performing calculations with just a single CO molecule adsorbed to binary alloy surfaces, we are effectively considering the case where the CO partial pressure is sufficiently low that full saturation of dopant atoms in dimer and trimer configurations is not possible. At this CO coverage, we determine that the CO adsorption energy on an n-mer $E_{ads}^{n-mer}(CO)$ is greater than the CO adsorption energy on the corresponding SAA $E_{ads}^{SAA}(CO)$ for all Ni-doped and Pd-doped alloys, as well as Pt and Rh doped Ag(111) and Au(111) based SAAs (**Figure 65**). The most stable adsorption sites for a single CO molecule on these binary surfaces are the bridge sites connecting two adjacent dopant atoms in dimers, and the hollow sites surrounded by three dopant atoms in triangular trimers. Exceptions to this are Pt/Cu(111), Ir/Ag(111), Ir/Au(111) and Ir/Cu(111) for which it is more favourable for one CO molecule to adsorb on the top site of the SAA, dimer or trimer analogues rather than on two- or three-fold sites.

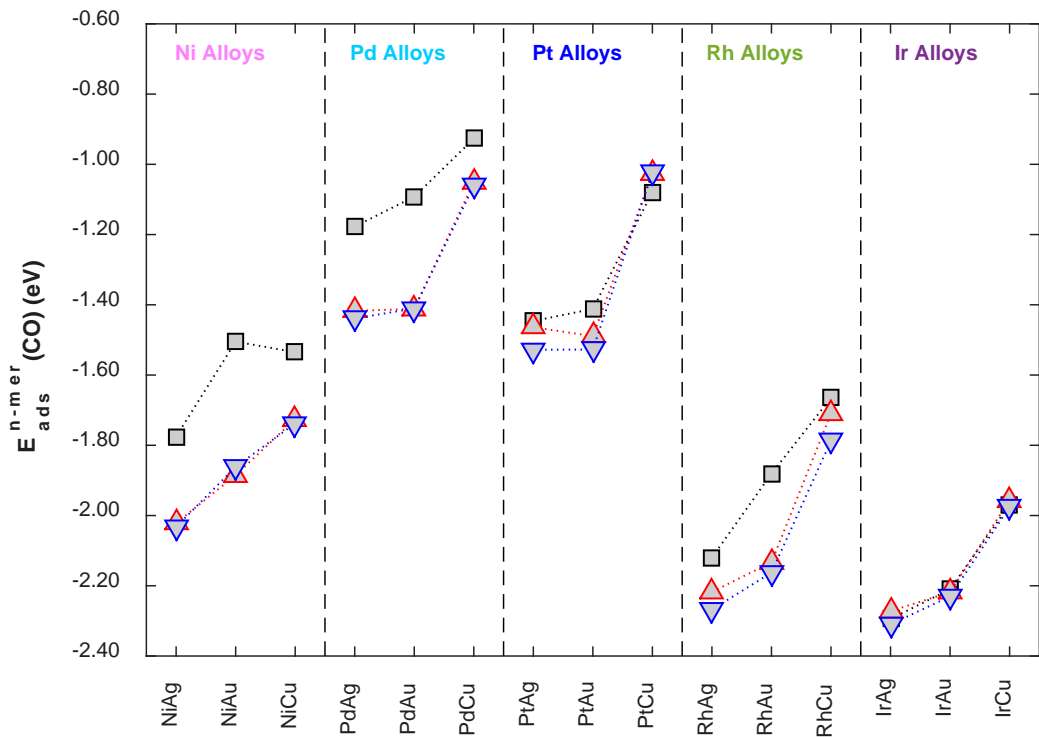


Figure 65: Adsorption energies of a single CO molecule in the most energetically favourable surface site for dimers (black squares) and triangular trimers surrounding fcc (red up-triangles) and hcp (blue down-triangles) of binary alloy combinations of Ni, Pd, Pt, Rh and Ir doped into group 11 (111) surfaces.

In order for a single CO molecule to induce aggregation, the adsorption energy of CO on an n-mer island $E_{ads}^{n-mer}(CO)$ must be more negative than that on a SAA and the difference must also offset positive values of $\Delta E_{agg}(n)$ to make the CO induced aggregation energy

$\Delta E_{agg}^{m \times CO}(n)$ negative (**Figure 66a**);

$$\Delta E_{agg}^{m \times CO}(n) = \Delta E_{agg}(n) - \{m \cdot E_{ads}^{SAA}(CO) - E_{ads}^{n-mer}(mCO)\}. \quad (102)$$

For binary alloys of Pd, Pt, Ir and Rh doped into Cu(111), $\Delta E_{agg}^{1 \times CO}(n)$ is always positive indicating that these metal combinations will have an energetic preference for dispersion into the SAA phase when exposed to low CO partial pressures. Pt/Ag(111) has values of $\Delta E_{agg}^{1 \times CO}(n)$ in dimers and trimers that are very close to 0 eV, indicating little or no preference for the SAA phase over other aggregated phases. All other alloys including Ni/Au(111), Pd/Au(111), Pt/Au(111), Rh/Au(111) and Pd/Ag(111) whose values of $\Delta E_{agg}(n)$ were all positive (favouring dispersion in the absence of CO) have $\Delta E_{agg}^{1 \times CO}(n)$ values that are negative, indicating that CO will induce aggregation in these cases.

Under reaction conditions, it is most likely that there will be sufficient CO present to have at least a 1:1 dopant:CO ratio and so we go on to investigate if multiple CO adsorbates may promote aggregation (**Figure 66b/c**). The adsorption energy of m CO molecules ($m > 1$) on m top sites of a cluster of n dopant atoms $E_{ads}^{n-mer}(mCO)$ is always notably more negative than that of a single CO molecule in its most favoured adsorption site. We also find that $E_{ads}^{n-mer}(mCO)$ is more positive than the sum of $m \cdot E_{ads}^{SAA}(CO)$ for all alloy combinations. In these cases, the CO geometries are tilted away from one another and no longer in line with surface normal as is the case with one CO molecule, indicating the presence of repulsive lateral interactions. The lateral interactions appear to be approximately pairwise additive on trimer clusters.

It follows on that $\Delta E_{agg}^{m \times CO}(n)$ is made more positive by the presence of multiple CO for the highly dilute binary surfaces we consider here. In fact, negative values of $\Delta E_{agg}(n)$ are offset when 2 or 3 CO molecules are co-adsorbed to clustered islands such that $\Delta E_{agg}^{m \times CO}(n)$ is positive for all cluster sizes for the majority of alloy combinations. Thus, for partial pressures of CO giving fractional coverages of CO on dopant atoms of 0.5 to 1, dispersion of dopant atoms into the SAA phase will be favoured for these alloys, rather than aggregation into clustered islands. The only SAAs that do not adhere to this statement are Ir/Ag(111) and Ir/Au(111); in these cases each additional CO molecule adsorbed to the surface reduces the negativity of $\Delta E_{agg}^{m \times CO}(n)$ through repulsive interactions between CO molecules, until 3 CO molecules on trimer configurations or 2 CO molecules on dimer configurations is sufficient to make $\Delta E_{agg}^{m \times CO}(n)$ positive.

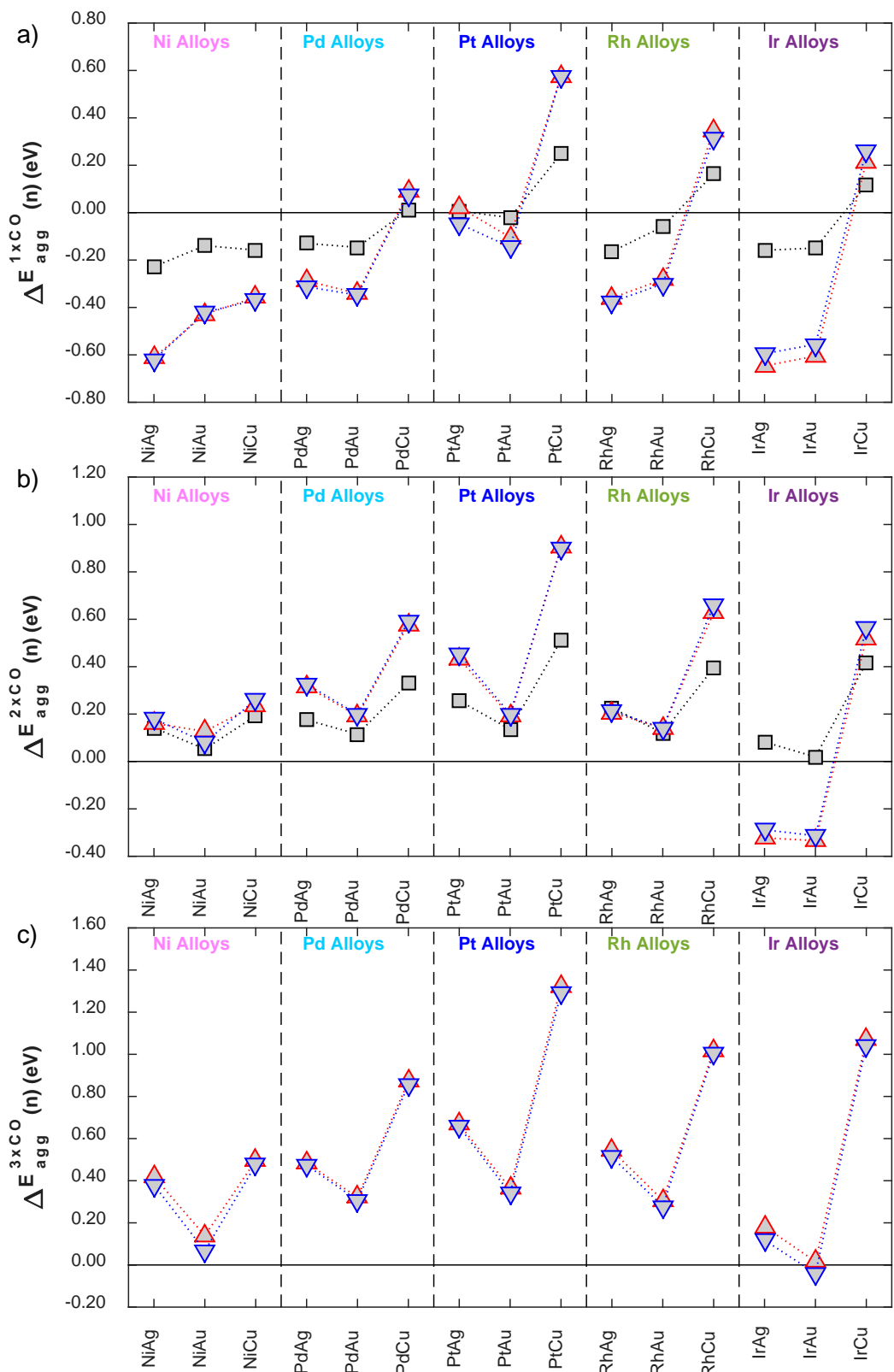


Figure 66: CO induced aggregation energies $\Delta E_{agg}^{m \times CO}(n)$ for clusters of n atoms relative to the SAA phase of Ni, Pd, Pt, Rh and Ir doped into the (111) surfaces of the group 11 metals with a) 1 adsorbed CO molecule; b) 2 adsorbed CO molecules; and c) 3 adsorbed CO molecules.

DFT results in the absence of CO, show that most surface alloys tend to be dispersed forming SAAs at high dopant atom dilution. Notable exceptions (at least from an energetic point of view) are Ni-, Ir- and Rh-doped Ag(111), as well as Ni/Cu(111) and Ir/Au(111). Adsorption of a single CO molecule changes this picture for all Au-based SAAs as well as for Ir- and Pd-doped Ag(111) as in the presence of relatively low amounts of CO on the surface, the formation of dimers/trimers may be favoured. On the other hand, for Pd, Pt, Ir and Rh doped into Cu(111) in addition to Pt/Ag(111) dispersion of dopant atoms is favourable despite the presence of CO. For high CO coverages, the repulsive CO-CO lateral interactions are expected to promote the dispersion of dopant atoms, yielding SAA structures for all binary metals considered here. These findings may present an interesting opportunity of controlling ensemble effects, by engineering novel materials with primarily dimers or trimers on the surface of these materials through manipulation of CO partial pressures.^{240, 261}

Conclusion

In this study, we have investigated the CO adsorption properties on highly dilute binary alloys of the platinum group metals doped into group 11 metal hosts, with focus on the fcc(111) surface. Using a combination of DFT with KMC, we have shown that Ni-, Pd- and Pt-doped SAAs offer resistance to catalytic CO poisoning as evidenced by reduced CO adsorption energies and CO peak desorption temperatures as compared to pure Ni(111), Pd(111) and Pt(111). On the other hand Rh- and Ir-doped SAAs bind CO more strongly than pure Rh(111) and Ir(111), indicating these SAAs may offer enhanced reactivity over their monometallic counterparts, though also a lack of CO tolerance. Additionally, we have evaluated the stability of SAAs compared to other binary alloy structures and determined that the formation of dispersed structures (i.e. the SAA phase) is energetically favourable in a number of cases. We have considered the effect of CO on these alloys and determined that CO favours the segregation of single dopant atoms into the surface layer of the host material. Moreover, at CO dopant fractional coverage of greater than 0.5, our calculations

suggest that CO will promote dopant atom dispersion in the surface layer, whereas lower CO coverages may favour aggregation leading to the formation of dimers or trimers.

Chapter 6 Concluding Remarks and Future Work

In this thesis we have employed Density Functional Theory (DFT) alongside kinetic Monte Carlo (KMC) to explore the surface chemistry and stability of a class of highly dilute binary alloys referred to as *Single Atom Alloys* (SAAs). This work has provided useful insight into the fundamental properties of SAAs, allowing for the identification and prediction of metal combinations that exhibit excellent catalytic activity, high reaction selectivity, resistance to surface poisoning and structural stability. Ultimately, the work presented here will facilitate the optimisation and rational design of SAA catalysts.

Summary and Conclusion

We began by considering the adsorption behaviour of an assortment of small, catalytically relevant adsorbates on pure metal and SAA surfaces. We determined that SAAs tend to exhibit intermediate binding strength compared to their monometallic constituents. However, our results suggest that this “intermediate” behaviour is not quite as simple to predict as in the case of binary alloys with higher dopant atom densities whereby a simple relationship may be derived based on the relative number of each constituent.

In fact, it is a lack of simple predictability in the adsorption behaviour of SAAs that makes these novel materials so exciting, giving them the potential to exhibit unusual properties that are distinct from their monometallic analogues as well as other alloy systems. This is evidenced in our discussion in Chapter 3; we see that SAAs are unique in that they are capable of escaping traditional linear scaling relations which pure metal and other alloys systems almost universally adhere to. The ubiquity of linear scaling relationships inevitably imposes limitations on the optimal performance of a catalyst and therefore, SAAs that are capable of breaking such relationships, provide an opportunity to design new materials that have enhanced catalytic properties.

In Chapter 4, we evolved our screening study of many adsorbates and simple chemistries on several SAAs into a targeted study on the activation of C-H bonds by Pt/Cu SAAs. This

study was carried out in collaboration with the Sykes and Flytzani-Stephanopoulos experimental research groups at Tufts University allowing for a multidisciplinary study using atomistic simulations, model surface science experiments and micro-reactor catalysis.

We performed calculations on the catalytic dehydrogenation of methane on Pt/Cu(111) SAA, as well as on pure Pt(111) and Cu(111). From DFT we were able to determine adsorption energies and C-H scission activation barriers for methane derived species on each surface. Our data suggests that Pt/Cu(111) SAA breaks the linear scaling relationship followed by Cu(111) and Pt(111), allowing the surface to exhibit good C-H scission activity for high valency carbon species in conjunction with positive reaction energies. It follows that Pt/Cu(111) SAAs are capable of harnessing the reactivity of pure Pt yet also retaining the coke resistance of pure Cu. We modelled the kinetics on each surface of sequential C-H bond scissions from adsorbed methyl, predicting temperatures of methane desorption.

Our simulations and data are in excellent agreement with surface science experiments from the Sykes laboratory, supporting the reliability of our work. We successfully matched methane desorption peak temperatures and predicted the levels of carbon deposition that are complementary to temperature programmed desorption and high-resolution scanning tunnelling microscopy experiments, respectively.

In order to assess the capabilities of the Pt/Cu(111) SAA under realistic conditions, the Flytzani-Stephanopoulos group performed micro-reactor, nanoparticle experiments for H-D exchange in butane to gauge the activity of C-H scission. These experiments showed that unlike monometallic Pt nanoparticles, Pt/Cu nanoparticles are resistant to coke formation and deactivation, yet still exhibit good activity that is far enhanced compared to pure Cu nanoparticles. Though we did not explicitly model nanoparticle structures, we modelled C-H scission reactions on the most prominent facet and these experiments are in good qualitative agreement with our simulations.

It is with realistic operating conditions in mind that in Chapter 5, we investigated the stability of a set of SAAs in addition to their resistance to catalytic poisoning. In many chemical

processes, carbon monoxide (CO) is present not only as a substrate, but also as a background gas in air or indeed as an impurity in streams of other common gases, such as hydrogen and oxygen. Interaction of CO with transition metal surfaces can result in strong chemisorption that blocks surface sites whereon substrates in a reaction are catalysed by the surface. We highlighted SAAs that bind CO more weakly than pure platinum group metals and consequently offer good CO tolerance.

We also considered the structural consequences of CO adsorption on SAAs. In order to quantify this, we considered the thermodynamic structural stability of SAAs with respect to segregation and aggregation of platinum group metal atoms in highly dilute binary alloys. Our results showed that the stability of SAAs is dependent on the metal constituents; for example, in the case of the Pt/Cu SAAs discussed in Chapter 4, there is a thermodynamic preference for a single Pt atom to remain in the surface layer of Cu(111) as a dispersed, isolated atom. Additionally, we determined that exposure to CO may induce surface islanding or dispersion, again depending on the alloy constitution, but also the partial pressure of CO. We posed that this gives rise to an interesting opportunity, whereby it may be possible to fine-tune the ensemble size of dopant atom clusters in highly dilute binary metal alloys through manipulation of the CO partial pressure; this will allow for the development of new materials that could exhibit novel and exciting catalytic properties.

In summary, the work described in this thesis has contributed to the development of *Single Atom Alloy* catalysts and will continue to offer guidance to experimentalists, facilitating the rational design and optimisation of catalytic materials.

Further Avenues of Research

Finally, we outline some interesting prospects for furthering research based on the work detailed in this thesis. The relative infancy of research involving SAAs, as well as their novelty, make them an attractive subject to investigate. In particular, we highlight that the number of experimental publications and projects appearing on SAAs is increasing rapidly, though theoretical research focussed on the prediction of SAA behaviour remains relatively

elusive. Theoretical research, akin to that presented in this thesis, may be performed in a fraction of the time and at a fraction of the cost of equivalent experimental research, making it an extremely powerful and useful tool for the catalysis community. Therefore, we briefly highlight below some avenues of theoretical research on the topic of SAAs that will undoubtedly aid in the advancement of this up-and-coming field of study.

Fast Prediction of SAA Catalytic Behaviour using Descriptors

We have shown how SAAs exhibit novel properties that their monometallic counterparts do not. We have primarily attributed this to SAAs escaping from traditional linear scaling relationships that are almost universally adhered to by monometallic transition metals. Though this is a tremendously exciting finding, it does however remove an element of predictability when considering the reactivity of SAAs.

Previously with transition metal catalysts, one could easily estimate the adsorption energy of many catalytically relevant intermediates by using thermo-chemical scaling from the adsorption energy of just a single adatom. Moreover, using differences in adsorption energies to obtain reaction energies, one could subsequently employ the Brønsted-Evans-Polanyi relationship to predict activation energies. This information is then sufficient for one to gauge the surface catalytic activity of a material.

Breaking these linear scaling relationships using SAAs results in novel catalytic properties beyond the realms of that achievable by traditional transition metal catalysts, albeit makes the design of SAA catalysts much trickier. It follows that, if by some other means, a degree of predictability can be restored and applied to SAAs it will be possible to engineer new catalysts without the need for extensive computational work. In order to do so, one must determine the cause of the variation of properties between different binary metal combinations or identify a descriptor that is well correlated with such changes.

Hammer and Nørskov¹⁹ developed the d-band model for transition metals and alloy materials thereof, that correlates the adsorption energy with the weighted average of the surface d-band density of states. The d-band model assumes that the s/p state contribution

to the surface chemical reactivity is constant and thereby any variations when considering different transition metal surfaces can be approximated by the occupation of the d-band at the Fermi level. This has proven tremendously useful in the facile approximation of surface binding properties, without the need for expensive computational calculations. Unfortunately, our work shows that due to the high dilution of the single atom in the host metal within a SAA, in addition to the large contribution to the adsorption properties from the s-/p-bands of the noble metal hosts, the d-band model cannot be applied to SAAs.

Wang and Hu^{173, 262} were able to derive a “bonding equation” to approximate adsorption energies on surfaces whereby a single, unreactive metal is doped into a catalytic metal host; in other words, an inverse SAA. This equation is formulated by combining the d-band model with additional terms evaluating the strain effects caused by having a size mismatch between two metallic elements, as well as adsorption-site-specific terms accounting for the extent of host and dopant bonding contributions to the adsorbate.

We noted in our discussion in Chapter 3 that deviations from linear scaling can be attributed to different species bonding in different sites whereby the contribution from each metal atom varies. Given that the “bonding equation” of Hu and co-workers takes this into account,^{173, 262} it was anticipated that this could also be applied to SAAs. However, a brief attempt to apply the “bonding equation” to SAAs was unsuccessful and we pose that this is due to the high dilution of the catalytic dopant atom in the noble metal host (which has a full d sub-shell), thereby making the d-band model terms in the “bonding equation” impractical for application here.

The derivation of a “bonding equation” that is applicable to SAAs would prove tremendously useful. At present, reliable adsorption energies of species on SAAs can only be ascertained using computationally expensive techniques such as DFT, though a descriptor based model in the spirit of the work of Hu, Hammer, Nørskov and others would make screening for useful chemistries that can be performed by SAAs much more efficient.

Such a model would require an in depth analysis of the electronic structure of SAAs, quantifying differences in the surface band structure between SAAs and monometallic analogous as well as determining the effect of isolating the single dopant atom. We envisage an investigation whereby the local density of states of SAA surfaces, and that projected on single dopant atoms as well as shared dopant-host sites, are analysed with respect to hybridisation with adsorbate electronic states. Determining how changes in the extent of hybridisation manifest over different SAA combinations will allow the electronic element of the “bonding equation” to be modified, thereby facilitating application to adsorption on SAA surfaces. To ensure completeness and general applicability, such a screening would need to be performed over a wide range of chemical substrates and SAA surfaces.

Selective Hydrogenation of Unsaturated Hydrocarbons

In Chapter 3, we considered simple bond scission reactions in a number of small, catalytically relevant molecules and demonstrated that SAAs offer facile activation of H-H, C-H and O-H bonds. Regarding the former, this has been validated experimentally in several cases.^{6, 54, 56, 58-63, 66, 67, 237} Moreover, the hydrogenation activity of SAAs is shown to be very high compared to monometallic host materials, though extremely selective compared to monometallic dopant materials.^{6, 53, 56, 59, 60, 62} Low temperature experiments demonstrate that atomic H* can spillover from the catalytically active, single dopant atom onto facets of the pure host metal whereby hydrogenation reactions are thought to be performed with high selectivity.^{6, 54, 58, 61-63}

Activation of H_{2(g)} at the single dopant site followed by H* spillover onto the host metal and subsequent hydrogenation is an example of a catalytic bi-functionality. It remains a hot topic in the catalysis community as to whether or not catalytic bi-functionality can be exhibited by a heterogeneous material.^{17, 159, 263-265} Even with the array of advanced techniques available to experimentalists today, it is impossible for them to conclusively prove if indeed a heterogeneous catalyst is bi-functional or not; the net catalytic function is all that can be observed experimentally.^{17, 264, 265}

It follows that the only way to quantify the extent of the mono- or bi-functionality of SAAs is to model the system theoretically.^{17, 159, 263} We pose that one could use a combination of DFT and KMC to model a reaction such as the hydrogenation of acetylene on SAAs. This reaction is often used as an experimental case-study to test the performance of hydrogenation catalysts; the activity can be monitored by the production of hydrocarbon products with greater saturation and the selectivity can be gauged by considering the ratio between acetylene, ethylene and ethane.^{174, 175, 266-272}

We have already computed the H_{2(g)} activation barriers and H* adsorption energies on an assortment of SAAs, as reported in this thesis. In addition to this, DFT could be used to compute the adsorption energies of acetylene and its products of hydrogenation, as well as the relevant activation barriers linking these intermediates. The energetics and mechanistic pathways will need to be considered on the SAA and then on the pure host metal. All of the information from DFT can be coarse-grained into kinetic constants and used to describe elementary events in a KMC model of acetylene hydrogenation.

Analysis of reaction statistics from KMC simulations will shed light into the active pathways and the active sites onto which specific elementary events occur. We expect that H_{2(g)} activation will occur on single dopant atoms with subsequent spillover to the facets of the host metal allowing for a build of H* coverage on the surface. The extent of the H* coverage after spillover will be dependent on the adsorption energy of H* on the host material, as well as the system conditions.

For the catalyst to exhibit bi-functionality, the spilt-over H* must react on the facets of the host metal. Using KMC we will be able to determine if the dramatic, experimentally observed activity and selectivity improvements of SAA hydrogenation catalysts over their monometallic counterparts, is indeed the result of bi-functionality or simply attributed to all of the chemistry occurring at single dopant atom sites. This work will provide a conclusive answer the question of whether bi-functionality on heterogeneous catalytic surfaces is possible or not.

Carbon-Carbon Coupling on Pt/Cu Single Atom Alloys

We detailed the chemistry of C-H bond scission reactions in methane derivatives on the Pt/Cu(111) SAA surface in Chapter 4. We showed how Pt/Cu(111) SAA is able to combine low temperature C-H bond activation with high resistance to coke formation. Our kinetic modelling suggested that Pt/Cu(111) SAA and Cu(111) produce the same maximum yield of $\text{CH}_4\text{(g)}$ when dosing the surface with CH_3^* , reflecting the similarities of the surfaces in terms of coke resistance. The simulations do however suggest that some CH^* is left behind on both surfaces due to a lack of a source of H^* to hydrogenate this to $\text{CH}_4\text{(g)}$.

Experimentally, C_2 and C_3 hydrocarbons are observed as gaseous products during thermal desorption from both surfaces. The desorption of these products coincides with the temperatures of C-H activation and is rate limited by these scissions as the thermal desorption of these products alone occurs at much lower temperatures.^{211, 212, 225, 226} We therefore suggest that the remaining CH^* , left on the Pt/Cu(111) SAA and Cu(111) surfaces during our simulations, are in reality involved in C-C coupling reactions that result in C_2 and C_3 hydrocarbon formation.

It would be of interest to determine the how the mechanism of C-C coupling on Pt/Cu(111) SAA differs to that on Cu(111).²⁷³ One could determine the adsorption energies of coupled products as well as the minimum energy pathways to these species from CH_x^* precursors. By incorporating this data into the KMC model that we detailed in Chapter 4, one could study the effect of the C-C coupling mechanism on the carbon deposition of the surface, considering the formation of gaseous species and graphitic carbon. It is feasible to assume the CH^* we simulate to remain on the surface, could be an artefact of not accounting for any C-C coupling mechanisms in the KMC. Improving the model in this way will allow for analysis of the coupled product selectivity and activity exhibited by each surface.

In addition, a complete KMC model that includes C-C coupling could be used to identify conditions whereby the production of C_2 and C_3 products from methane is optimised. Combining low temperature C-H activation with high potential for C-C coupling could be the answer to designing a material capable of efficiently upgrading methane to higher order

hydrocarbons. Furthermore, considering other SAA combinations may provide advances towards this goal as, for example, Au and Ag surfaces can perform C-C coupling though are poor C-H activation catalysts²⁷⁴ and therefore their catalytic properties may be enhanced by single atom doping.

Structure-Activity Relations in Single Atom Alloy Nanoparticles

The studies performed and discussed in Chapters 3 and 4 of this thesis assumed that the structure of the material in question is well-defined; that is, under reaction conditions, the SAA structure is stable and indeed more favourable than other highly dilute structures. It was with this in mind that we performed the investigation in Chapter 5, considering the thermodynamic stability of the SAA structure within the limit of high dilution and how that stability is affected by the presence of strong binding CO adsorbates.

Our study was based on static DFT energetics calculated at 0 K, which neglect any entropic contributions. We pose that a Metropolis Monte Carlo type approach within the framework of the canonical thermodynamic ensemble can be used in order to better predict the structural variation of SAAs. The canonical ensemble fixes the number of particles in the system and is equivalent to using a specific dopant loading, experimentally. This model would involve a swapping algorithm, whereby the atoms may freely interchange within the surface. This does not account for kinetics, though should converge to the correct thermodynamic limit. An energetics model can incorporate the segregation and aggregation energies we have already computed from DFT and therefore the system can be relaxed with respect to these energies whilst accounting for configurational entropy.

An extension of this simple idea is to use DFT to ascertain the segregation and aggregation energies for facets other than the (111) surface. By doing so, for example with the (100) facet as well as (331), (311), (221) etc. one can have sufficient data to construct a nanoparticle lattice. We envisage Metropolis Monte Carlo simulations whereby the total lattice is a combination of low-index surfaces (i.e. (111) and (100)) representing facets, that are connected by high-index surfaces (i.e. (331), (311), (221) etc.) representing edges and

corners. The outcome of the simulation will give the distribution of dopant atoms within the nanoparticle.

Knowing how the dopant atoms arrange in a nanoparticle at different dopant metal loadings will be key to understanding the performance of SAA nanoparticles. From a theoretical point of view, this work will provide a calculation guide whereby only the facets containing dopant atoms that manifest in reality need to be considered in modelling. This rationale is also relevant for surface science experiments, where the chemistry of only a single facet of material is considered at any one time.

Our work in this thesis has focused solely on the (111) facet as this is the most common facet for Cu, Ag and Au as a result of having the lowest surface free energy compared to other facets.²⁴⁷ It may be the case that other facets are more active and are responsible for the observed activity in nanoparticle experiments. Indeed, monometallic nanoparticle edge and corner sites are generally more reactive than low-index facets due to low metal atom coordination number,²⁷⁵ however, it may be the case for SAAs that it is not favourable for single dopant atoms to segregate here.

In Chapter 5 we showed that CO has a notable effect on the segregation and aggregation of single atoms at high dilution in metal alloys. Thus, incorporation of CO into the Metropolis Monte Carlo (within a grand-canonical ensemble setup) would be valuable in determining its effect on the nanoparticle structure. CO is particularly important as an adsorbate, as it is often unavoidably present in trace amounts in gaseous streams. Moreover, we touched briefly upon manipulation of the CO partial pressure to promote aggregation in such a way that dimer and multimer surface architectures could be synthesised. This Metropolis Monte Carlo model would have the capacity to test whether indeed this is possible and qualitatively reproduce the phase changes in nanoparticles, as well as each individual facet upon changes in the CO partial pressure.

This study could be carried out with many different adsorbates to determine the structural consequences of their presence in highly dilute binary alloys. Other useful adsorbates to

consider would include atomic species such as O*, S* and H*, all of which are important to many catalytic processes, and are typically found at high coverages on the catalytic surface, thereby potentially inducing structural changes in the material.

Conclusion

We have highlighted just a few ideas that have manifested as a result of the work carried out and reported in this thesis. Pursuing the ideas suggested here would further our fundamental understanding of these materials and better guide the design of SAA catalysts.

Final Remarks

This thesis has focused on a novel class of materials known as single atom alloys. We have extensively explored the chemistry of these materials from the point-of-view of catalysis, using state-of-the-art computational methods. We have demonstrated that single atom alloys are capable of offering enhanced catalytic behaviour, with regard to activity, selectivity, stability and resistance to poisoning. Finally, we have briefly highlighted some interesting avenues of research that the work in this has opened up.

The author sincerely hopes that the readers have enjoyed the story contained within this thesis, as much as the author himself has enjoyed carrying out the work. Thank you.

Chapter 7 Bibliography

1. Deloitte, Global Chemical Industry M&A Outlook (2017).
2. Freedonia, World Catalysts - Industry Market Research, Market Share, Market Size, Sales, Demand Forecast, Market Leaders, Company Profiles, Industry Trends (2014).
3. J. Hagen, *Industrial Catalysis: A Practical Approach*, 3rd ed. (Wiley, 2015).
4. M. Schmal, *Heterogeneous Catalysis and its Industrial Applications*. (Springer, 2016).
5. J. M. Thomas, *Principles and Practice of Heterogeneous Catalysis*, 2nd ed. (Wiley, 2014).
6. G. Kyriakou, M. B. Boucher, A. D. Jewell, E. A. Lewis, T. J. Lawton, A. E. Baber, H. L. Tierney, M. Flytzani-Stephanopoulos and E. C. H. Sykes, *Science* **335** (6073), 1209-1212 (2012).
7. A. J. Medford, A. Vojvodic, J. S. Hummelshøj, J. Voss, F. Abild-Pedersen, F. Studt, T. Bligaard, A. Nilsson and J. K. Nørskov, *Journal of Catalysis* **328**, 36-42 (2015).
8. M. T. Darby, S. Piccinin and M. Stamatakis, in *Physics of Surface, Interface and Cluster Catalysis* (IOP Publishing, 2016), pp. 4-1-4-38.
9. R. A. v. Santen, M. Neurock and S. G. Shetty, *Chemical Reviews* **110** (4), 2005-2048 (2010).
10. M. Stamatakis and D. G. Vlachos, *ACS Catalysis* **2** (12), 2648-2663 (2012).
11. J. K. Norskov, T. Bligaard, J. Rossmeisl and C. H. Christensen, *Nat Chem* **1** (1), 37-46 (2009).
12. J. K. Norskov, T. Bligaard, B. Hvolbaek, F. Abild-Pedersen, I. Chorkendorff and C. H. Christensen, *Chemical Society Reviews* **37** (10), 2163-2171 (2008).
13. B. Christian Enger, R. Lødeng and A. Holmen, *Applied Catalysis A: General* **346** (1), 1-27 (2008).
14. J. R. Jennings, *Catalytic Ammonia Synthesis: Fundamentals and Practice*. (Springer Science, New York, 1991).
15. S. De, J. Zhang, R. Luque and N. Yan, *Energy & Environmental Science* **9** (11), 3314-3347 (2016).
16. M. Che, *Catalysis Today* **218-219** (Supplement C), 162-171 (2013).
17. A. Vojvodic and J. K. Nørskov, *National Science Review* **2** (2), 140-143 (2015).
18. J. Greeley, *Annual Review of Chemical and Biomolecular Engineering* **7** (1), 605-635 (2016).
19. B. Hammer and J. K. Nørskov, *Nature* **376** (6537), 238-240 (1995).
20. B. Hammer and J. K. Nørskov, *Surface Science* **343** (3), 211-220 (1995).
21. B. Hammer and J. K. Nørskov, in *Advances in Catalysis* (Academic Press, 2000), Vol. Volume 45, pp. 71-129.
22. J. K. Norskov, *The Journal of Chemical Physics* **90** (12), 7461-7471 (1989).
23. F. Abild-Pedersen, J. Greeley, F. Studt, J. Rossmeisl, T. R. Munter, P. G. Moses, E. Skúlason, T. Bligaard and J. K. Nørskov, *Physical Review Letters* **99** (1), 016105 (2007).
24. S. Wang, V. Petzold, V. Tripkovic, J. Kleis, J. G. Howalt, E. Skulason, E. M. Fernandez, B. Hvolbaek, G. Jones, A. Toftlund, H. Falsig, M. Bjorketun, F. Studt, F. Abild-Pedersen, J. Rossmeisl, J. K. Nørskov and T. Bligaard, *Physical Chemistry Chemical Physics* **13** (46), 20760-20765 (2011).
25. J. K. Nørskov, F. Abild-Pedersen, F. Studt and T. Bligaard, *Proceedings of the National Academy of Sciences* **108** (3), 937-943 (2011).
26. M. M. Montemore and J. W. Medlin, *Catalysis Science & Technology* **4** (11), 3748-3761 (2014).
27. A. Vojvodic, A. Hellman, C. Ruberto and B. I. Lundqvist, *Physical Review Letters* **103** (14), 146103 (2009).
28. R. P. Bell, *Proceedings of the Royal Society of London. Series A - Mathematical and Physical Sciences* **154** (882), 414-429 (1936).
29. M. G. Evans and M. Polanyi, *Transactions of the Faraday Society* **32** (0), 1333-1360 (1936).
30. M. G. Evans and M. Polanyi, *Transactions of the Faraday Society* **34** (0), 11-24 (1938).
31. Z.-P. Liu and P. Hu, *The Journal of Chemical Physics* **114** (19), 8244-8247 (2001).
32. V. Pallassana and M. Neurock, *Journal of Catalysis* **191** (2), 301-317 (2000).
33. A. Logadottir, T. H. Rod, J. K. Nørskov, B. Hammer, S. Dahl and C. J. H. Jacobsen, *Journal of Catalysis* **197** (2), 229-231 (2001).
34. A. Michaelides, Z. P. Liu, C. J. Zhang, A. Alavi, D. A. King and P. Hu, *Journal of the American Chemical Society* **125** (13), 3704-3705 (2003).
35. P. Ferrin, A. U. Nilekar, J. Greeley, M. Mavrikakis and J. Rossmeisl, *Surface Science* **602** (21), 3424-3431 (2008).
36. P. Ferrin, D. Simonetti, S. Kandoi, E. Kunke, J. A. Dumesic, J. K. Nørskov and M. Mavrikakis, *Journal of the American Chemical Society* **131** (16), 5809-5815 (2009).
37. B. Liu and J. Greeley, *The Journal of Physical Chemistry C* **115** (40), 19702-19709 (2011).

38. J. S. Yoo, F. Abild-Pedersen, J. K. Nørskov and F. Studt, *ACS Catalysis* **4** (4), 1226-1233 (2014).
39. J. Greeley and M. Mavrikakis, *Nat Mater* **3** (11), 810-815 (2004).
40. E. M. Fernández, P. G. Moses, A. Toftelund, H. A. Hansen, J. I. Martínez, F. Abild-Pedersen, J. Kleis, B. Hinnemann, J. Rossmeisl, T. Bligaard and J. K. Nørskov, *Angewandte Chemie International Edition* **47** (25), 4683-4686 (2008).
41. A. Vojvodic, F. Calle-Vallejo, W. Guo, S. Wang, A. Toftelund, F. Studt, J. I. Martínez, J. Shen, I. C. Man, J. Rossmeisl, T. Bligaard, J. K. Nørskov and F. Abild-Pedersen, *The Journal of Chemical Physics* **134** (24), 244509 (2011).
42. F. Viñes, A. Vojvodic, F. Abild-Pedersen and F. Illas, *The Journal of Physical Chemistry C* **117** (8), 4168-4171 (2013).
43. F. Calle-Vallejo, J. I. Martínez, J. M. García-Lastra, P. Sautet and D. Loffreda, *Angewandte Chemie International Edition* **53** (32), 8316-8319 (2014).
44. F. Calle-Vallejo, D. Loffreda, T. M. KoperMarc and P. Sautet, *Nat Chem* **7** (5), 403-410 (2015).
45. M. Fields, C. Tsai, L. D. Chen, F. Abild-Pedersen, J. K. Nørskov and K. Chan, *ACS Catalysis* **7** (4), 2528-2534 (2017).
46. J. Rodriguez, *Surface Science Reports* **24** (7), 223-287 (1996).
47. F. Besenbacher, I. Chorkendorff, B. S. Clausen, B. Hammer, A. M. Molenbroek, J. K. Nørskov and I. Stensgaard, *Science* **279** (5358), 1913-1915 (1998).
48. J. Greeley and M. Mavrikakis, *Catalysis Today* **111** (1-2), 52-58 (2006).
49. J. R. Kitchin, J. K. Nørskov, M. A. Barteau and J. G. Chen, *The Journal of Chemical Physics* **120** (21), 10240-10246 (2004).
50. J. R. Kitchin, J. K. Nørskov, M. A. Barteau and J. G. Chen, *Physical Review Letters* **93** (15), 156801 (2004).
51. P. Liu and J. K. Norskov, *Physical Chemistry Chemical Physics* **3** (17), 3814-3818 (2001).
52. F. Maroun, F. Ozanam, O. M. Magnussen and R. J. Behm, *Science* **293** (5536), 1811-1814 (2001).
53. J. Liu, J. Shan, F. R. Lucci, S. Cao, E. C. H. Sykes and M. Flytzani-Stephanopoulos, *Catalysis Science & Technology* **7** (19), 4276-4284 (2017).
54. F. R. Lucci, M. D. Marcinkowski, T. J. Lawton and E. C. H. Sykes, *The Journal of Physical Chemistry C* **119** (43), 24351-24357 (2015).
55. M. B. Boucher, M. D. Marcinkowski, M. L. Liriano, C. J. Murphy, E. A. Lewis, A. D. Jewell, M. F. G. Mattera, G. Kyriakou, M. Flytzani-Stephanopoulos and E. C. H. Sykes, *ACS Nano* **7** (7), 6181-6187 (2013).
56. J. Liu, F. R. Lucci, M. Yang, S. Lee, M. D. Marcinkowski, A. J. Therrien, C. T. Williams, E. C. H. Sykes and M. Flytzani-Stephanopoulos, *Journal of the American Chemical Society* **138** (20), 6396-6399 (2016).
57. J. Shan, F. R. Lucci, J. Liu, M. El-Soda, M. D. Marcinkowski, L. F. Allard, E. C. H. Sykes and M. Flytzani-Stephanopoulos, *Surface Science* **650**, 121-129 (2016).
58. F. R. Lucci, M. T. Darby, M. F. G. Mattera, C. J. Ivimey, A. J. Therrien, A. Michaelides, M. Stamatakis and E. C. H. Sykes, *The Journal of Physical Chemistry Letters* **7** (3), 480-485 (2016).
59. F. R. Lucci, J. Liu, M. D. Marcinkowski, M. Yang, L. F. Allard, M. Flytzani-Stephanopoulos and E. C. H. Sykes, *Nature Communications* **6**, 8550 (2015).
60. M. B. Boucher, B. Zugic, G. Cladaras, J. Kammert, M. D. Marcinkowski, T. J. Lawton, E. C. H. Sykes and M. Flytzani-Stephanopoulos, *Physical Chemistry Chemical Physics* **15** (29), 12187-12196 (2013).
61. A. E. Baber, H. L. Tierney, T. J. Lawton and E. C. H. Sykes, *ChemCatChem* **3** (3), 607-614 (2011).
62. M. D. Marcinkowski, A. D. Jewell, M. Stamatakis, M. B. Boucher, E. A. Lewis, C. J. Murphy, G. Kyriakou and E. C. H. Sykes, *Nat Mater* **12** (6), 523-528 (2013).
63. H. L. Tierney, A. E. Baber, J. R. Kitchin and E. C. H. Sykes, *Physical Review Letters* **103** (24), 246102 (2009).
64. J. Shan, N. Janvelyan, H. Li, J. Liu, T. M. Egle, J. Ye, M. M. Biener, J. Biener, C. M. Friend and M. Flytzani-Stephanopoulos, *Applied Catalysis B: Environmental* **205**, 541-550 (2017).
65. Z.-T. Wang, M. T. Darby, A. J. Therrien, M. El-Soda, A. Michaelides, M. Stamatakis and E. C. H. Sykes, *The Journal of Physical Chemistry C* **120** (25), 13574-13580 (2016).
66. F. R. Lucci, T. J. Lawton, A. Pronschinske and E. C. H. Sykes, *The Journal of Physical Chemistry C* **118** (6), 3015-3022 (2014).
67. G. Kyriakou, E. R. M. Davidson, G. Peng, L. T. Roling, S. Singh, M. B. Boucher, M. D. Marcinkowski, M. Mavrikakis, A. Michaelides and E. C. H. Sykes, *ACS Nano* **8** (5), 4827-4835 (2014).
68. H. Miura, K. Endo, R. Ogawa and T. Shishido, *ACS Catalysis* **7** (3), 1543-1553 (2017).

69. M. Born and R. Oppenheimer, *Annalen der Physik* **389** (20), 457-484 (1927).
70. F. Jensen, *Introduction to Computational Chemistry*. (John Wiley & Sons, 2006).
71. C. J. Cramer, *Essentials of Computational Chemistry: Theories and Models (2nd Edition)*. (John Wiley & Sons, 2004).
72. A. Szabo and N. Ostlund, *Modern Quantum Chemistry: Introduction to Advanced Electronic Structure Theory (Dover Books on Chemistry)*. (Dover Publications, 1996).
73. M. Morales, R. Clay, C. Pierleoni and D. Ceperley, *Entropy* **16** (1), 287 (2013).
74. D. Ceperley and B. Alder, *Science* **231** (4738), 555-560 (1986).
75. D. R. Hartree, *Mathematical Proceedings of the Cambridge Philosophical Society* **24** (01), 89-110 (1928).
76. V. Fock, *Z. Physik* **61** (1-2), 126-148 (1930).
77. E. Lieb and B. Simon, *Commun.Math. Phys.* **53** (3), 185-194 (1977).
78. R. J. Bartlett and M. Musiał, *Reviews of Modern Physics* **79** (1), 291-352 (2007).
79. C. Møller and M. S. Plesset, *Physical Review* **46** (7), 618-622 (1934).
80. K. Raghavachari, G. W. Trucks, J. A. Pople and M. Head-Gordon, *Chemical Physics Letters* **157** (6), 479-483 (1989).
81. T. Kato, *Communications on Pure and Applied Mathematics* **10** (2), 151-177 (1957).
82. W. Koch and M. Holthausen, *A Chemist's Guide to Density Functional Theory, 2nd Edition*. (Wiley-VCH, 2001).
83. P. A. M. Dirac, *Mathematical Proceedings of the Cambridge Philosophical Society* **26** (03), 376-385 (1930).
84. P. Hohenberg and W. Kohn, *Physical Review* **136** (3B), B864-B871 (1964).
85. W. Kohn and L. J. Sham, *Physical Review* **140** (4A), A1133-A1138 (1965).
86. J. P. Perdew and K. Schmidt, *AIP Conference Proceedings* **577** (1), 1-20 (2001).
87. S. Kurth, J. P. Perdew and P. Blaha, *International Journal of Quantum Chemistry* **75** (4-5), 889-909 (1999).
88. V. N. Staroverov, G. E. Scuseria, J. Tao and J. P. Perdew, *Physical Review B* **69** (7), 075102 (2004).
89. A. D. Becke, *The Journal of Chemical Physics* **84** (8), 4524-4529 (1986).
90. A. van de Walle and G. Ceder, *Physical Review B* **59** (23), 14992-15001 (1999).
91. R. Q. Hood, M. Y. Chou, A. J. Williamson, G. Rajagopal and R. J. Needs, *Physical Review B* **57** (15), 8972-8982 (1998).
92. O. Gunnarsson, M. Jonson and B. I. Lundqvist, *Physical Review B* **20** (8), 3136-3164 (1979).
93. S.-k. Ma and K. A. Brueckner, *Physical Review* **165** (1), 18-31 (1968).
94. A. D. Becke, *Physical Review A* **38** (6), 3098-3100 (1988).
95. J. P. Perdew and W. Yue, *Physical Review B* **33** (12), 8800-8802 (1986).
96. J. P. Perdew, J. A. Chevary, S. H. Vosko, K. A. Jackson, M. R. Pederson, D. J. Singh and C. Fiolhais, *Physical Review B* **46** (11), 6671-6687 (1992).
97. J. P. Perdew, K. Burke and M. Ernzerhof, *Physical Review Letters* **77** (18), 3865-3868 (1996).
98. J. P. Perdew, S. Kurth, A. Zupan and P. Blaha, *Physical Review Letters* **82** (25), 5179-5179 (1999).
99. C. Adamo, M. Ernzerhof and G. E. Scuseria, *The Journal of Chemical Physics* **112** (6), 2643-2649 (2000).
100. D. J. Tozer and N. C. Handy, *The Journal of Chemical Physics* **109** (23), 10180-10189 (1998).
101. J. P. Perdew and A. Zunger, *Physical Review B* **23** (10), 5048-5079 (1981).
102. B. Kristian, R. C. Valentino, L. Kyuho, S. Elsebeth, T. Thonhauser, H. Per and I. L. Bengt, *Reports on Progress in Physics* **78** (6), 066501 (2015).
103. S. Grimme, *Wiley Interdisciplinary Reviews: Computational Molecular Science* **1** (2), 211-228 (2011).
104. J. Klimeš, D. R. Bowler and A. Michaelides, *Journal of Physics: Condensed Matter* **22** (2), 022201 (2010).
105. J. Klimeš, D. R. Bowler and A. Michaelides, *Physical Review B* **83** (19), 195131 (2011).
106. J. Klimeš and A. Michaelides, *The Journal of Chemical Physics* **137** (12), 120901 (2012).
107. C. Kittel, *Introduction to Solid State Physics*. (Wiley, 2005).
108. M. C. Payne, M. P. Teter, D. C. Allan, T. A. Arias and J. D. Joannopoulos, *Reviews of Modern Physics* **64** (4), 1045-1097 (1992).
109. H. J. Monkhorst and J. D. Pack, *Physical Review B* **13** (12), 5188-5192 (1976).
110. V. Brazdova and D. Bowler, *Atomistic Computer Simulations: A Practical Guide*. (Wiley-VCH, 2013).
111. P. E. Blöchl, *Physical Review B* **50** (24), 17953-17979 (1994).
112. D. Marx and J. Hutter, *Ab Initio Molecular Dynamics: Basic Theory and Advanced Methods*. (Cambridge University Press, 2009).

113. A. F. Voter, F. Montalenti and T. C. Germann, Annual Review of Materials Research **32** (1), 321-346 (2002).
114. M. Stamatakis, Journal of Physics: Condensed Matter **27** (1), 013001 (2015).
115. M. Stamatakis, American Chemical Society Catalysis **2**, 2648 (2012).
116. A. Chatterjee and D. Vlachos, J Computer-Aided Mater Des **14** (2), 253-308 (2007).
117. A. Voter, in *Radiation Effects in Solids*, edited by K. Sickafus, E. Kotomin and B. Uberuaga (Springer Netherlands, 2007), Vol. 235, pp. 1-23.
118. A. P. J. Jansen, Computer Physics Communications **86** (1-2), 1-12 (1995).
119. J. J. Lukkien, J. P. L. Segers, P. A. J. Hilbers, R. J. Gelten and A. P. J. Jansen, Physical Review E **58** (2), 2598-2610 (1998).
120. D. Gillespie, *Markov Processes: An Introduction for Physical Scientists*. (Academic Press, 1991).
121. D. T. Gillespie, Journal of Computational Physics **22** (4), 403-434 (1976).
122. D. T. Gillespie, The Journal of Physical Chemistry **81** (25), 2340-2361 (1977).
123. P. Dufour, M. Dumont, V. Chabart and J. Lion, Computers & Chemistry **13** (1), 25-32 (1989).
124. M. Dumont and P. Dufour, Computer Physics Communications **41** (1), 1-19 (1986).
125. H. Kang and W. Weinberg, Accounts of Chemical Research **25** (6), 253-259 (1992).
126. E. Cinlar, *Introduction to Stochastic Processes*. (Prentice-Hall, Inc., 1975).
127. K. A. Fichthorn and W. H. Weinberg, The Journal of Chemical Physics **95** (2), 1090-1096 (1991).
128. K. Reuter, in *Modeling and Simulation of Heterogeneous Catalytic Reactions* (Wiley-VCH Verlag GmbH & Co. KGaA, 2011), pp. 71-111.
129. P. Pechukas, in *Dynamics of Molecular Collisions B*, edited by W. Miller (Plenum Press, New York, 1976).
130. D. McQuarrie, *Statistical Mechanics*. ({University Science Books}, 2000).
131. P. Hänggi, P. Talkner and M. Borkovec, Reviews of Modern Physics **62** (2), 251-341 (1990).
132. M. Neurock and E. W. Hansen, Computers & Chemical Engineering **22**, Supplement 1 (0), S1045-S1060 (1998).
133. E. W. Hansen and M. Neurock, Chemical Engineering Science **54** (15-16), 3411-3421 (1999).
134. K. Reuter, D. Frenkel and M. Scheffler, Physical Review Letters **93** (11), 116105 (2004).
135. D. Mei, J. Du and M. Neurock, Industrial & Engineering Chemistry Research **49** (21), 10364-10373 (2010).
136. M. J. Hoffmann, M. Scheffler and K. Reuter, ACS Catalysis **5** (2), 1199-1209 (2015).
137. M. Stamatakis, M. A. Christiansen, D. G. Vlachos and G. Mpourmpakis, Nano Letters **12** (7), 3621-3626 (2012).
138. W. Guo, M. Stamatakis and D. G. Vlachos, ACS Catalysis **3** (10), 2248-2255 (2013).
139. S. Piccinin and M. Stamatakis, Acs Catalysis **4** (7), 2143-2152 (2014).
140. M. Stamatakis, Y. Chen and D. G. Vlachos, The Journal of Physical Chemistry C **115** (50), 24750-24762 (2011).
141. J. Rogal, K. Reuter and M. Scheffler, Physical Review B **77** (15), 155410 (2008).
142. J. M. Sanchez, F. Ducastelle and D. Gratias, Physica A: Statistical Mechanics and its Applications **128** (1-2), 334-350 (1984).
143. J. Nielsen, M. d'Avezac, J. Hetherington and M. Stamatakis, The Journal of Chemical Physics **139** (22), 224706 (2013).
144. V. Blum, G. L. W. Hart, M. J. Walorski and A. Zunger, Physical Review B **72** (16), 165113 (2005).
145. A. van de Walle and G. Ceder, JPE **23** (4), 348-359 (2002).
146. A. B. Bortz, M. H. Kalos and J. L. Lebowitz, Journal of Computational Physics **17** (1), 10-18 (1975).
147. L. J. Karssemeijer, A. Pedersen, H. Jonsson and H. M. Cuppen, Physical Chemistry Chemical Physics **14** (31), 10844-10852 (2012).
148. M. Leetmaa and N. V. Skorodumova, Computer Physics Communications **185** (9), 2340-2349 (2014).
149. M. J. Hoffmann, S. Matera and K. Reuter, Computer Physics Communications **185** (7), 2138-2150 (2014).
150. E. W. Hansen and M. Neurock, Journal of Catalysis **196** (2), 241-252 (2000).
151. M. Stamatakis and D. G. Vlachos, The Journal of Chemical Physics **134** (21), 214115 (2011).
152. M. A. Gibson and J. Bruck, The Journal of Physical Chemistry A **104** (9), 1876-1889 (2000).
153. A. P. J. Jansen, (2003).
154. M. Stamatakis and D. G. Vlachos, Computers & Chemical Engineering **35** (12), 2602-2610 (2011).

155. C. J. H. Jacobsen, S. Dahl, B. S. Clausen, S. Bahn, A. Logadottir and J. K. Nørskov, *Journal of the American Chemical Society* **123** (34), 8404-8405 (2001).
156. P. Sabatier, *Berichte der deutschen chemischen Gesellschaft* **44** (3), 1984-2001 (1911).
157. A. A. Peterson and J. K. Nørskov, *The Journal of Physical Chemistry Letters* **3** (2), 251-258 (2012).
158. X. Hong, K. Chan, C. Tsai and J. K. Nørskov, *ACS Catalysis* **6** (7), 4428-4437 (2016).
159. M. Andersen, A. J. Medford, J. K. Nørskov and K. Reuter, *ACS Catalysis*, 3960-3967 (2017).
160. F. Calle-Vallejo, J. I. Martínez, J. M. García-Lastra, J. Rossmeisl and M. T. M. Koper, *Physical Review Letters* **108** (11), 116103 (2012).
161. X. Zhang, S. Yu, W. Zheng and P. Liu, *Physical Chemistry Chemical Physics* **16** (31), 16615-16622 (2014).
162. J. Greeley and J. K. Nørskov, *Surface Science* **601** (6), 1590-1598 (2007).
163. GreeleyJ, I. E. L. Stephens, A. S. Bondarenko, T. P. Johansson, H. A. Hansen, T. F. Jarillo, RossmeislJ, Chorkendorffl and J. K. Nørskov, *Nat Chem* **1** (7), 552-556 (2009).
164. J. Ko, B.-K. Kim and J. W. Han, *The Journal of Physical Chemistry C* **120** (6), 3438-3447 (2016).
165. Q. Fu, X. Cao and Y. Luo, *The Journal of Physical Chemistry C* **117** (6), 2849-2854 (2013).
166. J. L. C. Fajin, M. N. D. S. Cordeiro and J. R. B. Gomes, *RSC Advances* **6** (22), 18695-18702 (2016).
167. J. L. C. Fajín, M. N. D. S. Cordeiro, F. Illas and J. R. B. Gomes, *Journal of Catalysis* **313**, 24-33 (2014).
168. M. Gajdoš, A. Eichler and J. Hafner, *Journal of Physics: Condensed Matter* **16** (8), 1141 (2004).
169. Y. Xu, A. V. Ruban and M. Mavrikakis, *Journal of the American Chemical Society* **126** (14), 4717-4725 (2004).
170. J. L. C. Fajín, M. N. D. S. Cordeiro and J. R. B. Gomes, *Applied Catalysis A: General* **458**, 90-102 (2013).
171. J. Greeley and J. K. Nørskov, *Surface Science* **592** (1–3), 104-111 (2005).
172. J. Ko, H. Kwon, H. Kang, B.-K. Kim and J. W. Han, *Physical Chemistry Chemical Physics* **17** (5), 3123-3130 (2015).
173. Z. Wang and P. Hu, *Chemical Communications* **53** (58), 8106-8109 (2017).
174. G. X. Pei, X. Y. Liu, A. Wang, A. F. Lee, M. A. Isaacs, L. Li, X. Pan, X. Yang, X. Wang, Z. Tai, K. Wilson and T. Zhang, *ACS Catalysis* **5** (6), 3717-3725 (2015).
175. G. X. Pei, X. Y. Liu, X. Yang, L. Zhang, A. Wang, L. Li, H. Wang, X. Wang and T. Zhang, *ACS Catalysis* **7** (2), 1491-1500 (2017).
176. A. J. McCue and J. A. Anderson, *Journal of Catalysis* **329**, 538-546 (2015).
177. G. Kresse and J. Hafner, *Physical Review B* **47** (1), 558-561 (1993).
178. W. Dong, G. Kresse, J. Furthmüller and J. Hafner, *Physical Review B* **54** (3), 2157-2166 (1996).
179. G. Kresse and J. Furthmüller, *Computational Materials Science* **6** (1), 15-50 (1996).
180. G. Kresse and D. Joubert, *Physical Review B* **59** (3), 1758-1775 (1999).
181. M. Dion, H. Rydberg, E. Schröder, D. C. Langreth and B. I. Lundqvist, *Physical Review Letters* **92** (24), 246401 (2004).
182. G. Henkelman, B. P. Uberuaga and H. Jónsson, *The Journal of Chemical Physics* **113** (22), 9901-9904 (2000).
183. G. Henkelman and H. Jónsson, *The Journal of Chemical Physics* **111** (15), 7010-7022 (1999).
184. M. M. Montemore and J. W. Medlin, *The Journal of Physical Chemistry C* **117** (39), 20078-20088 (2013).
185. A. Michaelides and P. Hu, *The Journal of Chemical Physics* **114** (6), 2523-2526 (2001).
186. A. Michaelides and P. Hu, *The Journal of Chemical Physics* **112** (18), 8120-8125 (2000).
187. A. Michaelides and P. Hu, *The Journal of Chemical Physics* **114** (13), 5792-5795 (2001).
188. J. Kua, F. Faglioni and W. A. Goddard, *Journal of the American Chemical Society* **122** (10), 2309-2321 (2000).
189. A. Michaelides and P. Hu, *Journal of the American Chemical Society* **122** (40), 9866-9867 (2000).
190. M. Neurock, *Journal of Catalysis* **216** (1), 73-88 (2003).
191. G. Marek, E. Andreas and H. Jürgen, *Journal of Physics: Condensed Matter* **16** (8), 1141 (2004).
192. M. Lynch and P. Hu, *Surface Science* **458** (1), 1-14 (2000).
193. T. J. Lawton, J. Carrasco, A. E. Baber, A. Michaelides and E. C. H. Sykes, *Physical Review Letters* **107** (25), 256101 (2011).
194. M.-J. Cheng, E. L. Clark, H. H. Pham, A. T. Bell and M. Head-Gordon, *ACS Catalysis* **6** (11), 7769-7777 (2016).

195. J. J. H. B. Sattler, J. Ruiz-Martinez, E. Santillan-Jimenez and B. M. Weckhuysen, *Chemical Reviews* **114** (20), 10613-10653 (2014).
196. J. Alper, presented at the *The Changing Landscape of Hydrocarbon Feedstocks for Chemical Production: Implications for Catalysis*, 2016 (unpublished).
197. A. E. Shilov and G. B. Shul'pin, *Chemical Reviews* **97** (8), 2879-2932 (1997).
198. J. A. Labinger and J. E. Bercaw, *Nature* **417** (6888), 507-514 (2002).
199. J. Wencel-Delord and F. Glorius, *5*, 369 (2013).
200. Z.-J. Zhao, C.-c. Chiu and J. Gong, *Chemical Science* **6** (8), 4403-4425 (2015).
201. H. M. Swaan, V. C. H. Kroll, G. A. Martin and C. Mirodatos, *Catalysis Today* **21** (2), 571-578 (1994).
202. E. Ruckenstein and Y. H. Hu, *Applied Catalysis A: General* **133** (1), 149-161 (1995).
203. N. Taccardi, M. Grabau, J. Debuschewitz, M. Distaso, M. Brandl, R. Hock, F. Maier, C. Papp, J. Erhard, C. Neiss, W. Peukert, A. Görling, H. P. Steinrück and P. Wasserscheid, *9*, 862 (2017).
204. F. Jiang, L. Zeng, S. Li, G. Liu, S. Wang and J. Gong, *ACS Catalysis* **5** (1), 438-447 (2015).
205. M. A. Henderson, G. E. Mitchell and J. M. White, *Surface Science Letters* **184** (1), L325-L331 (1987).
206. D. H. Fairbrother, X. D. Peng, M. Trenary and P. C. Stair, *Journal of the Chemical Society, Faraday Transactions* **91** (20), 3619-3625 (1995).
207. A. Iglesias-Juez, A. M. Beale, K. Maaijen, T. C. Weng, P. Glatzel and B. M. Weckhuysen, *Journal of Catalysis* **276** (2), 268-279 (2010).
208. N. M. Galea, D. Knapp and T. Ziegler, *Journal of Catalysis* **247** (1), 20-33 (2007).
209. F. Yang, J. Koeller and L. Ackermann, *Angewandte Chemie International Edition* **55** (15), 4759-4762 (2016).
210. J. M. Meyers and A. J. Gellman, *Surface Science* **339** (1), 57-67 (1995).
211. N. D. S. Canning, M. D. Baker and M. A. Chesters, *Surface Science* **111** (3), 441-451 (1981).
212. J. L. Lin and B. E. Bent, *Journal of Vacuum Science & Technology A: Vacuum, Surfaces, and Films* **10** (4), 2202-2209 (1992).
213. G. Gajewski and C.-W. Pao, *The Journal of Chemical Physics* **135** (6), 064707 (2011).
214. S. Gautier, S. N. Steinmann, C. Michel, P. Fleurat-Lessard and P. Sautet, *Physical Chemistry Chemical Physics* **17** (43), 28921-28930 (2015).
215. Q. Qi, X. Wang, L. Chen and B. Li, *Applied Surface Science* **284**, 784-791 (2013).
216. S. Nave and B. Jackson, *The Journal of Chemical Physics* **130** (5), 054701 (2009).
217. A. Michaelides and P. Hu, *Journal of the American Chemical Society* **123** (18), 4235-4242 (2001).
218. L. J. Richter and W. Ho, *Physical Review B* **36** (18), 9797-9800 (1987).
219. G. Anger, A. Winkler and K. D. Rendulic, *Surface Science* **220** (1), 1-17 (1989).
220. K. Christmann, G. Ertl and T. Pignet, *Surface Science* **54** (2), 365-392 (1976).
221. D. M. Collins and W. E. Spicer, *Surface Science* **69** (1), 85-113 (1977).
222. V. A. Ukrainstev and I. Harrison, *Surface Science Letters* **286** (3), L571-L576 (1993).
223. A. J. McCue, A. Gibson and J. A. Anderson, *Chemical Engineering Journal* **285**, 384-391 (2016).
224. M. Argyle and C. Bartholomew, *Catalysts* **5** (1), 145 (2015).
225. M. Pascal, C. L. A. Lamont, M. Kittel, J. T. Hoeft, L. Constant, M. Polcik, A. M. Bradshaw, R. L. Toomes and D. P. Woodruff, *Surface Science* **512** (3), 173-184 (2002).
226. C. Chao-Ming and B. E. Bent, *Surface Science* **279** (1), 79-88 (1992).
227. X. Cheng, Z. Shi, N. Glass, L. Zhang, J. Zhang, D. Song, Z.-S. Liu, H. Wang and J. Shen, *Journal of Power Sources* **165** (2), 739-756 (2007).
228. P. Trens, R. Durand, B. Coq, C. Coutanceau, S. Rousseau and C. Lamy, *Applied Catalysis B: Environmental* **92** (3), 280-284 (2009).
229. W. Vogel, L. Lundquist, P. Ross and P. Stonehart, *Electrochimica Acta* **20** (1), 79-93 (1975).
230. J. J. Baschuk and X. Li, *International Journal of Energy Research* **25** (8), 695-713 (2001).
231. J. Wang, C. Liu, A. Lushington, N. Cheng, M. N. Banis, A. Riese and X. Sun, *Electrochimica Acta* **210** (Supplement C), 285-292 (2016).
232. A. Groß, *Top Catal* **37** (1), 29-39 (2006).
233. X. Xu, Y. Zhang and Z. Yang, *Applied Surface Science* **357** (Part B), 1785-1791 (2015).
234. M. Wang, Z. Fu and Z. Yang, *Physics Letters A* **377** (34), 2189-2194 (2013).
235. T. J. Schmidt, Z. Jusys, H. A. Gasteiger, R. J. Behm, U. Endruschat and H. Boennemann, *Journal of Electroanalytical Chemistry* **501** (1), 132-140 (2001).
236. S. F. Ho, A. Mendoza-Garcia, S. Guo, K. He, D. Su, S. Liu, O. Metin and S. Sun, *Nanoscale* **6** (12), 6970-6973 (2014).
237. H. L. Tierney, A. E. Baber and E. C. H. Sykes, *The Journal of Physical Chemistry C* **113** (17), 7246-7250 (2009).

238. B. C. Han, A. Van der Ven, G. Ceder and B.-J. Hwang, *Physical Review B* **72** (20), 205409 (2005).
239. Y. Ma and P. B. Balbuena, *Surface Science* **603** (2), 349-353 (2009).
240. B. Zhu, G. Thrimurthulu, L. Delannoy, C. Louis, C. Mottet, J. Creuze, B. Legrand and H. Guesmi, *Journal of Catalysis* **308** (Supplement C), 272-281 (2013).
241. A. Dhouib and H. Guesmi, *Chemical Physics Letters* **521** (Supplement C), 98-103 (2012).
242. H. Guesmi, C. Louis and L. Delannoy, *Chemical Physics Letters* **503** (1), 97-100 (2011).
243. M. Sansa, A. Dhouib and H. Guesmi, *The Journal of Chemical Physics* **141** (6), 064709 (2014).
244. M. Dhifallah, A. Dhouib, S. Aldulaijan, F. D. I. Renzo and H. Guesmi, *The Journal of Chemical Physics* **145** (2), 024701 (2016).
245. K. Yang and B. Yang, *Physical Chemistry Chemical Physics* **19** (27), 18010-18017 (2017).
246. B. Hammer, L. B. Hansen and J. K. Nørskov, *Physical Review B* **59** (11), 7413-7421 (1999).
247. R. Tran, Z. Xu, B. Radhakrishnan, D. Winston, W. Sun, K. A. Persson and S. P. Ong, *Scientific Data* **3**, 160080 (2016).
248. W. Liu, Y. F. Zhu, J. S. Lian and Q. Jiang, *The Journal of Physical Chemistry C* **111** (2), 1005-1009 (2007).
249. G. McElhiney, H. Papp and J. Pritchard, *Surface Science* **54** (3), 617-634 (1976).
250. D. A. Outka and R. J. Madix, *Surface Science* **179** (2), 351-360 (1987).
251. M. Kulawik, H. P. Rust, N. Nilius, M. Heyde and H. J. Freund, *Physical Review B* **71** (15), 153405 (2005).
252. G. Kresse, A. Gil and P. Sautet, *Physical Review B* **68** (7), 073401 (2003).
253. P. J. Feibelman, B. Hammer, J. K. Nørskov, F. Wagner, M. Scheffler, R. Stumpf, R. Watwe and J. Dumesic, *The Journal of Physical Chemistry B* **105** (18), 4018-4025 (2001).
254. A. Ruban, B. Hammer, P. Stoltze, H. L. Skriver and J. K. Nørskov, *Journal of Molecular Catalysis A: Chemical* **115** (3), 421-429 (1997).
255. W. Kirstein, B. Krüger and F. Thieme, *Surface Science* **176** (3), 505-529 (1986).
256. J. B. Miller, H. R. Siddiqui, S. M. Gates, J. N. R. Jr., J. T. Y. Jr., J. C. Tully and M. J. Cardillo, *The Journal of Chemical Physics* **87** (11), 6725-6732 (1987).
257. X. Guo and J. T. Y. Jr., *The Journal of Chemical Physics* **90** (11), 6761-6766 (1989).
258. P. A. Redhead, *Vacuum* **12** (4), 203-211 (1962).
259. C. T. Campbell, L. H. Sprowl and L. Árnadóttir, *The Journal of Physical Chemistry C* **120** (19), 10283-10297 (2016).
260. A. V. Ruban, H. L. Skriver and J. K. Nørskov, *Physical Review B* **59** (24), 15990-16000 (1999).
261. R. Bliem, J. E. S. van der Hoeven, J. Hulva, J. Pavleček, O. Gamba, P. E. de Jongh, M. Schmid, P. Blaha, U. Diebold and G. S. Parkinson, *Proceedings of the National Academy of Sciences* **113** (32), 8921-8926 (2016).
262. Z. Wang and P. Hu, *Physical Chemistry Chemical Physics* **19** (7), 5063-5069 (2017).
263. M. Andersen, A. J. Medford, J. K. Nørskov and K. Reuter, *Angewandte Chemie* **128** (17), 5296-5300 (2016).
264. J. Saavedra, H. A. Doan, C. J. Pursell, L. C. Grabow and B. D. Chandler, *Science* **345** (6204), 1599-1602 (2014).
265. G. Germani and Y. Schuurman, *AIChE Journal* **52** (5), 1806-1813 (2006).
266. D. A. Outka, C. M. Friend, S. Jorgensen and R. J. Madix, *Journal of the American Chemical Society* **105** (11), 3468-3472 (1983).
267. A. J. McCue, R. T. Baker and J. A. Anderson, *Faraday Discussions* **188** (0), 499-523 (2016).
268. X. Cao, A. Mirjalili, J. Wheeler, W. Xie and B. W.-L. Jang, *Front. Chem. Sci. Eng.* **9** (4), 442-449 (2015).
269. P. A. Sheth, M. Neurock and C. M. Smith, *The Journal of Physical Chemistry B* **107** (9), 2009-2017 (2003).
270. A. Clotet and G. Pacchioni, *Surface Science* **346** (1–3), 91-107 (1996).
271. A. McCue and J. Anderson, *Front. Chem. Sci. Eng.*, 1-12 (2015).
272. D. Mei, M. Neurock and C. M. Smith, *Journal of Catalysis* **268** (2), 181-195 (2009).
273. A. V. Zeigarnik, R. E. Valdés-Pérez and O. N. Myatkovskaya, *The Journal of Physical Chemistry B* **104** (45), 10578-10587 (2000).
274. A. Paul, M. X. Yang and B. E. Bent, *Surface Science* **297** (3), 327-344 (1993).
275. B. Ni and X. Wang, *Advanced Science* **2** (7), 1500085-n/a (2015).